THE UNIVERSITY *of* EDINBURGH

Fracture-Related Diagenesis: A Record Of Fluid Flow Through The Thamama Group, UAE

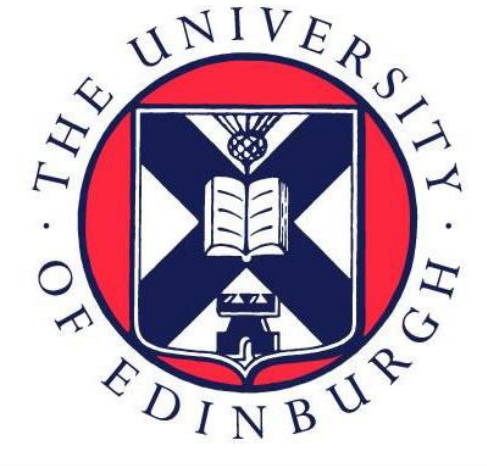

Mariam AL Blooshi

Thesis submitted for the degree of Doctor of Philosophy

School of Geosciences

The University of Edinburgh

2018

AUTHOR'S DECLARATION

I declare that this thesis has been composed solely by myself and that it has not been submitted, in whole or in part, in any previous application for a degree. Except where states otherwise by reference or acknowledgment, the work presented is entirely my own.

Mariam Al Blooshi

2018

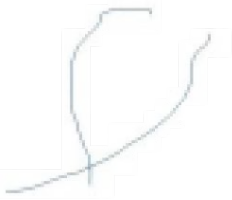

17/10/2018

ABSTRACT

Most of the hydrocarbon reservoirs in the world are carbonates, and most of these carbonate reservoirs are fractured. Fractures can form due to tectonic activity, mainly associated with fold and faults, and as a result of diagenesis. In many cases, the fractures in carbonates are cemented due to fluid flow, where these fluids precipitate cements. The presence of fractures can enhance reservoir fluid flow if the fractures were open and connected.

This thesis focuses on carbonate reservoir fractures, and understanding the evolution of fluids from the cements that have precipitated within them.

This thesis relates regional tectonic events to the formation of fractures, and of the environment and temperature of the fluids of precipitation in cement fractures the Early Cretaceous Thamama Group, in the United Arab Emirates (UAE). First, samples were studied from the subsurface in a highly faulted oil Field (A) located in South East Abu Dhabi. Core samples were taken from wells close to major faults in the field in both oil and water legs. Second, fractures in outcrop in Wadi Rahaba, Ras Al Khaima (RAK) in the Northern Emirates were studied where the Upper Thamama Group is exposed.

The field study in the outcrop included the fracture orientation and cement types. The fractures in the outcrop were divided into two main generations, F1, (en-echelon) and F2 and they were both fully or partially cemented. The main tectonic events that affected the fracture formation in the Thamama Group are foreland autochthon in the Precambrian to Lower Cretaceous, a frontal triangle zone in Neogene and Dibba zone which consists of Hawasina units (Triassic to Cretaceous), and the Sumeini units (Lower to Middle Cretaceous). F1 is related to the NS orientation fracture system consistent to the Arabian Trend sets caused by Cenozoic compression. F2 is related to the EW orientation fracture system matching Tethyan extensional trend sets.

Petrographic analysis of the subsurface thin sections revealed the presence of three main sets of fractures. Fracture Set 1 (cemented), Fracture Set 2 (open) and Fracture Set 3 (cemented, only in Lower Thamama). The fracture cement included equant and

blocky calcite as well as saddle dolomite. Cathodoluminescence (CL) analysis assigned the number of cement zones in each cement type in the fractures, and revealed more cement zones in the Lower Thamama reservoirs than the Upper. The most important diagenetic events were cementation and dissolution, which took place towards the end of the paragenetic sequence. The reservoirs contained significant amounts of stylolites, dissolution seams and bitumen, which were associated with most of the dissolution events.

$^{m}Mg/^{m}Ca$ obtained from in situ elemental analysis showed variation through the calcite and dolomite cement zones in the different reservoirs of the Thamama Group. This was inferred to be due to temperature changes. The Upper Thamama Reservoirs (A, B, and C) show lower $^{m}Mg/^{m}Ca$ (0.072-0.48) than the Lower Thamama reservoirs (F,G) (0,4-1.3), meaning that the Upper Thamama fracture calcite cements were precipitated at higher overall temperatures than the Lower Thamama reservoirs. Mn-Fe analysis allowed an understanding of the redox index through the different cement zones, in both Fracture Set 1 and Fracture Set 3. Analysis of Sr showed the absence of exotic fluids role in the diagenetic system.

In-situ (SIMS) $\delta^{18}O_{VPDB}$ values were obtained for the calcite cementation history of the two fracture sets in the five reservoirs of the Thamama Group. The $\delta^{18}O_{VPDB}$ analysis indicated that Fracture Set 1 has a longer cementation history than Fracture Set 3, and has wider range of temperatures (58-128°C).

A comparison of the outcrop analysis results and the subsurface reservoir was established at the end to distinguish the similarities and differences between the subsurface and outcrop in fracture types, fracture cement types and characteristics of the elemental analysis curve behaviours. The fracture cement in both subsurface and outcrop seemed to be precipitated at deep burial environment.

ACKNOWLEDGEMENTS

I would like to thank heartily and deeply my primary supervisor Rachel Wood for her unlimited guidance, support and positive energy during my whole PhD study. Thanks to my additional supervisors, Mark Wilkinson, Joyce Nielson and Sebestian Geiger as well as my industrial supervisors Sadoon Murad and Jorge Gomes for their readiness to help and Hisham Shebl for joining us and giving us in the field trip to RAK and sharing his expertiese. Thanks to John Craven, Chris Hayward, Mike Hall and Nicola Cayze for their technical assistance.

Thanks a lot for ADNOC for my PhD scholarship and ADNOC Onshore for funding my PhD project, providing the data and answering my questions about the field.

Thanks to my dearest friend, Amena Al Harthi who I was so lucky to have in the attic during my study period, just thank you for everything. Thanks to all my friends who I didn't mention their names here.

Thanks to my lovely kids for bearing with me big time being away for four years, and declaring that you are proud of me. I am the proudest mother.

Finally, special thanks to my special husband who made my last seven months of PhD a living heaven.

DEDICATION

For my sweet kids and beloved husband.

CONTENTS

List of Figures

List of Tables

CHAPTER 1: Introduction

1.1 Introduction

Carbonate formations house 60% of known conventional hydrocarbon reserves (Bagrintseva, 2015). Fractures in carbonates are significant, as at least 85% of carbonate reservoirs are naturally fractured (Lamarche et al., 2012). Carbonate rocks have a high sensitivity to brittle deformation due to their unique diagenetic evolution from deposition to burial. They are complex due to their heterogeneous nature in terms of origin, diagenesis, and geometries of in-situ formation. Their reservoir and geomechanical properties are also highly dependent on the gain or loss of porosity during diagenesis and deformation (Lamarche et al., 2012). Rocks often fracture during the evolution of a sedimentary basin, due to the relation between stress, rock strength and fluid pressure (hydrofractures) (Nollet et al., 2009; Asfar et al., 2014). Diagenesis and fracturing can significantly alter the petrophysical properties of subsurface carbonate reservoirs as these control pore size and connectivity, and so permeability (Vandeginste, 2013).

Fracturing is mainly controlled by factors such as lithological properties, grain size, layer thickness, and stratigraphic characteristics including facies, depositional cycles and diagenesis. Tectonic processes can increase the number of fractures during the final steps of diagenesis and uplifting (Hoseinabadi et al., 2016).

The presence of open fractures in carbonates can allow fluids to pass through the matrix by connecting the matric porosity to fracture systems. This in turn can promote diagenetic processes such as cementation and dissolution. It is therefore important to understand the role of fractures in either enhancing or reducing the porosity and permeability of a reservoir because fractures may both control the initial oil distribution, and enhance or impede oil recovery (Bourbiaux, 2010). A combination of the effective stress conditions and the availability of supersaturated fluids, will cause pre-existing fractures which formed due to the relation between stress, rock strength and fluid pressure to stay open, collapse or seal with

precipitating minerals (Laubach et al., 2004; Nollet et al., 2005a; Laubach & Ward 2006). In addition, understanding fluid flow in fractured strata is essential to develop conceptual models that explain the spatial and temporal distribution and connectivity of reservoir porosity and permeability on regional and basinal scales (Haeri-Ardakani et al., 2013). Fluid flux along fractures during basin evolution is often expressed in the formation of vein minerals. Cements in fractures therefore provide a record of the origin and geochemical evolution of fluids during thermal–tectonic evolution of sedimentary basins.

This thesis explores the relationship between diagenesis and fractures, using a case study from an onshore carbonate hydrocarbon field (Field A) in the Lower Cretaceous Thamama Group, located in the Abu Dhabi region of the United Arab Emirates (UAE). The Thamama Group is present in many reservoirs across the onshore and offshore of the UAE (Figure. 1.1A). Field A was subjected to two major stress movements that affected the whole SE area of Abu Dhabi, the Oman mountain orogeny and Zagros belt thrust movement (Ali et al., 2008). In addition to subsurface core, an outcrop of the Thamama Group in Ras Al Khaimah in the Northern Emirates was also studied (Figure 1.1B).

Figure 1.1A: The two location of the study. A: onshore oil field, SE Abu Dhabi. B: outcrop in Ras Al Khaima, Northern Emirates (map from Grainer et al, 2003).

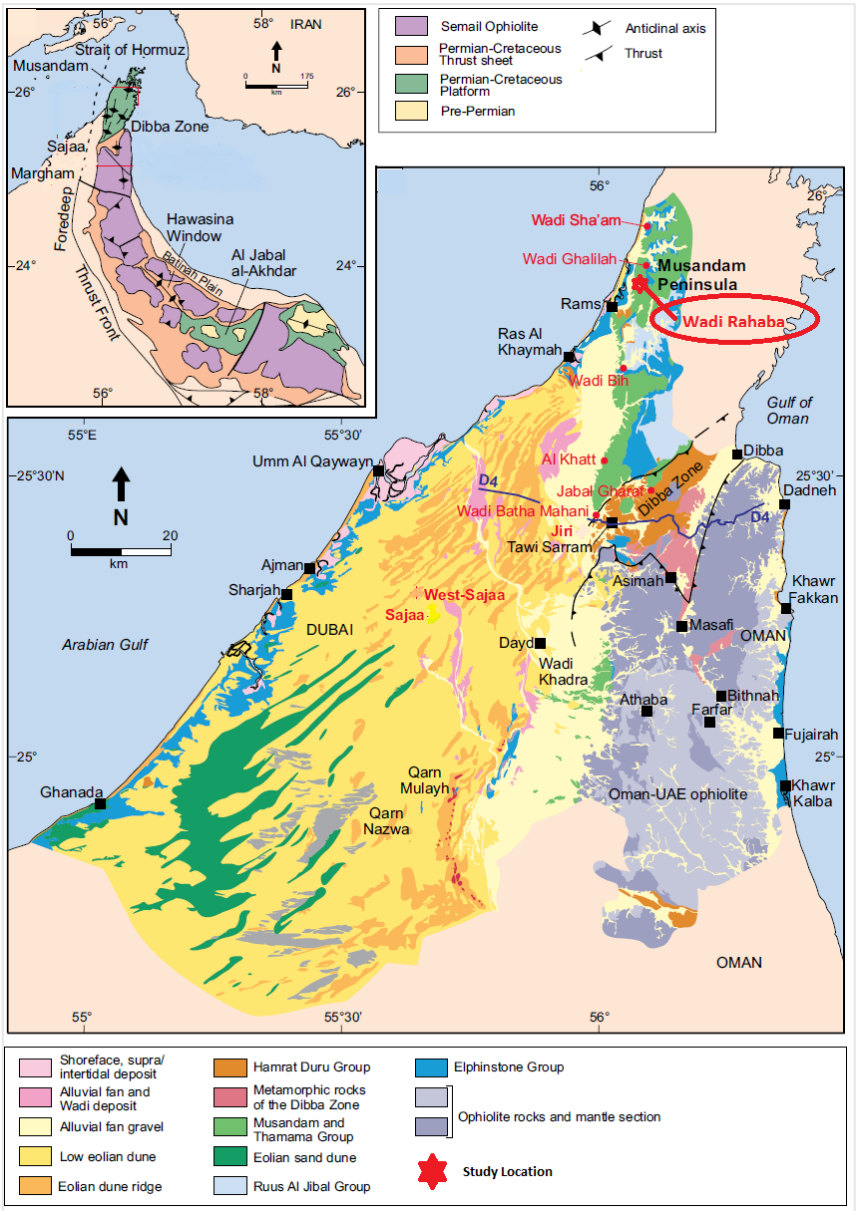

Figure 1.1B. Location of Wadi Rahaba in Ras Al Khaymah, UAE (Modified from Breesch et al., 2011).

The study focuses on five reservoirs of the Thamama Group. The Upper Thamama (Reservoirs A, B and C) and the Lower Thamama (F and G). Reservoir A belongs to Shuaiba Formation, B and C belong to Kharaib Formation and F & G belong to Lekhwair Formation.

Fractures generated in association with folding may significantly influence the migration and concentration of fluids within and around these various structures,

however, in order to predict the role that these fractures have in controlling fluid movement it is important to understand the timing of their formation (Cosgrove & Ameen, 2000).

There is no published work on the timing of cementation or details of diagenesis of the fractures of Field A. This thesis explores the role of tectonics in the evolution of the fractures in Field A, and, in particular, the relationship of diagenesis to fracture formation as a result of changes in fluid movement creating both cementation or dissolution events.

1.2 Thamama Group, UAE

1.2.1 Depositional history and stratigraphic settings

The Cretaceous of the U. A. E. represents a time of productive development of carbonate platforms and offshore banks and buildups (Hamdan and Alsharhan, 1991). The extensive flooding of the Arabian Peninsula produced a carbonate sequence that formed the Lower Cretaceous in the UAE (Alsharhan, 1989).

The Thamama Group is Lower Cretaceous age and it is a carbonate sequence ranging between 2198 ft and 3281 ft in thickness, where the sediments were deposited over 24 Ma (Berriasian to mid-late Aptian) under carbonate platform to shallow basinal conditions (Alsharhan and Kendall, 1991).

The Thamama Group is described as a shallow marine carbonate sequence that is composed of grainstones, packstones and wackstones, becoming dolomitic toward the base of the Group (Sims et al., 2013). The Group is composed of cyclic porous (reservoir) and non-porous (dense) carbonates, and is divided into four formations: Habshan, Lekhwair, Kharaib and Shuaiba (Alsharhan and Nairn, 1986; Ali et al., 2008). Figure 1.2 summarizes the main stratigraphic groups and tectonic events (Ali et al, 2008). They are: Lower Jurassic active rifting (200-183 Ma), which led to the opening of the West Indian Ocean (Lamotte et al., 2015), Semail Ophiolite obduction which occurred during the Upper Cretaceous after deposition of the Thamama,

Wasia and Aruma Groups (65- 92 Ma), and the Zagros orogeny (13-48 Ma) (Austermann and Iaffaldano, 2013). Dating method used was Strontium isotopes.

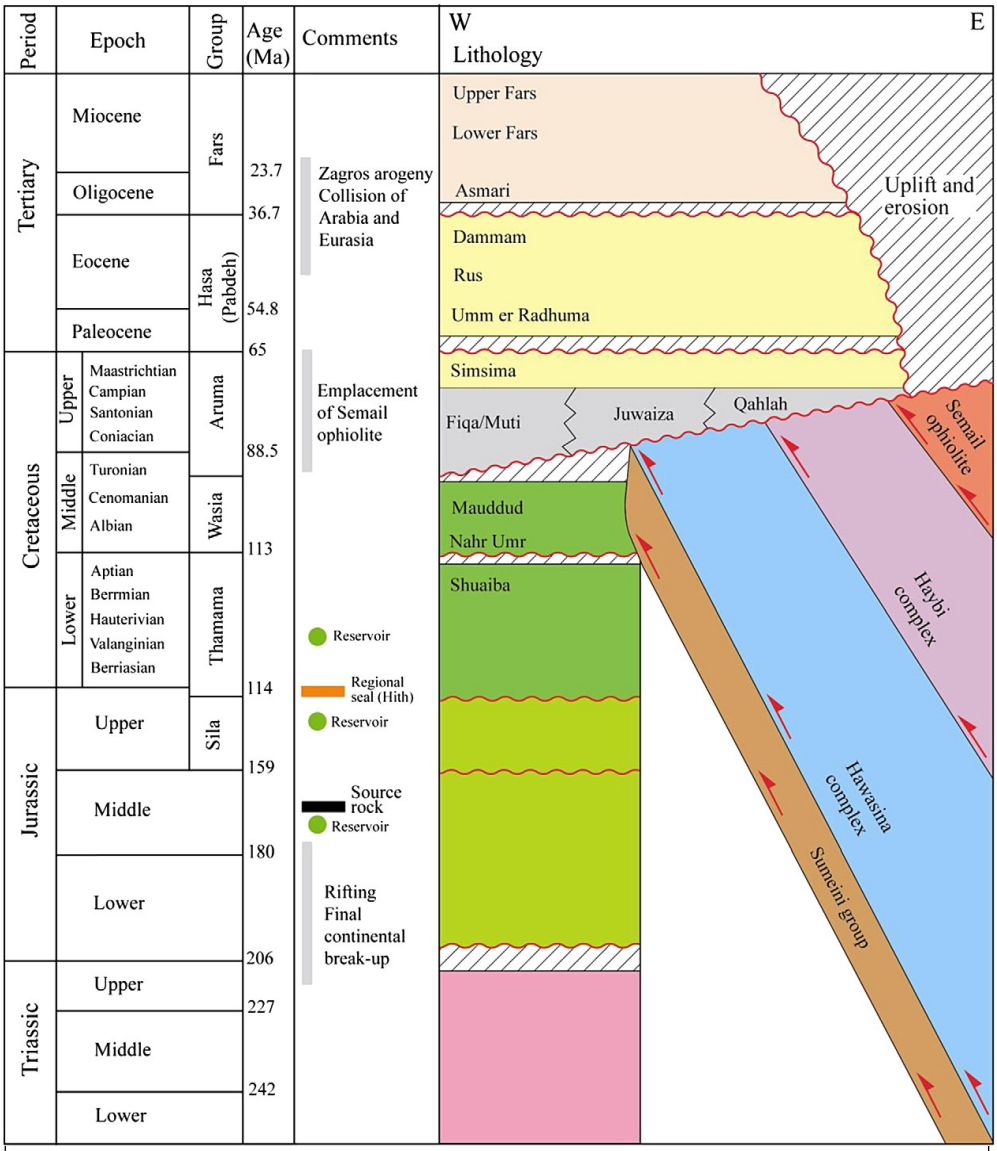

Figure 1.2: Cretaceous Stratigraphy of the UAE and the main tectonic events (Ali et al, 2008)

The main interest of this thesis is in the reservoir zones within the Lekhwair, Kharaib and Shuaiba Formations, further divided into reservoirs (Figure 1.3). Onshore fields follow a letter scheme, A to H, and offshore fields have a classification following a roman numeral scheme. Reservoir A belongs to the Shuaiba Formation, Reservoirs B and C belongs to the Kharaib Formation, and the three onshore Reservoirs (A, B and

C) are categorized as Upper Thamama Reservoirs. Onshore Reservoirs F and G belongs to the Lekhwair Formation and they together form the Lower Thamama.

During deposition of the Lekhwair Formation (Hauterivian to early Barremian), minor tectonic pulses created a series of minor transgressions and regressions (Alsharhan, 1989). The lower boundary of this formation is marked by minor erosional surfaces. Its upper surface is truncated and on-lapped by the Kharaib Formation, and its lowest cycle onlaps the Arabian platform over the Habshan Formation (Alsharhan and Kendall, 1991). In addition, the control of carbonate production is an interaction between eustatic sea-level fluctuations and climate fluctuations.

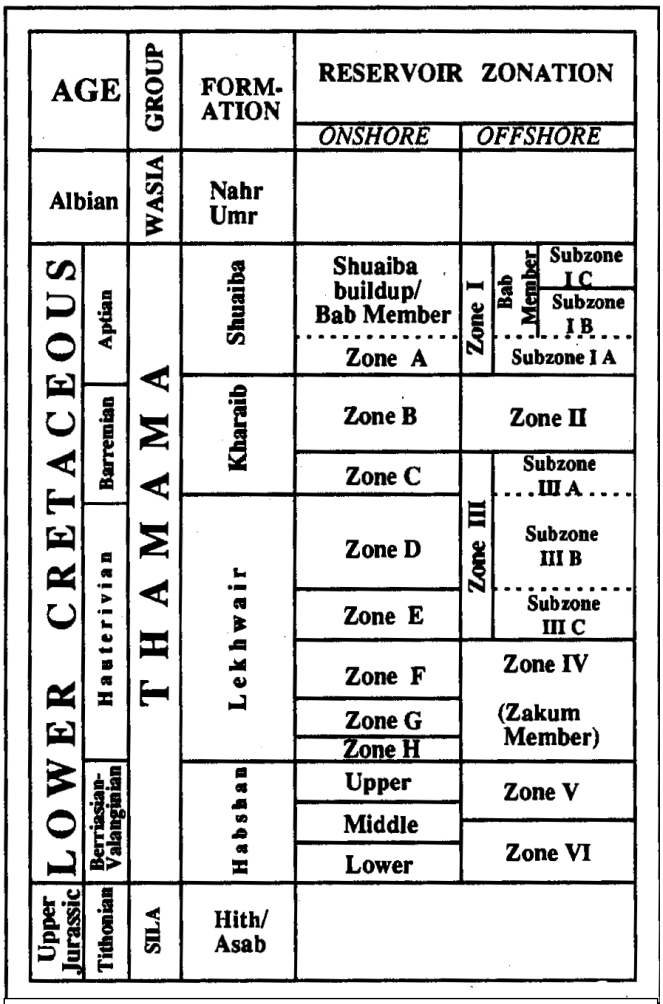

Figure 1.3: Cretaceous Stratigraphy of the Thamama Formation in the onshore and offshore UAE (Alsharhan, 1990)

Shallow, cyclic sedimentation took place in the area. Each cycle is composed of a lower part, consisting of dense argillaceous lime mudstones-wackestones and minor mudstone that grade upwards into peloidal packstone-grainstones (Alsharhan, 1989).

The Lekhwair Formation is categorized as alternating cycles of shallow, sub-tidal turbulent-water grain-rich limestones, with deeper-water sub-tidal mud-rich carbonates. The depositional surface on the shallow carbonate ramp was extremely flat leading to the persistence of these cycles and their extensive development throughout the stratigraphic section (Alsharhan, 1989).

The Kharaib Formation (Barremian to early Aptian) is bounded at its base by a minor discontinuity at the top of Lekhwair Formation, and is capped by the basinal limestones of the Shuaiba Formation (AlSharhan and Kendall, 1991). The formation has laterally persistent lithofacies, which can be traced over 130 km (Budd, 1989). It is composed of two sedimentary cycles (AlSharhan and Kendall, 1991); the porous, grain-supported limestones (skeletal-pelletal grainstones and packstones) represent regressive phases, whereas the mud-supported tight limestone (skeletal wackestones and mudstones) units represent marine transgressions (Budd, 1989). These HSS deposits shallowing upward shallow-water-shelf cycles are interpreted to have formed as high-energy grainstone/packstone, that was deposited at or above wave base (often a hydrocarbon reservoir) during the high-stand phase of the sea-level cycles, and as leached microporous wackestones, with dense argillaceous stylolitic mudstone (often a seal over a reservoir, where the micro pores have minimal effect). There are two explanations for the sources of these dense intervals. That they were deposited in a low energy, subtidal setting related to the transgressive phase of the sea-level cycle (Alsharhan and Kendell, 1991), or that they were deposited in a restricted shallow-lagoonal setting (Rathod, 2003; Al Mansoori et al, 2008).

The porous units were laid down on very shallow, epeiric shelf seas above wave-base level. These carbonate cycles formed during substantial fluctuations in the rate of production and deposition of carbonate sediments on a regionally extensive carbonate ramp (Alsharhan, 1989).

The Shuaiba Formation (early to mid-Aptian) is the upper most and the last event in the deposition of the Thamama Group, and it records the differentiation of the stable craton in early Aptian time into an intrashelf basin surrounded by shallow carbonate shelf facies. The Shuaiba intrashelf basinal facies occupies a depression in the stable craton, which was most likely formed by differential rates of subsidence due to rapid crustal cooling. It consists mainly of well-bedded gray to dark gray-brown dense and argillaceous lime mudstones and wackestones, followed by packstones, intercalated rudist and algal boundstones and grainstones (Budd, 1989). There are also gray shales and inter-beds with deep-water marine fauna in the upper part of Shuaiba (Alsharhan, 1989; Yin et al., 2018). The Shuaiba Formation is about 75 m thick.

1.2.2 Sequence stratigraphy and depositional environment

The Thamama Group is divided into two second-order supersequences (Mueller et al., 1993; Strohmenger et al., 2006): the Habshan Formation supersequence and the younger supersequence (Figure 1.4) which encompasses the interval between the top Habshan and top Shuaiba formations.

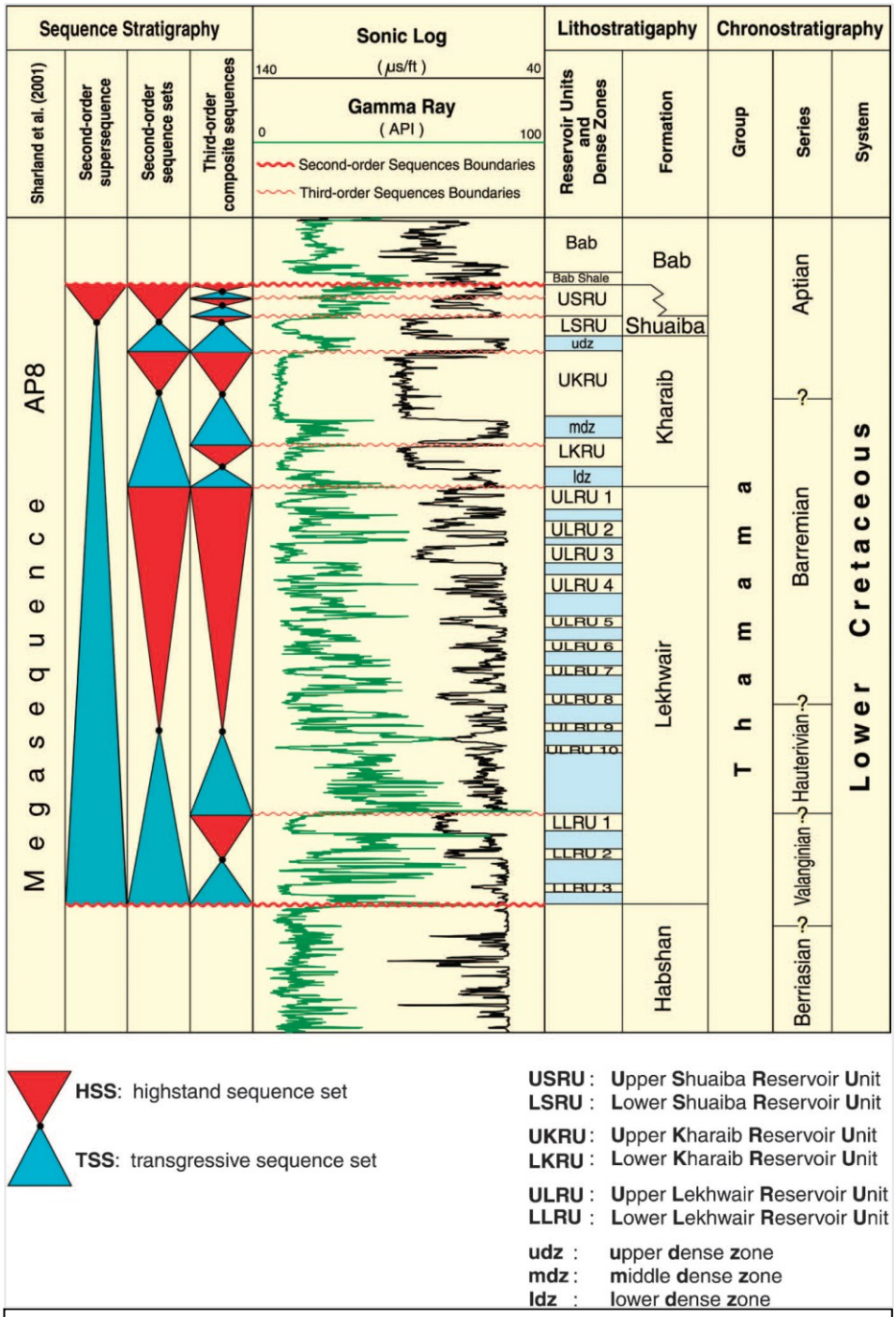

Figure 1.4. Upper Thamama Group, UAE, sequence stratigraphic framework (Strohmenger et al., 2006)

This supersequence's transgressive sequence includes the Lekhwair (including Reservoirs F and G), and the Kharaib formations (Valanginian to early Aptian) (Reservoirs B and C); while Shuaiba formation (Reservoir A) is part of the late

transgressive sequence set (early Aptian) and the highstand sequence set (Late Aptian) of this longer term depositional cycle (Strohmenger, 2006).

Lekhwair Sequence-stratigraphic Framework, facies and depositional environment

The cyclic character of the lithology of the Lekhwair in offshore Abu Dhabi varies from open marine subtidal to inner shelf lagoonal to intertidal carbonates, with compositions that range from shaley stylolitic micrites to micrites to grainstones upwards (Alsharhan, 1989), and is thought to have been driven by high-frequency changes in sea-level.

The Lekhwair Formation represents sediment deposited during a gentle sea-level rise, superimposed on which are six minor higher frequency variations which produced six shoaling-upwards sedimentary cycles (Alsharhan, 1991).

The top of the Lekhwair system is marked by a bored hard-ground which exhibits strong early diagenesis including an early episode of lithification that occurred after a burrowing stage and before a boring stage. This event may have been accompanied by minor subaerial exposure as indicated by an early leaching of aragonitic bioclasts, with the resulting voids later filled by sediments (Granier et al., 2003).

In the onshore Abu Dhabi, similar shoaling cycles can be seen with porous grainstone and packstone at the top, microporous wackestones in the middle, and argillaceous impermeable dense mudstones at the base. The dense limestones represent the transgressive phase of subtidal, open shelf setting responding to rises in sea-level, whereas the porous limestones represent the regressive phase of a shallower water, near wave base setting (Alsharhan, 1991).

The diverse biota, the scarcity of miliolids and the succession of homogeneous facies points to normal, stable marine conditions. The few sedimentary structures that have been observed indicate storm influence, and the texture of the sediments suggests relatively deep, lagoonal environments above storm wave base (Pittet et al., 2002).

The uppermost part of the Lekhwair formation consists of mud and wackestones with aragonitic and non-aragonitic foraminifers and algae. This "aragonitic algal debris facies" is characteristic of an inner platform depositional environment (Granier et al., 2003). The presence of mudstone and wackstones suggests low-energy conditions. Decimetre-scale rudist floatstones and rudstones truncate the low-energy deposits. Bedding is rare in these deposits, and the facies are quite homogeneous (Pittet et al., 2002).

Kharaib and Lower Shuaiba Sequence-stratigraphic Framework, facies and depositional environment

The Kharaib Formation, corresponds to the late transgressive sequence set (TSS) of a second-order supersequence. It is a second-order sequence set made up of two third-order composite sequences. The lower third-order composite sequence starts at the base of the lower dense zone and is capped by a sequence boundary (exposure surface) about 20 ft below the middle dense zone (Strohmenger, 2006). Kharaib is overlain by a third-order composite sequence that is bounded on top by a regionally correlative sequence boundary below the upper dense zone (Strohmenger, 2006). According to Strohmenger et al., 2004; 21 lithofacies types were defined for Kharaib and Lower Shuaiba formations based on texture, grain types, sedimentary structures, faunal content, and lithologic composition. Thirteen lithofacies types correspond to the reservoir units, range from open platform, deeper subtidal, lower ramp, to shallow subtidal to intertidal, upper-ramp environments. Eight lithofacies types occur in the dense zones which represent organic- and siliciclastic-rich, inner-platform, restricted lagoonal deposits (Strohmenger, 2006). The depositional environment of Shuaiba varies from shallow shelf to deep-water slope sediments (Jangmaw, 2005).

Although the latest sequence stratigraphy based on Stohmenger (2006) has been followed until now in the oil industry, this view was opposed recently by Ehrenberg et al. (2018). The opposition was based on evidence from cores that suggests that the repetitive alternations of rudstone and floatstone (coarse) beds with encircling packstone to wackestone (fine-grained beds) that reflect periodic storm events rather

than cyclic variations in water depth. Ehrenberg therefore agrees with the Pittet et al. (2002) view, which noted the storm effect on the Thamama group lithologies.

1.3 Tectonic evolution of the Thamama Group

The Arabian Plate has been widely influenced by eaustatic sea-level changes and is known to have a complex tectonic history (Hag and Al Qahtani, 2005). The Arabian Peninsula is known to have three natural boundaries (Alsharhan & Nairn, 1986); the Red Sea separating it from Africa, The Arabian Gulf with the Gulf of Oman separating it from Iran, and the Arabian Sea, which is the Southern boundary. It is described by Alsharhan & Nairn (1986) to be broadly flexured with two NE-SW trending elements (Figure 1.5):

1- The Rub Al Khali depression in the south
2- The Central Arabian Arch, which is a broad anticlinal structure to the north

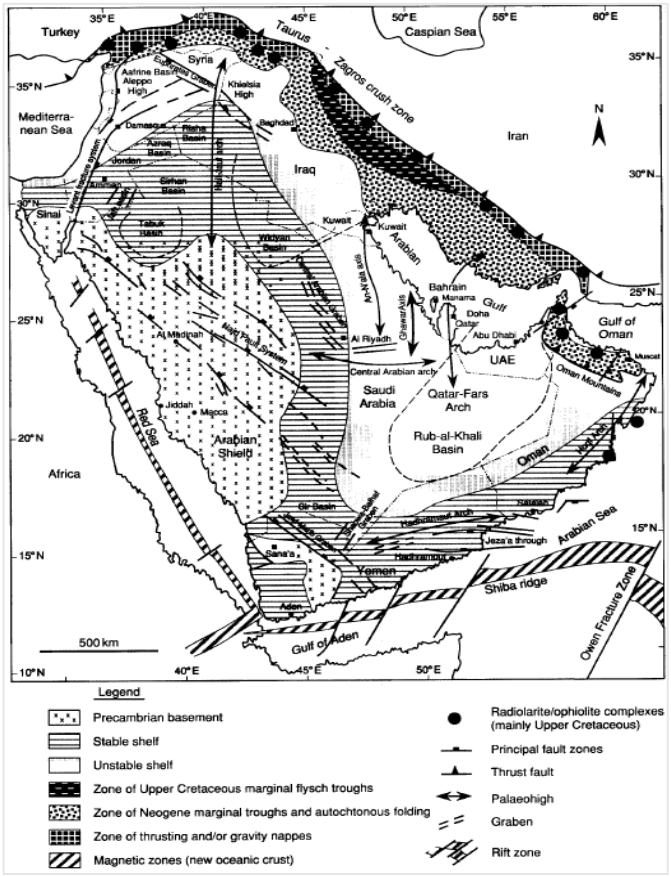

Figure 1.5: Main structural elements in the Arabian Plate (Al-Jallal & Alsharhan, 2005)

In the Late Precambrian, the major tectonic event was the Najd shear-zone-related rifting (530-630 Ma), which resulted in the development of rift salt basins filled with carbonates and continental clastics in the Hormuz region (Sultan et al., 1988; Alsharhan, 2014).

During the Cambrian to Permian, the Arabian Peninsula formed part of the Gondwana passive margin. The Arabian Plate has behaved as a coherent block and has been theoretically stable since the end of Precambrian. During the Cambrian, subsidence started after peneplanation on the Arabian Plate and during the Ordovician, a gentle hinterland uplift on Arabia took place and glaciation on the Arabian Platform (440 Ma) followed an isostatic rebound. In the Devonian, the Hercynian Orogeny began in the Arabian Plate which resulted in several phases of

compression and block faulting and relative uplift, collision of Gondwana and Laurassia and formation of the Arabian Platform. The Hercynian Orogeny ended in the Early Carboniferous, causing the Arabian Plate to tilt gently to the NE margin and the Palaeotethys to form, while during the Late Carboniferous, the Hercuynian Carboniferous unconformity in the Arabian Plate resulted in back-arc rifting and basaltic volcanic in Northern Arabia as well as initiation of subduction beneath the NE margin of Gondwana (Eyles, 1993; Ziegler, 2001; Alsharhan, 2014). Throughout most of the Phanerozoic, the whole region of the Middle East was an integral part of the African plate. The opening of the Red Sea–Gulf of Aden resulted in 6-7^0 anticlockwise rotation of the Arabian Plate relative to the African Plate, and the Dead Sea transform fracture system was formed. As the Arabian Plate moved north during the Pliocene, it gave rise to the Taurus– Zagros orogenic ranges and sutured Arabia onto Eurasia (35 Ma) (Allen et al., 2004; Allen et al., 2008; Vincent et al., 2007; Alsharhan, 2014) (Figure 1.6).

The basement in Arabia now is formed from the Precambrian-Cambrian rocks and record three major orogenic sequences: Kibaran, Heijaz and Najd. These North-South trending preserved sutures; represent episodes of plate collision and magmatism. The Hormuz salt basin developed along the east side of the Peninsula around 520 Ma (Bahroudi and Koyi, 2003; Alsharhan and Kendall, 1986).

Alsharhan and Kendall (1986) have identified four distinct salt basins: (1) the Dhufar-Ghaba in South Oman, (2) the Fahud, (3) the Southern Gulf, and (4) the Northern Gulf. The salt of these basins exerted a major influence on the structure of the area throughout the Phanerozoic. The differences in overburden thickness and lithology have determined the unique style of salt tectonics for each basin (Murris, 1980; Alsharhan and Kendall, 1986; Huc et al., 2000).

The salt diapirism in the Southern part of the Arabian Gulf produced several islands, which carried erratic Early Palaeozoic rocks to the surface causing extrusion of the Hormuz Salt. Seismic surveys have detected shallow salt piercements in offshore Abu Dhabi (Alsharhan and Kendall, 1986).

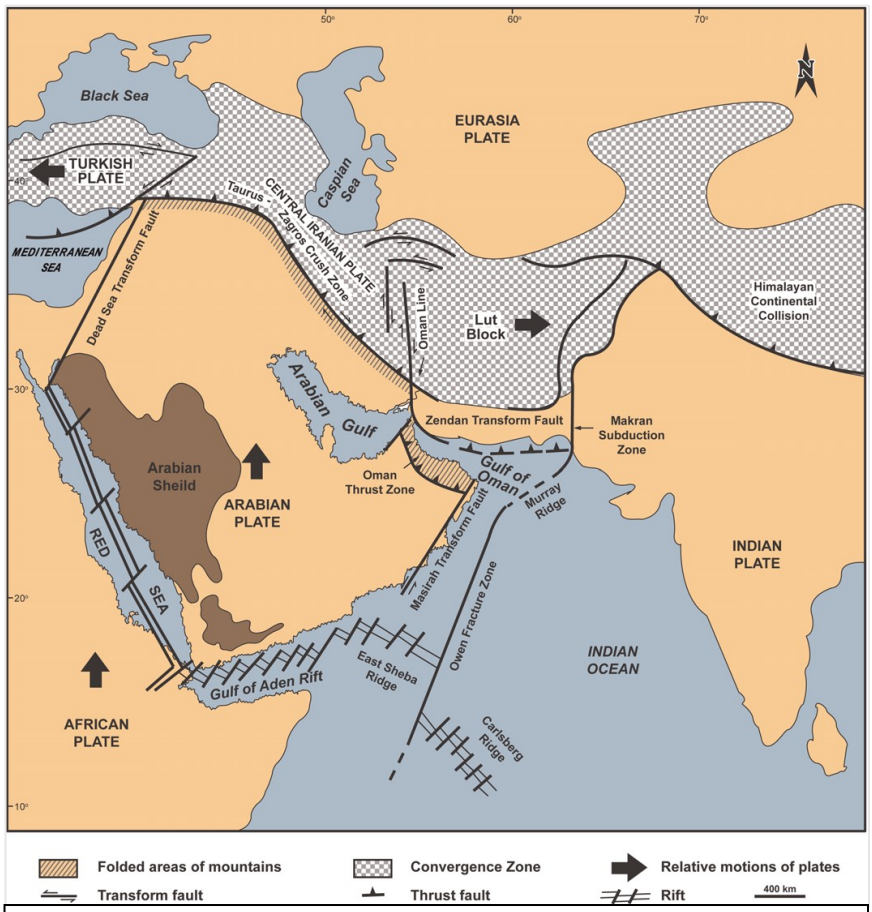

Figure 1.6: Plate tectonic map of the Middle East (Alsharhan, 2014)

During the Middle Permian, rifting started in the eastern border of the Arabian Plate, resulting in the opening of Neo-Tethys Ocean (Fontana et al., 2012). From the Middle Permian to Early Cretaceous, over 3km of carbonate sediments were deposited on a carbonate platform. The Triassic was a period of regional uplift and transgression (Alsahrhan & Kendall, 1986), whilst the Late Triassic witnessed the initial break up of Pangea (185 to 100 Ma), which ended the spreading in Neothys-1 in Oman and Zagros, and started the Neotethys-2 of Zanjan-Taffan in East Iran and the deposition of the Hawasina. Back-arc rifting in the Northern Arabia resulted from closing of the Palaeotethys and opening of Neothethys during the Early Triassic, followed by deep-marine continental margin development in Oman and oceanic crust in East Iran in the Late Jurassic. The rifting of the South Arabian margin and tilting of the Northern margin took place in the Middle Jurassic (Veevers,

2004; Alsharhan, 2014; Rollinson et al., 2014). The Cretaceous was an interval when many tectonic activities took place. During the Early Cretaceous, The Hawasina obduction started in Oman. An eastward-directed subduction arose during Middle Cretaceous, and the obduction of the Semail ophiolite started along the NE margin of the Arabian Plate. In the Late Cretaceous, the Semail Ophiolite obduction ended on the Arabian Platform and the Hawasina obduction continued and ended by the Maastrichtian (Fontana et al., 2012; Alsharhan, 2014). The closure of Neotethys and initial rifting in the Red Sea happened during the Eocene and led to collision of the Arabian Plate with Asia and tilting of the Plate to the NE margin. Finally, the Zagros and Oman fold belt formed during the Miocene after collision on the Eastern Arabian margin (Nissen et al., 2011; Alsharhan, 2014).

The geological evolution of the United Arab Emirates during the Mesozoic can be directly related to the opening of the southern Neotethys Ocean during the Triassic and its eventual closure in Late Cretaceous to Palaeogene times. The majority of the rock units in this area were formed within Neotethys, but their present-day distribution is largely the result of processes associated with closure of this ocean (Phillips et al., 1998).

The tectonic evolution of the southern margin of Neotethys can be divided into three main stages (Phillips et al., 1998; Muttoni et al., 2009; Goodenough et al., 2014):

Stage 1 – Initial rifting and formation of the Neotethys Ocean, followed by a prolonged period of stable, passive margin sedimentation which extended from the Permian to Late Jurassic times

Stage 2 – Late Jurassic to Early Cretaceous uplift and erosion of the shelf margin, coincident with increased carbonate-clastic sedimentation in the outer ramp, distal slope and basinal areas

Stage 3 – Late Cretaceous increased instability, breakup of the platform margin and foreland basin sedimentation accompanying the obduction of the Oman-UAE ophiolite (the volcanic complex with the slope deposits and the

basin sediments all obducted on the autochthonous Arabian Platform (Fontana et al., 2012) (Figure 1.7).

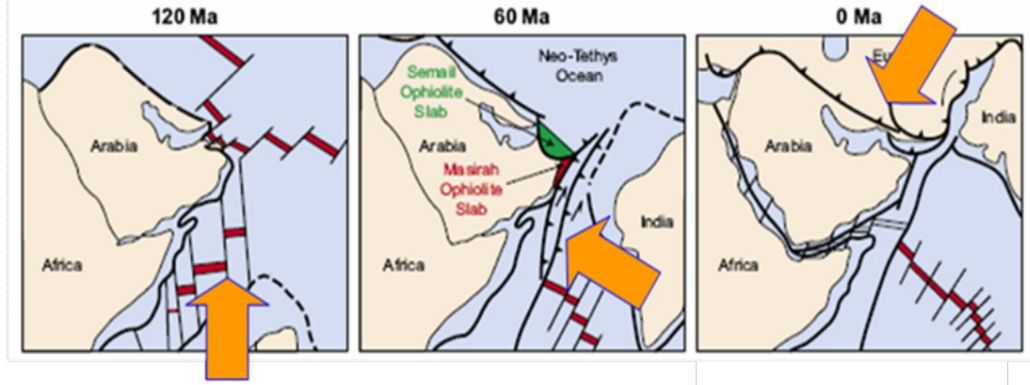

Figure 1.7: Sketch maps showing the evolution of the Indian-Arabian Plates convergence over time and subsequent ophiolites obduction in NE and East of Arabia (Sirat et al., 2013)

The two main tectonic provinces in the UAE are a passive plate- margin (intracratonic) region, including Abu Dhabi and offshore and part of onshore Dubai - Ras Al Khaimah, and a foreland basin, which developed to the west of the uplifted area, as a flexural response of the Arabian lithosphere to the ophiolite obduction (Fontana et al., 2012), and adjacent foreland fold- and thrust-belt region in onshore northern UAE (Alsharhan, 1989).

Large, gentle folds of various shapes and sizes dominate the passive plate-margin region, mostly periclinal in style, with flank dips generally less than 5°. North-South folds are dominant in the area and may represent an alignment of drape-folds over an east- dipping north-south listric normal fault in the basement, reactivated in reverse slip in response to east-west Oman stresses. East of the Falaha syncline, the structural style is dominated by NE-SW trending fold-axes representing a series of drape folds over a reactivated basement right-slip fault. Our field of interest lies within this area. To the NE. a NW-SE trending fold is associated with a dominant system of faults, which runs parallel to this trend. The NE-SW and NW-SE trends are similar to the trends that define the central Arabian Arch. In the central part of offshore Abu

Dhabi, folds aligned east-west related to Zagros folding are superimposed on the older north-south trending growth-structures of the Arabian folds (Alsharhan, 1989).

The trap development of the fields (in onshore Abu Dhabi) nowadays has resulted from repeated structural reactivation of the basement and the Oman mountains stress that took place during the Late Cretaceous is the reason for the folds structure grown trapping the hydrocarbons discovered to date in Abu Dhabi (Sirat et al., 2014).

Both the onshore and offshore of the UAE oilfields are situated in a tectono-stratigraphic region, which is known as the Arabian Platform of Unstable Shelf (Sirat et al., 2007) (Figure 1.8).

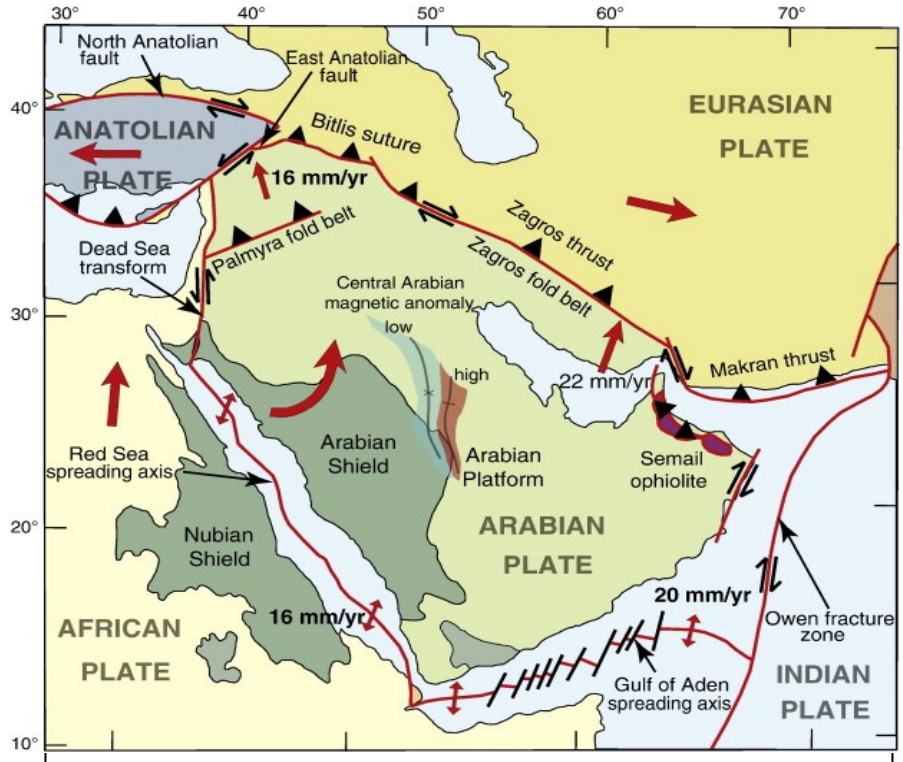

Figure 1.8: Simplified map of the Arabian Plate, with plate boundaries, showing Arabian Platform (Stern and Johnson, 2010)

Repeated E-W extensional tectonism have formed the 'old grain' of the Arabian Peninsula which is composed of igneous and metamorphic rocks of the crystalline Precambrian crust, and underlie both the interior Homocline and the Arabian

Platform (Henson, 1951; Sirat, 2007). The Plate tectonic setting of Arabia, is part of the dynamic plate tectonic framework of the Alpine Orogeny (Sirat, 2007).

The structural style of the foreland basin was affected in the East of the UAE due to the rejuvenated jostling of basement blocks, which caused the deformation of the sedimentary cover and the subsequent foreland basin, which contained mainly carbonate platform (Sirat et al., 2007). Another deformation has occurred since the Late Eocene to present by the collision between the Arabian and Eurasian plates (Alpine/Zagros orogeny). This is when the gentle open folding of the carbonates formed (Sirat et al., 2007).

1.3.1 Fracturing and fault system

When studying the relationship between fractures (including faults, joints and veins) and their conductivity in the oil industry, it was found that the regional and in-situ stresses have effect on specific attributes of fractures. That includes fracture geometry (strike orientation and dip), fracture type (tensile versus shear fractures), size (length, width and aperture), frequency (intensity of fracture per unit length), and fracture roughness (smoothness of the fracture planes; plumose versus slickensides) (Sirat et al., 2013).

In naturally fractured reservoirs like Field A, fracture networks play a key role in reservoir development (Berototti et al., 2014). The density of fractures in the Earth's crust decreases with depth. The upper 0.5-1 km is much more densely fractured than the rocks below. This is thought to be the result of the reduction of the overburden and confining stresses combined with weathering associated with exhumation (Cosgrove & Ameen, 2000). Fractured carbonate reservoirs are frequently very heterogeneous with admiration to both matrix and fracture properties. This heterogeneity is caused by fracturing at different scales, caused by deposition and diagenesis (Wennberg et al., 2016).

There many types of fractures, including fold-associated- or extensional fractures (buckle fold, forced folds formed above dip-slip basement faults, forced folds formed above oblique-slip basement faults), fault-associated (shear fractures), and fractures caused by diagenesis (Sapiie, 2010; Cosgrove & Ameen, 2015; Wennberg et al., 2016; Shafiei et al., 2018). In reservoirs, fractures can act in two ways, either by focusing the fluid flow (e.g., joints, sheared joints, and sheared pressure solution seams), or forming impermeable features (e.g., pressure solution seams) (Agosta et al., 2010). Understanding the contribution of faults and fractures in reservoir fluid flow is challenging, due to their complexity and the wide variation of their contribution nature (Aydin, 2000).

Normal faults tend to be aligned parallel or perpendicular to the fold axis. Those forming parallel to the fold axis form in response to the local extension that occurs in the hinge region of the fold above the neutral surface (Cosgrove & Ameen, 2000).

The presence of faults and fractures in the oil fields affects the production in them significantly, and most of the fields in Abu Dhabi are faulted and fractured (Morad et al, 2010). The fracture systems are thought to be formed during two major tectonic events, mentioned above as the two compressional stress regimes that affected the Arabian Gulf, separated by a period of tectonic relaxation. They are 1) the Oman stress and Dibba Zone in the Late Cretaceous from the East, NE, and the SW, 2) Zagros stress from the South, and the SW and the NE during the Oligocene-Miocene (Ziegler, 2001; Sirat et al, 2007; Fontana et al., 2012).

Murris (1980) described the main transform faults as follows (Figure 1.9):

1) The Zagros “crush-zone” to the North-East which is a major right-lateral strike-slip fault zone of late Tertiary to recent age and separates the Zagros Fold Belt from the tectonically very complex Hamdan-Sirjan zone of interior Iran.
2) Dibba line; where the crush zone terminates, which is a North- NE South-SW striking oceanic/continent transform fault lineament that separates continental

basement to its West from the oceanic realm of the Gulf of Oman-Makran to its East, forming the boundary between the Afro-Arabian plate and oceanic Tethys.

3) The Masira Line, which separates the Arabian continent from the Indian Ocean.

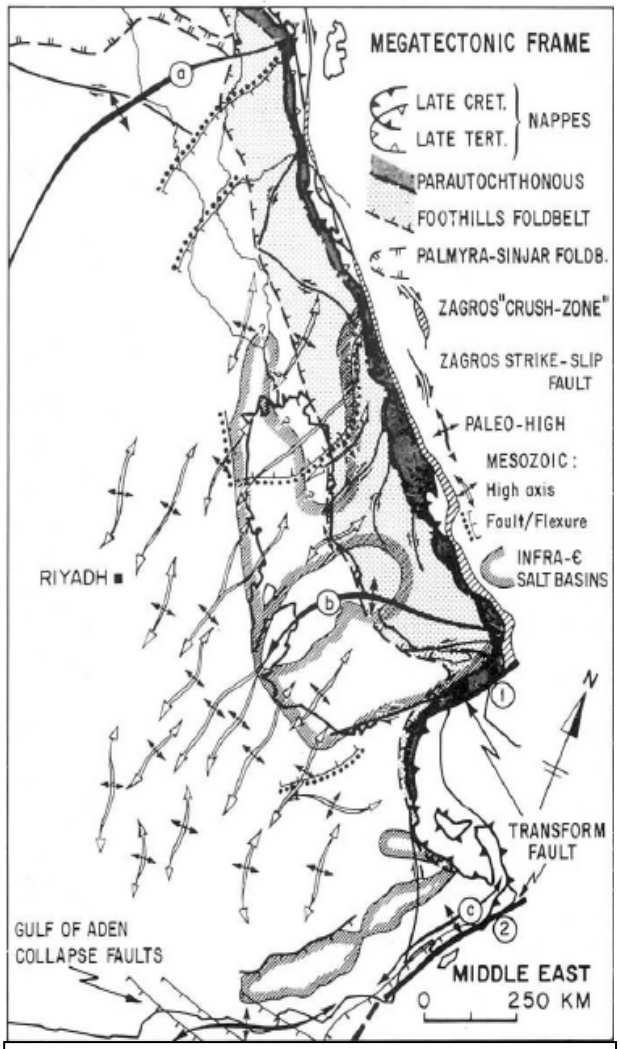

Figure 1.9: Transform faults of the Middle East (Murris, 1980).

Alsharhan and Nairn (1997) have defined some more faults in the area (Figure 1.10):

1) Maradi Fault, which trends North West-South East, parallel to and South of the Oman Mountains, and it has a left-lateral slip component.

2) Saiwan-Nafun Fault, which is activated during the Late Cretaceous. This fault had a displacement varying from down to the East in Southern Oman, to down to the West in central Oman, providing evidence of sinistral rotational movement. It is composed of a sequence of reactivated, en echelon basement fractures, with a combined throw approaching 492 ft.
3) Oman Line, which is a long-lived crustal feature of regional importance, that marks the Southeastern end of the Zagros range. It also marks the sudden termination of the post-Paleozoic sequence of the Arabian Gulf. It is considerable dextral transcurrent motion along the Oman line occurred at the southeastern termination of the Zagros Range.
4) Owen Fracture Zone. The zone is a 2,000 km long fracture zone, roughly parallel to the continental margin of southern Arabia. Probably it is no longer an active fault.

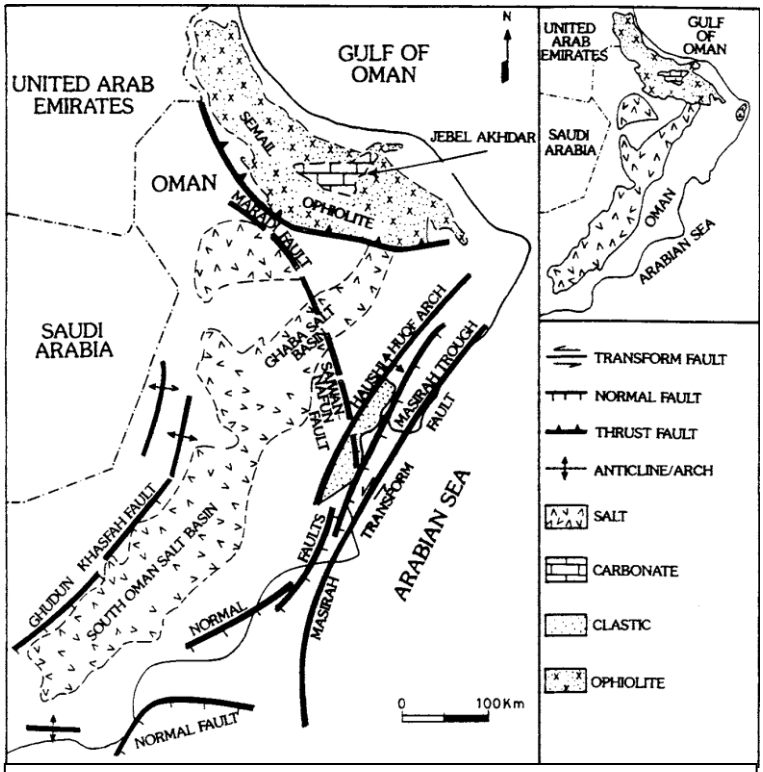

Figure 1.10: Major structural elements in southeastern Arabia (Alsharhan and Nairn, 1997).

According to Sirat et al. (2007) the basement blocks, which maybe influential as the pre-existing structural grains, have four main trends:

1- The extensional N-S Arabian trend
2- Left lateral strike-slip NE-SW Aulitic trend
3- Right lateral strike-slip NW-SE Earthy-raean trend
4- The extensional E-W Tethyan trend

Two subseismic fracture systems within the Tertiary and Cretaceous of the onshore and offshore of Abu Dhabi respectively have been identified. The E–W orientation fracture system that corresponds to the Tethyan Trend sets, ± 20°−30° in strike ranges for the shear sets, and the N–S orientation fracture system that corresponds to the Arabian Trend sets, ± 20°−30° in strike ranges for the shear sets (Figure 1.11). The faults are mapped based on seismic maps of the onshore and transitional zone-fields in Abu Dhabi and Oman areas, as well as outcrop mapping of the Al Ain area (Eastern part of Abu Dhabi). The solid lines are proven seismic faults while the dashed lines represent the faults thought to be possible extensions (Morad et al., 2010).

Field A is in the SE of Abu Dhabi along with some other fields with the same trend, and the closest one of them is believed to have the same regional structural history and evolution. This nearby field has three major tectonic events affecting the development of fracture sets described by Sirat (2012):

(1) pre and syn-folding fractures including the N75W, N45W and N15W fractures, with a possibility to develop extensional fractures syn- and post-folding at the crustal part of the fold parallel to the fold axis in NE direction.
(2) fault-related fractures, the product of the counterclockwise shifting of the SHmax with time, which exerted simple shear stress at an angle to the pre-existing N75W and the N45W faults resulting in forming Riedel shear (R, R’ and P) fracture types.

(3) post-folding fractures associated with the uplift and exhumation, as indicated by the major unconformity at Simsima time (Upper Cretaceous). These fractures are mainly horizontal to sub-horizontal fractures and occurred due to stress relief.

Other post-folding fractures are mainly due to that counterclockwise rotation of the SHmax as stated earlier, where new fracture sets with the EW and NE directions at shallow depth have been developed when SHmax was at NE direction at Eocene to Miocene times. The tectonic-related fractures are more connected and larger in size.

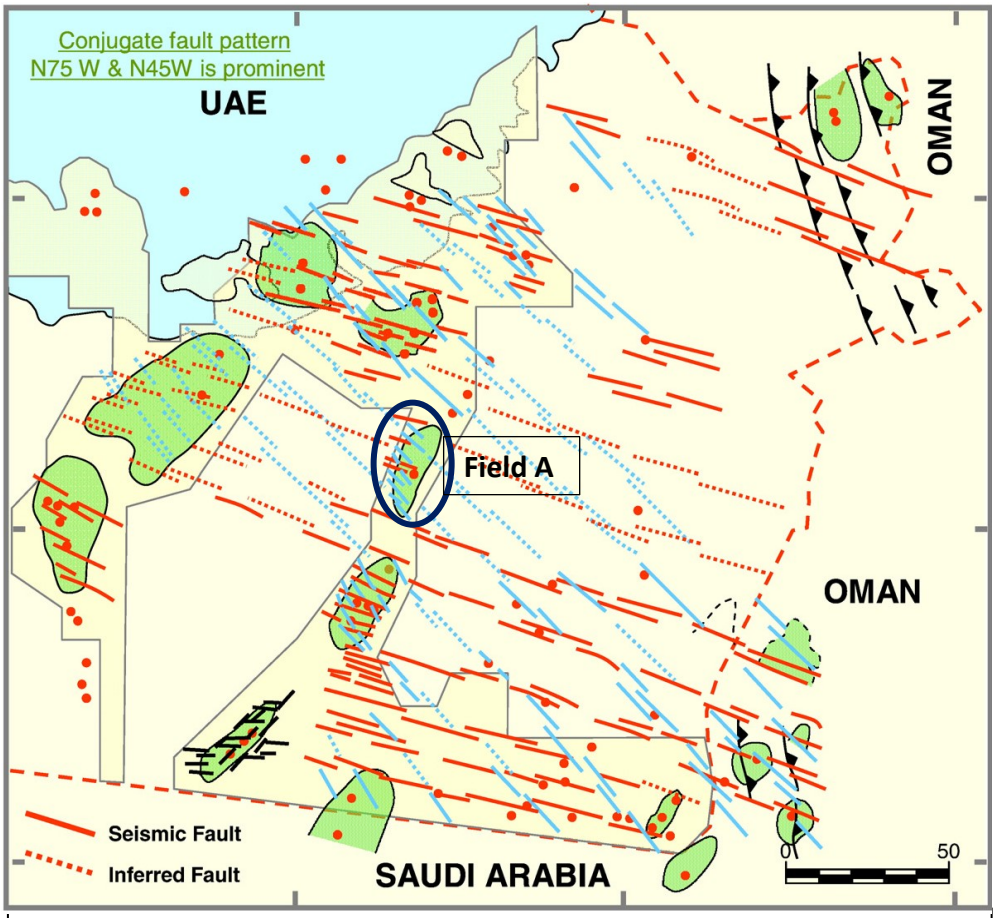

Figure 1.11: Regional structural fault patterns in the study area, showing position of Field A. Blue faults are in different direction (Morad et al., 2010).

1.3.2 Field A

Field A as in other onshore Abu Dhabi fields, is an anticline that formed during the Campanian-Maastrichtian period, due to a N60°W compressional stress field (Ali and

Farid, 2016). Field A is considered as a basement drape-over anticline (Noufal et al., 2016). Based on seismic and log data, our field is dominated by normal faults of different sizes, as well as strike-slip faults; which creates two strain fields. The result is that one set of fractures, characteristic of a particular strain field, may subsequently be overprinted by another set characteristic of a different strain field.

The structure in Field A can be summarized by the following events (Greenwood et al., 1980; Beydoun, 1991; Exxon report, 1993):

1- Establishment of NS structural grain during Pan-African orogogenesis (~950-640 Ma). This persists throughout the Phanerozoic evolution of the area and was offset by the Najd strike-slip fault system. The Mesozoic reactivation of this structural grain served to localize the Field A antiform.
2- Initiation of broad Paleozoic basins across the Najd fault system during Cambrian to Carboniferous, including the Rub al Khali basin where Field A formed.
3- The developing of the Field A anticline in two stages (Mid-Late Cretaceous), EW closure during Cenomanian and a NS closure during Turonian. This structural event is believed to related to the Oman Ophiolite obduction.
4- Formation of the Field A normal faults at the Late Cretaceous, in parallel with a southward tilting of the strata at the field. Most of the faults at Field A are oriented perpendicular to this southward tilting.

In Field A there are major faults that exceed 240 ft throw as well as smaller faults that have throws of less than 10 ft (Maroof, pers. comm) (Figures 1.12, 1.13, ADNOC Onshore unpublished data based on seismic interpretation). The majority of these faults are trending NW-SE (Dewever et al., 2011).

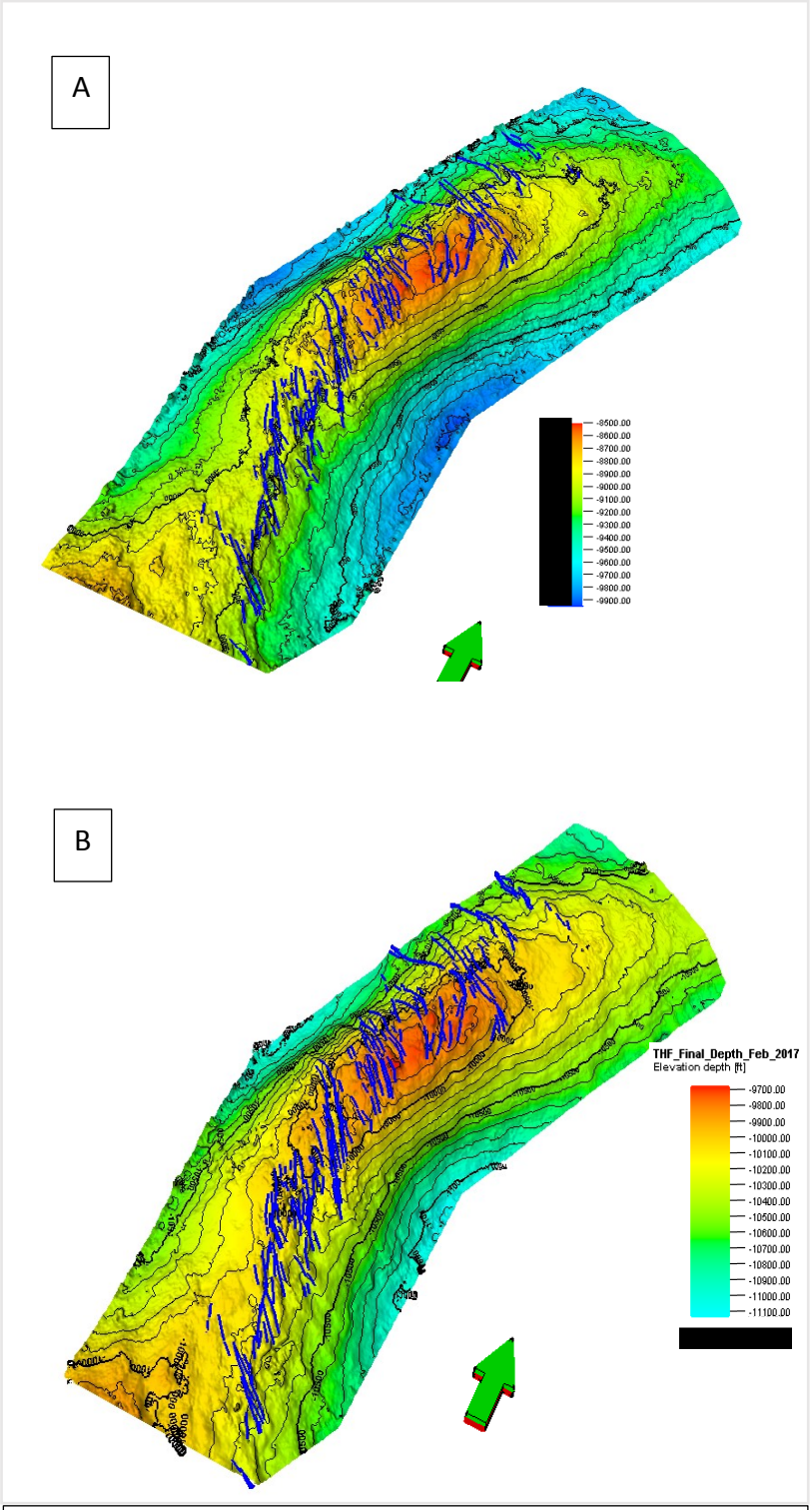

Figure 1.12: Seismic depth maps of the Upper and Lower Thamama reservoirs with interpreted faults. A. Reservoir B. B: Reservoir F. (ADNOC Onshore 2018).

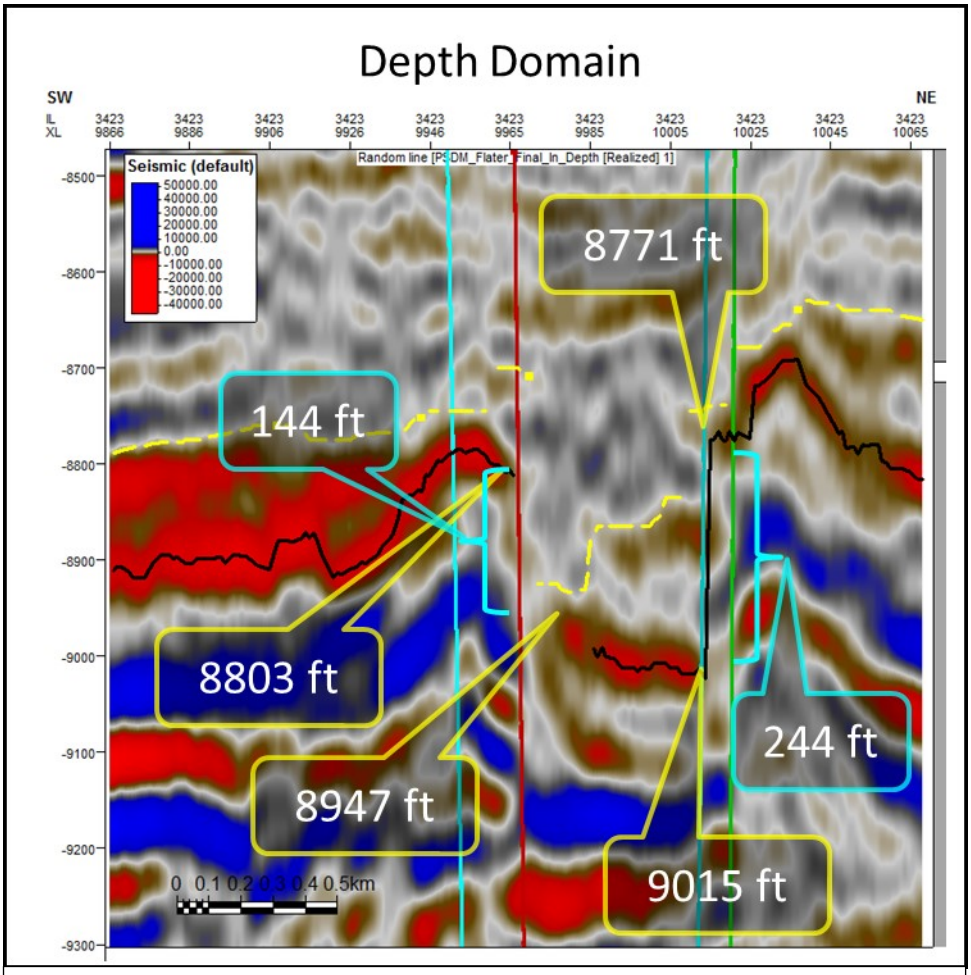

Figure 1.13: Seismic depth cross section across Field A main graben. Fault throws: 244 ft and 144 ft (ADNOC Onshore 2018 unpublished data).

1.4. Diagenesis and reservoir quality in Thamama Group

First, the main environments and processes of diagenesis will be summarized briefly, followed by a brief summary of previous work on the evolution of reservoir quality in the Thamama Group.

1.4.1 Carbonate diagenetic environments and processes

The main environments of carbonate diagenesis are as follows (Tucker & Wright, 1990; Pitman et al., 1998; Machel, 2005; Flugel, 2010):

1- Meteoric Diagenesis

Also known as freshwater diagenesis. This occurs in continental areas along a shelf margin. Meteoric diagenesis starts with magnesium loss from high Mg calcite, followed by the disappearance of aragonite plus replacement of aragonite by calcite. Meteoric diagenesis takes place in the meteoric vadose zone and the meteoric phreatic zone, in addition to the shallow mixing zone of fresh and marine water. The most common diagenetic products for meteoric diagenesis are cementation resulting from solution and precipitation, new porosity types resulting from dissolution, and petrographic and chemical changes that are connected to mineralogical stabilization. Meteoric water is involved in the dissolution of calcite during shallow diagenesis, although later, during the early stages of hydrocarbon generation, the organic acids and CO_2 promote more extensive carbonate dissolution.

2- Mixing zone and marine vadose environment

This environment appears in shallow subsurface and near coastal settings, by the coastal interface of land and sea. Precipitation of aragonite and dolomite cements are common in this environment. The vadose environment is considered to be an extremely complex diagenetic environment (McLaren, 2001). The most common diagenetic process in this environment is dissolution.

3- Marine diagenesis

Marine phreatic diagenesis occurs at the shallow or deep seafloor or below that, and on tidal flats and beaches. Dissolution and important differences in the calcium carbonate preservation of deep-sea sediments that occur in this environment are due to high hydrostatic pressure, low water temperature and high partial pressure of CO_2

in the deep sea. Marine cement types are very common and can vary, with fibrous and isopachous cements being common.

4- Burial diagenesis

Burial diagenesis includes shallow to intermediate to deep burial diagenetic settings. Here compaction and pressure solution lead to particular cements and diagenetic textures. It is important to study burial diagenesis because it is vital for the reconstruction of the full carbonate rock history and the evaluation of properties and porosity. Burial environments are divided into shallow burial (few meters to tens of meters of burial) and deep burial. Shallow burial diagenesis is affected by changing pore water chemistry in the mixing zone as well as temperature and pressure. Deep burial diagenetic processes are controlled by (1) pressure (lithostatic, hydrostatic and tectonic), (2) temperature, where increasing temperature controls the transformation of stable organic matter and hydrocarbons, and (3) pore water chemistry (impacts on transport and speed of pressure solution). The most common diagenetic processes during deep burial are related to physical compaction (due to sediment overburden) where the decrease in thickness of sediments, porosity and permeability, leads to distortion of grains resulting in compressed fabrics. Chemical compaction is another diagenetic event of this environment (starting at depth of overburden of 100 m to several thousands of meters). During this process, stylolites and pressure solution start to appear. Cementation is an important process in burial diagenesis, and it produces coarse calcite spar cements enriched in iron and manganese and poor in strontium. Regular cement found here include equant, blocky, syntaxial and drusy calcite and saddle dolomite. There is also minor solution porosity, which is caused by dissolution of carbonate and calcium sulphate minerals. The last important diagenetic process of this environment is burial dolomitization, which is often characterized by an anhedral crystalline fabric and coarse dolomite crystals.

Porosity types

Several factors lead to loss of porosity, which are chemical compaction, mechanical compaction and cementation (Hosa & Wood, 2017). Some scholars believe chemical compaction to have more effect on porosity loss than mechanical compaction (Croizé et al., 2010). For the Cretaceous in general, the porosity type and distribution is linked to early diagenesis and to later structural events (Wanger, 1990).

Primary porosity includes intergranular porosity that is controlled by organism's growth cavities shape and location, as well as from carbonate cement dissolution, intraparticle porosity, depositional porosity and framework and fenestral porosity. On the other hand, secondary porosity includes porosity formed by dissolution, porosity associated with other diagenetic events like, dolomitization, breccia and fractures (Moore, 1989; Pitman, 2001).

Types of compaction

Chemical compaction

Chemical compaction is a result of dissolution-precipitation mechanisms, usually encouraged by tectonic stress (pressure-solution) at grain contacts which increase mineral solubility. Chemical compaction happens at burial depth (~ 2–3 km) (Schneider et al., 1996; Croizé, 2010; Machel, 2005). The resultants features are stylolites, dissolution seams and fitted fabrics (Clari & Martire, 1996).

Mechanical compaction

Mechanical compaction can start at early burial diagenesis, yet it is agreed amongst many researchers that carbonates are not significantly affected by it (Goldhammer, 1997). Mechanical compaction happens due to stress, pore fluid expulsion and rearrangement of solid particles during burial and can result in an irreversible deformation sub-critical crack growth (Croizé et al., 2010; Bruch et al., 2016).

Cementation

Bathurst (1972) defined cement as “all passively precipitated, space filling carbonate crystals which grow attached to a free surface”. Cementation necessitates large fluid fluxes and is common in intermediate to deep burial settings due to the raised temperatures, fluid mixing and chemical compaction (Machel, 2005). Cementation takes place in the three diagenetic environments mentioned above. The high energy intertidal zone and the shelf margin framework reef are the two major sites of marine cementation (Moore, 1989). Cement precipitation in fractures can be used to constrain when the fractures formed, either by tying fracture-cement sequences to dated cement sequences in the rock or using cement accumulations and thermal history to estimate fracture age (Laubach et al., 2010).

Calcite cementation

Calcite cement can be referred to the growth of precipitated calcite into open pore space between or inside grains as well as into holes newly created by aragonite dissolution (James & Choquette, 1984). The main calcite cement types of interest in this study include circumgranular, drusy, granular, syntaxial overgrowth, equant, dogtooth and blocky.

Dolomite cementation

Dolomite cementation might be related to fracturing and faulting in many cases, because fractures and faults form channels for dolomitizing fluids passage (Purser, 1994). The two types of dolomite cementation found in this study are rhombic and saddle dolomite.

1.4.2 Diagenesis and reservoir quality in the Thamama Group, UAE

Several studies have been undertaken on the Thamama diagenetic history (Alsharhan, 1985; Moshier, 1987; Nielson, 1997, Nielson et al., 1998; Lambert et al, 2006; Callot et al., 2010; Cox et al., 2010; Al-Ghamdi, 2013) but there is no

agreement on all the events and timings. Reservoir quality is modified by various diagenetic alterations like calcite cementation, dissolution, recrystallization and dolomitization which are accomplished by fluid flux in sedimentary basins like the Thamama Group (Morad et al, 2010). Other minerals like pyrite, kaolin and sphalerite were found in lesser quantities in the Thamama (Ehrenberg et al., 2016).

Figure 1.14 for example shows a paragenetic sequence of the Shuaiba Formation (Alsharhan et al. 2012).

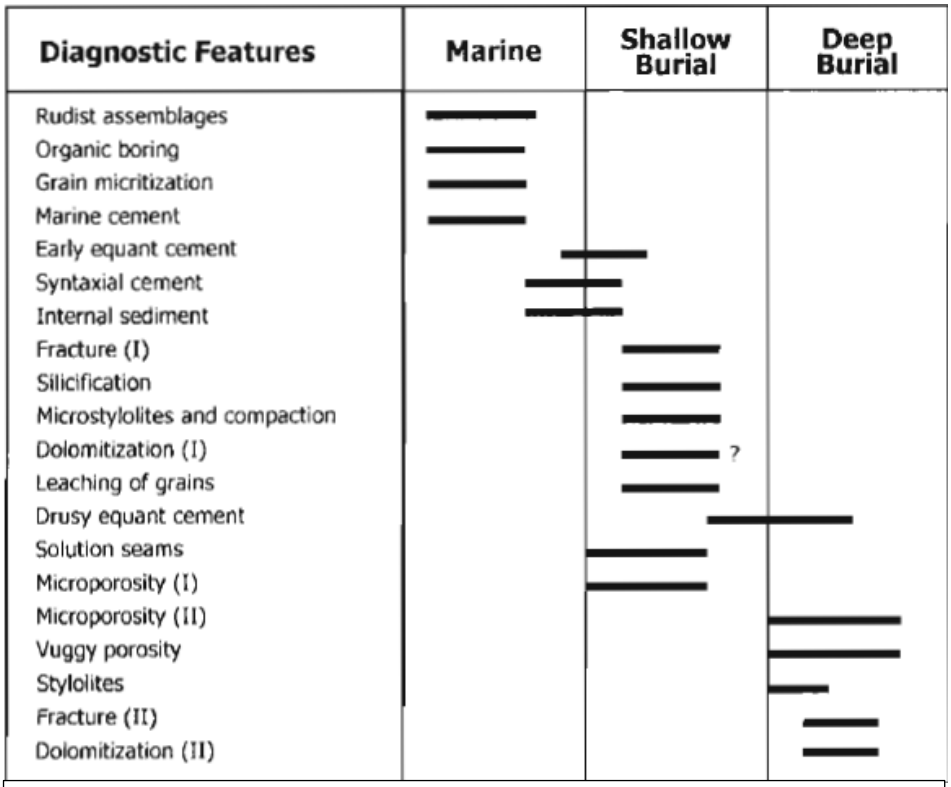

Figure 1.14: Paragenetic sequence of the diagenetic processes affecting the Shuaiba Formation (Alsharhan et al., 2012)

Several diagenesis processes were identified which are typical of shallow burial conditions. These are; mechanical compaction, dissolution of biogenic aragonite, replacement of HMC by LMC, precipitation of non-luminescent calcite and inclusion-rich dolomite. The first diagenetic event differs, however, amongst scholars. According to Lambert (2006), the first diagenetic phase corresponds to

inclusion-rich calcite cements, while Budd (1989) suggests that the first diagenetic event was most likely mineralogical stabilization in an unconfined meteoric aquifer formed in the Thamama during a period of subaerial exposure immediately after Shuaiba deposition. Mohamed et al., (2017) found that micritization is the earliest diagenetic event in Early Cretaceous and noted that this reduces the reservoir quality.

In the Shuaiba facies, a greater proportion of grain-supported facies are porous relative to mud-supported facies (Budd, 1989). The Shuaiba Formation therefore has a relatively high porosity because of preserved macroporosity (intergranular, vuggy, mouldic), and so the reservoir quality is better in grainstones and packstones compared to the wackestones and lime mudstones in the Kharaib Formation where the pore system in the finer units is dominated by micropores (Neilson et al., 1997). Microporosity is the dominant pore type in thick intervals of many Thamama hydrocarbon reservoirs and it is believed to be responsible for most of the holding capacity in them (Moshier, 1989 and Budd, 1989). Micro-vugs occur in association with microporosity and microrhombic calcite, but they are rare in the Shuaiba Fomation (Budd, 1989).

Dolomite cement is observed in association with the stylolites. Burial diagenesis is evidenced by saddle-shaped dolomite and iron-rich calcite spars followed by iron-rich dolomites (Lambert, 2006). According to Lambert, the final diagenetic step is a dissolution phase which affects LMC and dolomite. Micritic calcite allochems such as agglutinated foraminifera are partially dissolved. Porosity created by the final dissolution phase is never filled. It is not affected by stylolitisation between allochems indicating that this final dissolution phase occurred after chemical compaction (Lambert, 2006). Porosity and permeability variations in grainstones and packstones at a reservoir scale are controlled by the variation in amount of equant sparry calcite cement (Neilson et al, 1997).

Oil has an inhibiting effect on diagenetic processes in carbonates, and has been noted in the Thamama (Neilson, 1997; Neilson et al., 1997; Cox et al., 2010). This is backed-up by some facts listed by Neilson (1997); first, physical or chemical

coverage of mineral surfaces by petroleum or related organic compounds may shield parts of the surface from diagenetic fluids. Second, the mass transfer processes of diffusion and water flow may be slowed, where diffusion is the rate-limiting process for calcite dissolution and precipitation at the temperatures of petroleum emplacement. Third, petroleum emplacement may inhibit the release of mineralizing solutions from the cement sources.

The Kharaib Formation, is known to have moderate to high porosity but low to moderate permeability carbonates, as well as high to very high porosity and high permeability carbonates (Al Mansoori et al., 2008). No cement or filling, except by hydrocarbons, is observed in the porosity created by burial dissolution in the Kharaib Formation. Also, porosity created by dissolution is largely preserved from mechanical and chemical compaction in spite of the present depth, suggesting hydrocarbon filling immediately after dissolution (Lambert, 2006).
Neilson (1997) states that reservoir quality is preserved where petroleum emplacement has occurred relatively early, prior to burial cementation by equant sparry calcite, while reservoir quality is destroyed where it has occurred after significant burial cementation. Three typical micrite microtextures are distinguished in the Kharaib Formation; rounded micrites, micro-rhombic micrites, and compact anhedral micrites. Micrite inclusions in micrite crystals indicate a second generation of crystals or micro-cements (Lambert, 2006).

There have been relatively few detailed studies on the fracture-filling cements in the Thamama Group. Alsharhan (1985) referred to the staining in fracture filling that indicated ferroan calcite. The presence of multiple generations of fractures in the Thamama Group filled by generations of calcite, which show successive luminescence patterns was noted by Moshier (1988). Breesch et al. (2009) described the calcite of a fault plane in the Thamama outcrop cements to be composed of stretched fibers with a dull luminescence, calcite twinning with no luminescence and irregular blocky to fibrous crystal infill. The presence of anhydrite, bitumen as well as the main fracture filled cement (calcite) was mentioned by Al Bloushi (2013) in the Shuaiba (Reservoir A). Low Magnesium Calcite (LMC) spar cements in fractures

where found in Kharaib Formation (Reservoirs B & C) by Lambert et al., (2006), and blocky calcite fracture fill in Reservoirs A and B was reported by Russell (2001). Lambert (2006) also noted that non-luminescent LMC spar cements (sometimes developed on echinoderm debris)are always crosscut by fractures, present no relationship with stylolites, and are covered by later cements. In top reservoir levels, these cements are poorly developed, in contrast to reservoir bases .
Fractures filled with calcite cutting rudist valves in the Shuaiba were mentioned by Al Ghamdi (2013), where he referred their formation to hydrothermal fluids. Tension gashes cemented with calcite were observed in the Upper Thamama in a nearby field (Xie, 2015). A study by Paganoni et al., (2016) listed the fracture fill cements to include calcite, dolomite pyrite, kaolin, anhydrite, sphalerite, fluorite and saddle dolomite in Field A.

It is interesting to note that fracturing is relatively uncommon in the formations examined by Lambert, except where associated with stylolites. Fractures are partially filled by dolomite rhombs or LMC spars, specifically in the dense intervals below the reservoirs (Lambert, 2006; Ehrenberg et al., 2016). Microstylolites are observed essentially between allochems in grainstones. Stylolites and all associated phases are rare in top reservoir intervals, but they are abundant, in muddy facies in the lower section of reservoirs. They are parallel to bedding, indicating a dominant vertical lithostatic stress. Well-developed stylolite levels show lower porosity and permeability (Lambert, 2006).

1.5 General relationship of fractures to stress and diagenesis

Understanding the link between fractures, stress and diagenesis will aid understanding the timing of fractures. The timing of fractures can be considered in relation to other events in a complex diagenetic sequence, such as precipitation, dissolution, mineral reaction and all the events captured relative to fracture growth. Diagenesis and fracturing can alter the petrophysical properties of carbonate reservoirs significantly (Vandeginste et al., 2013). The study of the relationship

between deformational structures and chemical changes to sediments is called structural diagenesis (Laubach et al., 2010) and it is important in many applications, like predicting the fate of deep injected fluids and extracting hydrocarbons from deep reservoirs.

Tectonic activity can be related to diagenesis in several ways. Regional tectonics affect diagenetic variables by many factors, such as rates of subsidence, uplift and deformation, volcanism, heat flow and transport of formation waters. The effect includes primary detrital-chemical assemblage, composition of early interstitial waters, rates and depth of burial, length of time buried, geothermal and pressure gradients and oscillatory vertical movements (Siever, 1979). Plate tectonics can be used as a framework for relating diagenesis to geological and geophysical parameters; regional tectonics, including rates of subsidence, uplift and deformation; volcanism and plutonism, heat flow and transport of formation waters (Siever, 1979).

Fractures associated with fault-slip may increase or decrease fault-zone porosity and permeability, possibly focusing or impeding fluid flow, perturbing thermal gradients, enhancing or restricting reactions and transport of chemical components, besides altering porosity, permeability, mineralogy, texture, and mechanical properties of fault and host rock (Laubach et al., 2010).

Arndt et al (2014) highlighted how evolution of effective stress states and the growth of faults influence the hydraulic connectivity in fracture networks. He emphasized the fact that the growth of fracture networks in deeply buried, low permeability rocks during crustal deformation plays a critical role in generating fluid pathways and facilitates fluid redistribution between various crustal reservoirs. In actively deforming regions, fluid pathways in fracture networks are governed by the dimensions of fractures and the evolution of connectivity in an array of fractures between the upstream and downstream parts of flow systems.

A number of scholars have found a relationship between fracturing and diagenesis. The frequent diagenetic changes due to unstable nature of carbonate minerals can

result in early cementation, secondary porosity development and can influence fracture density (Vandeginste et al., 2013). In Oman, she concluded both depositional facies and early diagenesis will influence the degree to which a rock unit will fracture. In a complex diagenetic sequence, there is a possibility to indicate the timing of fractures in relation to other events, depending on a succession of precipitation, dissolution and mineral reaction events captured, relative to growth of fractures (Gale et al., 2004). The integration of stable isotope data and fluid inclusion data from incrementally grown veins, with understanding of deformational control on the development of fluid pathways and their permeability history, offers the potential to explore the dynamics of coupling between growth of fracture networks, fluid migration, and fluid–rock interaction during crustal deformation (Arndt et al, 2014). For example, some filled fractures probably form at the same time as folding. Others, however, form much later during the exhumation of the rock, as a result of a decrease in confining pressure and the release of the residual stress locked into the rock at the time of folding (Cosgrove & Ameen, 2000). In a wide range of structures, the key to unlocking the timing sequence and rate of fracture development, is combining diagenetic models, fine resolution of cement sequences, and geochemical and isotopic data (Laubach et al., 2010).

Gale et al. (2004) mentioned two processes by which fractures can be filled. (1) synkinematic cement, where cement precipitates on the fractures walls during fracture growth. (2) postkinematic cements, where the cement growth post-dates the fracture formation.

Larger scale fractures caused by brittle failure can also develop at an early stage in the diagenetic history due to early lithification and cementation of carbonates, such as in steep-sided platforms (Vandeginste, 2013).

Heidari et al. (2013) studied fracturing and vein filling in order to understand the post-depositional history of carbonate rocks of the Guri Member (Lower to Middle Miocene) in Iran. Heidari and his team reconstructed the diagenetic models of the Guri Member into four stages including marine, meteoric, burial, and uplifting. Most

of the fracture cement they recorded was blocky calcite. Vandeginste et al. (2013) investigated the mutual influence of depositional facies on diagenesis and interpreted early fractures in the Berriasiane-Valanginian Habshan Formation in Jebel Madar (Oman). She documented the inter-relationship between sedimentary facies, early diagenesis and early fracture formation, and highlighted that sediment-filled early fractures are dolomitized in the same way as the stratabound beds based on their similar mud-rich nature. Sirat et al. (2016) studied the influence of tectonic compression, anticline formation and uplift events of Zagros Orogeny related to a Paleogene marine carbonate in eastern UAE and how this induced brecciation, karstification and carbonate cementation in the matrix vugs as well as along faults and fractures. He used structural analysis in the outcrop, stable isotopes and fluid inclusion microthermometry to constrain the origin and geochemical evolution of the fluids. Sirat noticed that the fluid flow was related to two tectonic deformation phases; deactivated deep-seated strike-slip faults which resulted in in the precipitation of saddle dolomite in fractures and vugs, and compression and uplift of the anticline which was associated with incursion of meteoric waters and mixing with the basinal brines which resulted in the precipitation of blocky calcite cement. Methods such as identifying cross-cutting relationships and cement mineralogy from the outcrop as well as petrography, cathodoluminesence imaging and geochemical analyses (electron microprobe, fluid inclusion, oxygen, carbon and strontium isotopes) were applied by Marfil et al. (2005) to reveal the origin and evolution of the fluids in Upper Jurassic limestones of the Eastern Iberian Range of Spain. He identified three types of structures where cement was filling stylolites and fractures. Marfil also used $\delta^{18}O_{VPDB}$ and $\delta^{13}C_{VPDB}$ values to constrain the temperature of the cement fluids.

Burruss et al. (1983) worked in Northern Oman, and found that several generations of calcite-filled fractures can be distinguished by their crosscutting relationships to stylolites and other fractures, by the morphology of calcite fracture filling, and by the type of fluid inclusions in the calcite. The multiple episodes of fracturing and extensive stylolitization suggest that the diagenetic history records burial and tectonic events during development of the Oman orogeny.

1.6 Research hypotheses and objectives

This thesis investigates the relationship between fracturing and diagenesis, and the effect of tectonism on the diagenesis of the fractures and whether these fractures have any impact on the reservoir quality. Here the main hypotheses of the project and objectives are outlined:

Hypothesis 1: Fractures can be related to tectonic events

Objectives:

1- Determine if the timing of fractures throughout the Thamama coincides to major stress changes, when comparing the relative and absolute timing.

   The fieldwork in Wadi Al Rahabah to study the Thamama outcrop will allow fracture distribution, orientation and diagenesis to be integrated and compared to tectonic events.

2- Relate fractures to the paragenetic sequence.

   Relating fractures to tectonic events requires knowledge of the timing of these tectonic events. A paragenetic sequence is established for each reservoir where the fractures are placed within that framework. This includes observing and noting the number of different fracture sets, and the relative timing of fracture formation and the evolution of fill relative to the other diagenetic events.

3- Determine if changes in stress can be related to changes in the chemistry of evolving fluids in each reservoir, as manifest in changes of cementation and dissolution.

4- Determine if fractures can be related to diagenetic events in each reservoir.

Hypothesis 2: Fracture cements record fluid flow through the reservoirs

Objectives:

1- Establish relative chronology and absolute temperature of the fracture calcite cement to the paragenetic sequence using in-situ $\delta^{18}_{OVPDB.}$

2- Determine the chemistry of the evolving fluids using trace elements analysis on the fractures cements.

Hypothesis 3: The presence of fractures contributes to fluid flow in the reservoir

Objectives:

1- Understand the role of fractures within the evolution of permeability of the reservoir.

2- Asses the contribution of fractures in enhancing or destroying reservoir quality.

1.7 Localities studied and data sources

The area of study includes two localities: Field A in the SE of Abu Dhabi and an outcrop in Ras Al Khaimah in the Northern Emirates (Figure 1.1).

The outcrop was in Wadi Rahaba (25°55'41.91" N, 56°04'57.99" E) and represents the surface analog for The Thamama Formation in the subsurface of Abu Dhabi.

Outcrop analogs of subsurface reservoirs allow for a detailed investigation of the facies architecture and structure of these carbonate bodies. They provide the continuous, large-scale coverage of a seismic line as well as the fine-scale resolution of core measurements (Strohmenger, 2006).

Materials made available for this study by ADNOC Onshore (Abu Dhabi National Oil Company) were 5 structure maps, 1 for each reservoir, an Exxon Mobil report on Field A structure and sequence stratigraphy, 2 diagenesis reports for Field A and 1 diagenesis report for Reservoir b in a nearby oil field.

1.8 Sample selection, preparation, and methods

1.8.1 Sample selection and preparation

Fifteen samples from the outcrop at Wadi Rahaba were chosen for fracture cements and were collected for thin section preparation (more details given in Chapter 5). All the thin sections were studied for petrography analysis (cross-cutting relationships and building a paragenetic sequence) and six of them were used for the EPMA analysis for the purpose of comparison with the subsurface elemental data.

By studying the field structure map provided by ADNOC Onshore (Figure 1.15), the most representative wells were selected. The selection of wells took into consideration their location adjacent to the major faults of the field, and penetration through both oil and water legs.

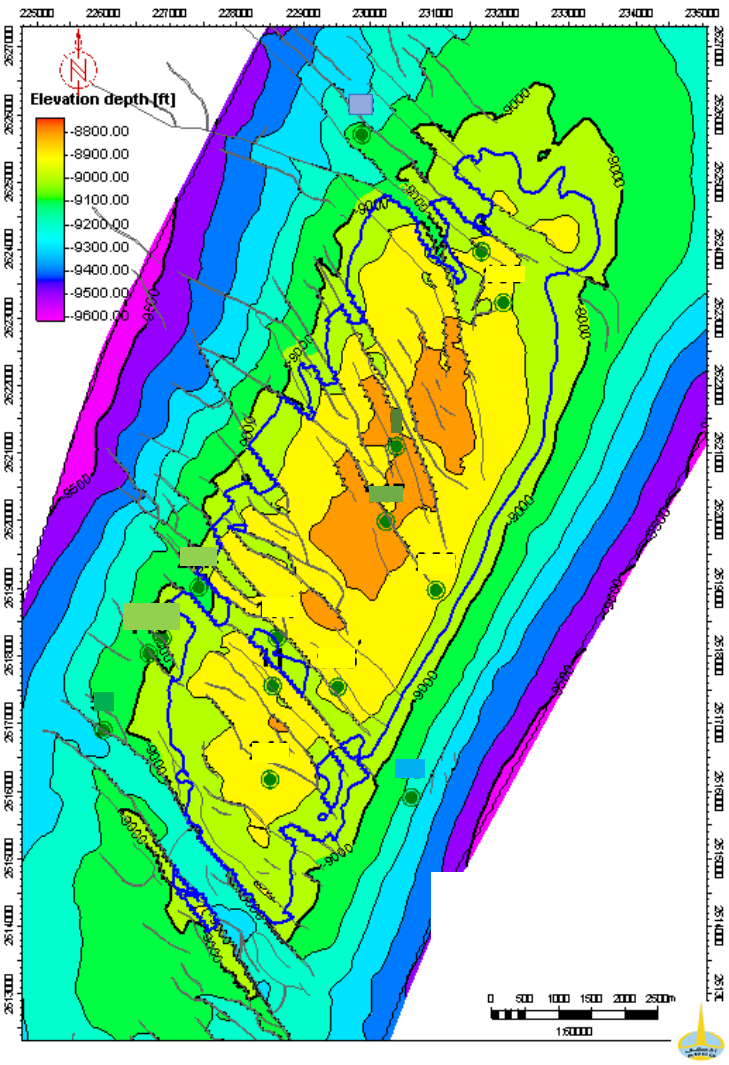

Figure 1.15: Depth structure map of the studied field showing the main faults and position of sampled wells (ADNOC Onshore, 2014)

Once the wells were selected, a visit was paid to ADNOC Onshore core store to choose the best representative core samples to be studied. Core slab samples were prepared in coordination with the core store staff. The samples covered reservoir and dense intervals in both oil and water bearing zones. Petrographic and high resolution thin sections were sent to be prepared from these core slabs in the UoE labratoy (Figure 1.16).

Core samples included 97 core slab samples from 8 wells; 5 in the oil zone and 3 in the water zone (Table. 1.1).

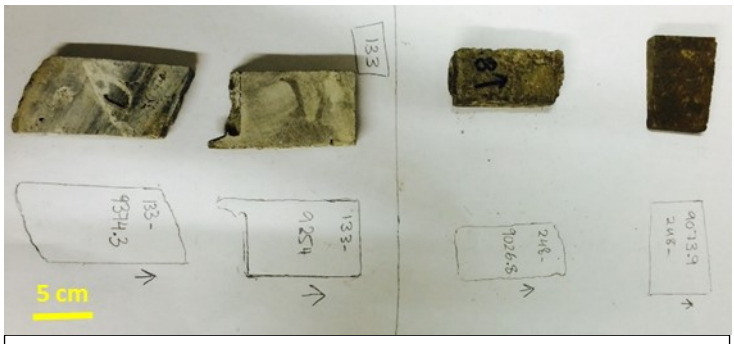

Figure 1.16: Core slabs before soxhlet treatment

Zone	Well Name	Zone	No. Samples
Oil	well 1	Reservoir F	2
		Dense F	3
		Reservoir G	11
		Dense G	5
	well 2	Reservoir C	10
		Dense C	2
	well 3	Reservoir B	9
	well 4	Bab Member	2
		Reservoir A	6
		Dense A	1
	well 5	Dense A	8
		Reservoir B	12
		Dense B	2
Water	well 6	Reservoir B	13
	well 7	Reservoir C	3
	well 8	Reservoir F	5
		Dense F	3

Table 1.1: Samples taken from subsurface

The oil stained samples were cleaned by Soxhlet extaction using methanol and toluene (Figure 1.17).

Polished thin sections (PTS) with blue colored epoxy were prepared. The thin sections were used for petrographic examinations (conventional and cathodoluminescence (CL)) to evaluate cement types and morphologies.

Figure 1.17: Oil stained samples cleaned by Soxhlet extraction

1.8.2 Methods

The methods used are summarized in the following diagram (Fig. 1.18):

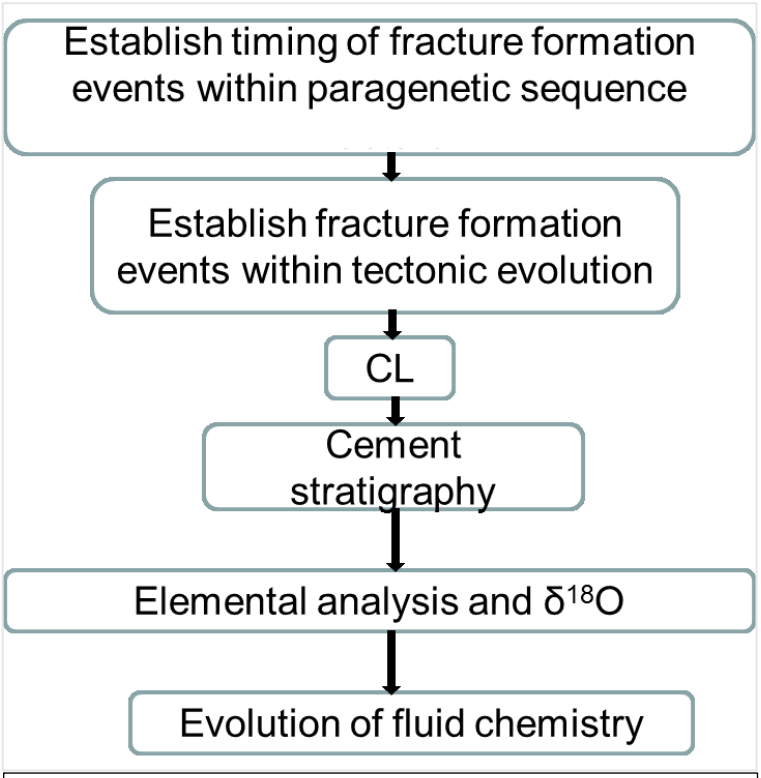

Figure 1.18: Diagram showing the methodology of the research work

Fieldwork to establish fracture formation events within tectonic evolution

Field work included measuring fracture orientation, fracture spacing, network and aperture. Some cemented fractured samples were collected to study the type of cement in them and compare it to the subsurface cement. The study started by studying the main faults in the area and understanding the tectonic system that lead to this faulting, and studying the fractures related to these major faults. A close study to the fractures was undertaken to identify the relative timing of their formation and to constrain the timing of cementation and dissolution. Cross-cutting relationships between intersecting veins was logged and their relation was determined as well as structural superposition (intersection relationships, i.e., dextral or sinistral strike separation) (Arndt et al, 2014). The outcrop study also included different diagenesis processes such as cementation, neomorphism, dissolution, compaction and fracture

formation and tying them together to produce a time relationship between their occurrence and the tectonic events in the area. A comparison was done between the findings in the outcrop in relation to those in the subsurface, regarding the fracture fill minerals, and fracture orientation in relation to the regional stress.

Petrography

Petrographic study of thin sections to find cross-cutting relationship between fractures and other events like cementation, dissolution, stylolites, and bitumen emplacement.

Cathodoluminescence (CL) and cement stratigraphy

CL analysis was used to identify different luminescence cement zones. It is believed that manganese Mn^{2+}, substituted into regular lattice sites in the crystalline structure, is the main activator and ferrous iron Fe^{2+} the main inhibitor of luminescence (Czerniakowski et al., 1984). Calcite and dolomite cements with higher Fe^{2+} relative to Mn^{2+} show dull luminescence, while cements with lower Fe^{2+} and fairly higher Mn^{2+} will display bright luminescence. Cement zones in fractures were tracked to build cement stratigraphy. The cement stratigraphy was then used as the fracture work in which to measure in-situ $^{18}O_{VPDB}$ and trace elements of each cement zone. A cathodoluminescence cold cathode CITL 8200 MK3A was used at UoE lab to examine thin sections and identify different cement zones.

Elemental analysis

The electron probe microanalysis (EPMA) technique is based on criteria that each element in a solid rock emits distinct x-ray spectrum when bombarded with an electron beam. The characteristic of each emitted x-ray spectrum line reveals the presence and concentration of a particular element (Hutchins,

1979). The EPMA technique was used to obtain the elemental concentrations of minerals (Ca, Mg, Sr, Mn, Fe, O) present in the calcite and dolomite cement for cement stratigraphy evaluation, in order to understand the origin of a fracture fluid at the time of cementation. The trace element composition of carbonate minerals gives an indication of the type of fluid present at the time of crystallization and can aid analysis of the paleo fluid flow, as well as determining the origin of the fracture and pore water. The $^{m}Mg/^{m}Ca$ ratio can be compared with in-situ $\delta^{18}O_{VPDB}$ data to constrain the precipitation temperature of calcite cement.

Samples were coated with a thin layer of carbon and placed in the electron microprobe (Cameca SX100) at the University of Edinburgh EPMA labratory (Figure 1.19). Analysis was applied on 18 polished samples that contained fractures from all of the Thamama Reservoirs. The analyzed cements were mostly blocky with some equant calcite. Samples were bombarded with an incident electron beam (5µm diameter). Calcite-Silicarb_Ca standard was placed in a separate holder and was calibrated before and after the analyses. The obtained concentrations were reported in Weight % and Parts Per Million (ppm).

Figure 1.19: Electron Probe Micro Analysis (EPMA) lab for elemental analysis.

Scanning Electron Microscope (SEM)

SEM was used to map 5 thin sections, to be used further in navigation under the ion microprobe. Thin sections were cleaned and coated by a thin layer of carbon in preparation for the SEM imaging. The samples then were placed under high vacuum evaporation and bombarded by an electron beam (10 kV voltage), to obtain high resolution images. The resolution of the instrument range is 1.9 nm at 1 kV to 1 nm at 15 kV. SEM images, however, failed to help navigate through the ion microprobe images and therefore were discarded.

In-situ $\delta_{18}O_{VPDB}$ assessment

Ion microprobe provides accurate micrometer scale measurements of isotopic ratio using focusing of a primary ion beam (Cs) (Valley and Kita, 2009). The $\delta^{18}{}_{OVPDB}$ values for five polished thin sections were assessed in situ via SIMS, to understand the evolution of the fracture fill cement chemistry and temperature of the fluid from which the cement precipitated. The same thin sections were used in EPMA and CL analysis, for comparison purpose of temperature, fluid composition and relative timing. Samples were 24 - 24.5mm in diameter and less than 12 mm thick. The analysis covers the area within +/- 5 mm of the center. The calcite standard was mounted in the center of the sample which is ideal for higher precision, using an ultrasonic drill to make hole (~ 2.5 mm) in the center of the sample and place the standard in the hole. The samples were cleaned with Acetone and Ethanol, followed by gold coating before being placed in Cameca 1270 ion microprobe (SIMS) at the UoE. The internal precision of each spot can be ranged between 0.009 and 0.015 (% standard Error). The external precision is estimated according to the consecutive analysis of a UWC (University of Wisconsin Calcite) standard (~0.3‰-0.4‰). Reflected light microscope images were used to navigate through the samples after unsuccessful SEM navigation trial.

1.9 Thesis outline

Chapter 2 describes the paragenetic sequence of each reservoir in the Thamama Reservoirs A to G, elaborating on the number and distribution of fracture formation within the paragenetic sequences. It also illustrates the relative time of different diagenetic events in each reservoir. Calcite and dolomite cement CL zones are explained in detail, emphasizing only on the fracture cements and listing the observations for possible reasons the variety in numbers of cement zones. A detailed scenario is predicted for the fracture formation of the Thamama reservoirs and is explained based on the paragenetic sequence findings.

Chapter 3 examines the two main calcite cement types in the fractures of the Thamama reservoirs, equant and blocky calcite. Detailed elemental analyses are performed and discussed, including $^{m}Mg/^{m}Ca$ for temperature changes, Mn and Fe for redox, and Sr for exotic fluids indications. An expected temperature profile for the fluids that have passed through the fractures and precipitated calcite cements is illustrated at the end of the chapter.

Chapter 4 studies the saddle dolomite cement that fills some fractures and specifically potential changes in the temperatures of precipitation, the Mn-Fe relationships, as well as potential exotic fluids using Sr concentrations.

Chapter 5 discusses the field data obtained in Ras Al Khaimah, UAE. It illustrates the field fracture orientation, cement types found and establishes similar elemental analysis as given in Chapters 3 and 4. This chapter presents two comparisons, the first on differences in fracture properties (orientation, density, aperture and cement types) between the surface and the subsurface (Chapter 2), and the second on the difference in fracture cement types and elemental properties between the surface and the subsurface cement (Chapter 3).

Chapter 6 presents in-situ oxygen isotopes data ($\delta^{18}O_{VPDB}$) and possible determination of the absolute temperature data in different cement zones of calcite

cement in the Thamama reservoirs' fractures. A comparison is also made between the relative temperature data obtained from the $^{m}Mg/^{m}Ca$ in Chapter 3, and the absolute data calculated using the Kim and O'Neil equation (1997).

Chapter 7 concludes the thesis findings and create links between the results obtained from the previous chapters. It also suggests further areas of study to implement the fracture data obtained from this thesis into future reservoir characterization studies to enable a better understanding of Field A.

CHAPTER 2

Paragenetic sequence of fractures in the Thamama Group

2.1 Introduction

Diagenesis is often studied in detail by examining petrographic thin sections where cross cutting relationships allow the paragenetic order to be established. Some studies have found that the impact of dissolution and cementation is minor in Thamama Group reservoirs, emphasizing the role of fracture network in creating connectivity (Jeong et al., 2017).

Moshier (1988) noted the presence of multiple generations of fractures in the Thamama Group, filled by generations of calcite showing successive luminescence patterns.

There have been few detailed studies on the fracture-filling cements in the Thamama Group. Alsharhan (1985) referred to the staining in fracture filling that indicated the presence of ferroan calcite. The presence of anhydrite, bitumen, as well as the main fracture fill cement (calcite) was mentioned by Al Bloushi, (2013) in the Shuaiba (Reservoir A). Breesch et al. (2009) noted that calcite cements on a fault plane in the Thamama outcrop in Wadi Rahaba in RAK, had variously stretched fibres with a dull luminescence, calcite twinning with no luminescence, and irregular blocky to fibrous crystal infill. Additional study by Paganoni et al, (2016) listed the fracture fill cements to include calcite, dolomite, pyrite, kaolin, anhydrite, sphalerite, fluorite and saddle dolomite in Field A, however, sphalerite and fluorite were not found in this study's samples. Tension gashes cemented with calcite were observed in the Upper Thamama in a nearby field (Asab) (Xie, 2015). LMC (Low Magnesium Calcite) spar cements in fractures where found in Kharaib Formation (Reservoirs B & C) by Lambert et al., (2005), and blocky calcite fracture fill in Reservoirs A and B was reported by Russell (2001). Fractures filled with calcite cutting rudist valves in the Shuaiba were mentioned by Al Ghamdi (2013), where he referred their formation to hydrothermal fluids.

Limited work has therefore been undertaken to understand the timing of fracture formation within the context of the overall paragenetic sequence. This is a pre-requisite to understanding the geochemical characteristics of these cements as it forms a relative timeframe.

This chapter will describe the distribution of fractures, the relative timing of fracture formation within paragenetic sequences for Thamama Reservoirs A to G, and the relative timing of the diagenetic events shown within them.

2.2 Materials and methods

Eight subsurface cores from Field A were inspected in ADNOC core stores. The relative distribution and abundance of fractures was noted in each reservoir.

The Reservoirs studied for calcite cement stratigraphy within fractures are G oil, F oil and water, C oil and water, B oil and water, and A oil. Other reservoirs have either very low volumes of fractures cement, or the fractures were absent or very small.

15 Petrographic and 163 highly polished thin sections were prepared to study the cross-cutting relationships between different paragenetic events (Table 2.1). Cathodoluminescence (CL) was used to distinguish the cement zones in calcite and dolomite, particularly within fracture cement zones. Comparative cement stratigraphy was established via CL zones.

Fracture abundance and aperture have been estimated from petrographic thin sections, and are given as a relative abundance within thin sections.

Reservoir	Petrographic	Highly Polished	Total
A oil	0	30	30
B oil	0	27	27
B water	6	23	29
C oil	3	9	12
C water	1	5	6
F oil	1	10	11
F water	1	13	14
G oil	3	31	34

Table. 2.1. Number and type of thin section studied in each reservoir

2.3 Results

2.3.1. Fracture distribution and orientation in core

Generally, fractures are more abundant in core and have thicker apertures in the Lower Thamama Reservoirs than in the Upper Thamama Reservoirs (Figure 2.1). The volume of cement in fractures in the Thamama Reservoirs increases in the deeper, lower reservoirs such that the Lower Thamama Reservoirs have more fracture cement than the Upper Thamama Reservoirs. The spacing between fractures both within the same fracture sets and between different fractures sets - ranges from between ~1mm to ~1 cm in cores.

Fractures are present in the Thamama reservoirs in both macroscopic (aperture reaching several centimetres) form, which appear mainly in the Lower Thamama Reservoirs (F & G), and in microscopic scale (hairline fractures) that appear mostly in the Upper Thamama Reservoirs (A, B and C) (Figure 2.1). Tables 2.2 and 2.3 shows the characteristics of the three main fracture sets in terms of approximate aperture size, cement type and relative abundance.

	Reservoir C			Reservoir B			Reservoir A		
Fracture Sets	Aperture width	Cemented	Relative abundance	Aperture width	Cemented	Relative abundance	Aperture width	Cemented	Relative abundance
Fracture Set 1	Few µm width	Yes, blocky & equant calcite	Most abundant	Few µm width	Yes, partially, blocky calcite, saddle dolomite	Most abandant	Few µm width	Yes, blocky calcite	Most abundant
Fracture Set 2	Few µm width	Yes, partially, blocky calcite	Least abandant	< 1 mm width	No	Common	Few µm width	No	Least abandant
Fracture Set 3	Does not exist			Does not exist			Does not exist		

Table 2.2: The characteristics of the main fractures sets in the Upper Thamama Reservoirs

	Reservoir G			Reservoir F		
Fracture Sets	Aperture width	Cemented	Relative abundance	Aperture width	Cemented	Relative abundance
Fracture Set 1	up to 2 cm	Yes, blocky & equant calcite, saddle dolomite	Most abundant	up to 2 cm	Yes, blocky & equant calcite, saddle dolomite	Most abundant
Fracture Set 2	up to 1 mm	No	2nd most abundant	up to 1 mm	No	2nd most abundant
Fracture Set 3	up to 1.7 cm	Yes, blocky calcite, saddle dolomite	Least abundant	up to 1.7 cm	Yes, blocky calcite	Least abundant

Table 2.3: The characteristics of the main fractures sets in the Upper Thamama Reservoirs

Blocky calcite is the most abundant cement in the fractures of the Thamama Reservoirs (Fig.2.1). This appears in greater volumes in the Lower reservoirs (F & G) than in the Upper reservoirs (A, B and C).

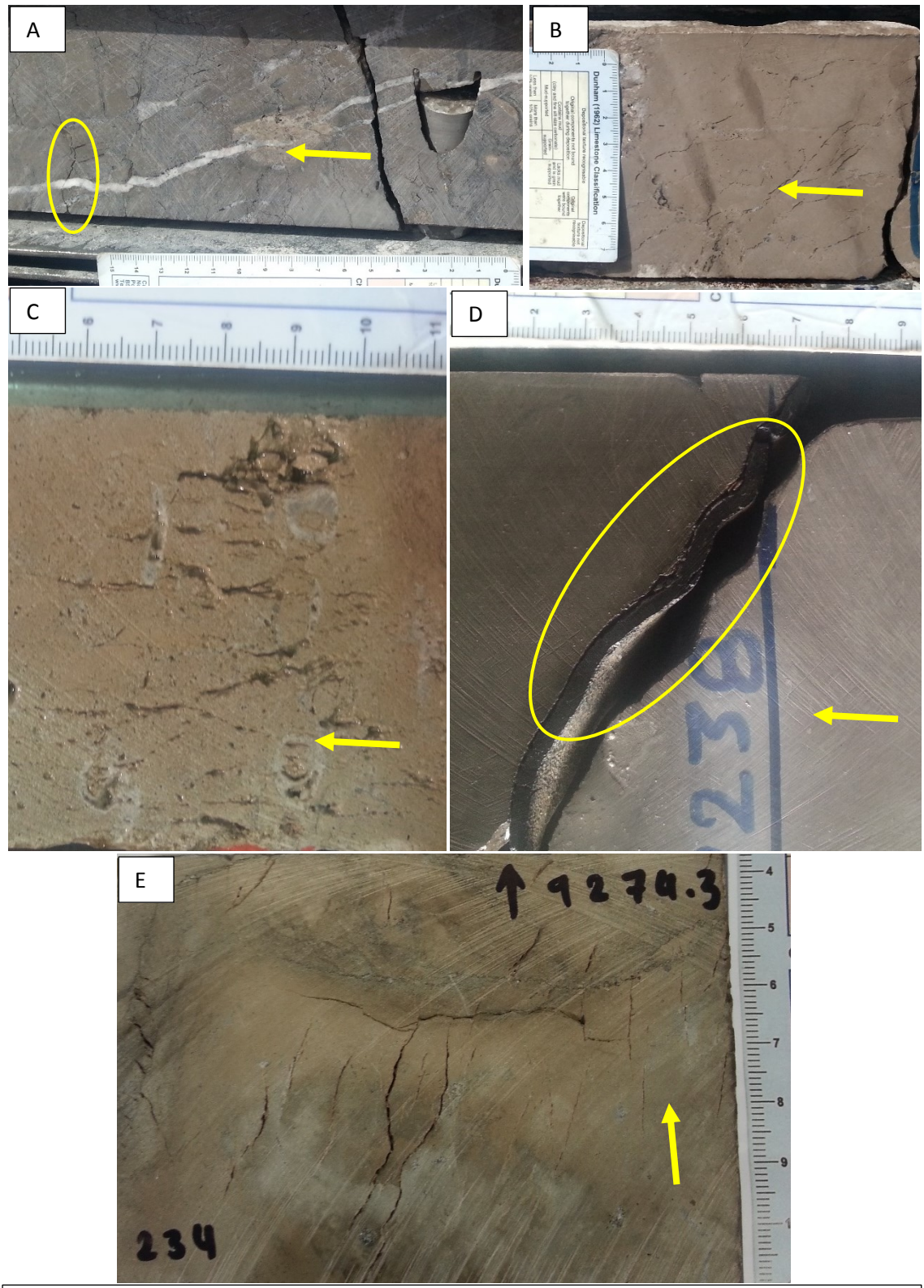

Fig. 2.1: Fracture types in core slabs (A) Open fracture cutting cemented fracture in Reservoir G oil. Open fractures density in Reservoirs G oil (B), B oil (C) and A oil (E). (D) Bitumen in fracture in Reservoir A oil. Yellow arrows pointed to stratigraphic younging

Saddle dolomite is the second most abundant fracture fill cement, but only appears in the Lower Thamama Reservoirs (F water & G oil) (Figs. 2.2A, B) and Upper Thamama Reservoir B water (Fig. 2.2C). Equant calcite is the least cement to appear in the fractures and it is found in small quantities in Reservoirs C, F and G.

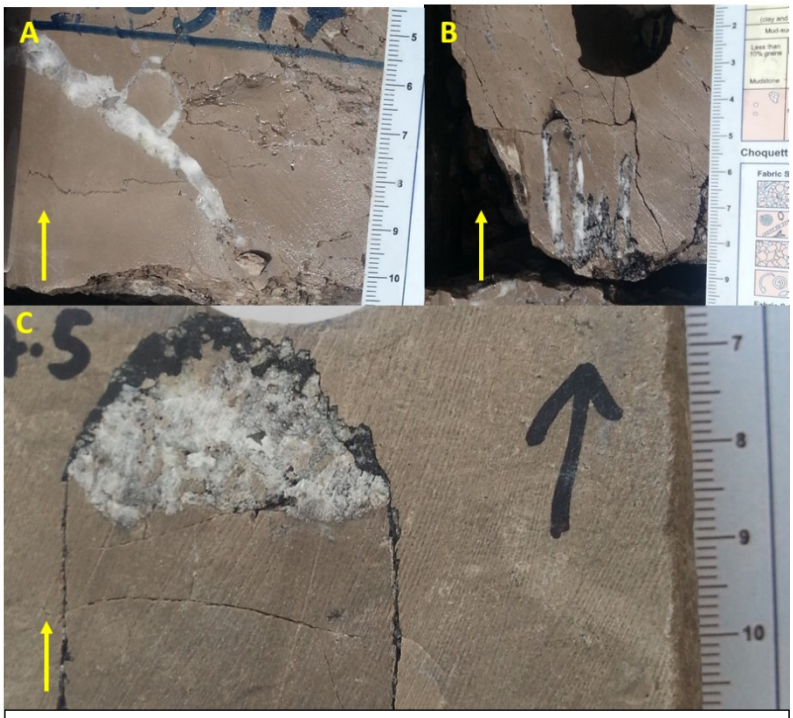

Fig. 2.2: Saddle dolomite in core slabs (A), (B) Saddle dolomite in fractures in Reservoir G oil. (C) Saddle dolomite in dissolution seams in Reservoir B water. Yellow arrows pointed to stratigraphic younging

Although each of the Thamama Reservoirs has a unique fracture set with up to 4 fractures present, three main fracture sets are present in most reservoirs (Fig. 2.3). The chronology of the fracture growth is observed from crosscutting relationships between fracture sets (Lavenu et al., 2013).

1. Fracture Set One (cemented)

They are the first set of fractures present in all of the Thamama Reservoirs, which form early in the paragenetic sequence. They are completely cemented (Fig. 2.3A) except for Reservoir B, where they are partially cemented.

2. Fracture Set Two (open or partially cemented)

The second set of fractures is open in all the Thamama reservoirs, except in Reservoirs B and C where they are partially cemented with blocky calcite. Fracture Set 2 cuts Fracture Set 1 perpendicularly, and is cut by Fracture Set 3 perpendicularly as well (Fig. 2.3B).

3. Fracture Set Three (cemented)

The third set of fractures is present the Lower Thamama Reservoirs (F & G) (Fig. 2.3C).

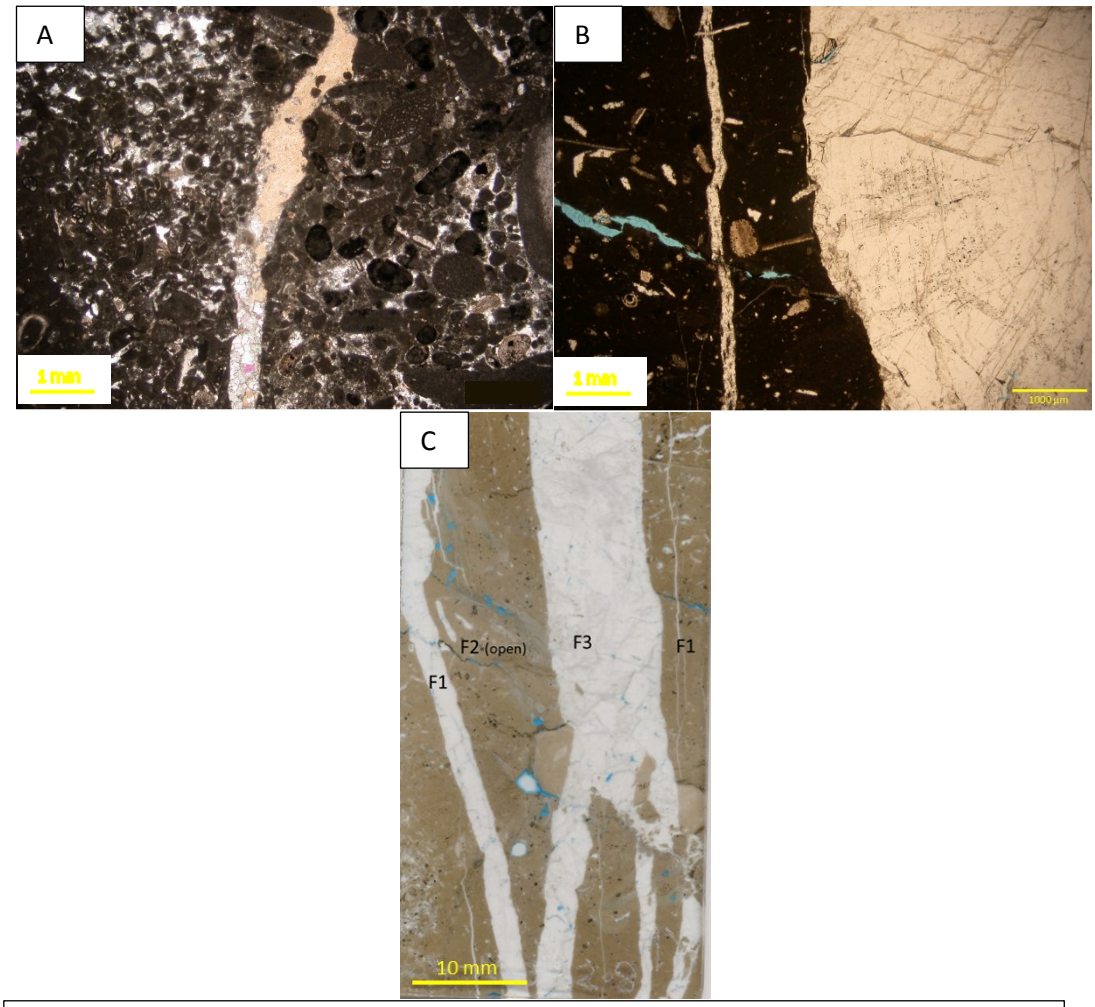

Fig. 2.3: Fracture types of Thamama in petrographic thin section. (A) Partially cemented fracture in Reservoir B oil (XPL). (B) Open fracture cutting cemented fracture in Reservoir G oil (PPL). (C) Thin section showing the three sets of fractures in Reservoir F oil (PPL).

2.3.2. Diagenetic events

Diagenetic cements and other events are briefly introduced here, with their distribution and inferred diagenetic setting: meteoric, marine phreatic, shallow burial and deep burial.

Calcite cementation:

Circumgranular Calcite

Circumgranular calcite is observed in the Upper Thamama Reservoirs (A oil, B oil and water, C oil and water) (Fig. 2.4A). This type of calcite cement is known to be precipitated in phreatic environments (Chilingarian et al., 1992).

Drusy calcite

Drusy calcite was mostly found in Reservoirs B and C (oil and water) (Fig. 2.4B). Drusy calcite can be precipitated from near-surface meteoric to deep burial environments, where crystal size can increase towards the centre of the pore-filling (Tucker & Wright, 1990).

Granular calcite

Granular cement was found in reservoirs A oil, B oil and water, C oil and water, F oil and water and G oil (Figure 2.4C). This type of calcite can form by recrystallization or grain growth (Larsen & Chilingar, 1979).

Syntaxial overgrowth

Syntaxial cement was found in B water and oil, C oil and F water (Figure 2.3D). This is an early marine cement, which grows on monocrystalline grains (echinoderms) (Meyers and Lohmann, 1978).

Equant calcite

Equant cement was found in all of the studied reservoirs (A oil, B oil and water, C oil and water, F oil and water and G oil) (Fig. 2.4E). This is the most common cement in limestones, and has more control over reservoir quality than any other carbonate cement because it occludes the most pore space (Loucks, 1983).

Dogtooth calcite

Dogtooth cement was only found in Reservoir C oil (Fig. 2.4F). It is distinguished by its scalenohedral and elongated rhombohedral crystals with sharp terminations, and can be an indication of either meteoric, marine-phreatic, shallow-burial or hydrothermal conditions (Flügel, 2009).

Blocky calcite

Blocky calcite was found in all the studied Thamama reservoirs, and it is the main cement type filling the fractures (Fig. 2.4G). Blocky calcite crystals that have no preferred orientation. Such cements usually form in burial environments (Haldar & Tisljar, 2014).

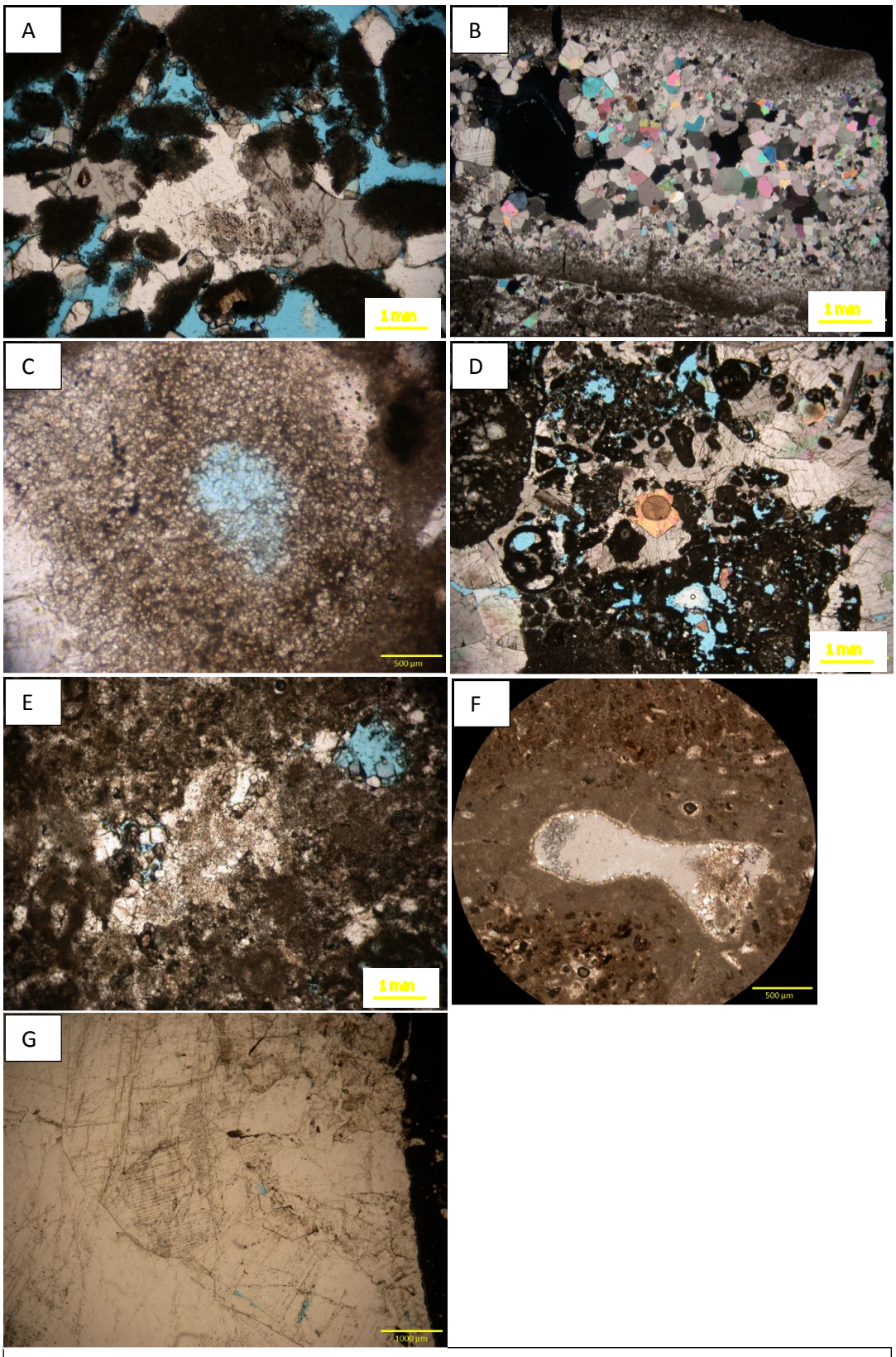

Fig. 2.4: Calcite cementation types. (A) Circumgranular in Reservoir G oil (XPL). (B) Drusy mosaic in Reservoir B oil (XPL). (C) Granular in Reservoir F oil (PPL). (D) Syntaxial in Reservoir F water (XPL). (E) Equant in Reservoir B water (PPL). (F) Dogtooth in Reservoir C oil (PPL). (G) Blocky calcite in Reservoir G oil (PPL).

Dolomite cements:

Rhombic (euhedral) dolomite

Rhombic dolomite appears in the matrix only (Figure 2.5A). Micro-rhombic dolomite appear along dissolution seams in Reservoirs A and B (Figure 2.5B).

Saddle dolomite

Saddle dolomite was found in fractures in Reservoirs G oil and F and B water and in matrix in all Thamama Reservoirs (Figure 2.5C).

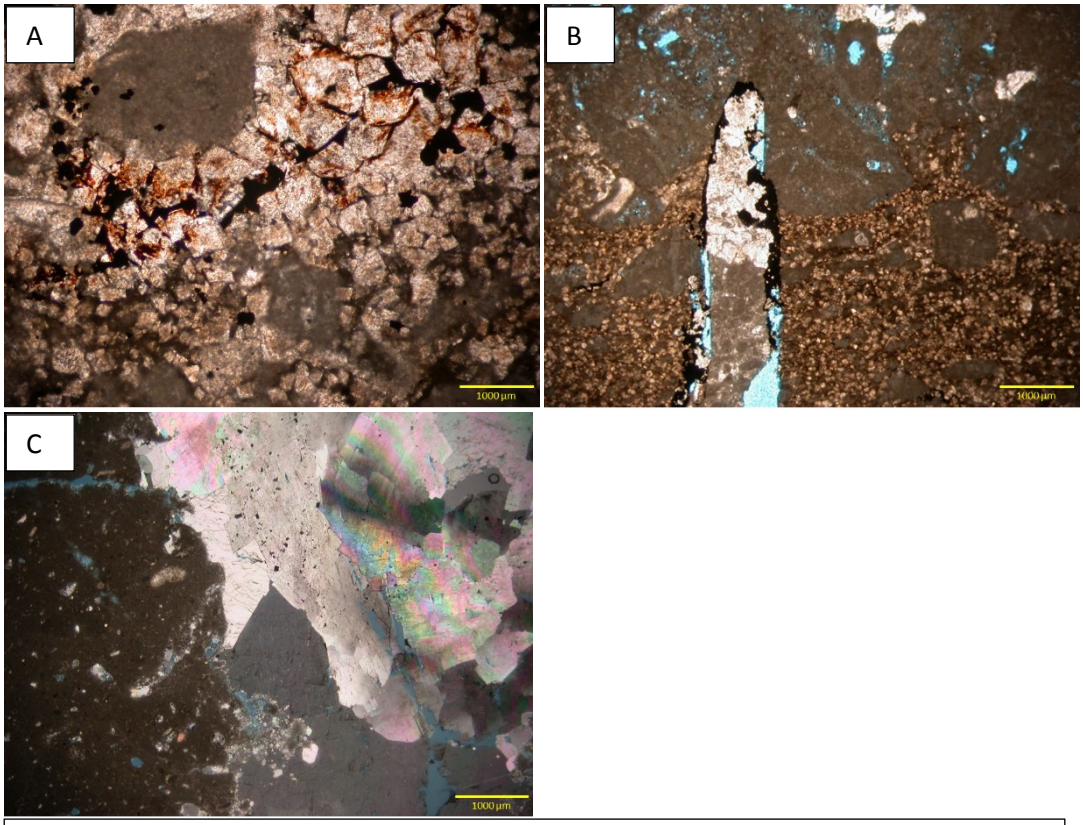

Fig. 2.5: Dolomite. (A) Rhombic dolomite in Reservoir C oil (PPL). (B) Micro-rhombic dolomite along dissolution seams in Reservoir B water (PPL). (C) Saddle dolomite with indulus extension in Reservoir G oil (XPL).

Micritization:

Micritization is pervasive throughout the Thamama (Fig. 2.6A). Micritisation is a process of detrital abrasion and microborings caused by bioerosion of endolithic algae in marine environments (Tucker & Wright, 1990).

Mechanical compaction:

Mechanical compaction is apparent in all studied Thamama reservoirs (Fig. 2.6B). This takes place during burial, originating mainly from pore fluid expulsion and rearrangement of solid particles (Brüch et al., 2016).

Hardgrounds:

Hardground was found in the Upper Thamama Reservoirs (A, B and C) at sequence boundaries (Fig. 2.6C) or on flooding surfaces. The hardground is a lithified surface that forms syn-sedimentarily to create a lithified sea floor (Wilson et al., 1992).

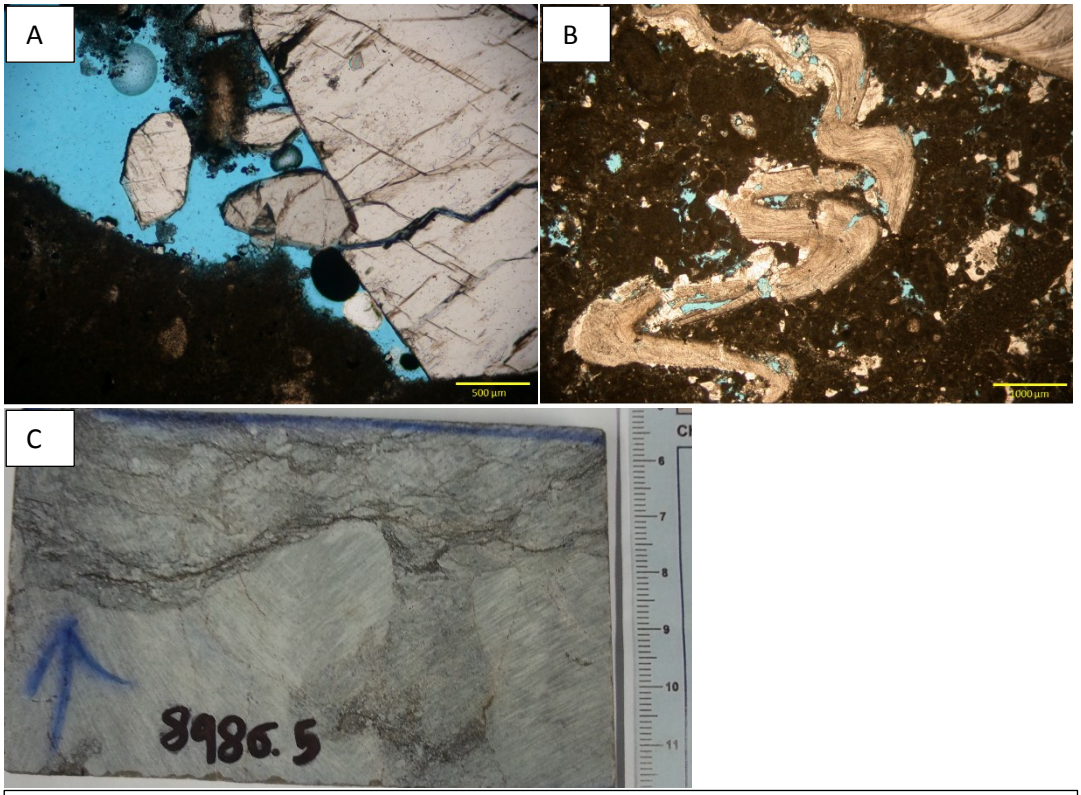

Fig. 2.6: Diagenetic processes. (A) Micritization in Reservoir G oil (XPL). (B) Mechanical compaction in thin section of Reservoir G oil (PPL). (C) Hard ground in core slab from Reservoir B oil.

Pyrite:

Pyrite aggregates were found in small quantities in all Thamama Reservoirs except Reservoir F. Framboidal pyrite was found in the Upper Thamama Reservoirs (A, B, C) (Figure 2.7A) and euhedral pyrite was found in Reservoir G (Fig. 2.7B).

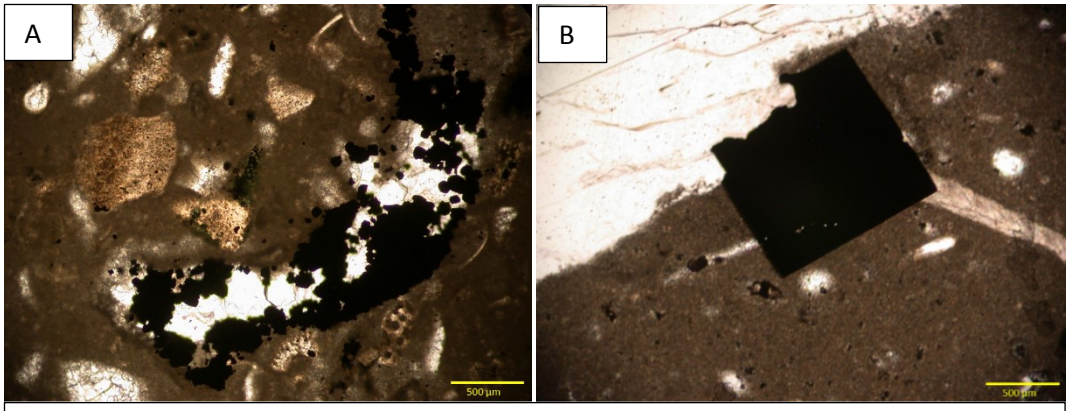

Fig. 2.7: Pyrite cement. (A) Framboidal pyrite in Reservoir A oil (PPL). (B) Euhedral pyrite in Reservoir G oil (PPL).

Bitumen:

Bitumen appeared in matrix and fractures, as well as associated with stylolites in all of the Thamama reservoirs (Figure 2.8A). This probably formed from liquid petroleum that lost volatiles, oxidation, and biologic degradation after seepage to the surface. Bitumen can occur as impregnations inhabiting the pore spaces of sandstones and carbonates in veins and dykes (Boggs, 2006).

Dissolution seams:

They are associated with bitumen and/or stylolites in all reservoirs (Figure 2.8B).

Stylolites:

They are closely associated with bitumen in most of the Thamama reservoirs (Figure 2.8C). Stylolites are also sometimes associates with fractures.

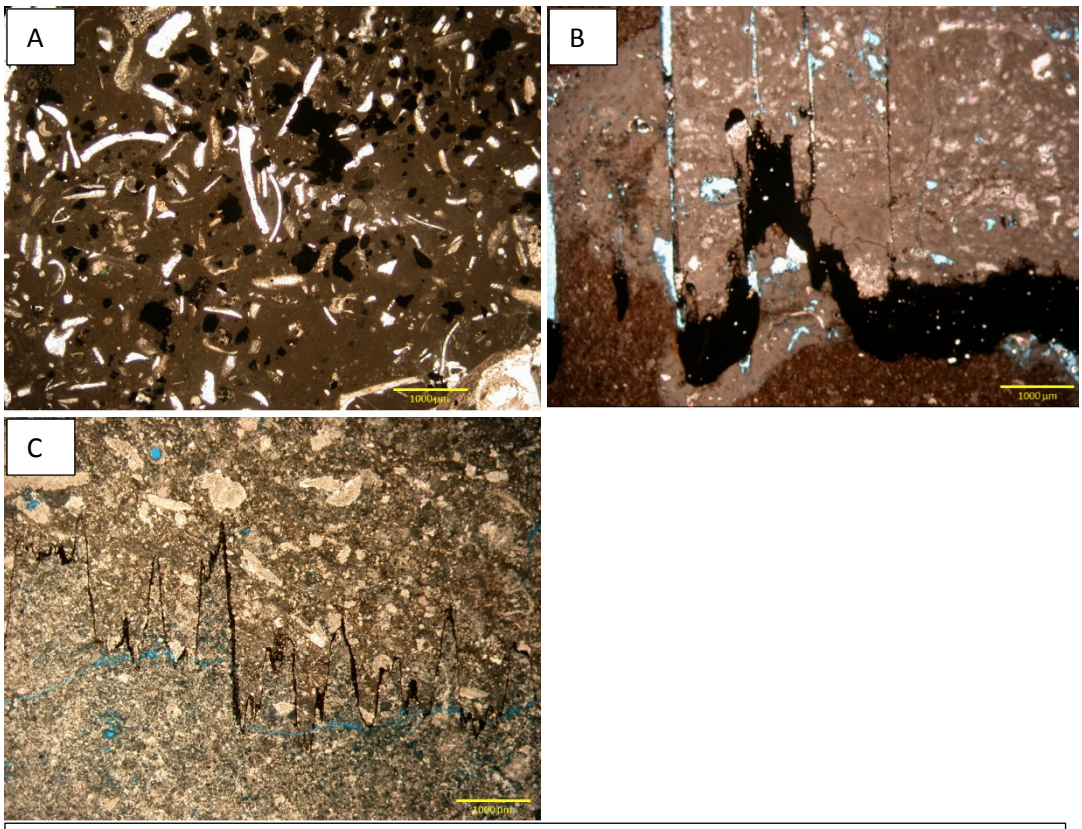

Fig. 2.8: (A) Bitumen in Reservoir B oil (PPL). (B) Dissolution seams in Reservoir F oil (PPL). (C) Stylolites in Reservoir B oil (PPL).

Kaolinite:

Small amounts of kaolinite were noted in Reservoir B only (Fig. 2.9A).

Glauconite:

Glauconite was only found in Reservoir A (Fig. 2.9B).

Anhydrite:

Anhydrite showed in small quantities in Reservoirs B and F (Figure 2.9C). It is known to be the most common replacive mineral in deep carbonates aquifers (Machel, 2005).

Dissolution:

Dissolution of aragonite in the Thamama affected the matrix and lead to re-texturing of the reservoir rocks (Russell, 2001). Dissolution of cement appeared throughout the

Thamama both in fractures and matrix (Figure 2.9D). Although less dissolution occurs in the burial environment than in the meteoric, buried carbonate sediments that are subjected to uplift and when placed within the meteoric zone might undergo extensive dissolution of earlier formed cements under the effect of chemically aggressive CO_2 charged meteoric waters (Boggs, 2006).

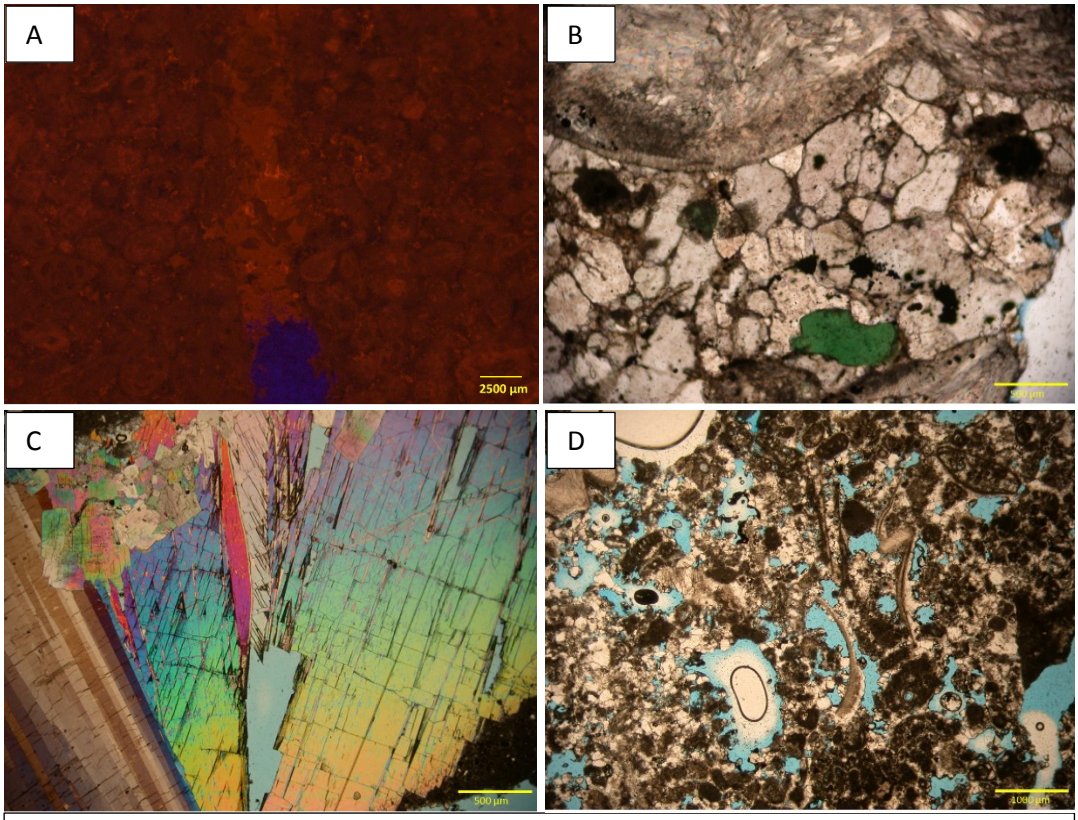

Fig. 2.9: Minor types of cements (A) Kaolinite in Reservoir B oil (CL). (B) Glauconite in Reservoir A oil (XPL). (C) Anhydrite in Reservoir F oil (XPL). (D) Dissolution in Reservoir C water (PPL).

2.3.3. Paragenetic sequences

Paragenetic sequences were established for all five reservoirs, where the fracture timing of formation and cementation was noted and the number of fracture events was highlighted. Relative fracture abundance is also given. The paragenetic sequence was constructed based on petrographic cross-cutting relationships, and overlapping and superposition principles for relative chronological classification (Lavenu et al., 2013), and placed within three diagenetic settings: marine phreatic, shallow burial and deep burial.

In general, Fracture Set 1 is cemented with equant and blocky calcite and saddle dolomite in some reservoirs, and Fracture Set 3 is cemented with blocky calcite and sometimes saddle dolomite in some reservoirs. Some fractures are associated with stylolites.

In Reservoir B, the paragenetic sequence for oil and water legs are combined., as there were no difference between the two.

Micritization was the first process in all of the reservoirs and is interpreted as an early marine phreatic event. Early cements such as equant calcite formed in the marine phreatic realm and extended to shallow burial in some reservoirs, while late cements like blocky calcite formed during shallow to deep burial. Dissolution was often the last event of all paragenetic sequences.

Reservoir G

Fig. 2.10 shows the paragenetic sequence of Reservoir G, where there are 23 diagenetic events. Here there are four fracture sets. The first two appear in the middle of the paragenetic sequence, inferred to form during shallow burial right after the marine phreatic events and with no separation between them. These are Fracture Set 1, which was cemented and reached ±2 cm width. Fracture Set 2 is open, a few μm to 1mm in width, and less abundant than fracture set one. The cement in Fracture Set 1 includes equant and blocky calcite and saddle dolomite. The final two sets of fractures appear in the latest stages of the paragenetic sequence during the deep burial, after the occurrence of bitumen and were followed by dissolution. This is a minor set of fractures that does not belong to the three main sets of fractures

mentioned and is associated with stylolites. The third set (Fracture Set 3) is open, a few mm in width, and is the least abundant in the Reservoir). The fourth set of fractures reaches 1.7 cm in width and is cemented with blocky calcite and saddle dolomite.

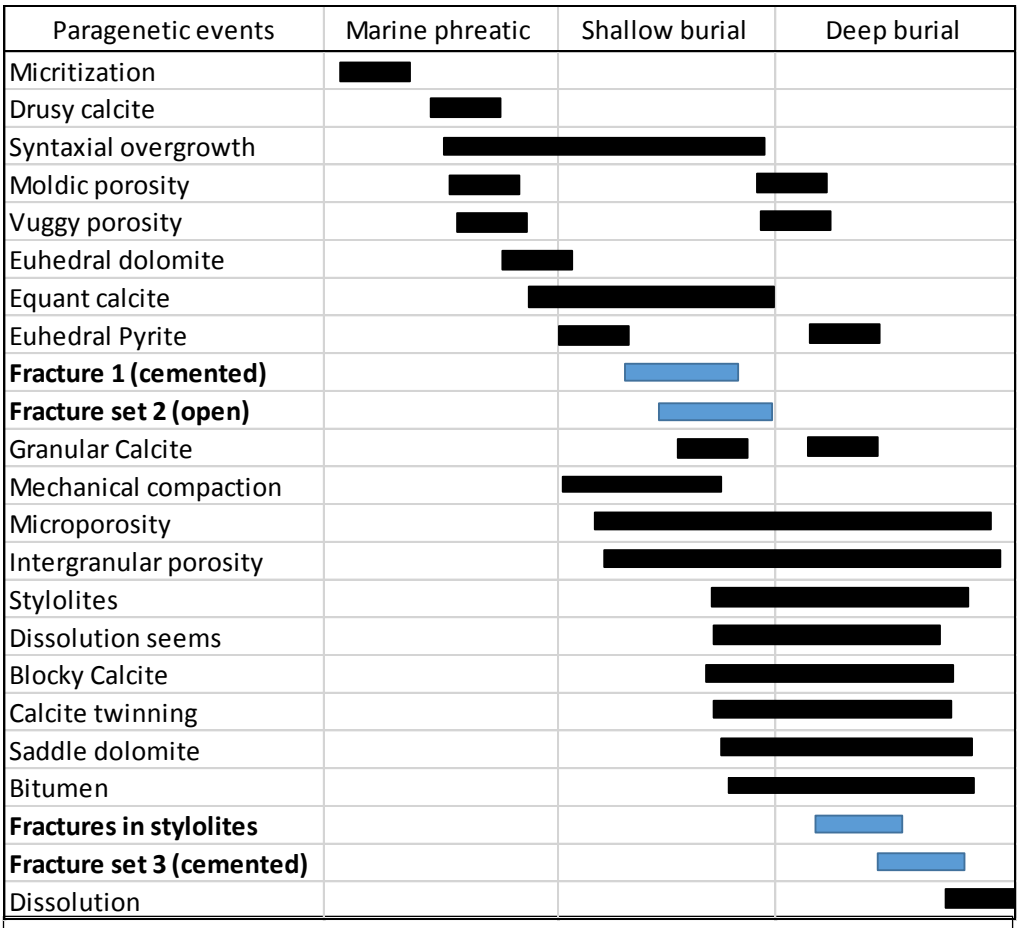

Fig. 2.10: Paragenetic sequence for Reservoir G.

Reservoir F

Reservoir F has the same four fracture sets as Reservoir G and 23 paragenetic events. They include 3 fractures sets that are part of the 3 main fracture sets and 1 minor fracture set that only appears in Reservoir F. The difference in Reservoir F is that the first set of fractures (which are cemented, reach ±2 cm in width) appear very early in the marine phreatic sequence. Fracture Set 1 is cemented with equant and blocky calcite as well as saddle dolomite as in Reservoir G. Eight paragenetic events

separate the first from the second set of fractures, which are open, a few µm to 1mm, and less abundant than fracture set one. The third set of fractures is open, a few µm width, and is least abundant in the Reservoir. This set is associated with stylolites and it is followed immediately by bitumen (Fig. 2.11). These are inferred to appear during shallow burial. After another six paragenetic sequences, the fourth set of fractures (Fracture Set 3), which reach 1.7 cm in width and appear very late in the deep burial and are cemented with blocky calcite.

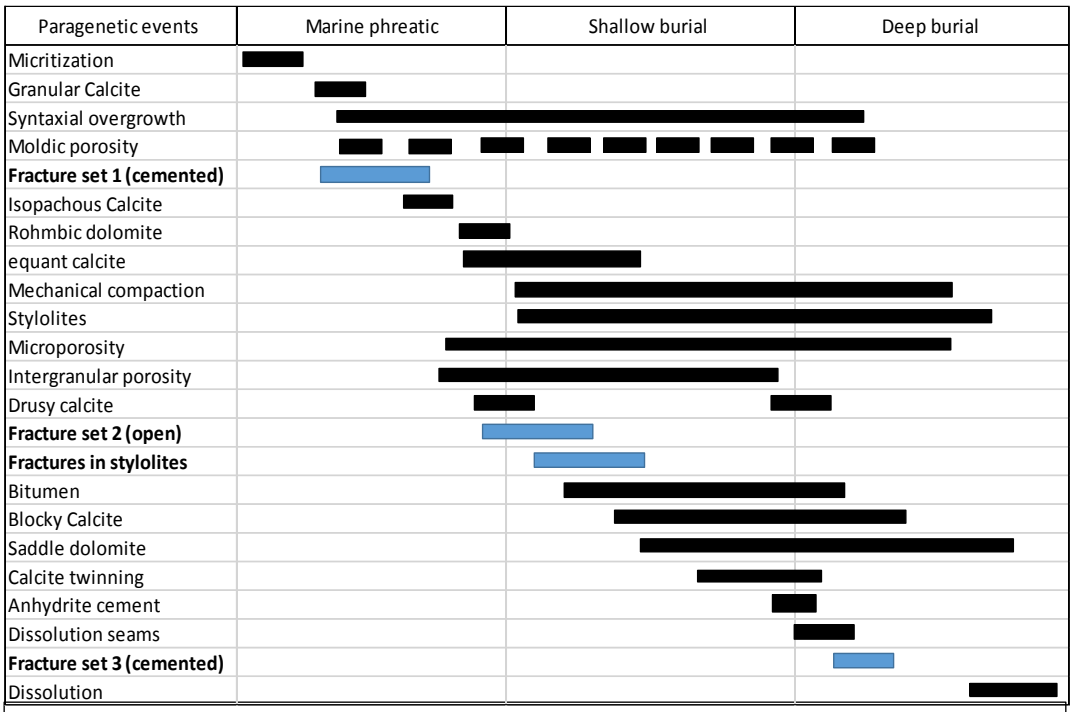

Figure 2.11: Paragenetic sequence for Reservoir F.

Reservoir C

Reservoir C is the only reservoir with 2 fracture sets and 25 paragenetic events (Fig. 2.12). Fracture Set 1 (cemented, a few µm width) appeared in the middle of the paragenetic sequence, during shallow burial and was filled with equant and blocky calcite. Fracture Set 2 (a few µm width); unlike the Lower Thamama Reservoirs (F & G), appeared during the shallow burial and is partially open. There were three paragenetic events separating the two fracture sets.

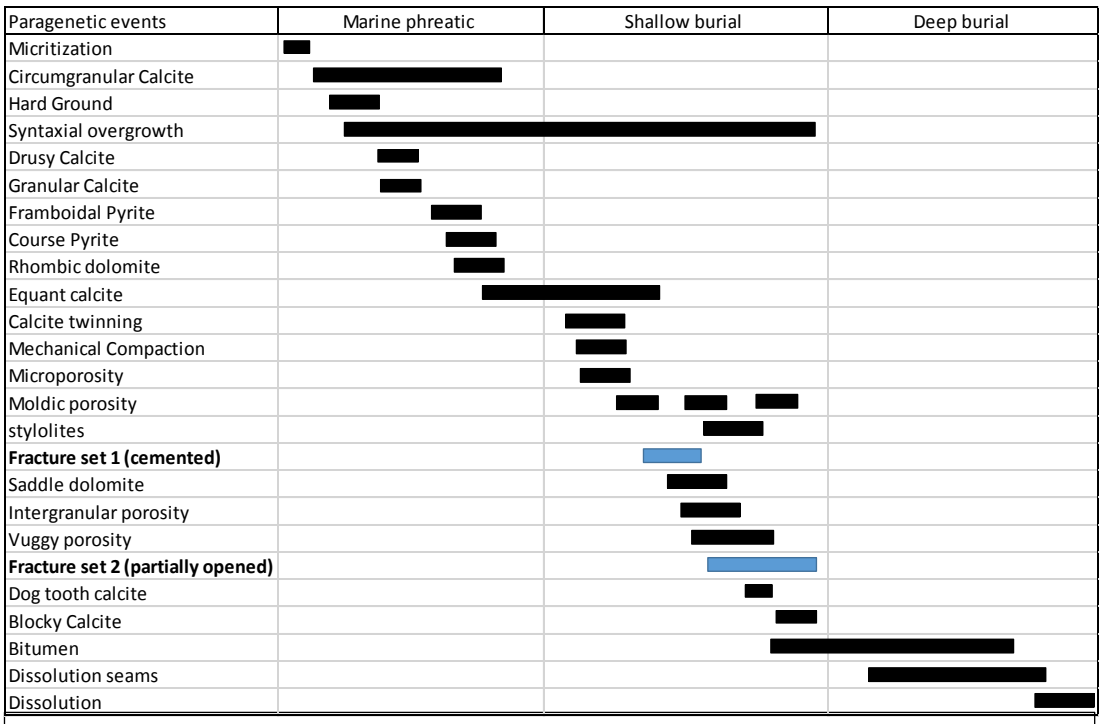

Figure 2.12: Paragenetic sequence for Reservoir C

Reservoir B

Reservoir B underwent 28 of diagenetic events (Fig. 2.13). There are four sets of fractures where two of them (the partially open and open) correspond with two of the main sets of fractures (Fracture Set 1 cemented and Fracture Set 2 opened) that appeared in most of the reservoirs. The first two sets of fractures (a few μm width appeared during the shallow burial. These were both partially filled with blocky calcite cement. After six paragenetic events the third set of fractures appeared, cutting through the bitumen, which appeared immediately before it. The third set of fractures was minor (a few μm width,) that formed only in Reservoir B initiating in shallow burial and extending to the deep burial. The last set of fractures (Fracture set 4 in Reservoir B) and corresponding to Fracture Set 2 in the main set of fractures, is open and <1mm width. This formed after a further six paragenetic events and formed mainly during deep burial.

Fig. 2.13: Paragenetic sequence for Reservoir B

Reservoir A

Reservoir A had four fracture sets, including major and minor sets, and 23 diagenetic events. Two of them, the cemented Fracture Set 1 (a few µm width) and the open Fracture Set 2 (a few µm width) belong to the main fracture sets. Fracture Set 1 was cemented by blocky calcite, and formed during the marine phreatic and shallow burial realms. One paragenetic event separates Fracture Set 1 from Fracture Set 2, whose formation extends longer in the shallow burial realm. After six more paragenetic events, the minor, partially opened fracture set 3 formed in the shallow burial realm. After another two paragenetic events, the forth fracture set (minor) formed, which is open and cross-cuts stylolites (Fig. 2.14).

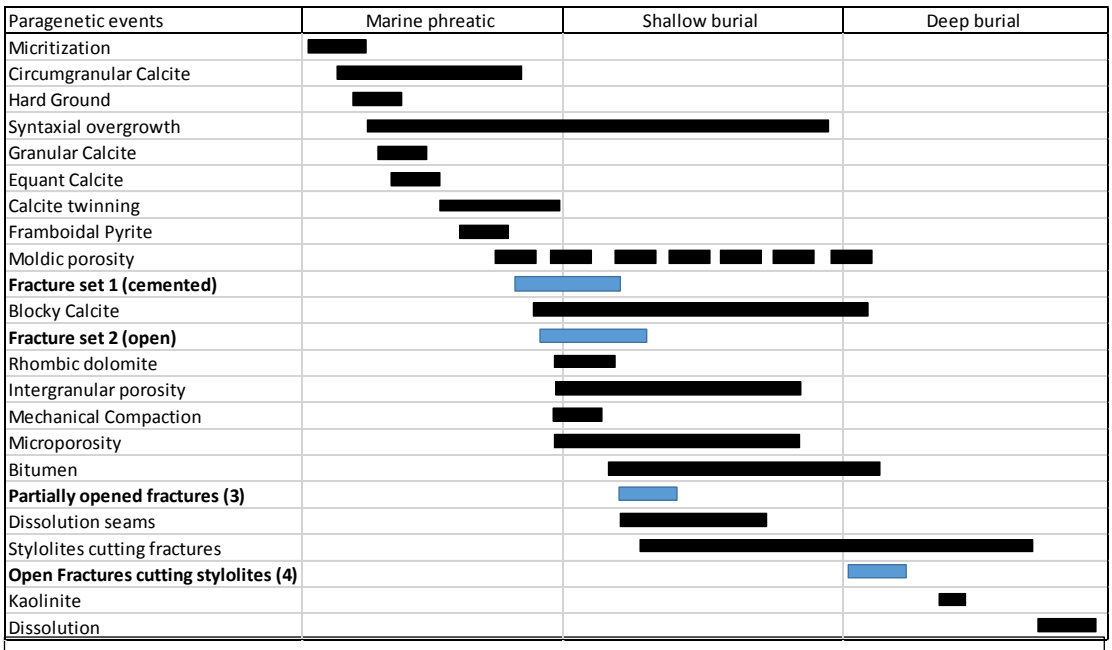

Fig. 2.14: Paragenetic sequence for Reservoir A

2.3.4 Cement stratigraphy

Identification of stages or zones of precipitated cement can be an important tool in determining the sequence of diagenetic environments (James & Choquette, 1984). Cathodoluminescence (CL) allows a cement stratigraphy to be established using CL zones (Boggs & Krinsley, 2006). Mn activates luminescence and Fe quenches luminescence (Searl, 1987; Yamin et al., 1996). Each of the Thamama reservoirs fracture sets has a number of cement zones in both calcite and dolomite cements. Only blocky and equant calcite, and saddle dolomite cements were found in fractures.

Equant calcite cement zones

Equant calcite cement only appeared in 3 reservoirs in Fracture Set 1, these are G, F and C - all in the oil leg. No equant calcite was found in Fracture Set 3.

Reservoir G oil

In Fracture Set 1 there were three equant calcite cement zones in Reservoir G oil. Cement zone 1 is bright red, cement zone 2 is dull red and cement zone 3 is medium red (Figures. 2.15, 2.16).

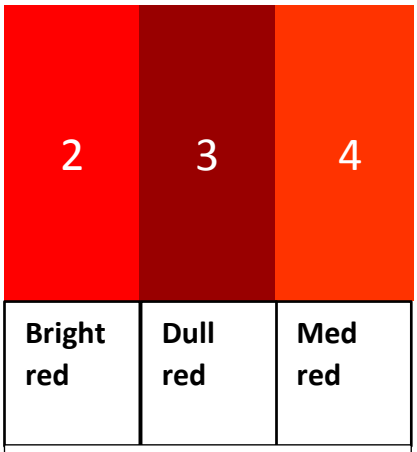

Fig. 2.15. Reservoir G oil equant calcite cement zones, Fracture Set 1

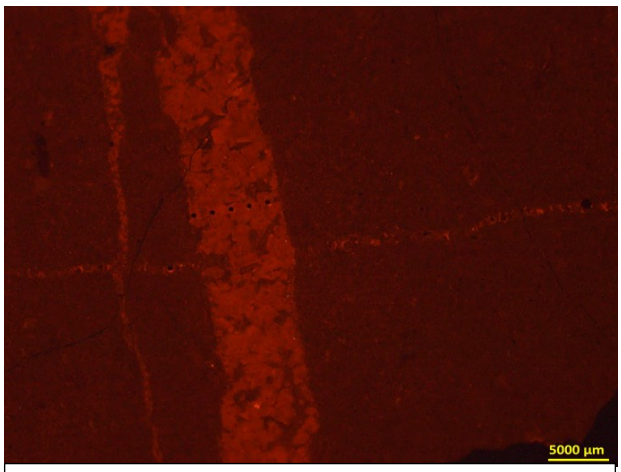

Fig. 2.16. CL image for Reservoir G oil equant calcite cement zones, Fracture Set 1

Reservoir F oil

As in Reservoir G, Reservoir F oil has three cement zones in Fracture Set 1. Cement zone 1 (Medium red), cement zone 2 (Medium bright red) and cement zone 3 (Dark red) (Figures. 2.17, 2.18).

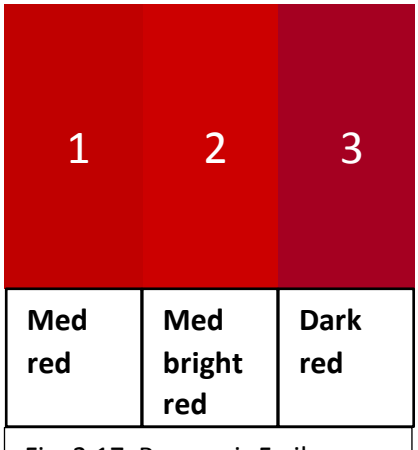

Fig. 2.17. Reservoir F oil equant calcite cement zones, Fracture Set 1

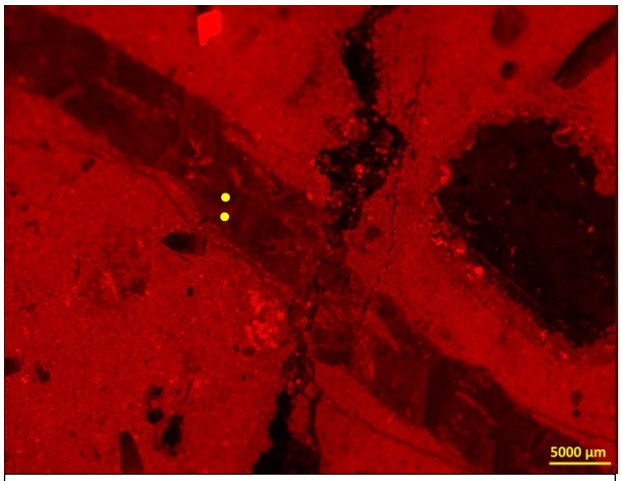

Fig. 2.18. CL image for Reservoir F oil equant calcite cement zones, Fracture Set 1

Reservoir C oil

There were two cement zones in Reservoir C. Cement zone 1 is dark-medium red and cement zone 2 (Bright red) (Figures. 2.19, 2.20).

Fig. 2.19. Reservoir C oil equant calcite cement zones, Fracture Set 1

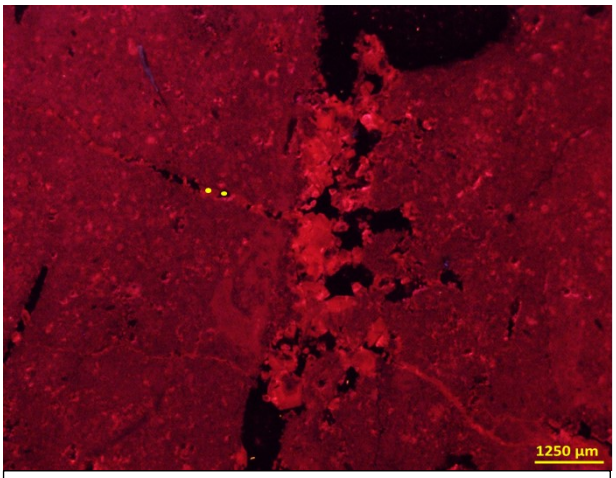

Fig. 2.20. CL image for Reservoir C oil equant calcite cement zones, Fracture Set 1. Lots of dissolution noticed

Blocky calcite cement zones

Reservoir G oil

This cement has five cement zones in Fracture Set 1. The most volumetrically important was cement zone 1. The colour scheme for the five cement zones was; non luminescent red for cement zone 1, bright red for cement zone 2, dull to medium red for cement zone 3, bright red for cement zone 4 and medium red for cement zone 5 (Figures 2.21, 2.22).

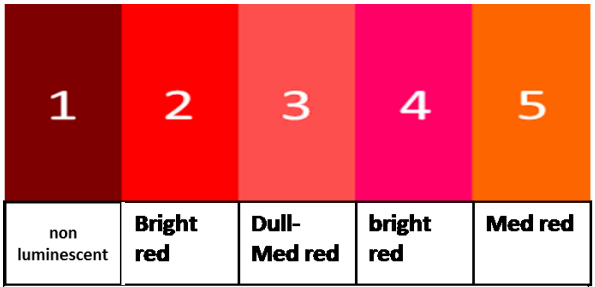

Fig. 2.21. Reservoir G oil cement zones in blocky calcite cement of Fracture Set 1

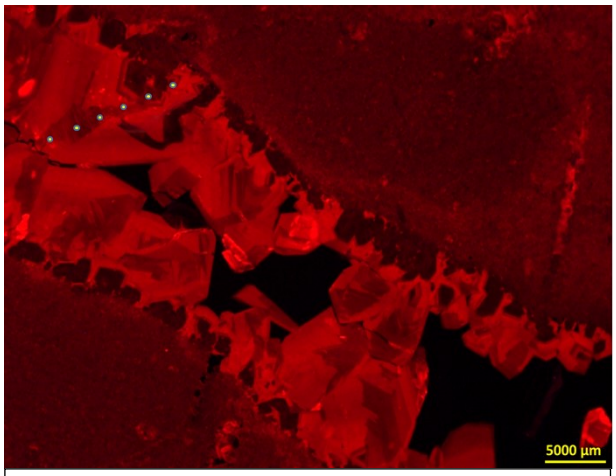

Fig. 2.22. CL image for Reservoir G oil cement zones in blocky calcite cement of Fracture Set 1

In Fracture Set 3, Reservoir G has also five cement zones (Figures. 2.23, 2.24).

1	2	3	4	5
Dark dull	**Bright red**	**Bright light red**	**Bright med red**	**Med red**

Fig. 2.23. Reservoir G oil cement zones in blocky calcite cement of Fracture Set 3

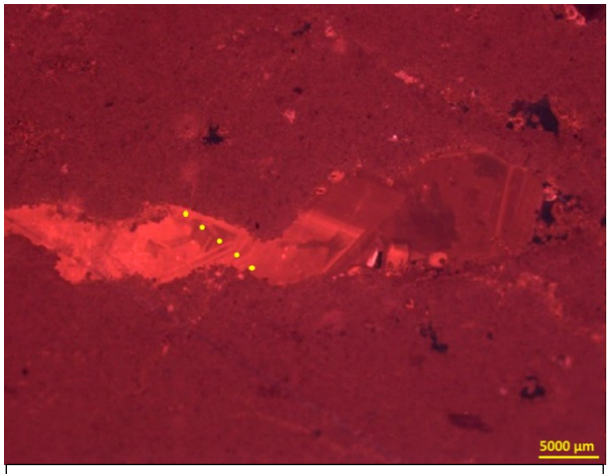

Fig. 2.24. CL image of Reservoir G oil cement zones in blocky calcite cement of Fracture Set 3

Reservoir F oil

Reservoir F oil has six cement zones (Figures 2.25, 2.26). The most volumetrically important cement zones are 3, 2 and 1 respectively. Cement zone 1 is dull red, cement zone 2 is medium to bright red, cement zone 3 is dull to dark red, cement zone 4 is bright red, cement zone 5 is dull to medium red and cement zone 6 is bright red.

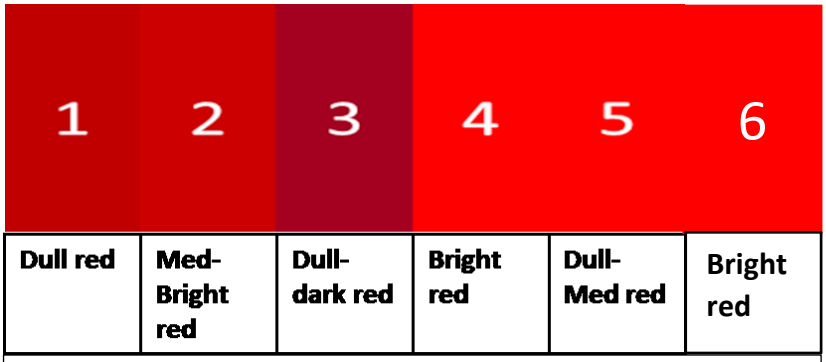

Fig. 2.25. Reservoir F oil cement zones in blocky calcite cement of Fracture Set 1

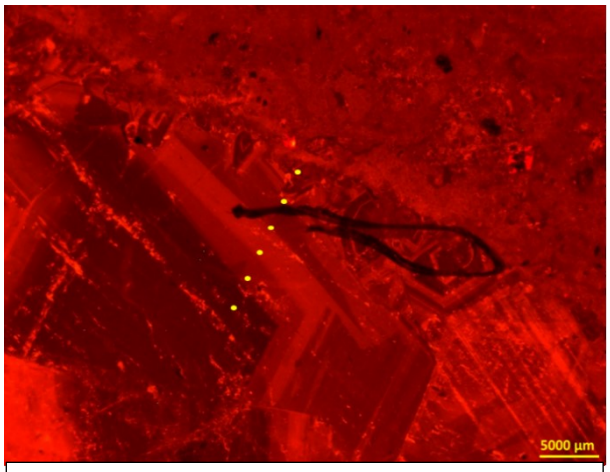

Fig. 2.26. CL image for Reservoir F oil cement zones in blocky calcite cement of Fracture Set 1. (Black line is an irremovable scratch or mark)

Unlike Fracture Set 1, the blocky calcite cement in Fracture Set 3 has only 3 cement zones. These are cement zone 1 (dark red), cement zone 3 (dull dark red) and cement zone 4 (bright red) (Figures. 2.27, 2.28).

Fig. 2.27. Reservoir F oil cement zones in blocky calcite cement of Fracture Set 3

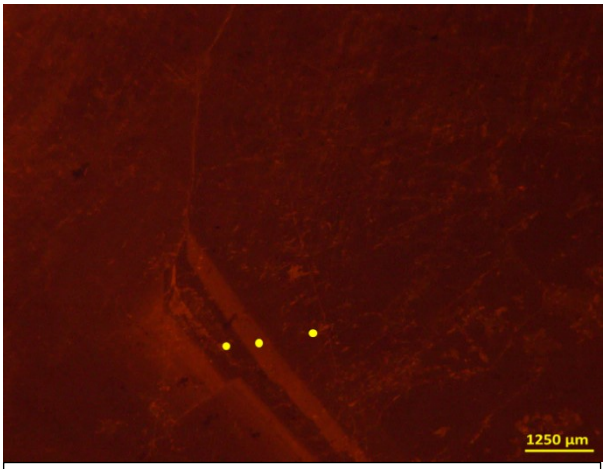

Fig. 2.28. CL image for Reservoir F oil cement zones in blocky calcite cement of Fracture Set 3

Reservoir C oil

In Fracture Set 1, the number of blocky calcite cement zones in Reservoir C oil is restricted to one cement zone, which is cement zone 3 (Bright red) (Figures. 2.29, 2.30).

Fig. 2.29. Reservoir C oil cement zone in blocky calcite cement of Fracture Set 1

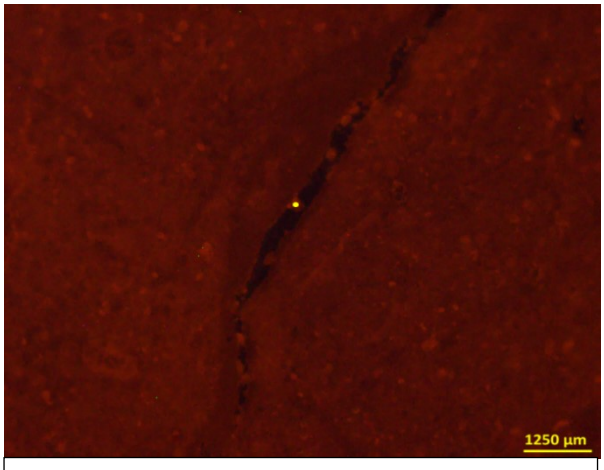

Fig. 2.30. CL image of Reservoir C oil cement zone in blocky calcite cement of Fracture Set 1

Reservoir B oil and water

In Fracture Set 1 in reservoir B oil, only two cement zones were noted. The first cement zone in fractures is dull to medium red, the second cement zone (bright red) (Figures 2.31, 2.32).

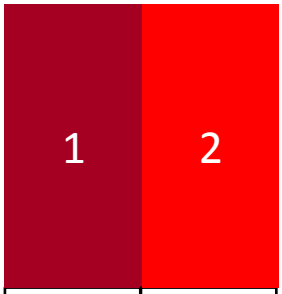

Fig. 2.31. Reservoir B oil blocky calcite cement zones in Fracture Set 1

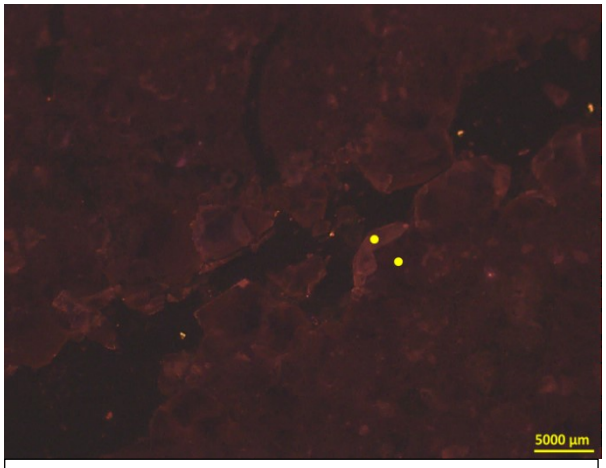

Fig. 2.32. CL image for Reservoir B oil blocky calcite cement zones in Fracture Set 1. Yellow dots highlight each cement zone.

Reservoir B water had three cement zones. Cement zone 1 is non-luminescent, cement zone 2 is bright red and cement zone 3 is dark red (Figures 2.33, 2.34).

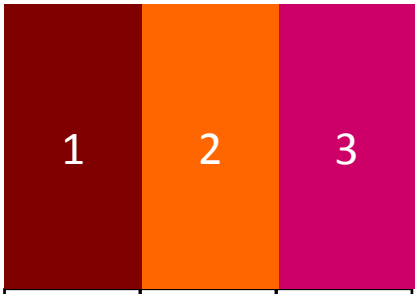

Fig. 2.33. Reservoir B water blocky calcite cement zones in Fracture Set 1

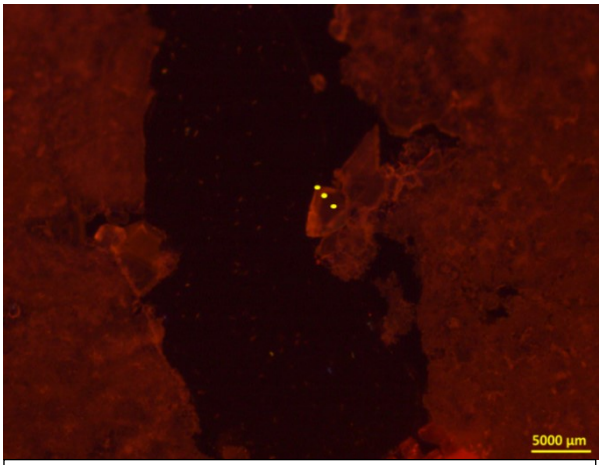

Fig. 2.34. CL image of Reservoir B water blocky calcite cement zones in Fracture Set 1. Yellow dots highlight each cement zone

Reservoir A oil

Fracture Set 1 in Reservoir A oil has 4 cement zones. Cement zone 1 is dull-dark red, cement zone 2 is medium red, cement zone 3 is bright red and cement zone 4 is bright light red (Figures 2.35, 2.36).

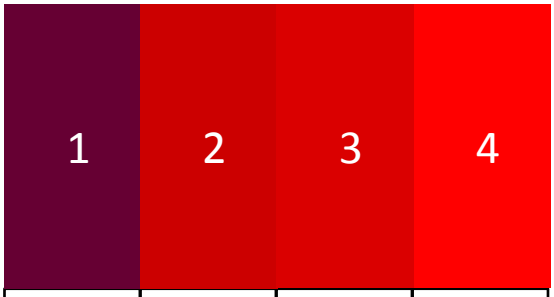

Fig. 2.35. Reservoir A oil blocky calcite cement zones in Fracture Set 1

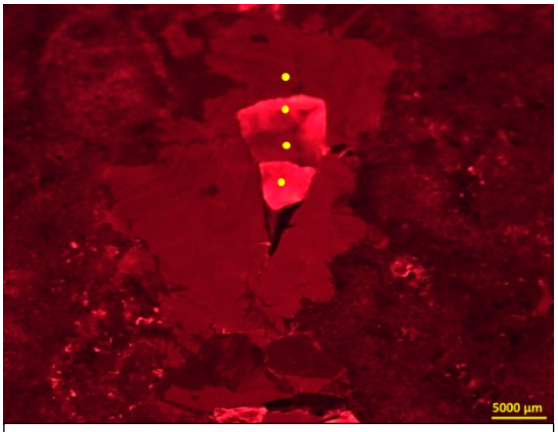

Fig. 2.36. CL image of Reservoir A oil blocky calcite cement zones in Fracture Set 1. Yellow dots highlight each cement

Dolomite cement zones

Reservoir G oil, Reservoir F water and Reservoir B water in Fracture Set 1 and Reservoir G oil in Fracture Set 3 had the greatest volumes of dolomite cement found in fractures. Only saddle dolomite was found in fractures, and these were highly zoned. The first zones are very dark red to non-luminescent cement followed by very bright cement zones, and this pattern repeats itself in cycles. However, this is reversed in Reservoir B water, where the first cement zone was a bright zone. Sometimes the cement zones are very thin and numerous so that they are classified as one cement zone, such as in cement zone 9 in Reservoir G oil.

Reservoir G oil

Reservoir G oil had 13 dolomite cement zones in Fracture Set 1 and 7 dolomite cement zones in Fracture Set 3. In Fracture Set 1, saddle dolomite cement zone 1 is non-luminescent (as in all of the studied reservoirs), cement zone 2 is bright red, cement zone 3 is dull red, cement zone 4 is very bright red, cement zone 5 is dull red, cement zone 6 is medium to dark red, cement zone 7 is very bright red, cement zone

8 is dull red, cement zone 9 is bright red, cement zone 10 is dull red, cement zone 11 is bright red, cement zone 12 is dull red and cement zone 13 is bright red (Figures 2.37, 2.38) It is noticed that the cement zones repeat in cycles.

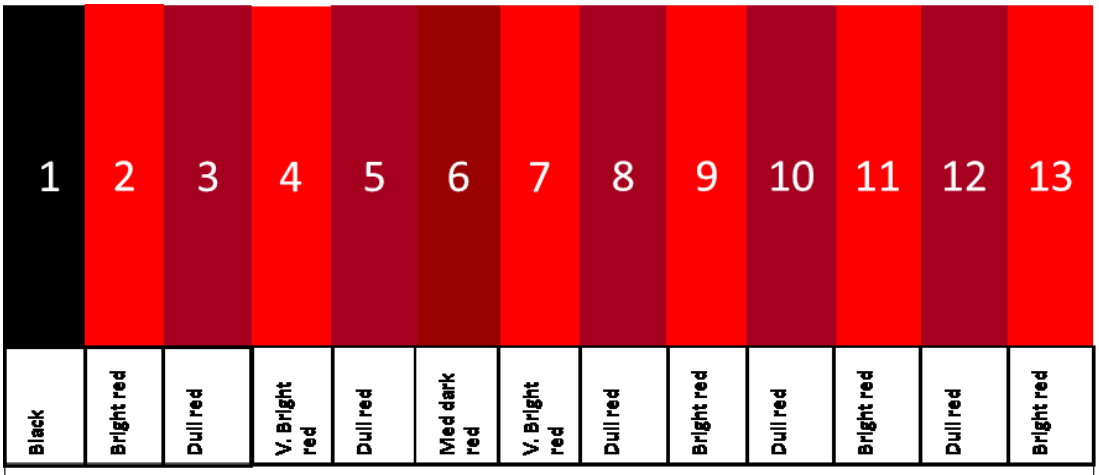

Fig. 2.37. Saddle dolomite cement zones of Fracture Set 1 in Reservoir G oil.

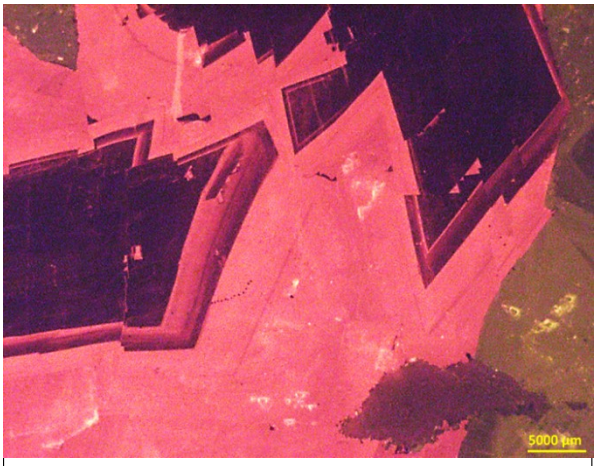

Fig. 2.38. CL image of Saddle dolomite cement zones of Fracture Set 1 in Reservoir G oil.

In Fracture Set 3, saddle dolomite cement zone 1 is non-luminescent, cement zone 2 is bright red, cement zone 3 is dark red, cement zone 4 is very bright, cement zone 5 is dull red, cement zone 6 is medium red and cement zone 7 is very bright red (Figures 2.39, 2.40). Fracture Sets 1 and 3 has 4 similar cement zones, 1, 2, 4 and 5.

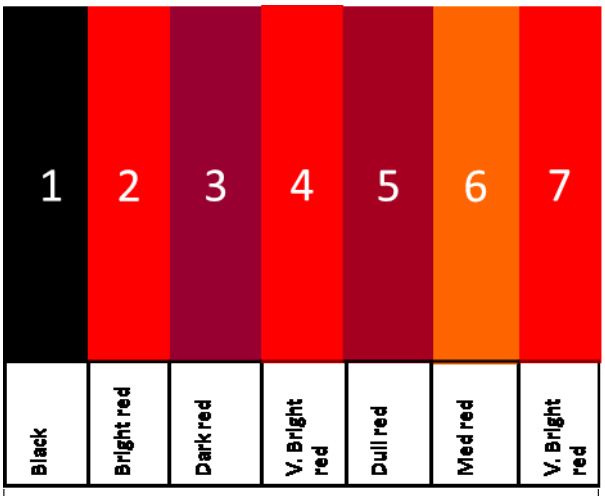

Fig. 2.39. Saddle dolomite cement zones of Fracture Set 3 in Reservoir G oil.

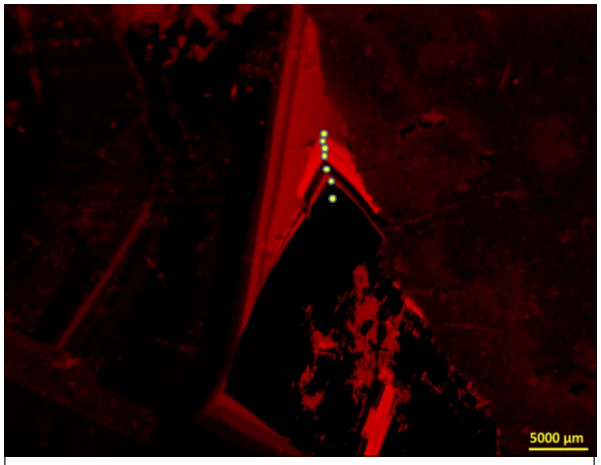

Fig. 2.40. CL image for Saddle dolomite cement zones of Fracture Set 3 in Reservoir G oil. Yellow dots highlight each cement zone.

Reservoir F water

Saddle dolomite in Reservoir F water was only found in Fracture Set 1. Cement zone 1 is non-luminescent, cement zone 2 is bright red, cement zone 3 is dark red, cement zone 4 is bright red, cement zone 5 is dark red and cement zone 6 is bright red (Figures 2.41, 2.42).

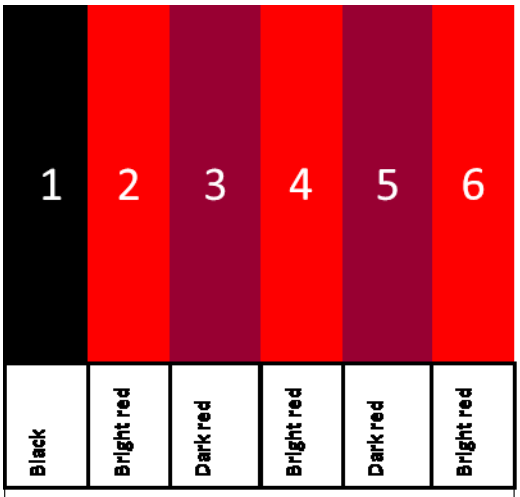

Fig. 2.41. Saddle dolomite cement zones of Fracture Set 1 in Reservoir F water.

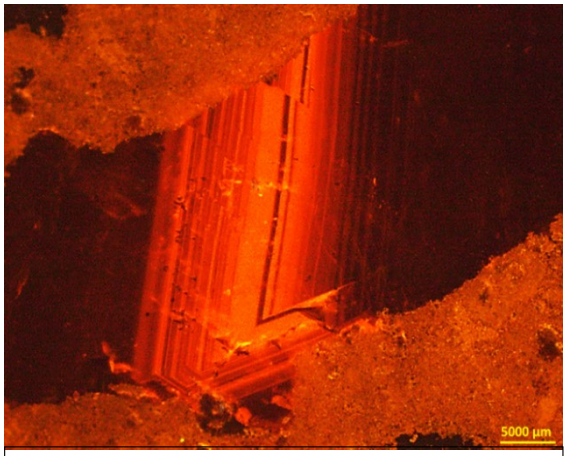

Fig. 2.42. CL image of Saddle dolomite cement zones of Fracture Set 1 in Reservoir F water.

Reservoir B water

Reservoirs B water has only two cement zones in the saddle dolomite in Fracture Set 1. They were cement zone 1 (bright red) and cement zone 2 (dark red) (Figures 2.43, 2.44).

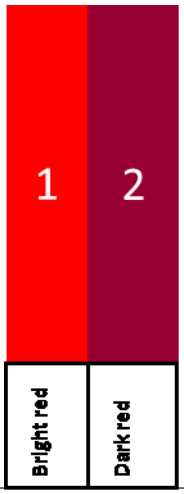

Fig. 2.43. Saddle dolomite cement zones of Fracture Set 1 in Reservoir B water.

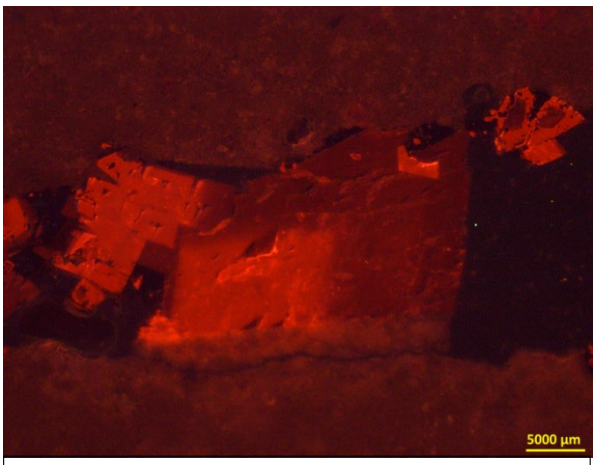

Fig. 2.44. CL image of Saddle dolomite cement zones of Fracture Set 1 in Reservoir B water.

2.4 Discussion

Figure 2.45 shows a summary of paragenesis for all reservoirs highlighting the main and minor fracture sets.

All of the Thamama reservoirs paragenetic sequences start with micritization and end with a dissolution event. The common events that appeared in all paragenetic sequences were micritization, moldic, intergranular and micro porosity creation, rhombic dolomite, equant calcite, blocky calcite, granular calcite, mechanical compaction, stylolites, dissolution seams, calcite twinning, bitumen, syntaxial overgrowth and dissolution. Some other paragenetic events appeared in most of reservoirs, such as drusy calcite cement, which appeared in all reservoirs except A. Vuggy porosity also appeared in all reservoirs except F and A. Framboidal pyrite appeared in all reservoirs except F, and saddle dolomite appeared in all reservoirs except A. Stylolites associated with fractures were missing in Reservoirs C and B while they appeared in all other reservoirs. Bitumen appeared in all of the Thamama reservoirs at the later stages of the paragenetic sequence.

Circumgranular calcite and hardgrounds were found in the Upper Thamama reservoirs (A, B and C) but were not found in the Lower Thamama reservoirs (F & G). Some paragenetic events were rare and appeared only in certain reservoirs, such as isopachous calcite cement which only appeared in Reservoir F, anhydrite cement which appeared in reservoirs F and B, coarse pyrite which appeared in reservoirs G and C, dogtooth calcite that appeared in reservoirs C and B, and kaolinite which appeared in reservoirs B and A.

Reservoir B showed the most paragenetic events, and this is the thickest reservoir of all of the Thamama reservoirs (~150 ft). In general, it is observed that the paragenetic events were lower in number in the Lower Thamama F and G and increased in number in Thamama C and B, but decreased again in Reservoir A.

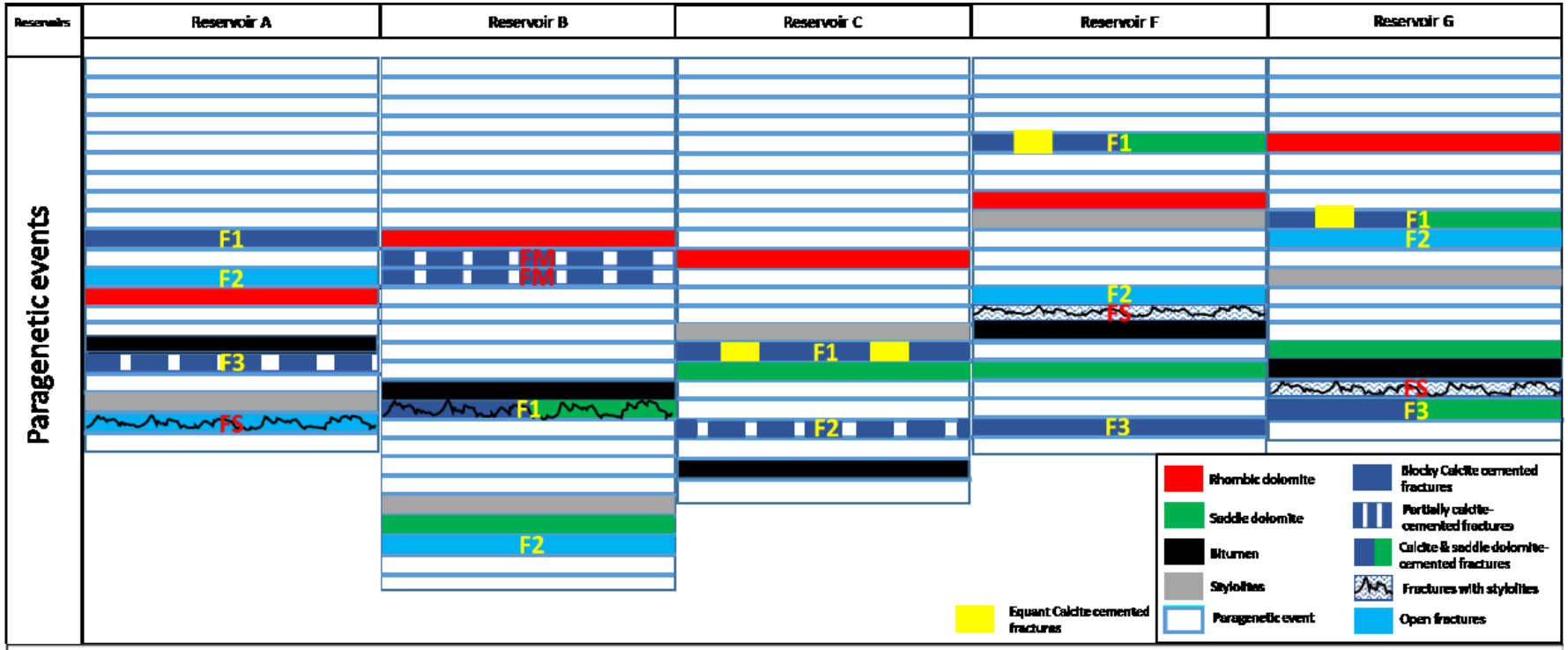

Fig. 2.45. The paragenetic sequence through the Thamama oil and water reservoirs. FS: fractures in stylolites, FM: minor fractures (other than the three main fracture sets in the Thamama reservoirs).

Rhombic dolomite appeared early before all fracture formation in all Thamama Reservoirs except in Reservoir A, where it took place after the second set of fractures, and in Reservoir F, where it is found after the first set of fractures. Reservoir B showed significant micro-dolomite rhombs along dissolution seams, which indicates their development in a burial setting postdating chemical compaction (Wilson, 2013). Saddle dolomite, however, was noted to appear late in the paragenetic sequence in all of the Thamama Reservoirs.

Based on the paragenetic sequences across the Thamama reservoirs, the diagenetic processes in the Thamama started early. Diagenesis continued after the oil entered the reservoirs, which occurred generally during the later stages when bitumen started to enter the system. Earlier diagenetic events included the cementation of equant, drusy, circumgranular calcite cements as well as rhombic dolomite, the latest events included blocky calcite and saddle dolomite cements as well as dissolution seams, stylolites and dissolution.

The timing of fracture formation is very variable, ranging between very early to very late in the paragenetic sequence. But in general it is observed that the fractures sets appeared during the middle and the late phase of the paragenetic sequence (shallow to deep marine), except for Reservoir F where Fracture Set 1 formed very early, inferred to be during marine phreatic conditions.

When studying the paragenetic sequence for the five Thamama Reservoirs, the first notable aspect is the similarities between the two reservoirs of the Lower Thamama (F & G). Fracture Set 3 only exists only in these two reservoirs, and formed late, during deep burial. Second, the filling cements in Fracture Set 1 is similar in both reservoirs, where it is filled with equant and blocky calcite as well as saddle dolomite. Finally, the third set of fractures in both reservoirs is a minor set of fracture and it is associated with stylolites, which might indicate that formation occurred at the same time in both reservoirs. Finally, both reservoirs have the same number of total diagenetic events.

Regarding the cement content of fractures, equant calcite was found in Fracture Set 1 in Reservoirs G, F and C only, while blocky calcite was the most common cement

type in all the cemented fracture sets. Saddle dolomite appeared in Fracture Set 1 in Reservoirs G, F and B and in Fracture set 3 of Reservoir G. The absence of saddle dolomite in Fracture Set 3 in Reservoir F might be due to the substantial number of diagenetic events between the forming of saddle dolomite and the forming of Fracture Set 3, where there are three paragenetic events separating them (calcite twinning, anhydrite and dissolution seams). By contrast, only one event separates saddle dolomite than Fracture Set 3 in Reservoir G, which is Bitumen.

The characteristics found in many cements (either calcite or dolomite and sometimes anhydrite) of the samples indicates a burial environment: the crystals cross-cut stylolites, crystals appear in fractures, crystals fill compacted pores, crystals have relatively large size, blocky and equant crystals, crystals showing well defined cathodoluminescence zonation ranging from bright to quenched repeatedly. Although some of the characteristics above are not unique to burial diagenesis, most of them combined can be interpreted as such.

Lower Thamama reservoirs (F & G) are more fractured than the Upper Thamama (A, B and C). This might indicate that the Lower Thamama rocks are lower in porosity due to extensive cementation, therefore are more prone to fracture and stylolite development (Nelson, 1982).

The extensive cementation that appears in the Lower Thamama can be logically explained by the presence of fractures which allowed the flow of alien formation fluids through the system (Machel, 2005). The cements in the fractures are mainly filled by blocky calcite and saddle dolomite. These cements often form at elevated temperatures, which suggests that the fluids precipitated them may have been hydrothermal or over-pressured. This is tested in Chapter 6 using SIMS oxygen isotopic analysis.

The fractures in the Thamama that formed during the tectonic activity of the Late Cretaceous are those which are of relatively large aperture (reaching few centimetres in the Lower Thamama). The other hairline fractures may have formed as a result of the pressure from in-situ hydrocarbon generation (Machel, 2005).

In some reservoirs, Fracture Set 2 appeared immediately after the first set of fractures (Reservoirs B and G), while in others (Reservoirs C and F) they formed after several further diagenetic events. Reservoir A had one paragenetic event between the two sets of fractures. Two hypotheses are likely to explain why Fracture Set 2 is open. First, diagenesis might have affected the open-seal system in the Thamama fractures. One of the diagenetic attributes that affects fractures, is sealing some fractures while leaving others open. The open set of fractures may also not be parallel to the current maximum horizontal stress (Laubach et al., 2010), which is the horizontal tensile tectonic stress in the lithosphere at the Red Sea (Schubert, 1987). Second, the active tectonic movement of the rifting of the Red Sea, which has been active since the Oligocene (Lyakhovsky et al., 1994), may affect Fracture Set 2.

The number of fracture cement zones vary in number in the Thamama reservoirs (Table 2.3). There are four observations for the number cement zones:

1- Fracture Set 1 has more calcite and dolomite cement zones than Fracture Set 3
2- Lower Thamama reservoirs (F & G) have more cement zones than Upper Thamama reservoirs (A, B & C)
3- Blocky calcite cement in fractures has more cement zones than equant calcite
4- Saddle dolomite has more cement zones than calcite cement

We can infer that the greater number of cement zones in Fracture Set 1 suggests a longer cementation history than Fracture Set 3. The second fact is logical since the Lower Thamama reservoirs have a greater volume of cement in the fractures than the Upper Thamama reservoirs. The third fact can be explained by recalling the crystal size in blocky calcite cement, which is bigger than the equant calcite cement, therefore more cement zones can develop. Applying the same logic of crystal size, saddle dolomite with big crystal sizes allows for more growth in cement zones. Saddle dolomite also showed luminescence colours ranging from orange to red, which is an evidence of formation by hydrothermal fluids (Boggs & Krinsley, 2006).

All cements in fractures were post kinematic.

Cement type	Reservoirs	Fracture Sets	
		Fracture Set 1	Fracture Set 3
Equant Calcite cement zones	Reservoir A oil	None	None
	Reservoir B	None	None
	Reservoir C oil	2	None
	Reservoir F oil	3	None
	Reservoir G oil	3	None
Blocky Calcite cement zones	Reservoir A oil	4	None
	Reservoir B	Oil 2 Water 3	None
	Reservoir C oil	1	None
	Reservoir F oil	6	3
	Reservoir G oil	5	5
Saddle dolomite cement zones	Reservoir A	None	None
	Reservoir B water	2	None
	Reservoir C	None	None
	Reservoir F water	6	None
	Reservoir G oil	13	7

Table 2.4: Calcite and dolomite cement in Fracture Sets 1 & 3 in the five Thamama reservoirs.

Figure 2.46 shows a schematic of the distribution of main fracture sets in the Thamama reservoirs. The possible reasons for not seeing Fracture Set 3 in the Upper Thamama are that the samples for Reservoirs G and F oil were taken from the same well that lies inside the main graben of Field A. Alternatively, the cause of Fracture Set 3 might be overburden pressure and not a tectonic movement as suggested in Chapter 1. This overburden pressure might have affected the lower reservoirs more than the upper reservoirs, due to their stratigraphic location.

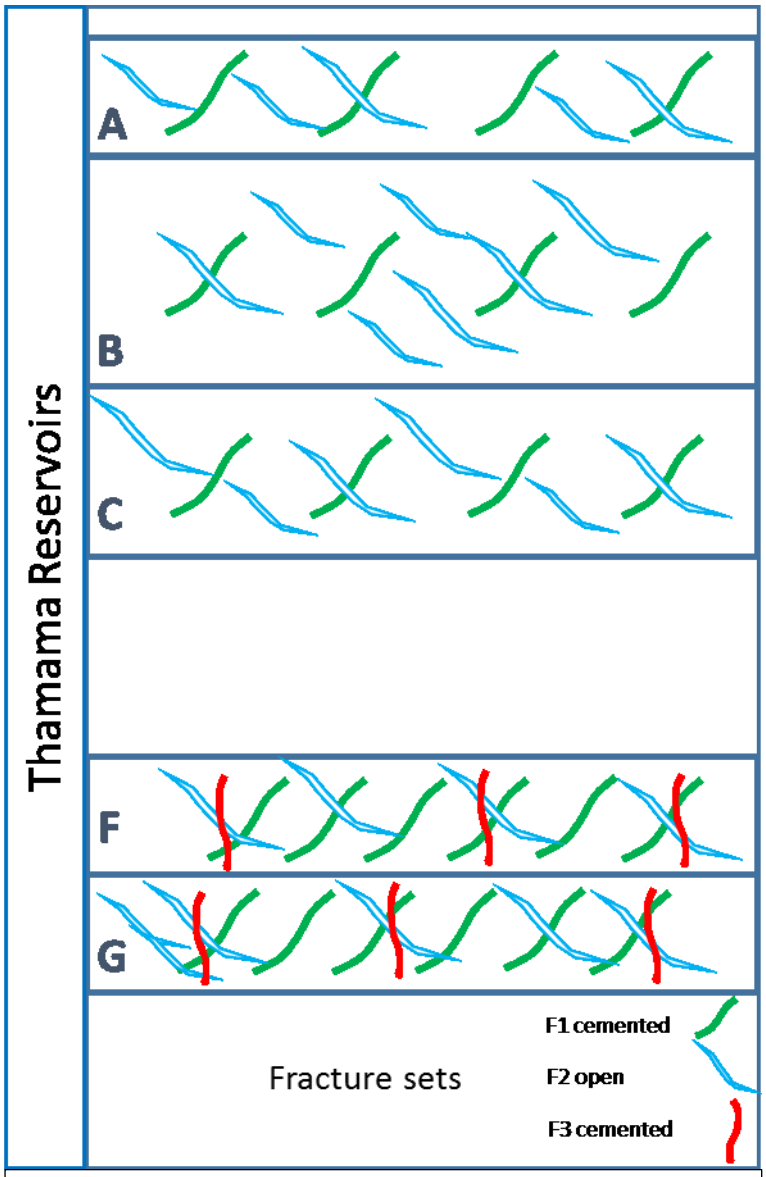

Fig. 2.46. Schematic of the distribution of the main three fracture sets in the Thamama reservoirs

2.5 Conclusions

- Lower Thamama reservoirs (F & G) are more fractured than the Upper Thamama (A, B and C).
- Lower Thamama reservoirs (F & G) show Fractures Sets 1, 2 and 3, but the Upper Thamama (A, B and C) only show Fractures Sets 1 and 2. The reason for Fracture Set 3 not to exist in the Upper Thamama is that it was possibly

formed by overburden pressure which has more influential effect in the Lower Thamama than the Upper Thamama.

- Field A fault associated fractures in the Thamama that formed during the tectonic activity of the Late Cretaceous (as assumed by ADNOC Onshore reports) are those which are of relatively large aperture (reaching few centimetres in the Lower Thamama). The other hairline fractures may have formed as a result of the pressure from in-situ hydrocarbon generation.
- Fracture Set 1 was opened by Late Cretaceous Ophiolite obduction and was cemented with equant calcite in the Lower Thamama.
- Fracture Set 2 was opened after Fracture Set 1, possibly by the Red Sea horizontal stress. It either was never cemented due to the ongoing horizontal movement, or the cement was dissolved. This assumption is made based on the openness of fractures, suggesting ongoing movement.
- Fracture Set 3 was opened in the Lower Thamama Reservoirs F and G due to tectonic movements, or due to pressure-temperature gradient. Another possibility that it formed due to overburden pressure, which is the most agreed on in this thesis.
- Each Fracture Set shows a short history of cementation, due to the late type of blocky calcite cement (Bourque and Raymond, 1994). Nonetheless, Fracture Set 1 has longer cementation history than Fracture Set 3, due to the additional presence of equant calcite cement and the greater number of cement zones.
- Cements in the Thamama subsurface were post-kinematic
- The extensive cementation that appears in the Lower Thamama shows that fractures were conduits that allowed the flow of alien formation fluids through the system. The cements in the fractures are mainly filled by blocky calcite and saddle dolomite. Equant calcite was found in Fracture Set 1 in Reservoirs G, F and C only. Saddle dolomite appeared in Fracture Set 1 in Reservoirs G, F and B and in Fracture set 3 of Reservoir G.
- The timing of fracture formation is very variable, ranging between very early to very late in the paragenetic sequence. But in general it is observed that the fractures sets appeared during the middle and the late phase of the paragenetic sequence (shallow to deep marine), except for Reservoir F where

Fracture Set 1 formed very early, inferred to be during marine phreatic conditions. Fracture Set 3 only exists only in these two reservoirs, and formed late, during deep burial and is associated with stylolites.

- The characteristics found in many cements (either calcite or dolomite and sometimes anhydrite) of the samples indicates in total a burial environment: the crystals cross-cut stylolites, crystals appear in fractures, crystals fill compacted pores, crystals have relatively large size, blocky and equant crystals, crystals showing well defined cathodoluminescence zonation ranging from bright to quenched repeatedly.

CHAPTER 3

Evolution of fluid chemistry through the Thamama Group fracture calcite cements via elemental analysis

3.1 Introduction

Studying the major and minor elements in fracture cements enables an understanding of the origin of fluids from which cements were precipitated, and how these have evolved through time. Trace elements can provide useful information regarding the characteristics of the fluids and diagenetic environments responsible for the cementation and dolomitization events (Moore, 2001). Diagenetic studies have integrated petrographic with geochemical data (such as Fe, Mn, Mg, Sr abundance) in order to correlate calcite cementation and dolomitization events, and to constrain the sources and migration paths of precipitating fluids (e.g. Kaufman et al., 1986; Lueftinger et al., 2003; Flynn et al., 2006; Geske et al., 2012).

There are several mechanisms that increase Fe concentration, including a reduction in water depth, an increase of terrigenous input, and reducing (anoxic) conditions (Hoseinabadi et al., 2016). Generally high Fe and Mn concentrations in subsurface brines indicate that they are reducing (Budd, 1989). In most oxidizing settings, organic material is sparse, and manganese is not incorporated into the diagenetic carbonate.

Four mechanisms incorporate trace elements into minerals; (1) impurities (fluid or mineral inclusions), (2) occlusions in lattice defects, (3) sorption onto growing crystal surfaces, and (4) solid solution substitution for a major element that is an essential structural constituent (lattice component) of the mineral (Banner,1995).

The dominant pore-water chemistry during calcite cement precipitation may be reflected by the content of Mn and Fe. Differences in dissolved Mn^{2+} and Fe^{2+} are attributed primarily to changes in redox conditions, because in carbonate aquifers, the pH of the pore-water is generally restricted to a quite narrow range (6.5-8.5) due

to carbonate buffering (Barnby and Rimstid, 1988). The Mn and Fe compositions of diagenetic calcites chiefly reflect the Eh conditions dominant during the various stages of calcite cementation, due to the limitation of Ca^{2+} content in pore water by carbonate buffering (Fig. 3.1). Manganese also has the greatest potential for substitution in anoxic subsurface environments (Land 1985). An increase of Mn content in diagenetic calcite is indicative of an open system and the effect of reducing waters (Barnby and Rimstid, 1989).

Conservative estimates for the concentrations of initial sediments for the Thamama Group are 20-300 ppm Mn and 200-1500 ppm Fe (Moshier, 1988; Huck et al., 2017). Additional Fe and Mn may have been oxidized and flushed from the system (Budd, 1988).

Manganese (Mn^{2+}) and iron (Fe^{2+}) are not only important in redox identification, but they are also the most important trace elements responsible for cathodoluminescence (CL) in carbonates, where Mn is known to activate luminescence while Fe quenches it (Searl, 1987; Yamin et al., 1996). While Mn^{2+} and Fe^{2+} are the elements that exert a major control over CL, it is hard to control the exact concentrations of Mn and Fe needed to activate or quench CL, respectively (Barnby and Rimstid, 1988). To activate luminescence, more than a few tens to 100 ppm Mn is required.

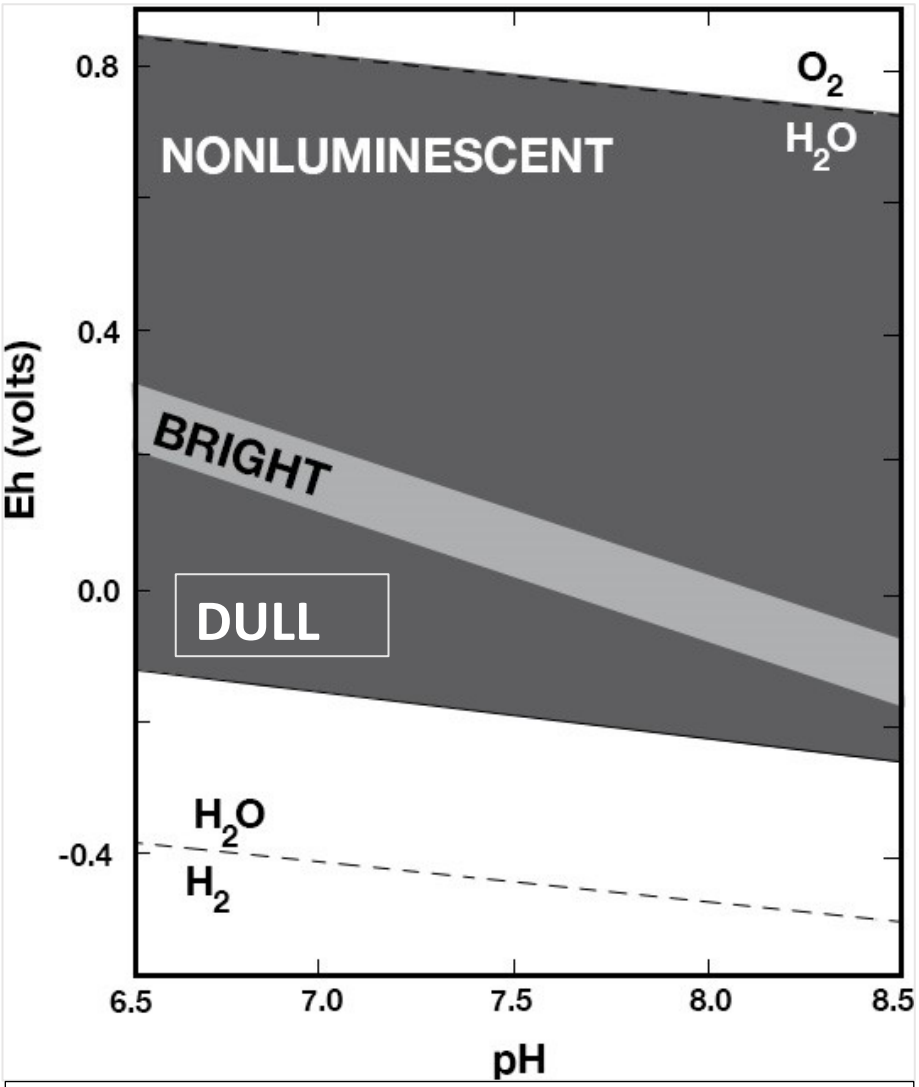

Fig. 3.1. Eh-pH diagram for environmental conditions of precipitation of non-bright- and dull-luminescent calcite cements (modified after Barnaby and Rimstidt, 1989).

The degree of diagenesis is best demonstrated by covariance of Sr^{2+} and Mn^{2+} where Sr is one of the most common trace elements associated with carbonates and it is most abundant in aragonitic sediments. Sr primarily substitutes in calcium lattice sites. (Yamin et al., 1996). Sr abundances can help delineate the pathway of fluid migration through the carbonate, when used in conjunction with other geochemical measurements (Yamin et al., 1996). Sr concentrations in diagenetic carbonates range from 20 ppm to greater than 10,000 ppm (Banner, 1995). Sr contents become lowered during diagenesis (because of the <1 value of the distribution coefficients) (Tucker and Wright, 1990). Variations of Sr concentration in carbonate systems

might also be a function of precipitation rate, mineral stoichiometry, crystal growth mechanism, fluid composition and temperature.

When determining distribution coefficient values for trace elements and Sr/Ca ratios of most modern sedimentary pore waters, uncertainties will be present. This is due to the lower Sr concentrations (20-70 ppm) in the ancient limestones' calcite and dolomite compares to the Sr concentrations of modern pore water (Banner, 1995). In ancient marine limestones, low Sr contents are common in diagenetically altered components, such as recrystallized allochems, micrite and pore-filling cements. Low Sr occurs because carbonate loses strontium during diagenesis, especially when aragonite transforms to calcite, and during dissolution (Hoseinabadi et al., 2016). When considering the behaviour of Sr in carbonates, evaluation of Sr-rich impurities such as gypsum, anhydrite, celestite, strontianite and saline fluid inclusions must be considered (Banner, 1995). Sr/Ca ratios are significantly higher in most saline fluids in burial environments than in seawater.

Mg and Ca are important elements when studying diagenesis, especially if combined with other elements like Sr. Non-CL-cements are interpreted to have precipitated as low-Mg calcite from marine pore fluids (Moshier, 1989). Mg/Ca in carbonate minerals in an abiotic setting is usually assumed to be principally controlled by the Mg/Ca solution and a temperature dependant partition coefficient (Saunders et al., 2014). This temperature dependence suggests that both marine and freshwater carbonate deposits may be important archives of palaeotemperature data.

A change in the seawater $^{m}Mg:^{m}Ca$ ratio may also be driven by variation in the production rate of oceanic ridges, and is a further control on the variation in carbonate-mineral precipitation (Morse et al., 1997). Hardie (1996) has also suggested that changes in the Mg/Ca ratio of seawater and changes in atmospheric pCO_2 are suggested as the most likely causes of the "calcite sea"-"aragonite sea" oscillations.

Analysis of the trace elements in fracture cements can therefore reveal the origin of the fluids that precipitated them, and therefore identify the environments in which they were precipitated, as well as the temperature and oxidizing/reducing conditions. This allows for comparison between both different fracture generations in the same

units, and also how this system has evolved through time in successive reservoirs. Finally, elemental analysis will allow a comparison between Fracture Sets in the water versus oil zones. Studying both oil and water legs is important because it is assumed that displacement of water by oil considerably inhibits the precipitation of diagenetic cement in a reservoir, while cementation continues in the aquifer below (Heasley et al., 2000). In this chapter, concentrations of the elements Ca, Mg, Mn, Sr, Fe are measured in multiple fracture cements to understand fluid evolution in the Thamama Group.

3.2 Objectives

To measure the concentration of Ca, Mg, Mn, Sr, Fe in fracture cements in order to infer the influence of trace elements on the type of cement precipitated in the fractures, and to better understand the nature and origin of fluids that precipitated them.

In particular, we aim to:

1- Infer changes in precipitation temperature from $^{m}Mg/^{m}Ca$
2- Infer whether fluids were oxidizing or reducing from Mn and Fe concentrations, or from closed versus open systems using Sr/Ca.

This will enable comparison between:

3- Fracture cements in the oil reservoirs and water reservoirs
4- Different fracture generations (Fracture Set 1 and Fracture Set 3)
5- Different reservoir zones of the Thamama Group (A, B, C, F, and G Reservoirs)
6- The two cement types found in the fractures (Blocky and Equant calcite cement)

3.3 Methods and Sampling

Sample preparation and Methodology

Doubly polished thin sections were carbon coated then analysed in a Cameca SX100 instrument. The electron probe microanalyser can make fully quantitative analyses of the elements (Mg, Ca, Sr, O, Mn and Fe). The technique uses an incident electron beam to generate X-rays with energies and wavelengths specific to the elements present in the sample. Instrument calibration is carried out by analysing reference materials (calcite) with known compositions. Routine detection limits are in the order of 0.009 to 0.05 wt %. $^{m}Mg/^{m}Ca$ was converted to molar ratio, and Sr/Ca data are presented as a ratio.

Different cement zones were found via cathodoluminesence (CL). First, the cement of interest is selected e.g. blocky calcite cement (Fig. 3.2). Second, the cement zones from the CL were assigned. Finally, the normal polarized thin section was superimposed on the CL image as well as the EMPA image to confirm the exact cement zones points (Fig. 3.3).

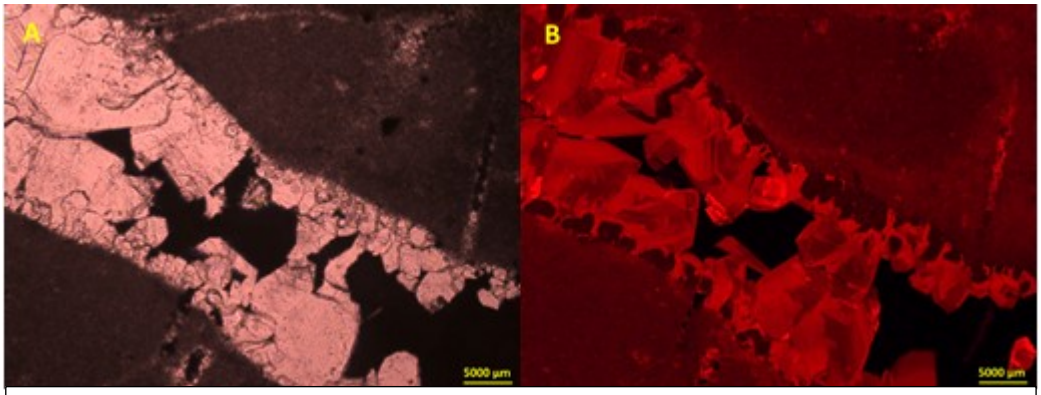

Fig. 3.2. Fracture filled with blocky calcite cement in Reservoir G oil cement. A: Thin section in normal polarized light CL thin section. B: Same thin section in CL

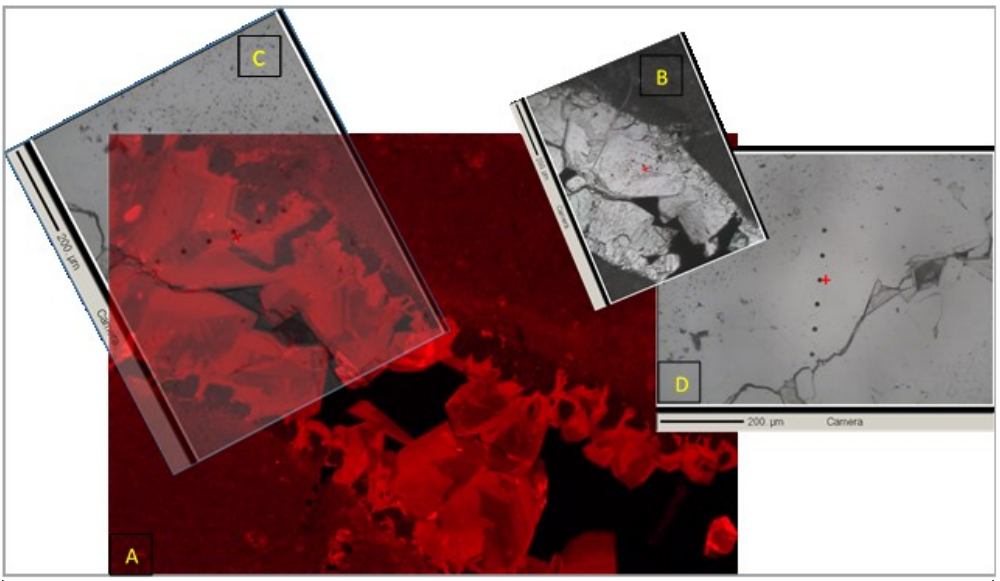

Fig. 3.3. A: CL image from a blocky calcite cement in Reservoir G oil. B: EPMA transmitted image of the same fracture in the CL. C: the same image in (B) transparent and enlarged to fit the CL image. D: the same thin section in (B) in reflected light.

Sampling

The distribution and number of samples analysed is summarized in Table. 3.1. Reservoir zones were sampled for Fracture Set 1 only in A, B and C, because Fracture Set 3 was either too small or absent. Fracture Set 3 only appeared in Reservoirs F & G oil. Fracture Set 3 was not recorded in the water zone. Fracture Set 2 is open with no cementation in all oil and water reservoirs.

The dominant type of calcite cements in fractures is blocky calcite. Equant calcite is present in smaller volumes in Reservoirs G, F and C. Equant calcite cement was found in 3 Reservoirs in Fracture Set 1, G, F and C. Sr in equant calcite was not sampled for cement zone 1 in Reservoir G. Equant calcite is not present in Fracture Set 3. Fracture Set 3 only contained blocky calcite cement. In Reservoir G, Mn in equant calcite cement was sampled in cement zones 2, 3and 4. Cement zone 2 is not present in blocky calcite cement in Fracture Set 3 in Reservoir G.

In sum, in the Lower Thamama (Reservoirs F & G) the cement zones with the greatest volume are CL cement zones 1 and 3. In Fracture Set 1, blocky calcite

appeared in all the zones while the equant was found only in Reservoirs G, F and C. The only reservoir that could be sampled in a water zone is Reservoir B, due to an absence of cemented fractures or the cement were too small to be analysed. In Reservoir C, most fractures were open due to dissolution. The fractures of Reservoir F water contained only dolomite, so these data will be discussed in Chapter 4. In some other reservoirs, the samples taken were only from oil leg of the reservoir. All detection limits are shown in Table. 3.2.

All data are given in Appendix 1

Fracture sets	Elements	Cement type	Oil Zones																				Water Zones		
			A				B		C			F						G					B		
			Cement zones																						
	Mg/Ca	Blocky calcite cement	n=120				n=35		nB=4, nE=10			nB=49, nE7=, nF3=23						nB=177, nE=11, nF3=86					n=11		
			1	2	3	4	1	2	1	2	3	1	2	3	4	5	6	1	2	3	4	5	1	2	3
Fracture set 1			5	5	11	6	10	6			4	10	7	3	8	4	1	49	13	75	22	6	6	4	1
	Sr/Ca		5	5	11	6	3	1			4	7	8	3	8	4	1	50	13	74	9	7	6	4	1
	Mn		5	5	11	6	3	2			4	6	9	3	8	4	1	49	13	68	15	7	4	2	1
	Fe		4	5	8	8	2	1			2	8	7	3	10	4	1	47	8	34	8	4	5	2	1
	Mg/Ca	Equant calcite cement							5	1		3	2	2					1	5					
	Sr/Ca								5	1		3	2	2					1	5	5				
	Mn								5	1		3		4					1	5	5				
	Fe								3	1		3		4				5	1	5	1				
Fracture set 3	Mg/Ca	Blocky calcite cement										17		4	3			72	4	11	3	1			
	Sr/Ca											17		4	3			46	1	5	3	1			
	Mn											17		4	2			14		1	3				
	Fe											17		4	2			14		1	3				

Table 3.1. Number of samples measured from blocky and equant calcite cement in Fracture Sets 1 and 3 in Thamama Reservoirs A, B, C, F and G oil zones, and Reservoir B water zone.

Fracture Sets	Zones	Cement type	Elemental detection limits (ppm)				
			Mg	Ca	Sr	Mn	Fe
Fracture Set 1	A oil	Blocky calcite cement D.L	54±5	1188±5	119±5	102±4	131±5
	B oil		58±3	1195±5	125±5	104±5	132±5
	C oil		52±1	1188±5	116±3	103±2	131±1
	F oil		67±3	1185±5	153±4	106±3	136±5
	G oil		67±3	1188±5	149±5	103±5	133±5
	B water		57±5	1095±5	117±4	104±5	132±5
	C oil	Equant calcite cement D.L	60±2	1182±5	130±4	103±5	132±5
	F oil		69±1	1187±5	153±5	105±5	132±4
	G oil		68±2	1193±5	148±4	100±1	131±2
Fracture Set 3	F oil	Blocky calcite cement D.L	68±3	1203±5	153±5	104±5	133±5
	G oil		67±2	1187±5	153±3	104±3	134±5

Table 3.2. Min detection limits for Mg, Ca, Sr, Mn and Fe (ppm) for blocky and equant calcite cement in Fracture Sets 1 and 3, in Thamama reservoirs A, B, C, F and G oil zones and Reservoir B water zone.

A summary of paragenesis for all reservoirs highlighting calcite cement precipitation in the fractures is given in Figure 3.4.

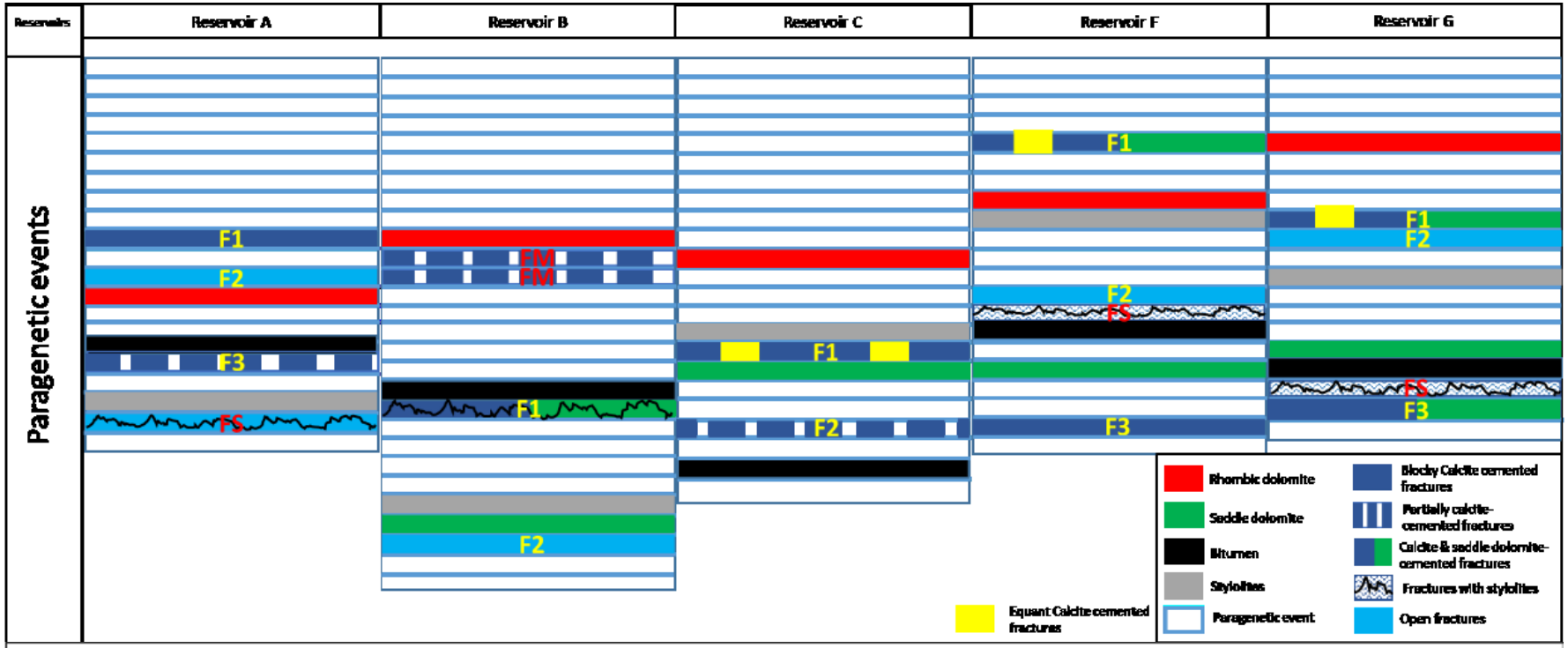

Fig. 3.4. Equant and blocky calcite cements in fractures appearance in the paragenetic sequence through the Thamama oil and water reservoirs. FS: fractures in stylolites, FM: minor fractures (other than the three main fracture sets in the Thamama reservoirs).

3.4 Results

In this section, plots summarising elemental data are given for each sampled CL zone for each cement type in each reservoir zone.

Results are given in stratigraphic order starting with the oldest (Reservoir G) and ending with the youngest (Reservoir A). Data are presented as molar Mg/Ca ($^{m}Mg/^{m}Ca$) and Sr/Ca, and as Fe and Mn concentrations. In each reservoir, Fracture Sets are presented separately. Data are given as box and whisker plots, where the box shows the mean and quartiles, with whiskers showing the full range of data.

Reservoir G

Fracture Set 1:

$^{m}Mg/^{m}Ca$ and Sr/Ca

Fig. 3.5A shows the distribution of $^{m}Mg/^{m}Ca$ values of Reservoir G oil for blocky calcite cement in Fracture Set 1. The mean ratio ranges from 0.6 to 0.9 for all the 5 CL cement zones. The highest mean value is at cement zone 4 (0.9) and lowest at cement zone 5 (0.6). Zones 1 and 3 are the most sampled cement zones.

The mean $^{m}Mg/^{m}Ca$ for equant calcite values range from 0.7 for cement zone 3, to 1 for cement zone 2 (Fig. 3.5B). The most sampled cement zone here is 3.

The Sr/Ca ratio of blocky calcite cement ranges from means of 0.009 to 0.014 for all the 5 cement zones. The highest value is at cement zone 2 (0.014) and lowest is at cement zone 4 (0.009). The most sampled zones are zone 1 and zone 3 (Fig. 3.5C). The graph in Fig. 3.5D shows the Sr/Ca for equant calcite in Fracture Set 1 of Reservoir G. Here the Sr/Ca values range from 0.009 for cement zone 2 to 0.016 for cement zone 3.

For equant calcite cement in Reservoir G, Sr/Ca started low in cement zone 2 and then rises slightly in cement zone 3, then lowers slightly in cement zone 4.

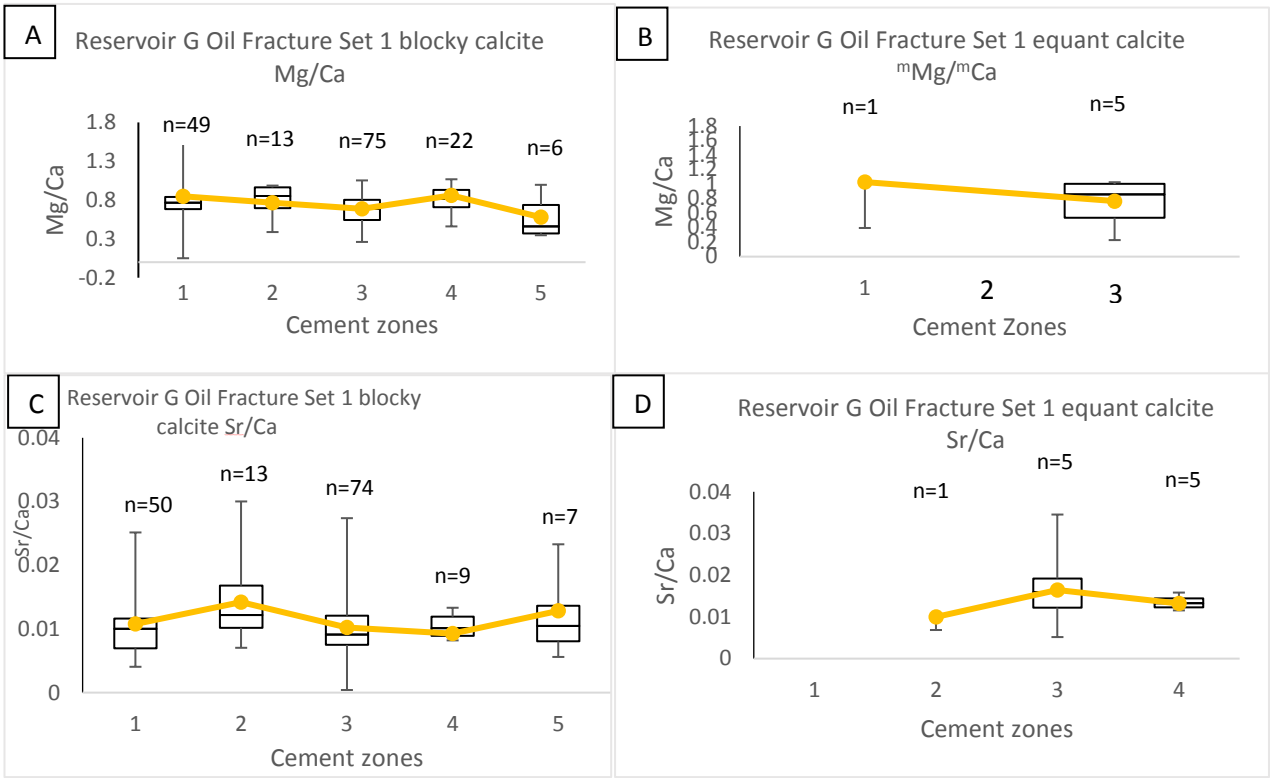

Fig. 3.5. Box and whisker plots for Mg, Ca, and Sr data (ppm) for each CL cement zone from Fracture Set 1 in Reservoir G. A: $^{m}Mg/^{m}Ca$ for Blocky calcite cement. B: $^{m}Mg/^{m}Ca$ for equant calcite. C: Sr/Ca for Blocky calcite cement 1. D: Sr/Ca for equant calcite. The yellow dots and line trace the mean. n = number of data points.

Mn and Fe

Fig. 3.5 shows the concentrations of Mn and Fe in both blocky and equant calcite cements. The mean Mn values range from 225 ppm in CL zone 1 to 167.5 ppm in CL zone 5 to for blocky calcite (Fig. 3.6A). The mean Fe values range from 2258 ppm in CL zone 1 to 132ppm in CL zone 5 (Fig. 3.6B). The mean Mn values range from 242 ppm in CL zone 1 to 200 ppm in CL zone 4 to (Fig. 3.6C). Mean Fe values range from 200 ppm in CL zone 1 to 2034 ppm in zone 2 (Fig. 3.6D).

In blocky cements, Mn values started to decrease from cement zone 1 to cement zone 3 in Zone G. Mn values started to increase again in cement zone 4, then drop to reach its lowest value at cement zone 5. Fe values show a very high value in cement zone 1, but reduce to a low value in cement zone 2 and even lower (almost at the detection

limit) in cement zone 3, then slightly increased in cement zone 4 followed by another drop in cement zone 5.

In equant cements, Mn values started decreasing from cement zone 2 to cement zone 4 very slightly. Fe was sampled in cement zones 1, 2, 3 and 4, where it started barely at the detection limit in cement zone 1 then increased dramatically in cement zone 2, and decreased again in cement zone 3 then reached its lowest value below the detection limit in cement zone 4.

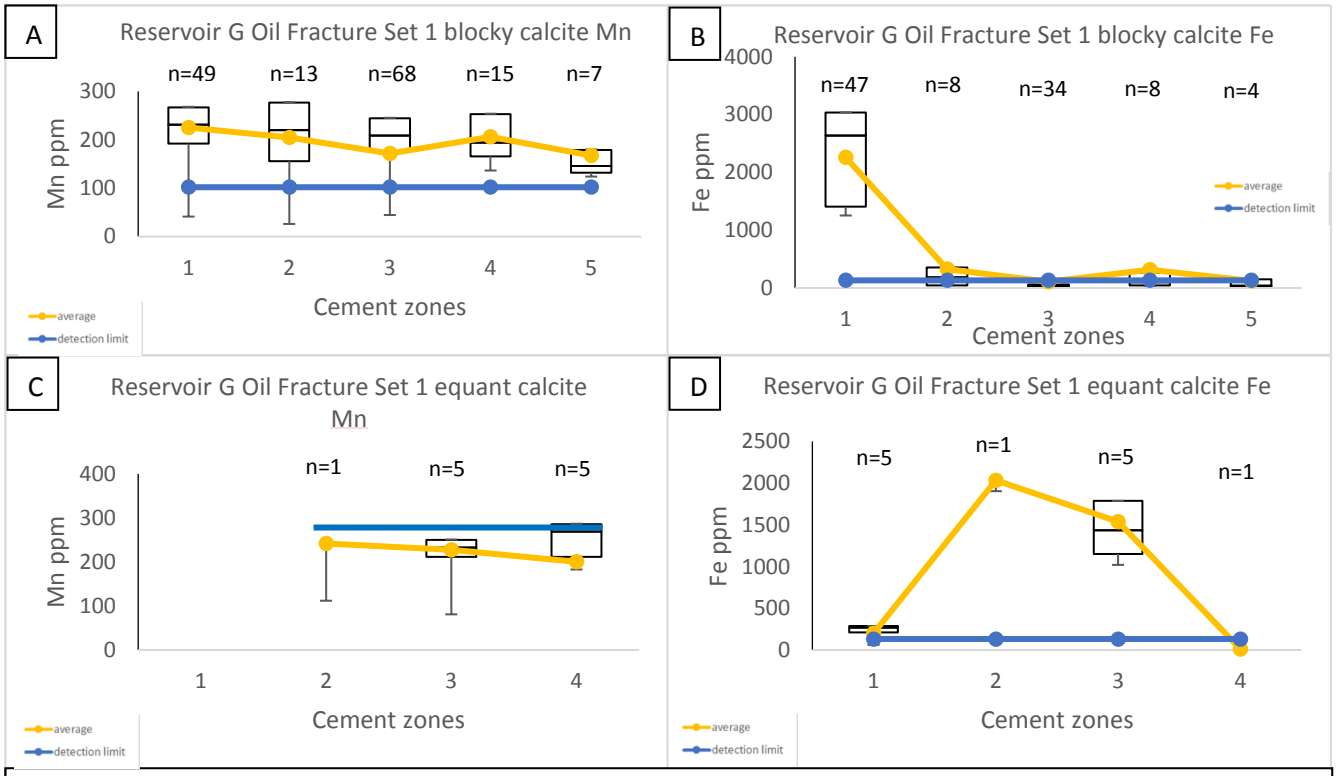

Fig. 3.6. Box and whisker plots for Mn and Fe concentrations (ppm) for each CL cement zone from Fracture Set 1 in Reservoir G. A: Mn in the blocky calcite cement. B: Fe in the blocky calcite cement. C: Mn in the equant calcite cement. Fe in the equant calcite cement. The yellow dots and line trace the mean. n = number of data points. The blue rectangles represent the zones with the most sample points taken. Blue Line shows the detection limit.

Fracture Set 3:

$^{m}Mg/^{m}Ca$, Sr/Ca, Mn and Fe

Fig. 3.7A illustrates the $^{m}Mg/^{m}Ca$ of blocky calcite cement of Fracture Set 3 in Zone G oil. The mean $^{m}Mg/^{m}Ca$ ratio ranges from 0.4 to 0.8 for all the 5 cement zones.

The highest value is at cement zone 2 (0.8) and lowest is at cement zone 5 (0.4). The most sampled zones are zone 1 and zone 3.

The Sr/Ca ratio is given in Fig. 3.7B. the mean ratio ranges from 0.008 to 0.018 for all the 5 cement zones. The highest value is at cement zone 5 (0.018) and lowest is at cement zone 4 (0.008). The most representative zone, where samples were taken from the most is zone 1.

The mean Mn values range from 144 ppm in zone 1 to 193 ppm in zone 3 (Fig. 3.7 C). The Fe values range from 296 ppm in zone 1 to 595.6 ppm in zone 3 (Fig. 3.7D). The most representative cement zone for Mn and Fe is Zone 1 and Zone 2 did not present for Mn and Fe.

For blocky calcite cement in Fracture Set 3 of Zone G, unlike in Fracture Set one, the $^{m}Mg/^{m}Ca$ values rise in cement zone 2 followed by gradual decrease in the following zones to reach the lowest value at cement zone 5.

Five cement zones contained Sr. The Sr/Ca values started to rise at cement zone 3 then falls at cement zone 4, after that it raised again to reach its highest value at cement zone 5.

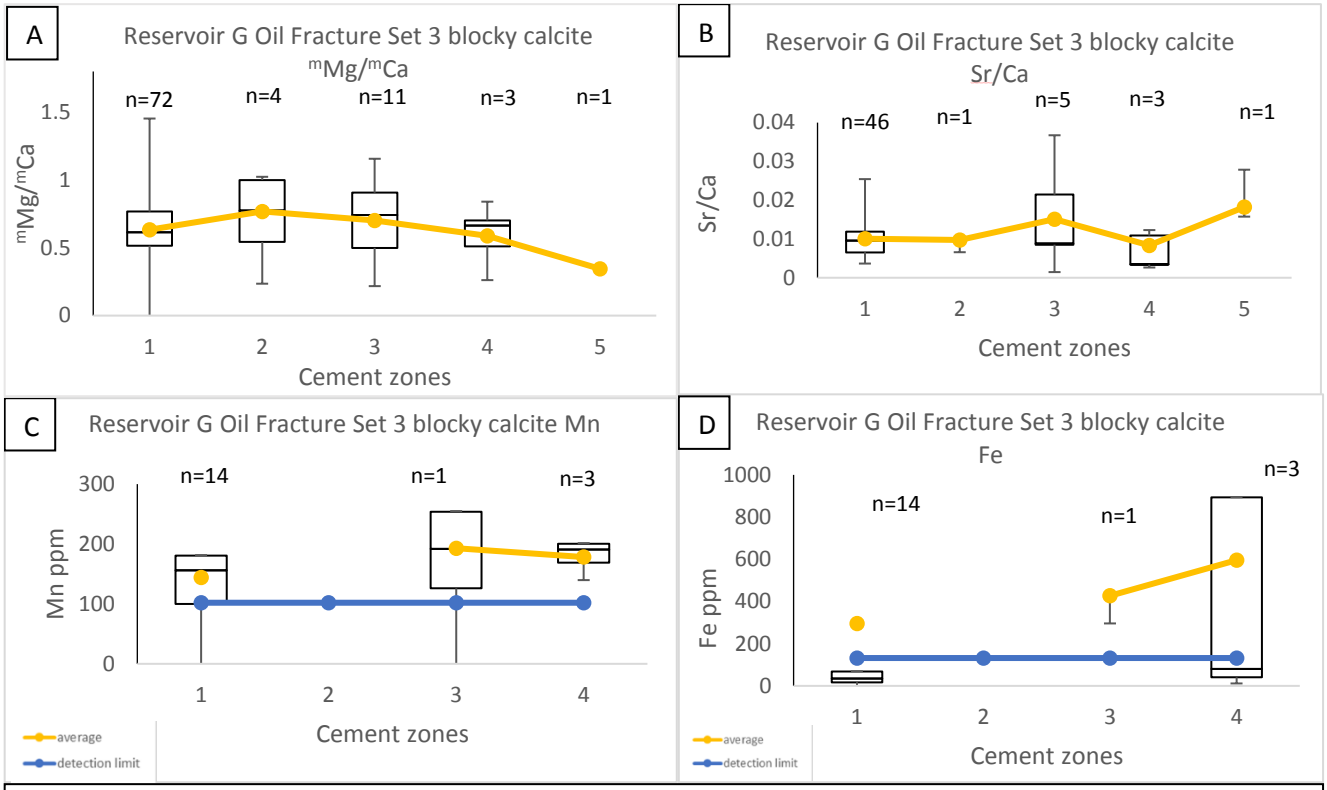

Fig. 3.7. Box and whisker plots for Mg, Ca, Sr, Mn and Fe data (ppm) for each CL cement zone from Fracture Set 3 in Reservoir G. A: $^{m}Mg/^{m}Ca$ for Blocky calcite cement. B: Sr/Ca of Zone G oil for Blocky calcite cement. C: concentrations of Mn (ppm) in the blocky calcite cement. D: concentrations of Fe (ppm) in the blocky calcite cement. n = number of data points. Yellow line shows the trend through the mean. Blue Line shows the detection limit.

Reservoir Zone F

Fracture Set 1

$^{m}Mg/^{m}Ca$ and Sr/Ca

Fig. 3.8A shows the fluctuations of $^{m}Mg/^{m}Ca$ values of Zone G oil for blocky calcite cement in Fracture Set 1. The mean ratio ranges from 0.7 to 1.3 for all the 6 cement zones. The highest mean value is at cement zone 3 (1.3) and lowest is at cement zone 6 (0.7). Zones 1 and 4 are the most sampled cement zones.

The mean $^{m}Mg/^{m}Ca$ for equant calcite values range from 0.7 for cement zone 3, to 1.3 for cement zone 2 (Fig. 3.8B). The most sampled cement zone here is 1.

The Sr/Ca ratio of blocky calcite cement ranges from means of 0.009 to 0.017 for all the 5 cement zones. The highest value is at cement zone 3 (1.3) and lowest is at cement zone 6 (0.7). The most sampled zones are zone 2 and zone 4 (Fig. 3.8C). The graph in Fig. 3.8D shows the Sr/Ca for equant calcite in Fracture Set 1 of Zone G. The values are all below the detection limits.

The Sr values rises in cement zone 2 then drops dramatically in cement zones 3 and 4 and started to rise again in cement zone 5. Sr values in cement zone 1 and cement zone 2 are similar.

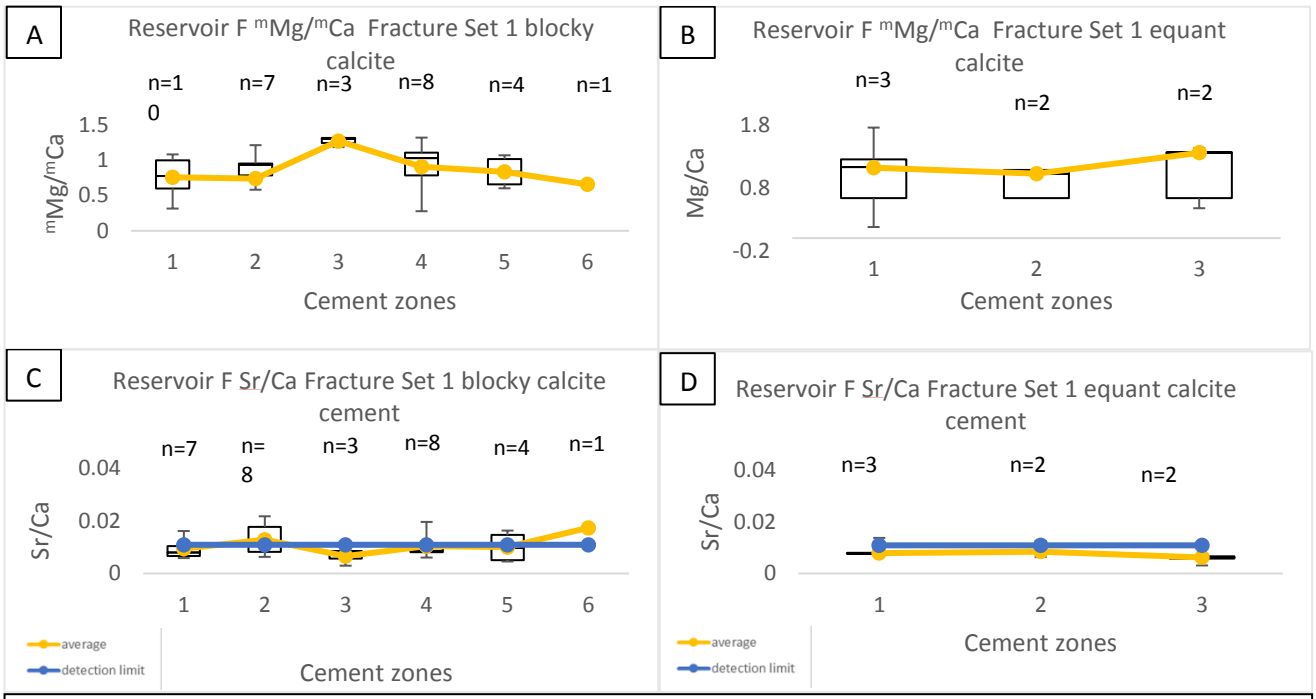

Fig. 3.8. Box and whisker plots for Mg, Ca, and Sr data (ppm) for each CL cement zone from Fracture Set 1 in Reservoir F. A: $^{m}Mg/^{m}Ca$ for Blocky calcite cement. B: $^{m}Mg/^{m}Ca$ for equant calcite. C: Sr/Ca for Blocky calcite cement 1. D: Sr/Ca for equant calcite. n = number of data points. Yellow line shows the trend through the mean. Blue Line shows the detection limit.

Mn and Fe

Fig. 3.9 shows the concentrations of Mn in the blocky calcite cement and equant calcite cements of Fracture Set 1 in zone F oil. The mean Mn values range from 169.6 ppm in CL zone 3 to 243.3 ppm in CL zone 1 Fig. 3.9A. Fig. 3.9B The Fe

values range from 1728 ppm in CL zone 2 to 9568.3 ppm in CL zone 3. The Mn in equant calcite cement is illustrated in Fig. 3.9C and shows two cement zones, CL zone 1 (205 ppm) and CL zone 3 (224.25 ppm). Mean Fe values range from 2941 ppm in CL zone 1 to 2497 ppm in CL zone 3 (Fig. 3.9D).

In the blocky calcite of Zone F, Mn values started high at cement zone 1, and decreased dramatically through cement zones 2 and 3 respectively. Mn rises in cement zone 4, then drops in cement zone 5, then increased again in cement zone 6.

Fe values for Zone F were high overall. Fe values decreased from cement zone 1 to cement zone 2, then rises to reach a very high value forming a spike at 9568 ppm at cement zone 3. The concentration drops again at cement zone 4, rises slightly at cement zone 5 then decreases at cement zone 6.

For equant calcite in Zone F, cement zone 2 is also not present. Mn started at a relatively high value, showed a lower value at cement zone 3 then increased very slightly in cement zone 4. The Fe started in a high value at cement zone 1 and a higher value in cement zone 3 then dropped to its lowest value at cement zone 4.

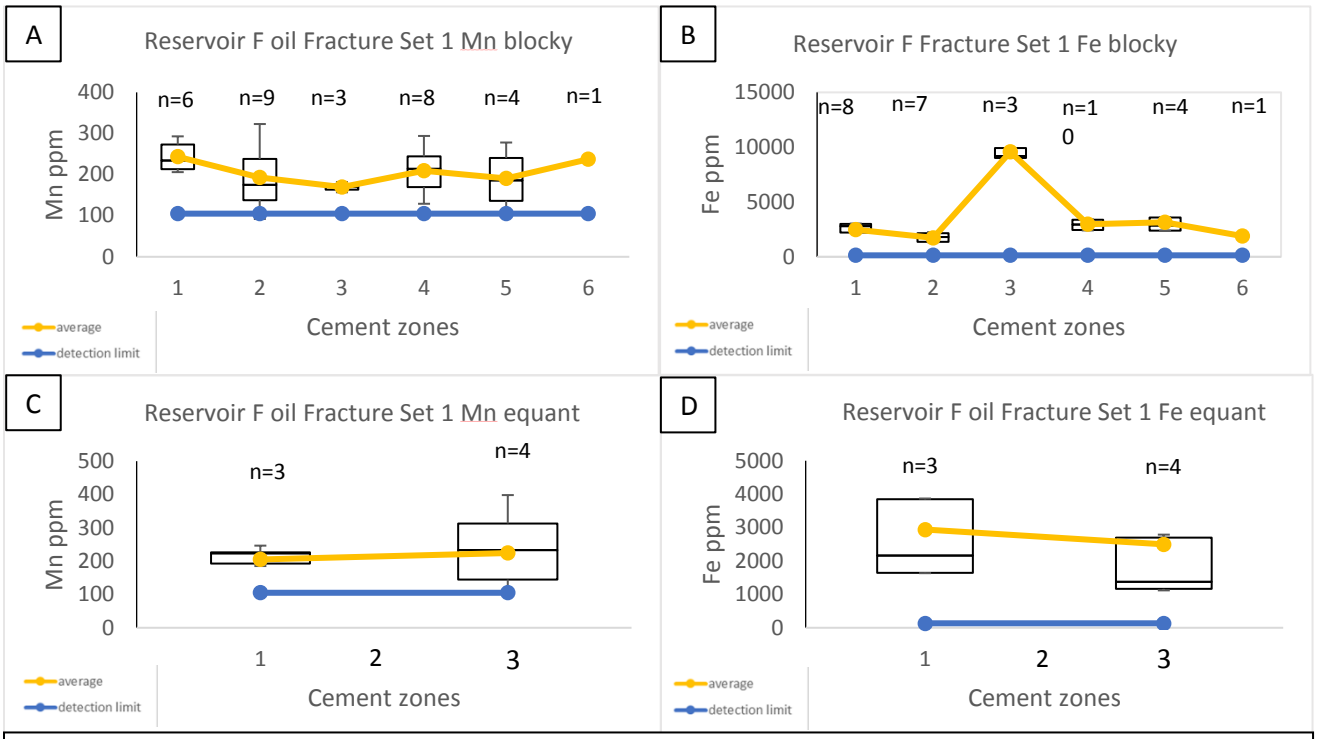

Fig. 3.9. Box and whisker plots for Mn and Fe concentrations (ppm) for each CL cement zone from Fracture Set 1 in Reservoir F. A: Mn in blocky calcite cement. B: Fe in blocky calcite cement. C: concentrations of Mn in equant calcite cement. D: Fe in equant calcite cement. n = number of data points. Yellow line shows the trend through the mean. The blue line is the detection limit.

Fracture Set 3:

$^{m}Mg/^{m}Ca$, Sr/Ca, Mn and Fe

Fig. 3.10A shows the $^{m}Mg/^{m}Ca$ of Zone F oil for Blocky calcite cement in Fracture Set 3. The mean $^{m}Mg/^{m}Ca$ ratio ranges from about 0.6 to 1.29 for all the 4 cement zones. The highest value is at cement zone 3 (1.29) and lowest is at cement zone 4 (0.6). Most samples were taken from zone 1.

The $^{m}Mg/^{m}Ca$ in cement zone 1 starts at a value close to its value in blocky calcite for Fracture Set 1. Cement zone 2 does not exist and the $^{m}Mg/^{m}Ca$ reaches a high value of 1.29 in cement zone 3, followed by a sharp drop in value (0.6) in cement zone 4. Cement zone 2 is not present.

Fig. 3.10B shows the Sr/Ca, where the ratio ranges from about 0.01404 to 0.01406 for the 4 cement zones. The highest value is at cement zone 1 (0.01406) and lowest is

at cement zone 4 (0.01404). Most samples were taken from zone 1. The Sr value in zone 3 is below detection limit and zone 2 is not present in the samples.

Fig. 3.10C represents the Mn concentration and it shows 3 cement zones: 1, 3 and 4. Cement zone 2 is not present in all Fracture Set 3. The lowest Mn value appears in cement zone 3 (232 ppm) and the highest Mn value is in cement zone 1 (254 ppm). Fig. 3.10D shows the Fe concentration, showing 3 cement zones; 1, 3 and 4. Cement zone 2 is not present in Fracture Set 3 samples. The lowest Fe value appears in cement zone 4 (1954 ppm) and the highest Fe value is in cement zone 3 (5149 ppm).

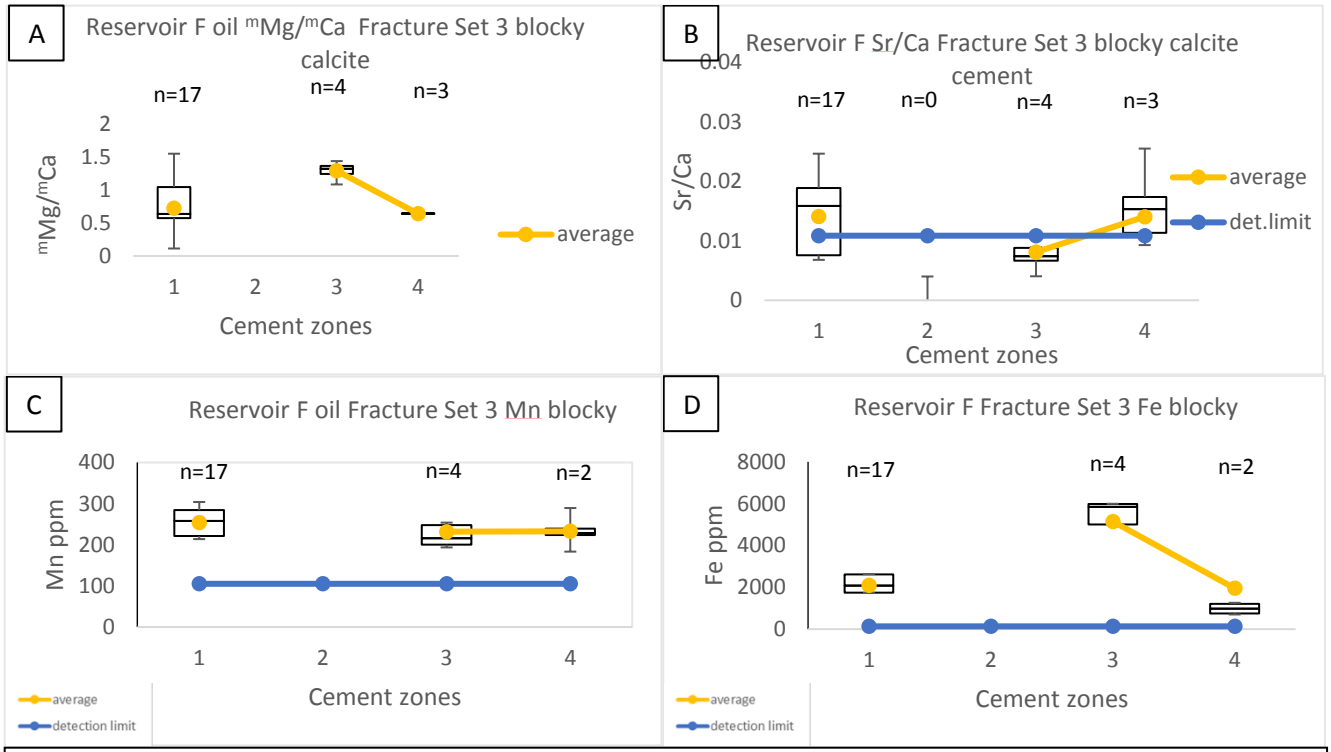

Fig. 3.10. Box and whisker plots for Mg, Ca, Sr, Mn and Fe data (ppm) for each CL cement zone from Fracture Set 3 in Reservoir F. A: $^{m}Mg/^{m}Ca$ for Blocky calcite cement. B: Sr/Ca of Zone G oil for Blocky calcite cement. C: concentrations of Mn (ppm) in the blocky calcite cement. D: concentrations of Fe (ppm) in the blocky calcite cement. n = number of data points. Box shows mean, median and quartiles, with whiskers showing full range. Yellow line shows trend through the mean. Blue line shows the detection limit.

Reservoir Zone C

Fracture Set 1:

$^{m}Mg/^{m}Ca$ and Sr/Ca

Fig. 3.11A shows $^{m}Mg/^{m}Ca$ values of Reservoir C oil for blocky calcite cement in Fracture Set 1. Only cement zone 3 was sampled because the volume of blocky calcite cement in Reservoir C fractures was very small compared to G and F of lower Thamama.

The mean $^{m}Mg/^{m}Ca$ for equant calcite values ranges from 0.48 for cement zone 1 to 0.42 for cement zone 2 (Fig. 3.11B). The only cement zone was sampled for Sr/Ca of blocky calcite cement is zone 3 (Fig. 3.11C). The graph in Fig. 3.11D shows the Sr/Ca for equant calcite in Fracture Set 1 of Reservoir C. Here the Sr/Ca values range from 0.006 for cement zone 2 to 0.012 for cement zone 1.

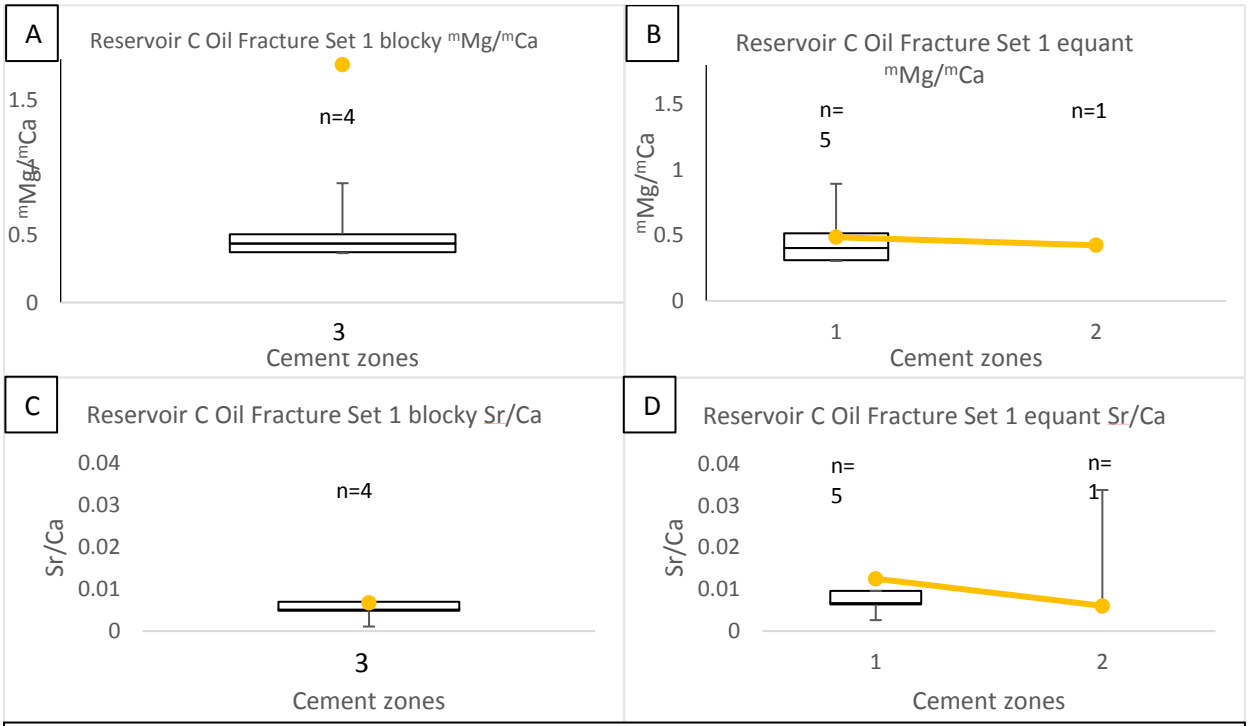

Fig. 3.11. Box and whisker plots for Mg, Ca, Sr data (ppm) for each CL cement zone from Fracture Set 1 in Reservoir C. A: $^{m}Mg/^{m}Ca$ for Blocky calcite cement. B: Mg/Ca for equant calcite. C: Sr/Ca of Zone C oil for Blocky calcite cement. D: Sr/Ca for equant calcite. n = number of data points. Yellow line shows the trend through the mean. N= number of data points.

Mn and Fe

Fig. 3.12 shows the concentrations of Mn and Fe in both blocky and equant calcite cements of Fracture Set 1 in Reservoir C oil. The only zone could be sampled is zone 3 due to the little amount of cement in the tiny fractures of Reservoir C in general (Fig. 3.12A). Fe concentration in blocky calcite found in cement zone 3 was below detection (Fig. 3.12B). The mean Mn values in equant calcite range from 103 ppm in CL zone 1 to 208 ppm in CL zone 2 to (Fig. 3.12C). Mean Fe values in equant calcite range from 270 ppm in CL zone 1 to 307 ppm in zone 2 (Fig. 3.12D).

The Sr/Ca in Fracture Set 1 was measured in both blocky and equant calcite cements. No clear trend was observed, as the only cement zone sampled was zone 3 as mentioned earlier. The average value for Sr/Ca in cement zone 3 is 0.006.

Both Mn and Fe were below detection limits in the only zone sampled which is cement zone 3.

Mn values in equant calcite cement started from a low value at cement zone 1 and increased to a higher value in cement zone 2. Fe values also increased from cement zone 1 to cement zone 2.

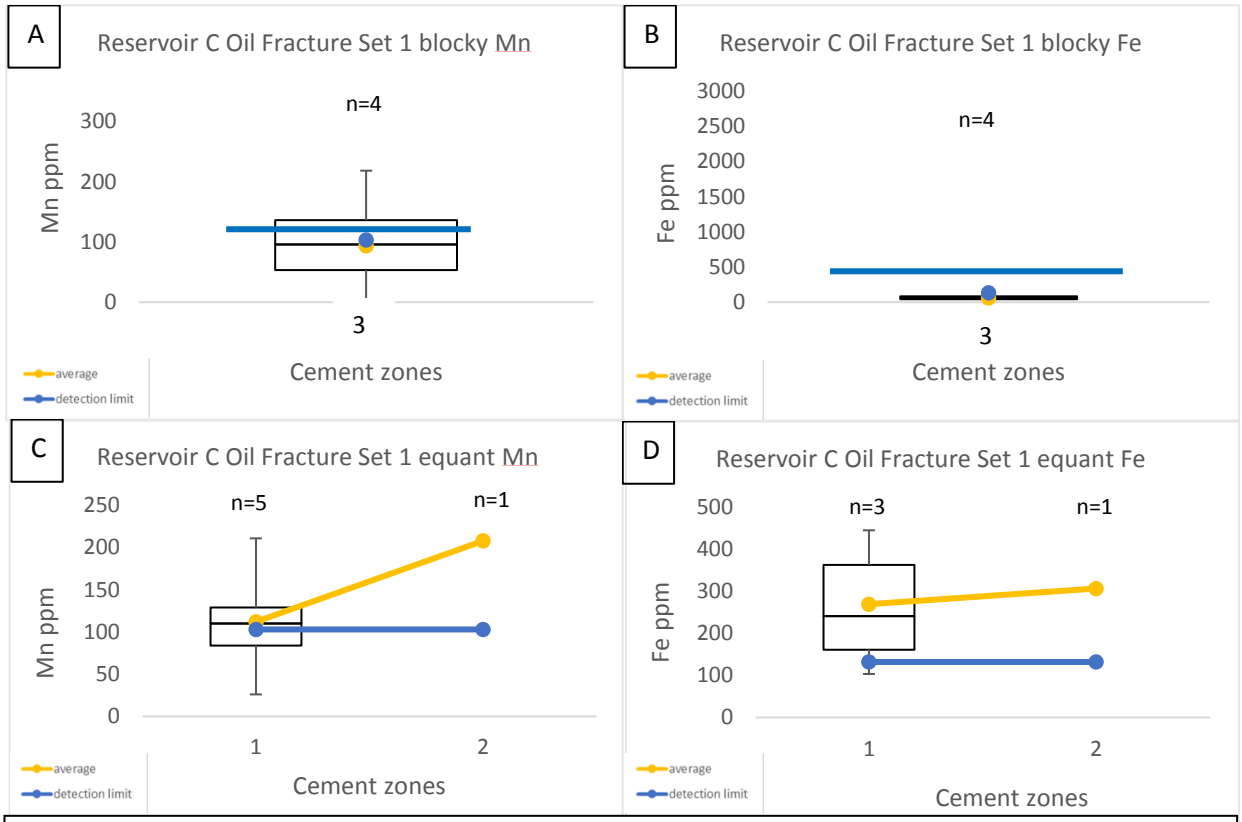

Fig.3.12 Box and whisker plots for Mn and Fe concentrations (ppm) for each CL cement zone from Fracture Set 1 in Reservoir C. A: concentrations of Mn in blocky calcite cement. B: concentrations of Fe in blocky calcite cement. C: concentrations of Mn in the equant calcite cement. D: concentrations of Fe in the equant calcite cement. n = number of data points. Box shows mean, and quartiles, with whiskers showing full range. Yellow line shows the trend through the mean. Blue Line shows the detection limit.

Reservoir Zone B oil

Fracture Set 1:

$^{m}Mg/^{m}Ca$, Sr/Ca, Mn and Fe

Fig. 3.13A shows $^{m}Mg/^{m}Ca$ for blocky calcite, where the cement zones sampled were 1 and 2. $^{m}Mg/^{m}Ca$ showed lower values in cement zone 2. The rest of cement zones were not recorded.

Fig. 3.13B shows Sr/Ca for blocky calcite where the cement zones sampled were 1 and 2. The value dropped from cement zone 1 to cement zone 2.

Mn values for blocky calcite of Fracture Set 1 in Reservoir B oil are shown in Fig. 3.13C. The cement zones sampled were 1 and 2. Mn value was almost at the detection limit in cement zone 1 (104 ppm) and increased slightly in cement zone 2 (120 ppm).

Fe values for blocky calcite of Fracture Set 1 in Reservoir B oil are shown in Fig. 3.13D. (D). The cement zones sampled were 1 and 2. All Fe values were below the detection limit.

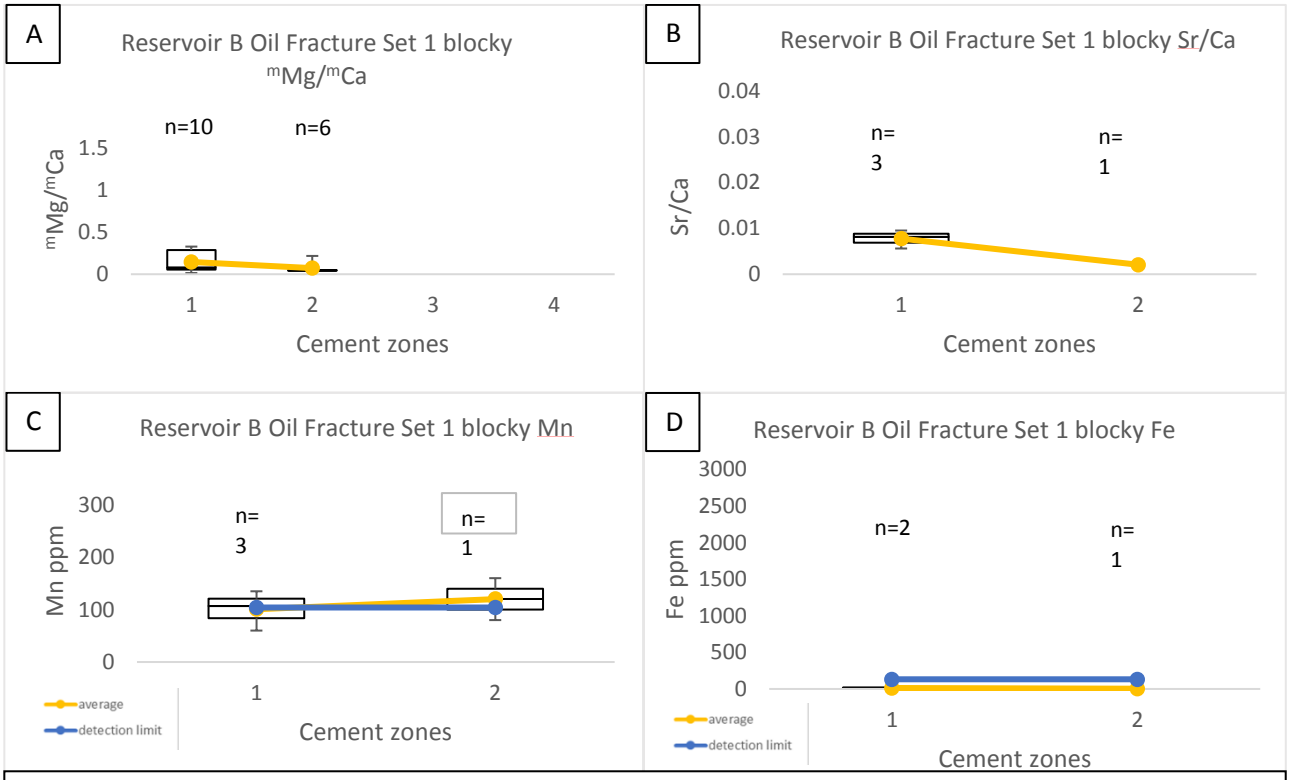

Fig. 3.13. Box and whisker plots for Mg, Ca, Sr, Mn and Fe concentrations (ppm) for each CL cement zone from Fracture Set 1 in Reservoir B oil. A: $^{m}Mg/^{m}Ca$ for Blocky calcite cement. B: Sr/Ca for Blocky calcite cement. C: concentrations of Mn in the blocky calcite cement. D: concentrations of Fe in the blocky calcite cement. n = number of data points. Yellow line shows the trend through the mean. Blue line shows detection limit.

Reservoir Zone B water

Fracture Set 1:

$^{m}Mg/^{m}Ca$, Sr/Ca, Mn and Fe

Fig. 3.14A shows the $^{m}Mg/^{m}Ca$ for blocky calcite, where the cement zones sampled were 1, 2 and 3. The Mg/Ca values for Reservoir B water decreased very little in cement zone 2 but decreased further in cement zone 3.

Fig. 3.14B shows Sr/Ca for blocky calcite, where the cement zones sampled were 1, 2 and 3. The Sr/Ca values were A low as they were in Reservoir B oil. The values increased slightly and gradually from cement zone 1 to cement zone 3. Mn and Fe recorded in zone B was all below the detection limit.

Both Mn and Fe values were below the detection limit (Figs. 3.14C and D).

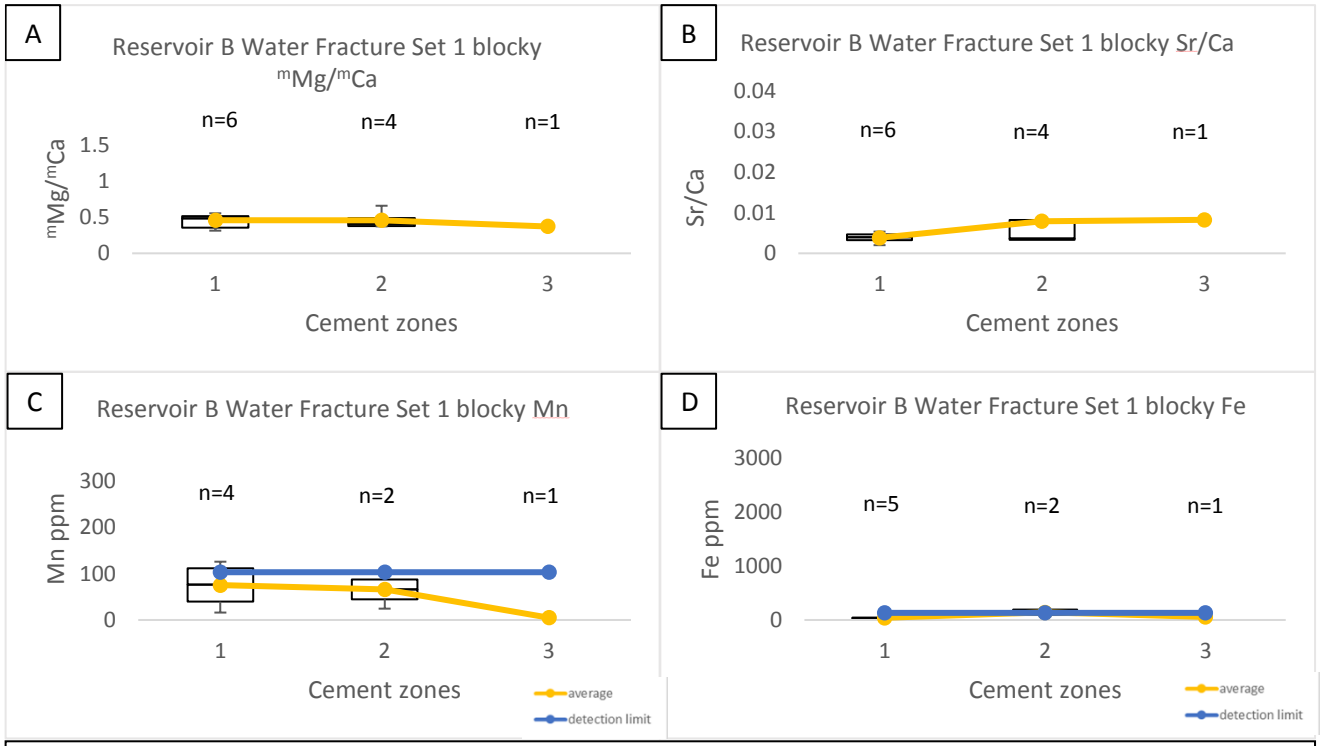

Fig. 3.14. Box and whisker plots for Mn and Fe concentrations (ppm) for each CL cement zone from Fracture Set 1 in Reservoir B water. A: $^{m}Mg/^{m}Ca$ for Blocky calcite cement. B: Sr/Ca for Blocky calcite cement. C: concentrations of Mn (ppm) in the blocky calcite cement. D: concentrations of Fe in the blocky calcite cement. n = number of data points. Box shows mean, and quartiles, with whiskers showing full range. Yellow line shows the trend through the mean. Blue line shows detection limit.

Reservoir Zone A oil

Fracture Set 1:

$^{m}Mg/^{m}Ca$ and Sr/Ca

For Reservoir A, $^{m}Mg/^{m}Ca$ values are around 0.5 in zones 1-3, then rise to 1 in cement zone 4 (Fig. 3.15A).

Four cement zones were sampled for Sr/Ca (Fig. 3.15B). There is a decrease from cement zone 1 to cement zone 2, followed by a rise in cement zone 3 then another drop in cement zone 4.

The lowest Mn value is 125 ppm in cement zone 3 and highest Mn value is 225 in cement zone 4 (Fig. 3.15C). The Mn values in Reservoir A rises slightly from cement zone 1 to cement zone 2, then dropped in cement zone 3 to increase again in cement zone 4. Fe values were all below detection limit except for cement zone 1, which was 497 ppm (Fig. 3.15D).

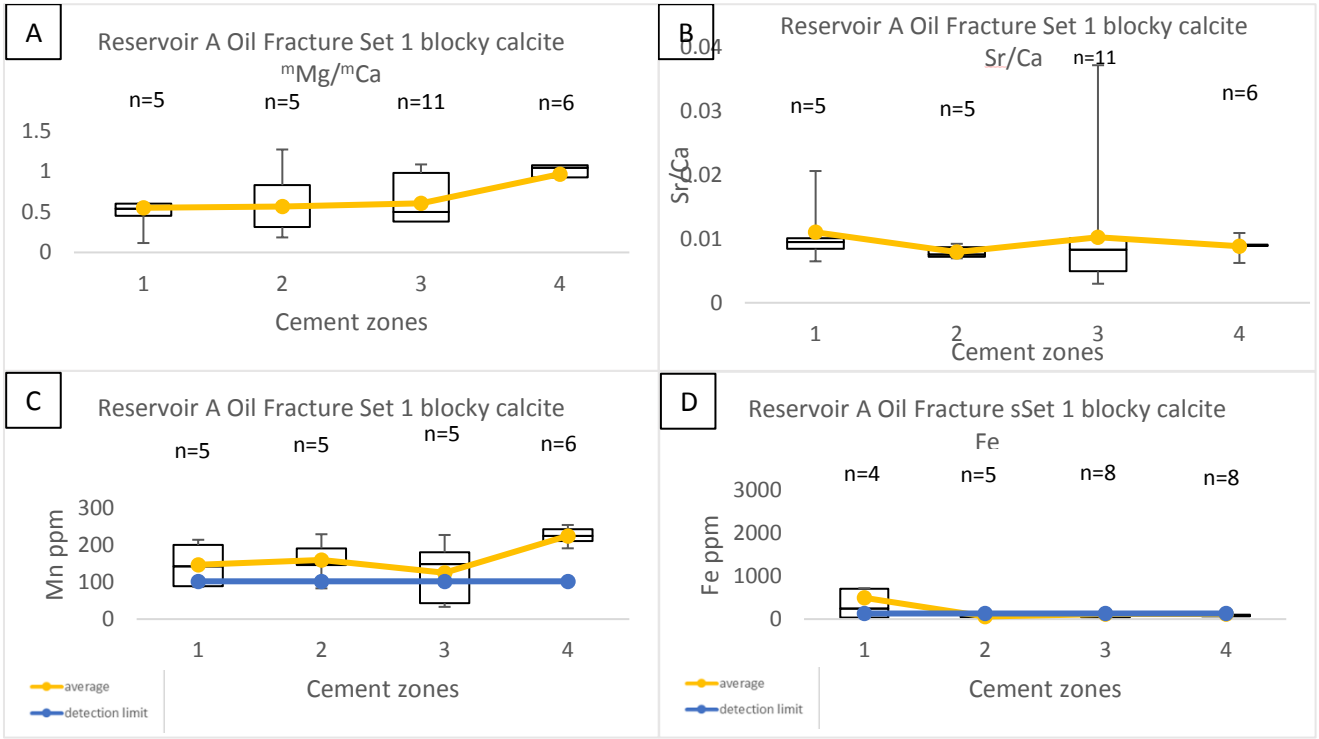

Fig. 3.15. Box and whisker plots for Mg, Ca, Sr, Mn and Fe concentrations (ppm) for each CL cement zone from Fracture Set 1 in Reservoir A oil. A: $^{m}Mg/^{m}Ca$ for Blocky calcite cement. B: Sr/Ca of for Blocky calcite cement. C: concentrations of Mn in blocky calcite cement. D: concentrations of Fe in blocky calcite cement. n = number of data points. Box shows mean, and quartiles, with whiskers showing full range. Yellow line shows the trend through the mean. Blue line shows detection limit.

3.5 Discussion

$^{m}Mg/^{m}Ca$

Potential changes in temperature can be traced from the summarised $^{m}Mg/^{m}Ca$ data (Fig. 3.16). The figure shows the changes in values through the different cement zones in all the reservoirs and the highlightred areas shows the whole range of data.

In general the Upper Thamama Reservoirs (A, B, and C) show lower overall $^{m}Mg/^{m}Ca$ than the Lower Thamama Reservoirs (F,G). We infer that the $^{m}Mg/^{m}Ca$ of pore water decreases with increasing temperature (Burton and Walter, 1991). The Upper Thamama fracture calcite cements were therefore precipitated at higher overall temperatures than the Lower Thamama examples.

In Fracture Set 1, the values of $^{m}Mg/^{m}Ca$ in equant calcite of Reservoir G oil suggests that the same high temperature was dominating in both cement zones 1 and 3. In Reservoir F oil, high equant calcite $^{m}Mg/^{m}Ca$ at the fracture walls suggests lower temperature during the precipitation of cement zones 1 and 3, with a temperature rise during precipitation of cement zone 2 (Fig. 3.6B). In Reservoir C oil, $^{m}Mg/^{m}Ca$ in equant calcite shows lower values than the blocky calcite, which suggests a higher temperature of precipitation in both cement zones 1 and 2.

Blocky cement mainly forms in burial diagenetic environments (Heidari et al., 2013). We infer from the blocky calcite $^{m}Mg/^{m}Ca$ values of Reservoir G oil that fluid temperature rose at cement zone 5. In Reservoir F oil, the $^{m}Mg/^{m}Ca$ values infer a rise in the temperature in cement zones 1, 4 and 6. No temperature trends are clear in Reservoir C oil but the average of $^{m}Mg/^{m}Ca$ in cement zone 3 indicates a lower overall temperature. $^{m}Mg/^{m}Ca$ suggests that the overall temperature in blocky calcite cement of Reservoir B oil was high. For Reservoir A oil, the slight decrease in temperature from cement zone 2 to cement zone 3, followed by sharp decrease towards cement zone 4 indicates that the crystals started to grow from relatively higher temperature towards lower temperature.

In Fracture Set 3, the $^{m}Mg/^{m}Ca$ values in Reservoir G oil indicates a potential temperature drop in cement zone 2 followed by gradual rise in temperature in the rest of cement zones, ending by cement zone 5 (Burton and Walter, 1991). In Reservoir F oil however, observing the $^{m}Mg/^{m}Ca$ suggests that the temperature increased from cement zone 3 to cement zone 4. Cement zone 1 was formed in a higher temperature like cement zone 4.

When observing $^{m}Mg/^{m}Ca$ of Reservoir B water, there is an indication of a gradual and slight increase in the temperature through the three cement zones, 1, 2 and 3.

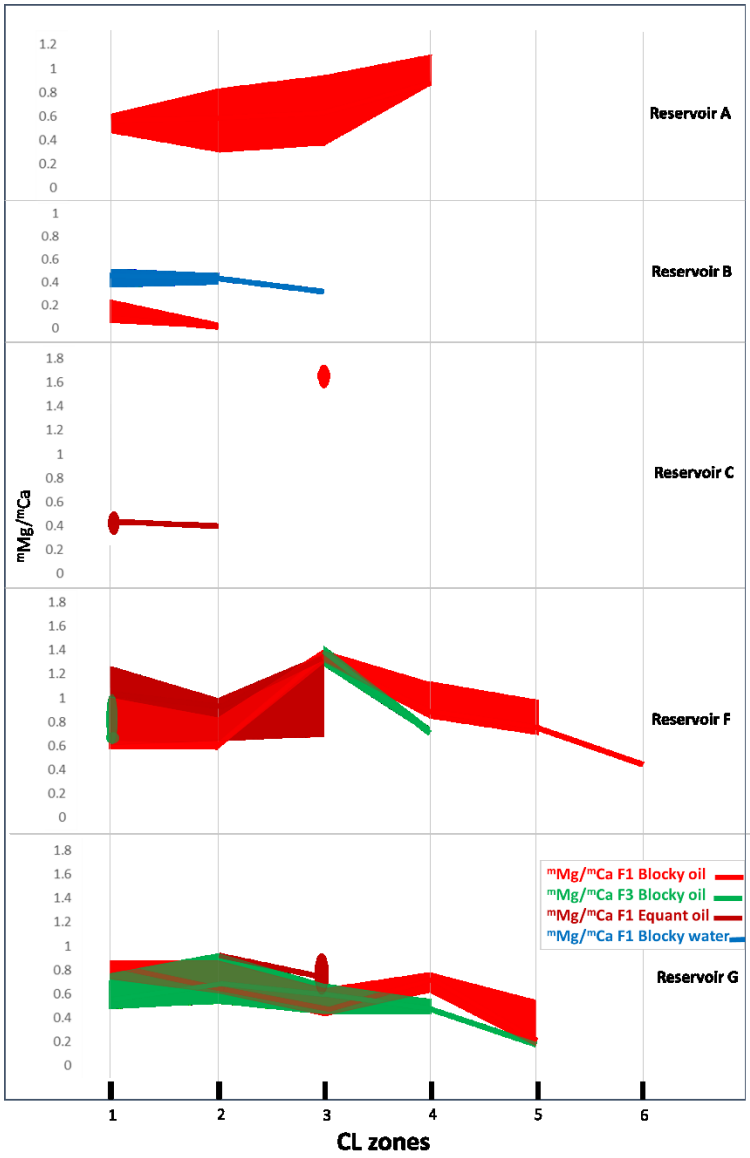

Fig. 3.16. Summary of $^{m}Mg/^{m}Ca$ for both equant and blocky calcite cement zones in Fracture Sets 1 and 3 of the Thamama oil and water reservoirs.

Sr/Ca

Summarised changes in Sr/Ca data are given in Fig. 3.17. In total, the Sr/Ca values are insignificant.

Upper Thamama Reservoirs (A, B, and C) have in general far lower Sr/Ca, and Lower Thamama Reservoirs (F,G) show similar Sr/Ca data ratios. Fracture Set 3 cements show similar values to Fracture Set 1 cements.

Fracture Set 1 in Reservoir G oil, burial environment was suggested in equant calcite in cement zones 2, 3 and 4. In Reservoir F oil, the relatively high Sr/Ca in equant calcite goes along with the blocky calcite in Fracture Set 1 of Zone F which therefore indicates a burial environment. Likewise, the Sr/Ca in Reservoir C oil cements is also indicative of a burial environment.

The Sr reduction may indicate burial diagenesis. The low values of both Sr and Mg in cement zone 3 of Reservoir G may suggest a flushing event (fresh water) (Budd, 1988). The slightly increased Sr/Ca in cement zones 2, 4, 5 and 6 of Reservoir F oil, indicates burial environments (Moore, 1989).

The Sr values of blocky calcites of Reservoir G oil, are high in both cement zones 5 and 3 in Fracture Set 1 and Fracture Set 3. This may be an indication of a deep burial environment (Hoseinabadi et al, 2016). A burial environment was expected in Fracture Set 3 blocky calcite according to the Sr values in Reservoir F.

The same burial environment suggested in Reservoir B oil is suggested in Reservoir B water when observing Sr/Ca values.

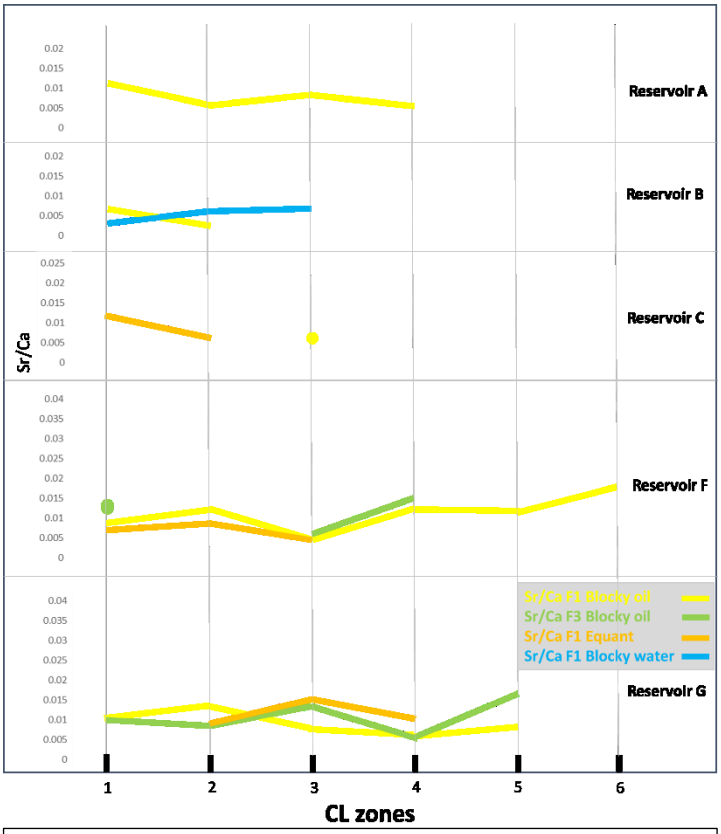

Fig. 3.17. Summary of mean Sr/Ca for both equant and blocky calcite cement CL zones in Fracture Sets 1 and 3 of the Thamama oil and water reservoirs.

Mn and Fe

Summarised data of Fe and Mn concentrations are given in Fig. 3.18.

Upper Thamama Reservoirs (A, B, and C) have far lower Fe and Mn concentrations and Lower Thamama reservoirs (F,G). Fracture Set 3 cements show similar values to Fracture Set 1 cements. This suggests an overall environment of oxic conditions Upper Thamama Reservoirs (A, B, and C) and reducing conditions in the Lower Thamama reservoirs (F,G).

In Fracture Set 1, high values of both Mn and Fe in equant calcite suggest a reducing environment in Reservoirs G, F and C oil (Budd, 2014). Also, the relatively high Mn values in Reservoir G blocky calcite, as well as the high values of both Mn and Fe in blocky calcite in Reservoir F oil, indicate anoxic environments. Reservoir F uniquely has high concentrations of both Mn and Fe, which indicates that the calcite might be

precipitated from anoxic subsurface brines (Budd, 1988). A spike of Fe noticed at cement zone 3, which might point to a fluid passage through an open fracture nearby (Fracture Set 2 (open)) that appeared to cross cut Fracture Set 1 in some samples, which suggests that fluids passed through could have caused such spike in the Fe trend.

The high Fe values in Fracture Set 3 of Reservoir G oil blocky calcite, agrees with the reducing environment observed in Fracture Set 1 blocky calcite. However, reducing environment is still unchanged in Reservoir F oil, due the high Mn and Fe values. The high values for Fe and Mn might be sourced from an exotic high saline fluids rich in these element.

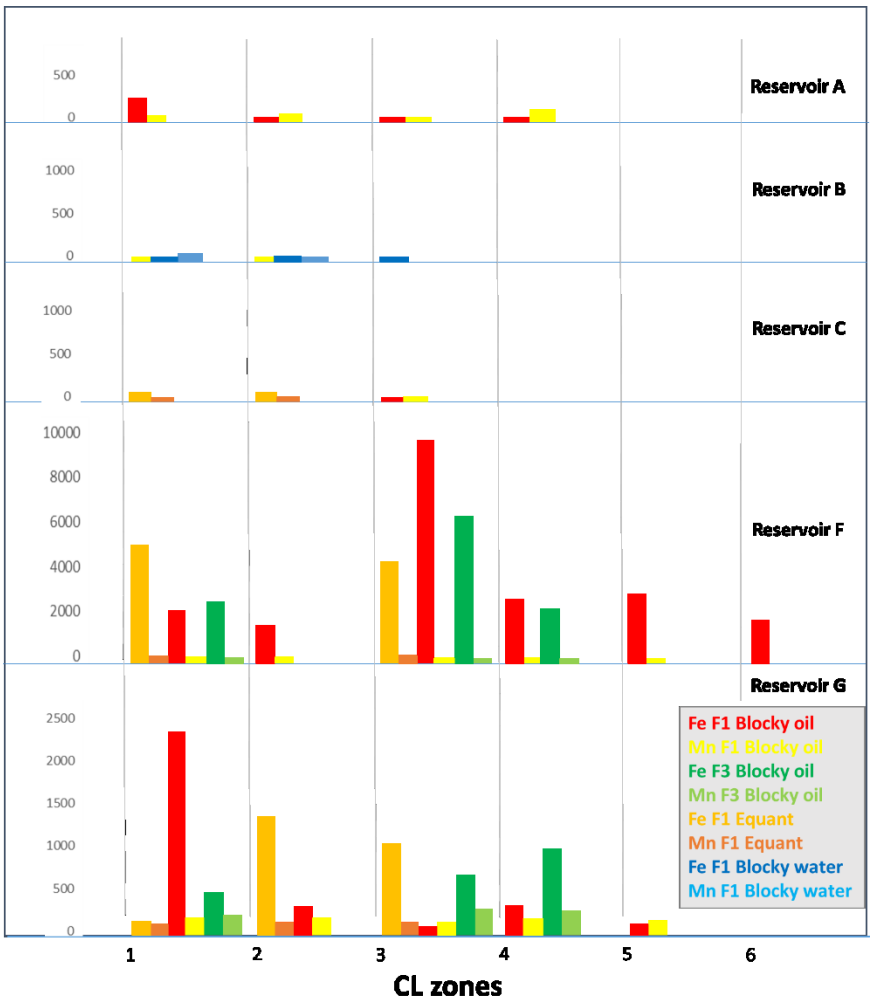

Fig. 3.18. Summary of Fe and Mn ppm concentration for both equant and blocky calcite cement zones in Fracture Sets 1 and 3 of the Thamama oil and water reservoirs.

3.6 Conclusions

- In general the Upper Thamama Reservoirs (A,B, and C) show lower $^{m}Mg/^{m}Ca$ than the Lower Thamama reservoirs (F,G). The Upper Thamama fracture calcite cements were therefore precipitated at higher overall temperatures than the Lower Thamama examples.

- The change in temperature in equant calcite cement zones is different from the blocky calcite zones. Equant calcite shows higher temperature in all of the reservoirs except Reservoir F oil, where the overall temperature is low (except in cement zone 2) and increases gradually through the cement zones. However, blocky calcite cement shows an overall high temperature in all the Reservoirs, and the temperature increases gradually through the cement zones in the Lower Thamama Reservoirs F and G oil.

- The change in temperature also differs between Fracture Set 1 and Fracture Set 3. Fracture Set 3 in Reservoir G oil shows higher overall temperatures than Fracture Set 1 in Reservoir G and Reservoir F oil. Both fracture sets show gradual increase in temperature through the cement zones.

- Lower Thamama reservoirs (F and G) have variations in temperature between the different cement zones. The temperature drops in cement zone 5 in Reservoir G oil and in cement zone 3 in Reservoir F oil. While the Upper Thamama reservoirs (A, B and C) have a consistent overall temperature through the reservoir. That might be due to fewer cement zones in the Upper Thamama reservoirs, which is in turn may be due to the smaller fractures and cement infilling them.

- Most of the Thamama fracture cement in both oil and water reservoirs was precipitated in the burial environments. The low amount of Sr confirms that no exotic fluid has entered the diagenetic system.

- Upper Thamama Reservoirs (A, B, and C) have far lower Fe and Mn concentrations and Lower Thamama reservoirs (F,G). Fracture Set 3 cements show similar values to Fracture Set 1 cements. This suggests an overall environment of oxic conditions in Upper Thamama Reservoirs (A, B, and C) and reducing conditions in the Lower Thamama reservoirs (F,G).

CHAPTER 4

Evolution of fluid chemistry in fractures of the Thamama Group via elemental analysis of dolomite cements

4.1 Introduction

Dolomite is a common diagenetic mineral in ancient carbonate rocks, which forms through a dissolution-reprecipitation reaction where a calcium carbonate originator is replaced by dolomite. The reaction takes place via the interaction with magnesium-rich fluids, in the form of three reactions (Armenteros, 2010; Kaczmarek & Sibley, 2011):

1) $Ca^{2+} + Mg^{2+} + 4HCO^{-3} = CaMg(CO_3)_2 + 2H_2CO_3$
2) $CaCO_3 + Mg^{2+} + 2HCO^{-3} = CaMg(CO_3)_2 + H_2CO_3$
3) $2CaCO_3 + Mg^{2+} = CaMg(CO_3)_2 + Ca^{2+}$

Dolomite rock is common in the upper part of Earth's crust, but modern dolomite formation in marine and lacustrine environments is rare and so the quantity of recent dolomite is very limited (Haas et al., 2014; Reeder, 2000). Indeed the chemical and hydrological conditions of dolomite formation are not well understood as petrographic and geochemical data can have multiple interpretations so that the origin of dolomite remains a subject of major debate (Machel, 2004).

Dolomite has an ideal chemical composition $CaMg(CO_3)_2$ and a symmetry structure 3, forming a trigonal subsystem of the hexagonal crystal system. Crystal size in dolomite is controlled by nucleation and growth kinetics, while crystal shape is controlled by growth kinetics only (Armenteros, 2010).

Kinetic inhibition forms a barrier to precipitation of dolomite from supersaturated seawater solution under modern earth-surface conditions. These barriers are identified by Wright & Wacey (2004) as:

-high hydration energy of the Mg^{2+} ion
-extremely low concentration and activity of $(CO_3)^{2-}$, and
-presence of very low concentrations of sulphate

In both ancient and modern sediments, a genetic link between bacterial sulphate reduction, raised alkalinity, and removal of sulphate have been reported regularly in dolomite formation. Sulphate can hinder calcite precipitation, which is consistent with dolomite inhibition. The same kinetics are involved with sulphates forming neutral ion pairs with Ca^{2+} (Wright & Wacey, 2004).

In dolomite precipitation, the primary constraints are (Armenteros, 2010; Lee 2013):

1) high Mg^{2+}/Ca^{2+} ratios,

2) generally high ionic strength solutions, promoted by evaporative concentration,

3) increased alkalinity due to sulphate reduction,

4) microbial mediation, and

5) Increasing temperature or pH and decrease in pressure and salinity.

There are a few forms and models of dolomitization, as summarised in Machel (2004):

1. *Penecontemporaneous dolomites, which* form almost syndepositionally, through the mediation of microbes (primary, early diagenetic). The main two preferred formation settings are shallow marine to supratidal and hemipelagic to pelagic.
2. *Post-depositional dolomites*, which form after deposition and removal of the carbonate sediment from the active zone of sedimentation. This mostly happens through progradation of the sedimentary surface, burial and subsidence, uplift and emergence and eustatic sea-level fluctuations (late diagenetic). Hyposaline environments are included here, with salinities below that of normal seawater. These environments include coastal and inland freshwater-seawater mixing zones, marshes, rivers, lakes, and caves. Post-depositional dolomite was found in these environments as cements. The preferred formation settings are near-surface to shallow-burial diagenetic settings at depths of less than about 600-1000 m.
3. *Hypersaline environments and the reflux and sabkha models, which* form dolomite where the salinities are greater than the salinity of normal seawater. They are common at latitudes < 30 ~ but sometimes occur at

higher latitudes. Dolomite is formed from water in which the salinity is controlled by surface evaporation (near surface) and shallow-burial diagenetic settings.

According to Wright & Wacey (2004), what causes the 'dolomite problem' are two main factors; the failure to precipitate dolomite at low temperatures experimentally or from seawater (which are both supersaturated and thermodynamically favoured carbonate phase), and the distinctive distribution of dolomite through geological time relative to limestone. The non-ideal metastable dolomite can persist over geological time, therefore there is no agreement as to the nature of the direct relationship between fluid chemistry and dolomite composition (Kaczmarek & Sibley, 2011).

Dolomitization is the formation of dolomite by replacement of micrite matrix and allochems, or occurring as intraparticle and interparticle cements precipitated from aqueous solutions. Replacement, in turn, is a process of cementation where $CaCO_3$ is replaced by $CaMg(CO_3)_2$ (Machel, 2004; Armenteros, 2010).

The Ca:Mg ratio in most sedimentary dolomite and dolomite in recent sediments, contains calcium in the excess of the ideal 1:1 Ca:Mg, so is calcite-rich. Approximately the ratio is 1.15:0.85 Ca:Mg, or 7-8% mol% excess $CaCO_3$. Crystalline dolomite is more stoichiometric than dolomicrites and dolomitized calcitic mudstones. Stoichiometry increases with increased textural alteration and ancient dolomites are known to be nearer to the ideal stoichiometry than Holocene dolomites (Armenteros, 2010). An excess of magnesium is rare, but the enrichment of calcium causes non-stoichiometry, and may occur in ferroan dolomites and ankerites. Such Ca-rich dolomites are less stable, more soluble, cation-disordered dolomite and reactive than stoichiometric dolomite (Reeder, 2000). During diagenesis, Ca-rich dolomite can dissolve and reprecipitate as stoichiometric dolomite.

Studying dolomite cement is important for the oil industry, as porosity and permeability is preserved better with increasing depth in dolomite. It is believed that around 13% of porosity is generated in the 'mole-per mole' replacement of calcite by dolomite (mass-balance constrains, where 2 moles of calcite are replaced by 1 mole of dolomite) (Machel, 2004; Jacquemyn, 2013).

Dolomite can retain or create porosity and permeability in great depths and high temperatures. The reason is that subsurface dolomite forms by dissolution and re-precipitation. Dolomitization can destroy, maintain or enhance porosity depending upon the original depositional fabric and nature as well as the volume of fluids passing through carbonates sediments. The presence of bitumen in secondary porosity can indicate that the dolomite can help having viable reservoirs during hydrocarbon migration. The presence of hydrocarbons may prevent further cementation, where the burial evolution process is halted before the complete loss of porosity (Warren, 2000).

Dolostone also has higher fracture porosities and permeabilities than limestones, but lower matrix porosities and permeabilities. This might be due to the fact that dolomite is less affected by burial compaction and cementation, as indicated by the observation that dolomites tend to have higher mean porosity and permeability than limestones only for burial depths >3 km. This is supported by laboratory work and field observations that under similar conditions for both dolomite and limestone, dolomite is shown to be more extensively fractured than limestone. As a result, it is concluded that dolomitic reservoirs are characterized by more effective fracture networks than limestones (Machel, 2004; Giorgioni et al., 2016).

Hydrothermal dolomitization is common, where dolomite is formed either as a cement or as a replacement in three ways (Machel, 2004):

1- Advection, usually by hydrothermal fluids,
2- Locally redistribution of older dolomite during stylolitization, and
3- As a by-product of thermochemical sulphate reduction in a closed/semi-closed system

Dolomitization caused by fluid flow rising through faults often produces saddle dolomite bodies, which are generally hydrothermal (Machel, 2004) (Fig. 4.1). It is believed that the syndepositional fractures and faults may serve as conduits that transmit brines deeply into underlying strata and affect early diagenesis, especially dolomitization.

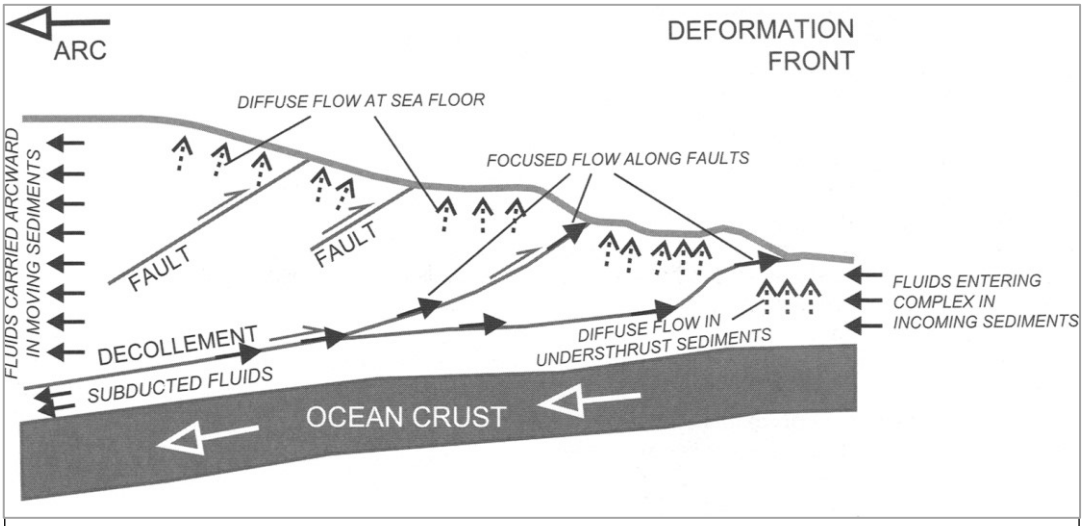

Fig. 4.1. Schematic cross-section of an accretionary wedge and potential fluid pathways. Flow within the decollement and other faults may be spatially focused in dilated networks, temporally transient, or both (Machel, 2004).

According to Lee (2013), there are several possible mechanisms that facilitate fluid movements and subsequent cement precipitation. These are gravity, compaction, thermal gradients, seismic pumping and tectonic stress. Fault-related dolomite is also common in sedimentary basins of the Jurassic and Cretaceous with diagenetic profiles due to the influence of fluids from depth. Fluid pressure at depth builds up, which provides a mechanism that creates brittle fractures (hydraulic fracturing) and fluid flow pathways. The precipitation of dolomite in the fractures takes place due to the reduction in fluid pressure and/or degassing of the arising fluid. When these fractures are cemented, the fault zone permeability will be reduced accordingly. This will allow further fluid pressure build-up, hence, beginning of following hydraulic fracturing events.

There are two major fluid flow mechanisms aided in fracture-related hydrothermal dolomitization (Warren, 2000; Haeri-Ardakani et al, 2013): first, thermal convection of dolomitizing fluids, and second, upward migration of brines from deeper basinal or basement sources.

Saddle dolomite is also known as baroque dolomite, or pearl spar. It might be a replacement or cement and has curved crystal faces, which are often visible with the unaided eye as the cement crystals may be large up to ~ 10 mm across. With respect

to the diagenetic settings and the crystal growth mechanism a special type of genesis is suggested by its crystallographic, geochemical and paragenetic characteristics (Barber et al, 1985; Tucker & Wright, 1990; Machel, 2004). Saddle dolomite shows a characteristic wavy extinction (Paganoni et al., 2016) and CL cement zonation. It occurs as a void-filling cement and as a replacement mineral. Saddle dolomite can be used as petrologic indicator of hydrothermal fluids, and/or heated saline fluids, as its formation is associated with the hydrothermal fluid flux, which are known to flow alongside fractures and faults during mountain thrust movement (Paganoni et al., 2016; Keke et al., 2016; Davis & Smith, 2005), where the presence of saddle dolomite implies the flow of hot (90–160°C), saline fluids along the unconformity. In addition, most high-temperature dolomite has a $\delta^{18}O$ less than -6.5%, where the dolomitization temperature is usually obtained by measuring the fluid inclusion homogenization temperature (Jacquelyn, 2013; Lee, 2013; Williams, 2015).

The temperature of formation for saddle dolomite is suggested to exceed 80°C (Machel, 2004), but it can also precipitate at lower temperatures from tremendously highly-saturated, highly salinity brine, where the minimum temperature for its formation is ca. 60°C. It is believed that saddle dolomite is formed within the oil window (60°C to 150°C), and is therefore linked with hydrocarbons (Tucker & Wright, 1990; Haas et al., 2014; Keke et al, 2016). It was globally precipitated from two to nine times higher in salinity brines than the modern seawater, based on fluid inclusion analysis (Davis & Smith, 2005).

The growth of saddle dolomite is considered comparatively rapid relative to normal diagenetic carbonates (Lee, 2013). Saddle dolomite usually has an 'astropetal' growth habit (upward vertically) in oil reservoirs, with respect to the ambient fluids such as oil and water (Barber, 1985).

To understand the origin of dolomite and characterize it, many geochemical methods can be used. Geochemical data enable a better understanding not only the origin of the dolomite, but also the formation time, fluid composition and dolomitization model (Asghari, 2014). The most common used methods are the stable isotopes of Oxygen and Carbon, Strontium (Sr) isotopes, trace elements and fluid inclusions

(Machel, 2004). More than one of these parameters may be used to define the fluid flow direction for the duration of dolomitization, under favourable circumstances.

Studying saddle dolomite in fractures has shown that it can contain varied amounts of Fe, Mn and Sr. During diagenesis, Fe^{2+} and Mn^{2+} are released to the pore waters where they can be incorporated in carbonate minerals, due to microbial reduction in the marine sediments (Burns & Baker, 1987). Mn and Fe, which have smaller radii than Sr are expected to have higher values in stoichiometric dolomites (Ca-poor dolomite) and the concentration of both of Mn and Fe commonly correlate positively in dolomite (Armenteros, 2010; Swart, 2015).The presence of Fe in the dolomite can reflect the diagenetic settings regarding redox index. Intermediate to deep burial settings are categorised by chemically-reducing conditions (Machel, 2004). Very high iron contents found in dolomites may indicate that those dolomites formed much more deeply in the sediments where the supply of Mg^{2+} was limited and Fe^{2+} replaced Mg^{2+} in dolomite (Burns & Baker, 1987).

Low Fe and Mn contents are an indication of early near-surface dolomite, because of the oxidizing influence of near-surface fluids. By contrast, high Fe and Mn concentrations are common for late burial dolomite (negative Eh pore-fluids) (Tucker & Write, 1990; Armenteros, 2010).

Strontium is an important trace element in dolomite (Asghari, 2014). The Sr concentration in dolomite is generally lower than in calcite formed under the same conditions as Sr is favourably substituted into the Ca sites in the crystal lattice (Swart, 2015). The texture of saddle dolomite (coarsely crystalline) tends to have lower Sr content, and is considered as late diagenetic indicator (Tanner, 2009). Theoretically, the partition coefficient of Sr in dolomite is only half that in calcite; therefore, dolomitization of calcite is a process that induces strontium loss (Chen et al., 2014).

Sr content can define the timing of dolomitization (Tucker & Wright, 1990), where Sr-rich dolomite is a result of a marine carbonate origin (Aragonite, HMC) as a result of early dolomitization, whereas Sr-poor dolomite results from the replacement of stable marine carbonate (LMC), suggesting later dolomitization. Sr replacement for calcium in aragonite and calcite is a sink for strontium in the marine environment

(Baker et al., 1982). Strontium can be absorbed and accumulated in diagenetic fluids in several ways (Keke et al, 2016):

1) Neomorphism of marine carbonate minerals by entering into aragonite crystal lattice, which may discharge the Sr ions into void-filling fluids. That happens when in a closed environment, when the sedimentary carbonates transforms into diagenetic minerals.

2) The dolomitization process, where only half of the Sr is able to enter the void-filling fluids.

3) In the presence of gypsum. The dolomite content of Sr can generally be related to the rock texture or timing of formation, where early (penecontemporaneous) finely crystalline dolomites are enriched in Sr in comparison to later-diagenetic, coarsely crystalline dolomites (Armenteros, 2010).

Hollis (2011) discussed the burial history of dolomitization during the Cenomanian/ Turonian unconformity in the Oligo-Miocene in hydrocarbon fields in Oman and UAE. Here, the burial history curves showed maximum burial depths of approximately 3 km. Plume-like fault and fracture related dolomite bodies up to several kilometres wide in the Aptian to Cenomanian Khami and Bangestan Groups in Lurestan Province, Iran, cross-cut the stratigraphy and form a halo around normal faults (Jacquemyn, 2013). At the core of these faults and associated fractures and within the fault breccia, saddle dolomite of multiple cement phases cements associated with live oil and bitumen have been described, supported strongly by fluid inclusion evidence as well as associated minerals formed by emplacement from hydrothermal fluids. Interestingly, the saddle dolomite appeared to be close to clay seams, which suggests that both dolomitization and stylolitization took place at the same time. However, stylolites are regularly regarded as fluid migration indicators rather than pathways. This is because preferential fluid flow along stylolites requires a reduction in the effective lithostatic pressure comparative to the original pressure-solution pressure, which is possibly induced by an increase of hydraulic pressure (Jacquemyn, 2013).

4.2 Objectives

Dolomite in the samples studied of the Thamama Group occurs in fractures, pores and matrix. This chapter will concentrate on the dolomite cement in the fractures, which occurs only as saddle dolomite. Rhombic dolomite was found in the matrix only and was not analysed.

The main objective is to measure the concentrations of Sr, Mn and Fe and Mg:Ca in fracture-hosted dolomite, in order to understand the origin of the dolomite, the nature and origin of the precipitating fluids, and the setting in which these dolomite cements were formed.

In particular, we aim to understand whether fluids were oxidizing or reducing using iron and manganese concentrations, and if the fluids are from closed or open systems as shown by strontium concentrations.

We will compare the dolomite in fracture cements in:

- The oil zones and water zones, to understand if hydrocarbons affected the dolomitization process,
- Different fracture generations (Fracture set 1 and Fracture set 3), to characterise and compare the fluids that precipitated the dolomite,
- Different reservoir zones of the Thamama Group (B, F, G zones), to observe the evolution of dolomite precipitating fluids through time and the possible migration pathways.

4.3 Methods and Sampling

Sample preparation and Methodology

As for calcite cement samples, doubly polished thin sections were carbon coated then analysed in a Cameca SX100 instrument. The electron probe microanalyser can make fully quantitative analyses of the elements (Mg, Ca, Sr, O, Mn and Fe). The technique uses an incident electron beam to generate X-rays with energies and wavelengths specific to the elements present in the sample. Instrument calibration is carried out by analysing reference materials (dolomite) with known compositions wt

%. Sr, Mn and Fe are presented in ppm. The accuracy is about 0.008% Mn, 0.010% Fe and 0.010% for Sr. All detection limits are shown in Table. 4.1.

The distribution and number of samples analysed of saddle dolomite cement in Fracture Sets 1 and 3 in Thamama Reservoir G oil, and Fracture Set 1 in Reservoir B water and F water is given in Table 4.2. The samples that contained significant dolomite were mostly found in Reservoirs G oil, F water (F water lays in the transition zone) and B water. Fracture sets 1 and 3 were sampled for dolomite in Reservoir G oil, while only Fracture Set 1 was sampled for Reservoirs B and F water.

All data are given in Appendix 2.

Fracture sets	Zones	Cement type	Elemental detection limits		
			Sr	Mn	Fe
Fracture set 1	G oil	Saddle Dolomite	122±3	93±3	147±5
	F water		126±3	94±2	154±5
	B water		124±5	93±5	122±5
Fracture set 3	G oil		122±3	93±3	137±5

Table 4.1. Min detection limits for Sr, Mn and Fe for saddle dolomite cement in Fracture Sets 1 and 3, in Thamama Reservoirs G oil and B and F water.

Fracture sets	Elements	Cement type	Oil Zones													Water Zones							
			G													B		F					
			Cement zones																				
			nF1=160, nF3=10													n=56		n=64					
Fracture set 1	Sr	Saddle dolomite	1	2	3	4	5	6	7	8	9	10	11	12	13	1	2	1	2	3	4	5	6
			76	13	22	14	1	8	17	1	2	0	1	1	3	18	32	33	10	16	0	1	3
	Mn		76	13	22	14	1	8	17	1	3	0	1	1	3	19	36	33	10	17	0	1	3
	Fe		76	13	20	14	1	7	16	1	3	0	1	1	2	20	34	33	10	17	0	1	0
Fracture set 3	Sr	Saddle dolomite	5	1	1	1	1	0	1														
	Mn		5	1	1	1	1	0	1														
	Fe		5	1	1	1	1	0	1														

Table 4.2. Number of samples measured from saddle dolomite cement in fracture sets 1 and 3 in Thamama Zone G oil, and Zones B and F

4.4. Timing of dolomite fracture cement formation

A summary of paragenesis for all reservoirs highlighting dolomite precipitation is given in Figure 4.2.

No saddle dolomite has been found in fractures or matrix in Reservoir A, or in fractures in Reservoir C. Rhombic dolomite appeared earlier in the paragenetic sequence in all the other reservoirs. Rhombic dolomite environments range between marine phreatic to shallow burial and saddle dolomite environments range from shallow burial to deep burial. It is also noticed in the studied samples that saddle dolomite appeared in fractures and large pores close to the fractures only.

Rhombic and saddle dolomite precipitation phases occur at distinctly different times in the paragenetic sequence. In Reservoir B there are fourteen paragenetic phases separating them, in Reservoir F, eight paragenetic phases separating them, and Reservoir G there are ten paragenetic phases separating them. By contrast, they occur with only four intervening paragenetic events in Reservoir C (see Section 2.3.3 for details).

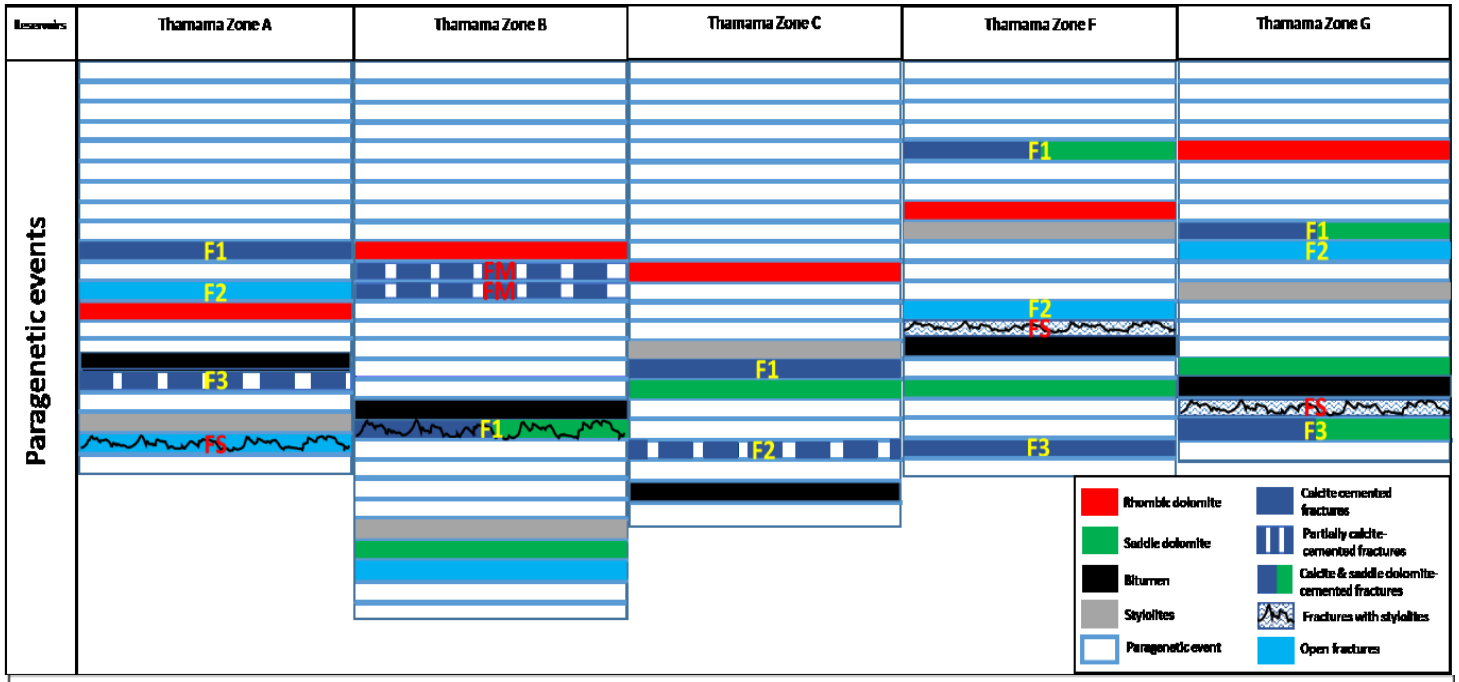

Fig. 4.2. Rhombic (in matrix) and saddle dolomite (in fractures and matrix) appearance in the paragenetic sequence through the Thamama oil and water reservoirs. FS: fractures in stylolites, FM: minor fractures (other than the three main fracture sets in the Thamama reservoirs).

Relative to each other, rhombic dolomite can be interpreted to be an early diagenetic event while saddle dolomite can be interpreted as a late diagenetic event.

Dolomite cement was mostly found in the fractures of Reservoirs G oil, F water and B water. The other reservoirs either have no dolomite in their fractures or only show very small aperture fractures (< 10 μm) with dolomite cement that makes analysis difficult. It would be helpful if the dolomite halos appeared adjacent to fractures, but that was not the case in the samples studied.

In Reservoirs G oil and B water, the dolomite was deposited in the stylolitic fractures. The volume of dolomite cement in the fractures is greater in the lower Reservoirs (F and G) than in B (See Section 2.3.2.2).

The occurrence of hydrocarbon inclusions in both burial calcite and dolomite cements can indicate that cementation was at least partly coincident with hydrocarbon migration. In Reservoir A oil, bitumen showed after rhombic dolomite precipitation, in Reservoir B water, saddle dolomite precipitated after bitumen emplacement. On the other hand, in Reservoir C oil, bitumen appears after saddle dolomite. Reservoir F water, like Reservoir B water, bitumen appeared before saddle dolomite. And in reservoir G oil, bitumen showed right after the saddle dolomite precipitation.

Saddle dolomite was sometimes associated with stylolites in Reservoirs G oil and B water, which indicates that both dolomitization and stylolitization took place during the same time in some areas of these two reservoirs. No stylolite-associated dolomite was found in the sample examined for Reservoir F water.

Cathodoluminescence (CL) of fractures dolomite shows colour differences between different cement zones. In 99% of the studied samples, the core of the crystals had very dark red to black colours, then the zones show alternative bright and dark red coloured zonation (See Section 2.3.4).

Reservoir G oil had the most cement zones for dolomite of the three reservoirs that contained dolomite in fractures, with thirteen cement zones in Fracture Set 1, and seven cement zones in Fracture Set 3.

Reservoir F water has six cement zones and Reservoir B water two cement zones.

4.5 Results

In this section, plots summarising elemental data are given for each sampled CL zone for saddle dolomite in fractures in the studied reservoir zones.

As in the previous chapter concerning fracture calcite cements, the results are given in stratigraphic order starting with Reservoir G to Reservoir B. Data presented here are as ppm concentrations. In Reservoir G oil, fracture sets are plotted separately, in Reservoirs B water and F water the dolomite cement was only found in Fracture Set 1. Data are given as box and whisker plots, where the box shows the mean and quartiles, with whiskers showing the full range. Measurements in minus were counted as zero.

The saddle dolomite cement volume found in the lower Thamama (Reservoirs F and G) was more than that found in the Upper Thamama (Reservoir B).

Reservoir G oil

Fracture Sets 1 and 3

Sr

Fracture set one has thirteen CL cement zones, but fracture set three has only seven CL cement zones.

Fig. 4.3A shows the distribution of Sr ppm values of Reservoir G oil for saddle dolomite cement in Fracture Set 1. The mean ppm value ranges from below detection limit in cement zone 11 to reach its highest value of 140.3 ppm in cement zone 13. No sample points were taken in cement zone 10. All values lay below the detection limit, except for cement zones 7 and 13. The most sample points were at cement zones 1, 3 and 7. Sr ppm mean values in Fracture Set 3 of Reservoir G range between 88 ppm in cement zone 3 to 188 ppm in cement zone 2 (Fig. 4.3B). No sample points

were taken in cement zone 6. All Sr values lay below the detection limit except for cement zones 2 and 4. The most sample points were taken from cement zone 1.

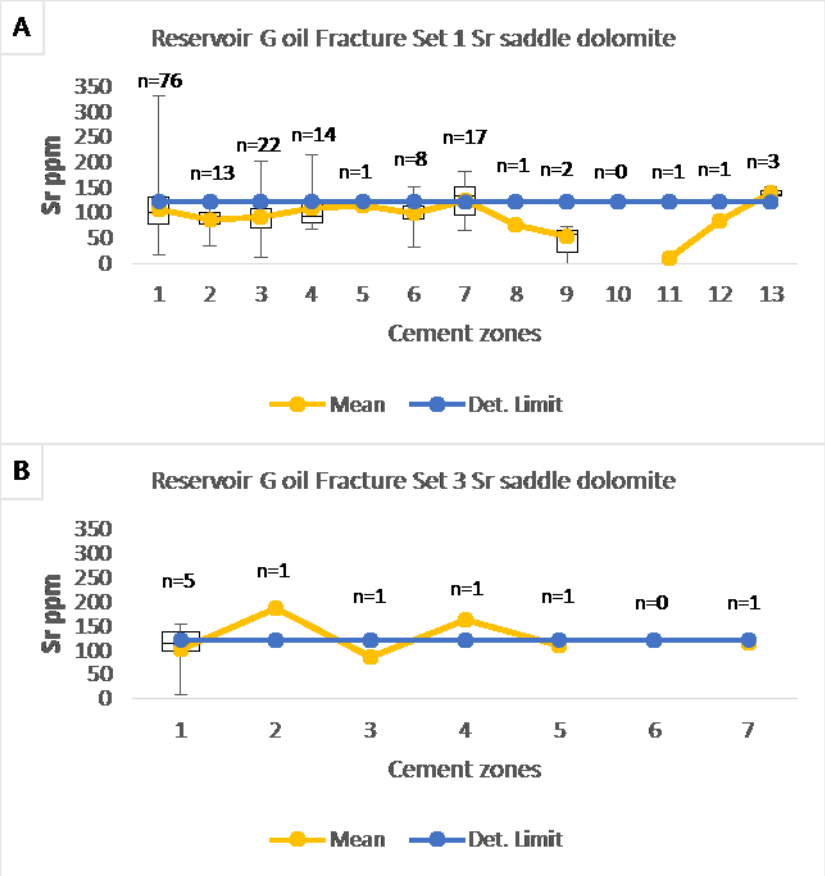

Fig.4.3. Box and whisker plots for Sr data for each CL cement zone in Reservoir G oil. A: Sr ppm for saddle dolomite cement in Fracture Set 1. B: Sr for saddle dolomite cement in Fracture Set 3. n = number of data points. The yellow dots and line trace the mean, the blue line represents the detection limit.

Mn and Fe

The mean Mn values for saddle dolomite range from 158 ppm for cement zone 12, to 241 ppm for cement zone 8 in Fracture Set 1. Cement zone 10 has no sample points (Fig. 4.4A). In Fracture Set 3, Mn values range from 181 ppm for cement zone 5, to 233 ppm for cement zone 4 (Fig. 4.4C).

Fe values in Fracture Set 1 range widely between values below detection limit in cement zone 13 to 30641.4 ppm in cement zone 1. The values decrease dramatically from cement zone 1 to cement zone 13 and cement zone 10 has no sample points (Fig. 4.4B). For Fracture Set 3, Fe values also range from very low value (18 ppm) in cement zone 7 to very high value (25815 ppm) in cement zone 1. Cement zone 6 has no sample points (Fig. 4.4D).

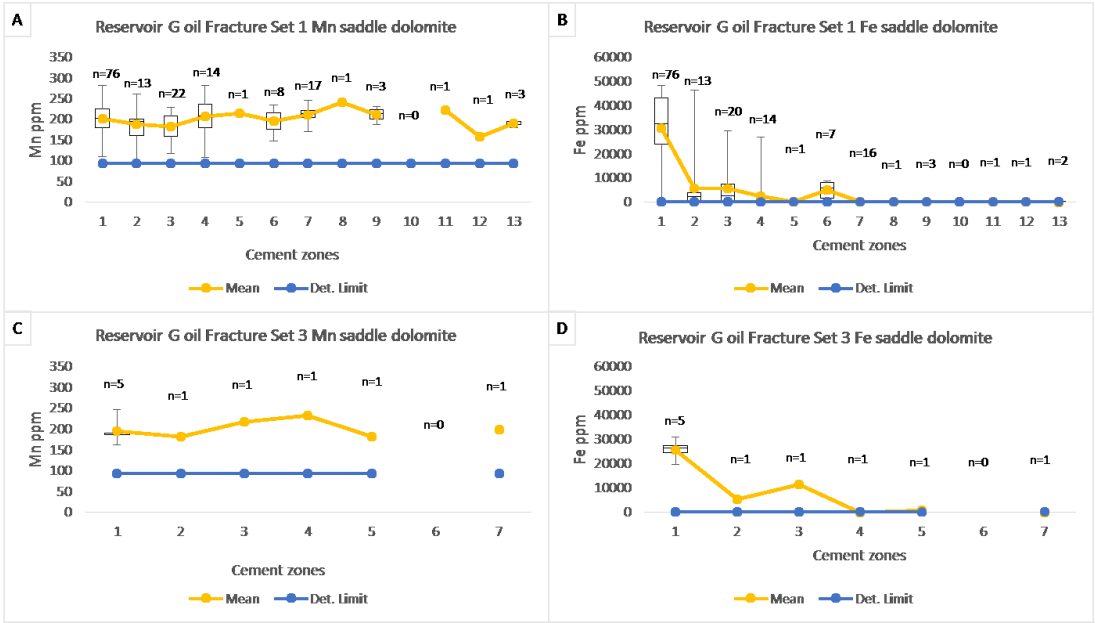

Fig: 4.4. Box and whisker plots for Mn and Fe concentrations (ppm) of saddle dolomite for each CL cement zone from Fracture Sets 1 and 3 in Reservoir G oil. A: Mn in Fracture Set 1. B: Fe in Fracture Set 1. C: Mn in Fracture Set 3. D: Fe in Fracture Set 3. The yellow dots and line trace the mean. n = number of data points. Blue Line shows the detection limit.

Mg:Ca

Mg:Ca is calculated for each cement zone in both Fracture Set 1 and Fracture Set 3 . Overall, higher values of Mg: Ca are shown for Fracture Set 1 than the values in fracture set 3. The highest Mg:Ca mean value for Fracture Set 1 was found in cement zone 1 which was 1:2.4. Values then decline rapidly to cement zone 2 and the lowest value mean was 1:1.9 found in cement zones 8, 9 and 11. For Fracture Set 3, the highest mean value was found in cement zone 1 as well (1:1.9), and likewise values

then decline rapidly to cement zone 2 and the lowest value was found in cement zone 7 (1:1.7) Fig. 4.5.

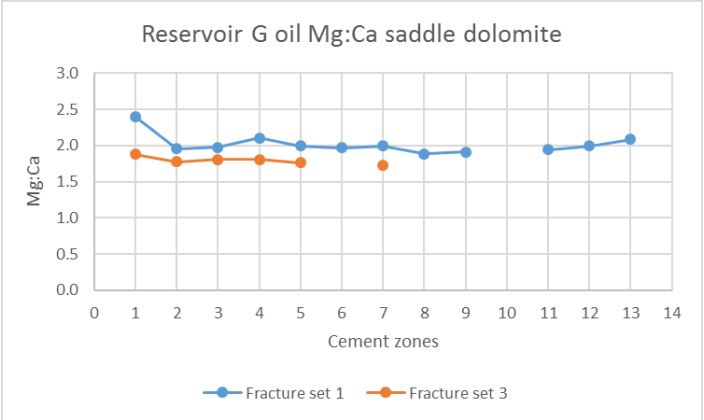

Fig. 4.5. Mg:Ca mean values for saddle dolomite in Fracture Sets 1 and 3 in Reservoir G oil.

Reservoir F water

Fracture Set 1

Sr

The distribution of Sr values of Reservoir F water for saddle dolomite cement in Fracture Set 1 is shown in (Fig. 4.6A). The mean ppm value ranges from 73.5 ppm in cement zone 3 to reach its highest value of 98.9 ppm in cement zone 2. No sample points were taken in cement zone 4. All values lay below the detection limit, except for cement zones 1 and 2.

Mn and Fe

The mean Mn values for saddle dolomite range from 123 ppm for cement zone 5, to 166 ppm for cement zone 1. Cement zone 4 has no sample points (Fig. 4.6B).

Fe values also range widely between zero ppm in cement zone 6 to 47577.1 ppm in cement zone 1. The values decrease intensely from cement zone 1 to cement zone 6, while cement zone 4 has no sample points (Fig. 4.6C).

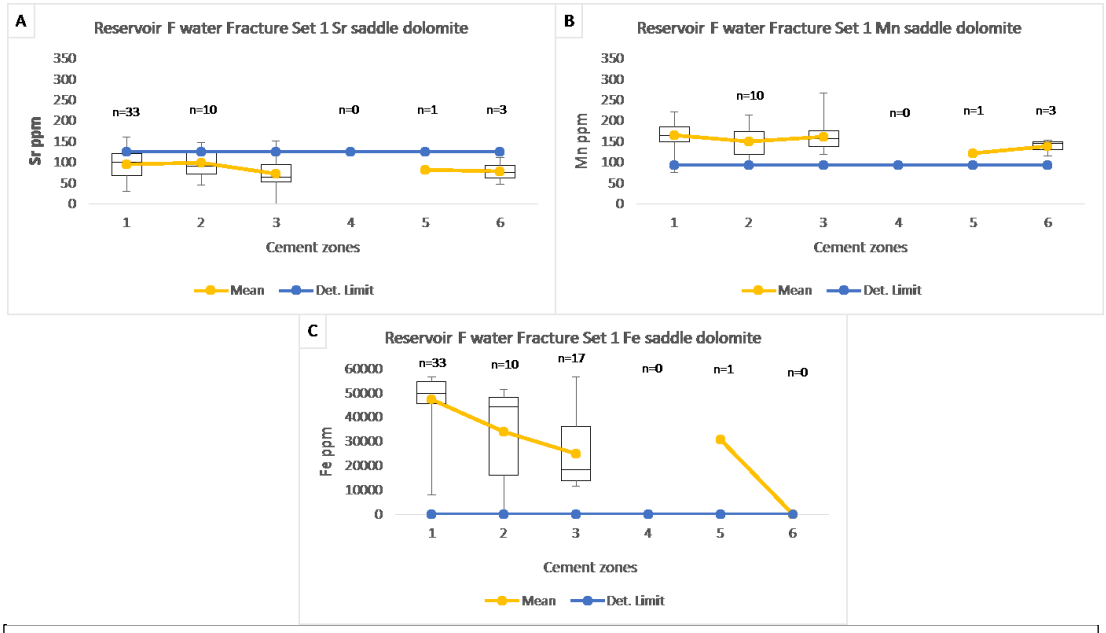

Fig.4.6. Box and whisker plots for Sr, Mn and Fe concentrations (ppm) of saddle dolomite for each CL cement zone from Fracture Sets 1 in Reservoir F water. A: Sr in Fracture Set 1. B: Mn in Fracture Set 1. C: Fe in Fracture Set 1. The yellow dots and line trace the mean. n = number of data points. Blue Line shows the detection limit.

Mg:Ca

The highest mean value for Fracture Set 1 was 1:2.1 in cement zones 1 and 2 and the lowest mean value was 1:1.8 in cement zone 6 (Fig. 4.7). Values show a slow decline through time.

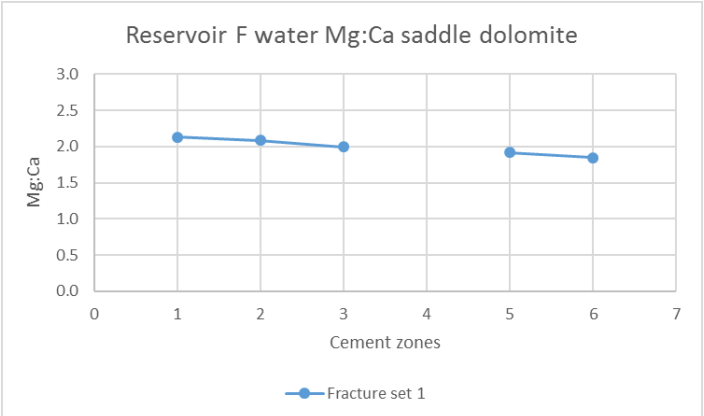

Fig. 4.7. Mg:Ca mean values for saddle dolomite in Fracture Set 1 of Reservoir F water.

Reservoir B water

Fracture Set 1

Sr

The distribution of Sr values of Reservoir B water for saddle dolomite cement in Fracture Set 1 is illustrated in (Fig. 4.8A). There are two mean ppm values, the lower is 56.2 ppm in cement zone 1 and the higher is 72.7 ppm in cement zone 2. Cement zone 1 is below the detection limit.

Mn and Fe

The mean Mn values for saddle dolomite starts from 43.3 ppm for cement zone 1 (below detection limit), to 66.9 ppm for cement zone 2. (Fig. 4.8B).

Fe values increases from 2940.8 ppm in cement zone 1 to 5085.9 ppm in cement zone 2 (Fig. 4.8C). Both of Mn and Fe values were lower in Reservoir B water than other oil and water reservoirs.

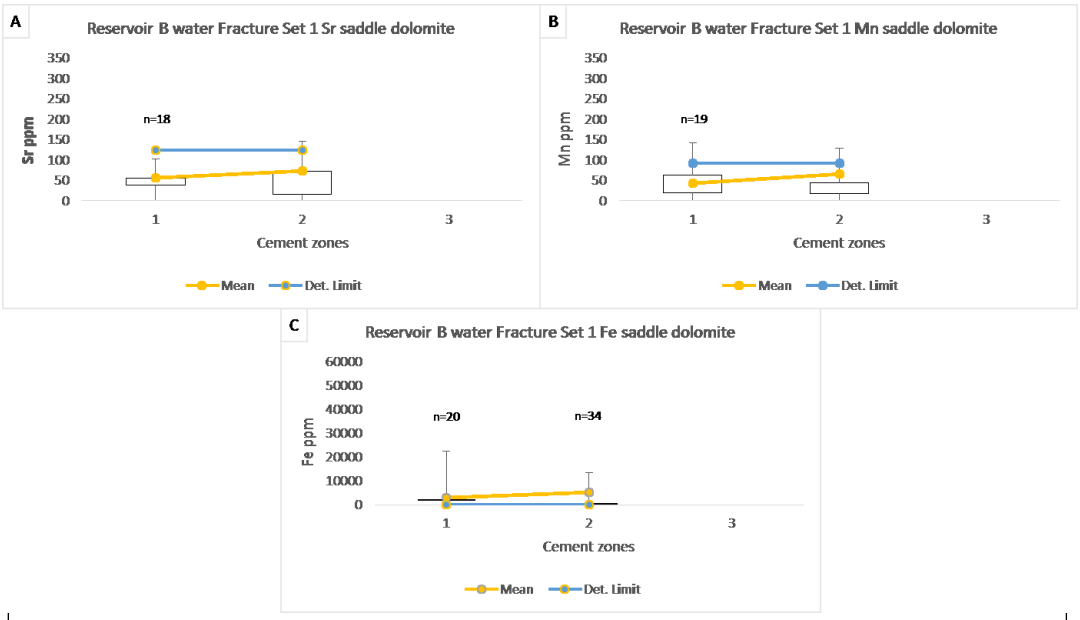

Fig.4.8. Box and whisker plots for Sr, Mn and Fe concentrations (ppm) of saddle dolomite for each CL cement zone from Fracture Sets 1 in Reservoir B water. A: Sr in Fracture Set 1. B: Mn in Fracture Set 1. C: Fe in Fracture Set 1. The yellow dots and line trace the mean. n = number of data points. Blue Line shows the detection limit.

Mg:Ca

The mean values in the two cement zones of Reservoir B water were the same (1:1.8) Fig. 4.9.

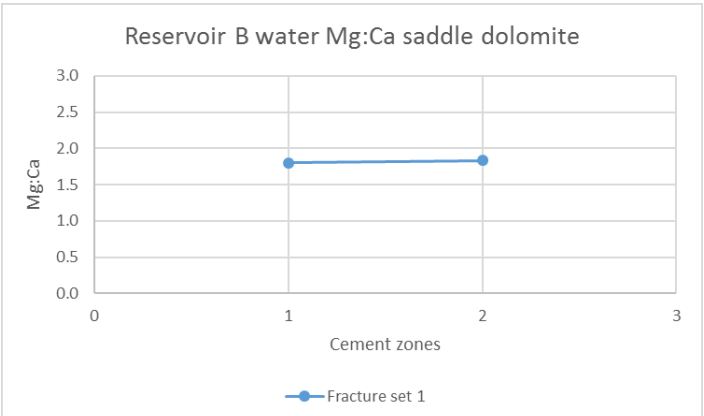

Fig. 4.9. Mg:Ca mean values for saddle dolomite in Fracture Set 1 of Reservoir B water.

4.6 Discussion

Sr

The values of Sr remained similar (under 100 ppm, below the detection limit) in both water Reservoirs F and B. But Sr rises slightly above 100 ppm in reservoir G oil for fracture set 1 (140 ppm in cement zone 13), and showed higher values in some cement zones in fracture set 3 (188 ppm in cement zone 2 and 160 ppm in cement zone 4) (Fig. 4.10). None of the Sr values were high enough to indicate the presence of an exotic fluid.

The reduction of Sr values simultaneously with increasing Mn and Fe values, can be related to high temperature diagenetic processes under reduction in both deep and burial conditions (Asghari, 2014).

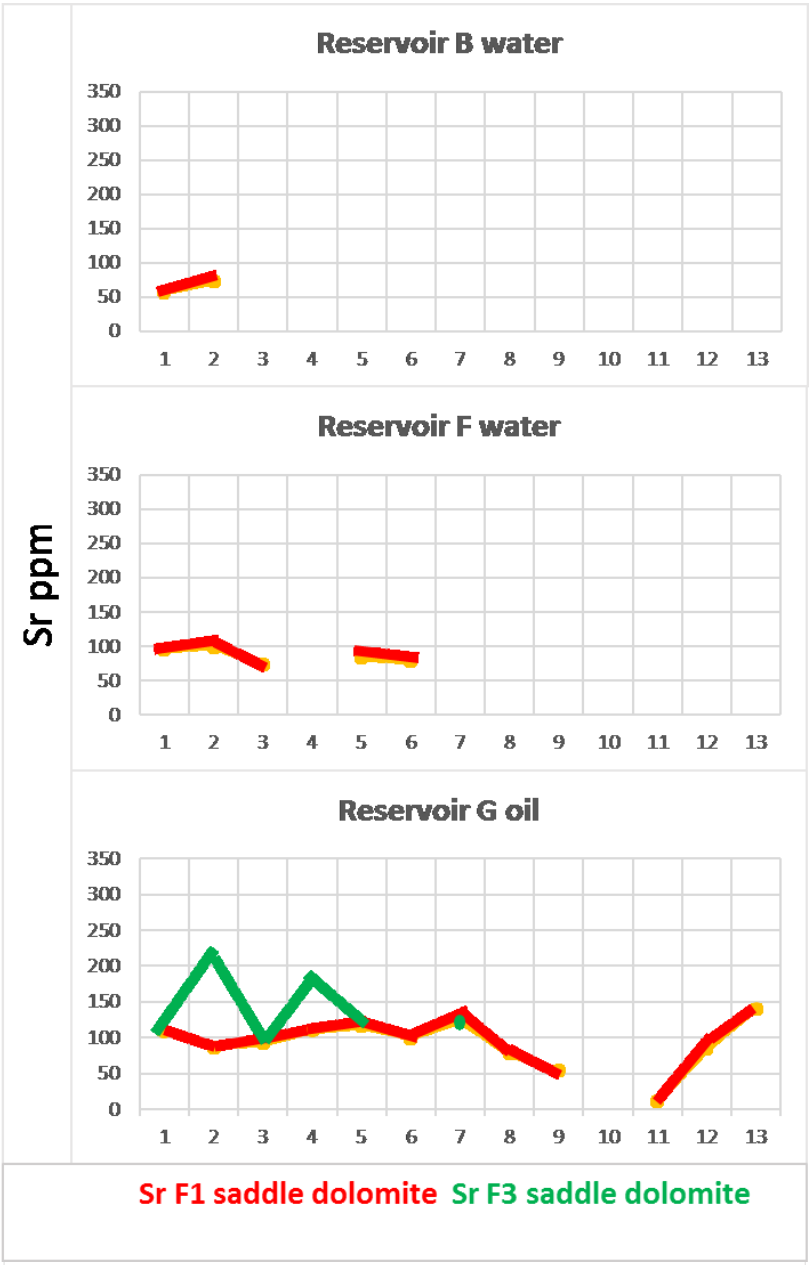

Fig.4.10. Sr in Reservoirs G oil, F and B water. The curves represent the mean values for Sr ppm in saddle dolomite in Fracture Sets 1 & 3

Mn and Fe

It was observed from the CL analysis, that almost 50% of the cement zones showed moderate to bright red colours. This can indicate high Mn and low Fe, which in turn indicates low oxygen levels (Callen, 2016). The appearance of dark and bright CL

zonation alternatively can be referred to Fe+ removal form the hydrothermal fluids causing shifting zoning characteristics from quenched luminescence to moderate luminescence (Callen, 2016). The cathodoluminescence zones are mostly regular, which suggests uniform distribution of Fe and Mg throughout the cement crystals (Lee, 2013).

Fracture Set 1 in Reservoir G oil showed the very high Fe values due to the presence of ferroan dolomite. This can be considered as a reducing environment and greater burial depth (Fig.4.11).

In Fracture Set 3 in Reservoir G oil, there are also high values in all of the cement zones (1 to 5) for both Mn and Fe. The dolomite is ferroan as in Fracture Set 1. This also suggests that all cement zones formed in reducing environment conditions and greater burial depth, due to high Fe and Mn content (Asghari, 2014). The slightly less reducing environment might be indicated through time due to the lowering Fe and Mn values towards cement zones 4 and 5. These two sets of fractures might have precipitated at the same fluid chemistry conditions, although they have formed at different times.

In Reservoir F water, the Mn values were all of low values (>100 ppm) below the detection limit. This, besides the high values of Fe might indicate the burial environment as mentioned above for Fracture Set 3 in Reservoir G oil (Asghari, 2014) and reducing conditions in the burial fluids (Tanner, 2009). Ferroan dolomite was found in all cement zones of Reservoir F water and is a strong indication of a reducing environment, as the presence of a high amount of Fe in the dolomite could confirm anoxic basinal conditions or increased amount of iron in the host fluid (Lee, 2013).

Reservoir B is different from Reservoirs F and G. Although the Fe and Mn overall values were lower in Reservoir B than F and G, the Fe values were still high (Fig.4.11).

It is known that the reducing conditions are evidence of deep basinal waters, which results in higher Fe and Mn levels in solution reflected in the cements. It might be that the increase in the Fe in cement zone 1 of both Reservoirs G oil and F water

corresponds to increasing availability of Fe^{2+} in the host solution due to greater reducing conditions. Burial cements are commonly known to be Fe and Mn rich, with late burial saddle dolomites often containing over 5 wt% Fe (Moore, 1985; Swart et al, 2005. Very high iron contents found in dolomites in Reservoirs F water and G oil, may also support the assumption that those dolomites formed at greater burial depth, where the supply of Mg^{2+} was limited and Fe^{2+} replaced Mg^{2+} in dolomite (Burns & Baker, 1987).

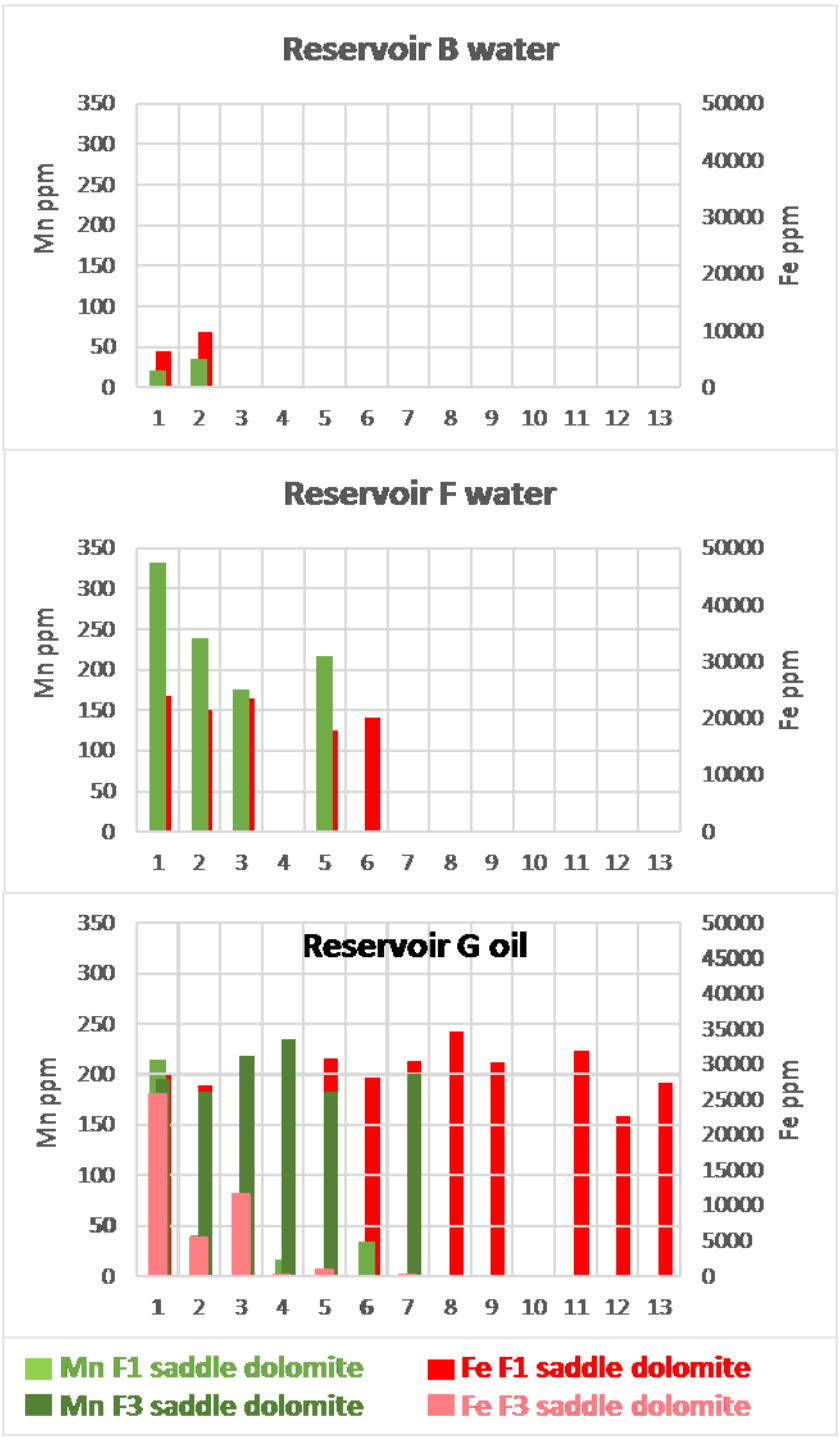

Fig.4.11. Mn and Fe in Reservoirs G oil, F and B water. The columns represent the mean values for Mn and Fe ppm in saddle dolomite in Fracture Sets 1 & 3

Saddle dolomite is linked with base-metal sulphide mineralisation from high temperature basinal fluids and is indicative of late stage diagenesis (Lee, 2013). The elevated levels of Fe especially in Reservoirs G and F, may indicate a through flux of metalliferous pore water in burial dolomites (Warren, 2000).

Mg:Ca

Cement zone 1 in all the studied reservoirs has the highest Mg:Ca mean value, but Reservoir B water has the same value over its two cement zones (Fig. 4.12). There is no evidence that the ferroan saddle dolomite found in Reservoir F water has any significant difference in values than the other saddle dolomite in the other reservoirs. The lowest Mg:Ca mean value in Fracture Set 1 in Reservoir G oil is equal to the highest value in Fracture Set 3 of the same reservoir.

The Mg is noticed to be depleting with time in the Lower Thamama reservoirs. This progressive loss of Mg is to be expected with burial cementation.

Most notably, cement zone 1 in the reservoirs shows different Mg:Ca values, with Reservoir G showing ~2.45 , Reservoir F ~2.2, and Reservoir B ~1.8. These values therefore decrease (becoming more calcic) through time.

One explanation is that during fluid migration along the flow path, the Mg/Ca ratio of these solutions should be reduced as Mg^{2+} is consumed and Ca^{2+} is freed during dolomitization. As limestones in stratigraphically higher positions are dolomitized, the saturation of the fluid with respect to dolomite will decrease along and down the flow path.

Another possibility is that the Mg:Ca is in some way tracking the source (parent fluid) such as seawater, which is known to show marked changes in Mg:Ca during the Lower Cretaceous (Steuber & Rauch, 2005).

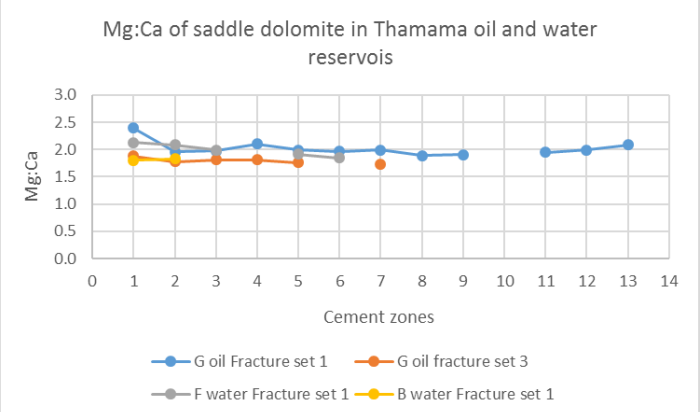

Fig. 4.12. Mg:Ca mean values for saddle dolomite in Thamama Reservoirs G oil, F and B water.

Geochemistry and stable isotopes

It is observed by Burns and Baker (1987) that negative $\delta^{13}C$ values correlate with low Fe, Mn and Sr values, and the positive $\delta^{13}C$ values are associated with high Fe, Mn and Sr values. This is the case in the Thamama dolomite, where the values of Fe is particularly high (Reservoir F water) and the values of Mn is moderate comparable to the low Sr (Paganoni et al., 2016). The ratios of carbon isotope in saddle dolomite primarily reflect the contributions of inorganic carbon that is derived from limestone host as well as organic carbon which is derived from microbial and thermal breakdown of organic material plus various hydrocarbons (Davies & Smith, 2006).

Dolomite cement along the stylolites and in micro fractures of the Upper Thamama (Reservoir B) Fracture Set 1 from Field A have been isotopically analysed . The $\delta^{18}O_{VPDB}$ values range between −10.0‰ and −7.1‰ (average −8.8‰), and $\delta^{13}C_{VPDB}$ values ranging from +2.8‰ to +4.2‰ (average +3.6‰) (Paganoni et al., 2016). The lowest $\delta^{18}O_{VPDB}$ values represent fracture filling saddle dolomite compared to the matrix saddle dolomite, which has higher $\delta^{18}O_{VPDB}$ values (Paganoni et al., 2016). A further study recorded the values of saddle dolomite in the Upper Thamama fractures to range between -7.89 to -8.76% $\delta^{18}O_{VPDB}$, so this also supports the origin of high temperature-late burial origin for the fractures dolomites (Rifai et al., 2006). As noticed from the very negative $\delta^{18}O_{VPDB}$ values in the Thamama dolomites, this is a supporting evidence that they have precipitated in burial environments from fluids

higher in temperatures than the host limestone (Warren, 2000). Based on the $\delta^{18}O_{VPDB}$ values, the expected temperature for saddle dolomite range between 67 to 112°C (Alsharhan, 1987).

Origin of Dolomite in fractures

Davies and Smith (2006) emphasized that the structurally controlled hydrothermal processes are characterized by very dynamic systems, with sudden changes in applied stress, pore-fluid pressure, and rates of fluid flow, adding that some processes and products are geologically instantaneous. They have found that the movement of structurally controlled hydrothermal fluids is favoured by specific structural settings, like extensional faults, deep strike-slip faults. That applies to the Tulip fracture found in field A (Fig. 4.13). The heated fluids are ejected quickly up through the fault zone in the direction of the easiest pressure relief (Wendte et al., 2010).

The presence of fractures probably aided in the flow of the diagenetic fluids. The Mg rich fluids invasion might have taken place through fractures and pore spaces as faults and associated fractures help to act as channels for migration of hydrocarbon and mineralizing fluids (Rifai et al., 2006; Wendte et al., 2010; Haeri-Ardakani et al., 2013).

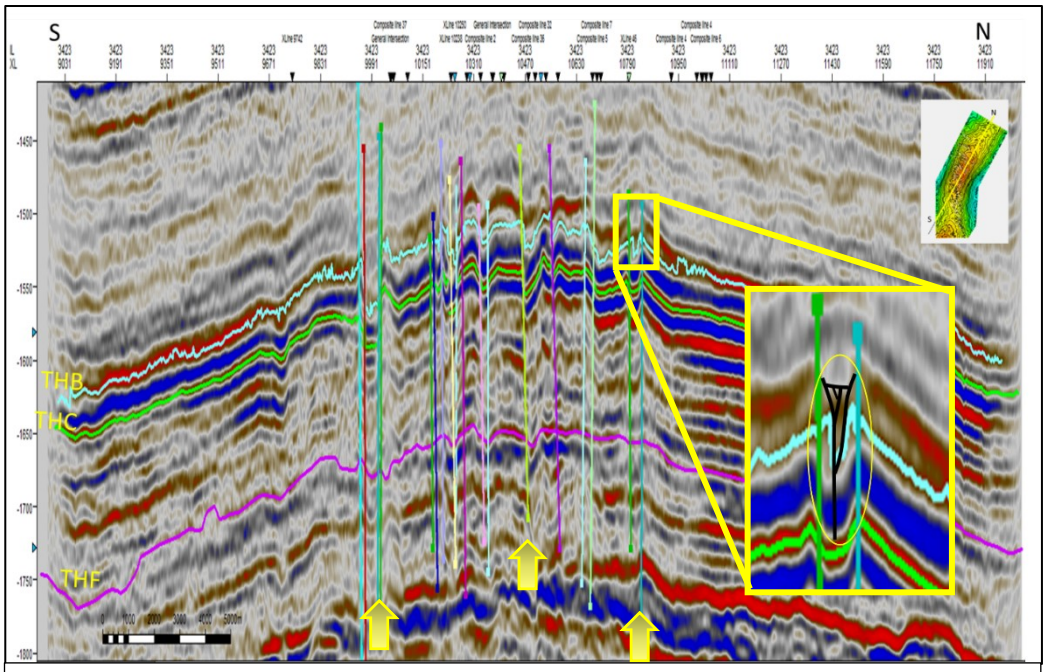

Fig. 4.13 Theoretical scenario for rising of dolomitization hydrothermal fluids through faults and associated fractures (yellow arrows). N-S seismic cross section (time) along Field A showing negative flower structure in the Thamama reservoirs. Yellow box: tulip structure. (THB): top horizon B, (THC): top horizon C, (THF): top horizon F (ADNOC Onshore, 2017).

A reason for linking the saddle dolomite of the Thamama reservoirs to the fractures, is the occurrence of dolomite as a cement in few localised areas such as fractures rather than in the matrix, indicative of formation from conduit-controlled flow (Wendte et al., 2010). Also, saddle dolomite appeared in fractures and large pores close to the faults only, confirming the fact that dolomite selectively replaces internal sediment infilling a network of fractures, signifying the development of dolomite from fluids that flowed through the fractures (Wendte et al., 2010).

In summary, Saddle dolomite in the Thamama might have precipitated in a deep burial environment. This environment is believed to be removed from active sedimentation by burial, where the pore-fluids chemistry is dominated by subsurface diagenetic processes (Machel, 1999). Another indication of the burial environment is the presence of pyrite (see Section 2.3.6). Pyrite was found in Reservoirs G oil and F water, which is suggestive of the involvement of warm intra-basinal fluids and is

frequently linked with late burial dolomitization of carbonate deposits (Rifai et al., 2006).

Considering that burial dolomites being subsurface cements that form below the active phreatic zone, reflux and mixing zones, some permeable intervals can be flushed by warm to hot Mg-rich basinal and hydrothermal waters (Warren, 2000). The fluids that originated dolomite can mostly be referred as hydrothermal fluids evolved from underneath the Thamama, with involvement of seawater to a lesser extent. The higher temperature of precipitating fluids is possibly sourced from fluid flux from depth (Lee, 2013).

Saddle dolomites in reservoirs G oil and B water were deposited in stylolitic fractures. This suggests a burial of 600 m or more where stylolites start to form. As saddle dolomite is associated with pressure-dissolution, where stylolites and pressure dissolution form basin brines are also local sources of magnesium in the burial model. The kinetic and thermodynamic barriers of dolomitization disappears as the temperature increases, therefore the presence of magnesium ion constitutes this process (Machel, 1999; Rifai et al., 2006; Asghari, 2014).

Considered source of diagenetic fluids in the Thamama may be (Davies & Smith, 2006; Breesch et al., 2010; Hollis, 2011; Morad et al., 2012; Haeri-Ardakani et al., 2013):

1) The underlying or adjacent source rocks, bearing in mind that dolomite fracture cementation is linked to hydrocarbon migration

2) Hydrothermal fluids resulting from the Late Cretaceous emplacement of the nappes onto the margin. Hydrothermal fluids flowed up through basement-rooted faults and associated fractures by thermal convection of dolomitizing fluids. The assumption of the Late Cretaceous age is not tested by this work

Based on the Heydari (1997) division of hydro-tectonic processes driving dolomitization, the diagenesis in the Thamama fits in the post-orogenic burial diagenesis. The reason is that the Thamama was affected by the orogenic events in the area of the Arabian Plate, which aided in the flow of diagenetic fluids.

4.7 Conclusions

- Saddle dolomite indicative of precipitation from hot fluids was found associated with fractures, with a greater volume present in the lower Thamama (Reservoirs F and G) than the Upper Thamama (Reservoir B).

- Saddle dolomite is localised to fractures and large pores close to the fractures only, confirming precipitation from fluids that flowed through the fractures.

- The occurrence of hydrocarbon inclusions in both burial dolomite cements can indicate that cementation was at least partly coincident with hydrocarbon migration. Fractures probably aided in the flow of hot, dolomitising fluids and hydrocarbons.

- Saddle dolomite was sometimes associated with stylolites in reservoirs G oil and B water, which indicates that both dolomitization and stylolitization took place during the same time in some areas of these two reservoirs.

- Sr is low in all dolomite in fractures indicating no influence of exotic fluids

- Dolomite in fractures in the Thamama is ferroan dolomite, indicating of formation in a reducing and deep burial setting.

- Fracture Set 1 has more is more Fe rich than Fracture Set 3

- Dolomite cement zone 1 in the reservoirs shows different Mg:Ca values, with Reservoir G showing ~2.45 , Reservoir F ~2.2, and Reservoir B ~1.8. These values therefore decrease (becoming more calcic) through geological time. It is possible that this is due to changes in seawater, which is known to show marked changes in Mg:Ca during the Lower Cretaceous.

CHAPTER 5: Fractures and cement fill geochemistry: Wadi Al Rahaba outcrop

5.1 Introduction

Fieldwork was undertaken in Wadi Rahaba, Ras Al Khaima, Northern UAE, as this offers a good analogue for the Upper Thamama Reservoirs B & C, and to a lesser extent the Hawar/ Dense Thamama (Thamama A).

The field study included studying the nature of fractures, including the number of fracture sets, orientation and density, as well as the nature of the infill. A detailed petrographic analysis was conducted in order to compare this with subsurface data, including construction of a paragenetic sequence to locate the timing of fractures within the tectonic events. EPMA analysis was performed on the most representative samples of cement infill of all fracture generations to compare with subsurface results.

5.2 Setting and Structure of Wadi Rahaba

Wadi Rahaba (Figs. 1.1B, 5.1) is located in north Ras Al Khaima, which is a part of the Musandam peninsula. The carbonates sequence exposed in the Musandam peninsula can be correlated to the subsurface wells drilled in the foreland basin (Searle, 1988).

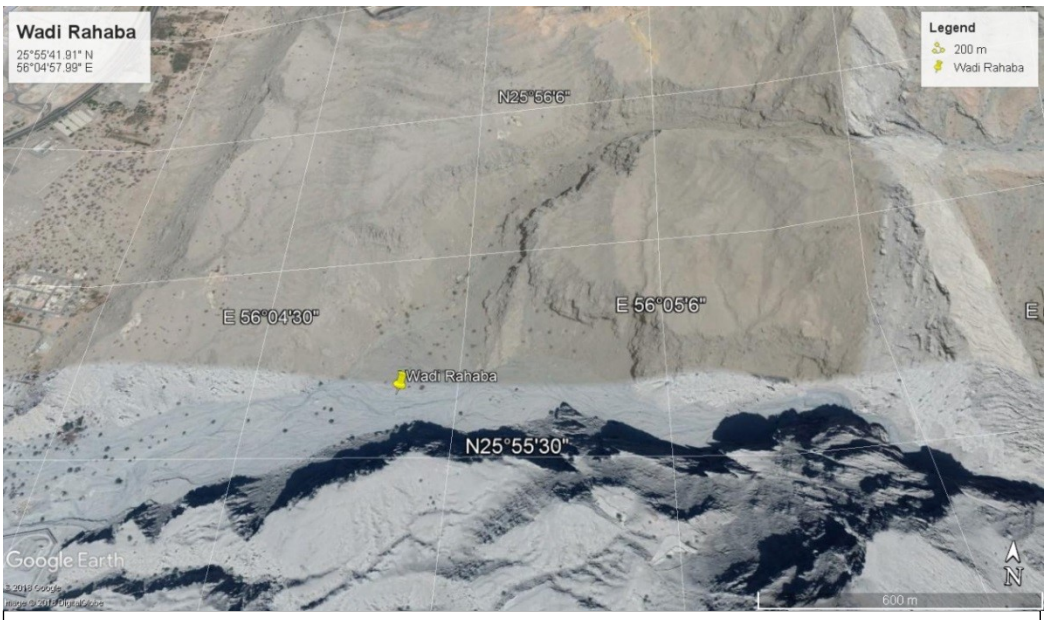

Figure 5.1: Satellite image for Wadi Rahaba in Ras Al Khaimah, Northern UAE.

West-verging thrust sheets are exposed in the Musandam mountains, which are formed of shallow water carbonates of the Permian to Mesozoic (Maurer et al., 2008). The evolution of fractures in this area can be related to tectonic and structural movement. On a large scale, three tectono-stratigraphic units are present (Callot et al, 2010): foreland autochthon in the Precambrian to Lower Cretaceous, a frontal triangle zone of Neogene units and the Dibba zone which consists of Hawasina units (Triassic to Cretaceous), and the Sumeini units (Lower to Middle Cretaceous). On a local scale, Marrei, (1978), Callot et al. (2013), and Searle et al. (2014) noted three main faults that affects the Musandam peninsula: the Hagab thrust, the Dibba normal fault, and the Semail thrust (Fig. 5.2).

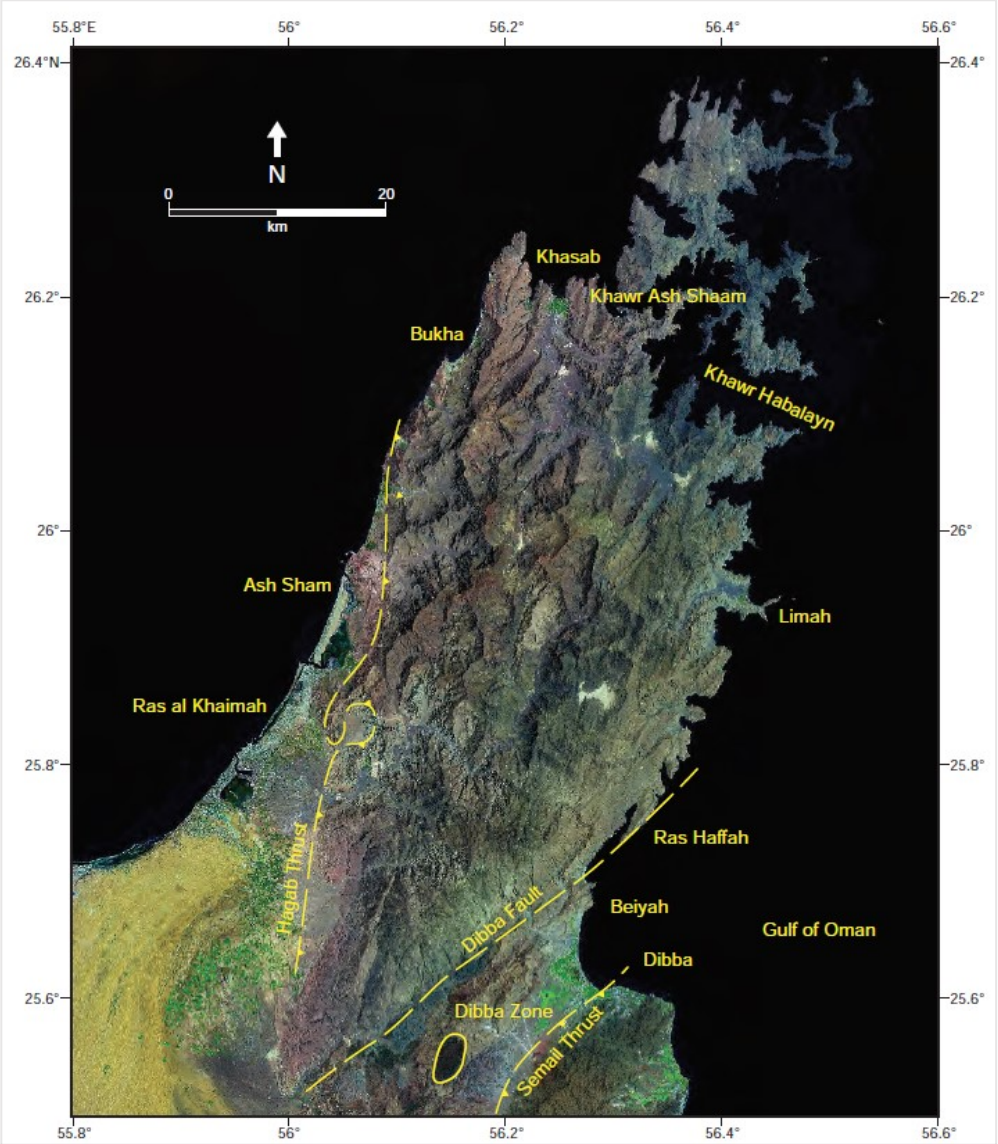

Figure 5.2. Three main faults affecting the Musandam Peninsula, the Hagab thrust, the Dibba normal fault and the Semail Thrust (Searle et al., 2014).

Elmahdy and Mohamed (2013) used remote sensing techniques to map the fractures in the Musandam Pennesula for the first time, for groundwater study. However, the mapped area was in Wadi Bih and there were no mention of the fracture orientation, as the main concentration was on faults. Most of the studies in the Musandam Peninsula concentrated on mapping faults, with rare studies done specifically on associated fracture orientations. Breesch et al. (2009) classified fractures from Late Triassic and Early Cretaceous age strata in the hanging wall and footwall of

Cenozoic fault in Wadi Ghalilah. He distinguished 3 main fracture generations in the hanging wall: 1) H_1: strikes N40W to N50W with nearly vertical angles or steeply northwards dipping. 2) H_2: strikes N20W over NS to N20E with steep dips of 70° to the west to nearly vertical. 3) H_3: strikes N30E to N50E and N80E, 60–70° dipping to the north. Five fracture orientations were noted in the footwall, 1) F_1: N20E and N70E with 60–70° dips to the east. 2) F_2: N20W to N45W with dips from 40° to 70° eastwards. 3) F_3: NS and N10E, dip: 60–80° to the east. 4) F_4: N45W70N. 5) F_5: strikes N70W and N80E, dips: 60° to vertical.

There have been no studies on fracture orientations in Wadi Rahaba.

5.3 Objectives

1- To compare between Upper Thamama Reservoirs (A, B and C) in the subsurface and outcrop. The comparison aims to include:

- Number of fracture generations
- Nature/state of fractures (open, cemented, partially cemented)
- Type of cement in fractures
- Changes in precipitation temperature from $^{m}Mg/^{m}Ca$
- Whether fluids were oxidizing or reducing from Mn and Fe concentrations, or from closed versus open systems using Sr/Ca

2- To measure fracture orientations in order to link them to the regional tectonics of the area

3- To trace fracture fluid evolution through the reservoirs.

5.4 Materials and methods

Wadi Rahaba was visited to undertake fracture observations and sample collection. The main logged information via three transects was:

1- The layers numbers and description (equivalent reservoirs)
2- General strike and dip

3- Fracture sets and state: open, cemented or partially cemented
4- Fracture orientations, dips and cross cutting relationships
5- Samples of cemented fractures in each layer.

Tables 5.1 to5.3 provide a description of the Wadi Rahaba beds and samples. Three transects were made to log the beds. Transect 1 included Reservoirs B and C, transects 2 included the rest of Reservoir B and transect 3 included Hawar and Shuaibah. Fifteen highly polished thin sections were prepared from sixteen field samples.

Six doubly polished thin sections were carbon coated and analysed in a Cameca SX100 instrument for EPMA analysis. The elements (Mg, Ca, Sr, O, Mn and Fe) were analysed. Instrument calibration is carried out by analysing reference materials (calcite) with known compositions. Routine detection limits are in the order of 0.009 to 0.05 wt %. $^{m}Mg/^{m}Ca$ was converted to molar ratio, and Sr/Ca data are presented as a ratio.

Exposed bedding plane surfaces for sought to obtain fracture density. Visible geology Stereonet program was used for plotting fracture orientations.

All data are given in Appendix 3.

Thamama Formation layers in Wadi Rahaba			
Transect 1: Reservoirs C & B			
Bed #	Thickness (m)	Rock Type	Comments
1	0.5	Packstone	-Grey-brown -2 fracture generations -Dense C -Sample 1/1
2	0.55	Packstone	-Rubbly and nodular -Heavily borrowed -Wavy contact between 2&3 -Sample 1/2
3	0.2-0.3	Packstone	-Well cemented corals -Sample 1/3
4	0.25	Packstone	-Heavily borrowed large Thallasinoides -Cemented oysters -Hardground, pigmented -Sample 1/4
5	1.1	Mudstone	-C dense, MFS -Recessive shaly marl -Sample 1/5
6	2.45	Packstone	-Reservoir C -Well cemented borrows -Pockets of grainy material; borrows -Highly cemented & open fractures, 3 orientations -Isolated Rudists -Recessive from top -Sample 1/6
7	1.4	Packstone	-Reservoir C -Recessive -Multiple horizontal stylolites -Sample 1/7
8	2.3	Packstone	-Dense B -Recessive -Grainy pockets -Multipe fill of cemented fractures -Sample 1/8
9	2.2	Packstone	-Reservoir B -Coarser grains -Burrowed top surface, firm ground going to hardground -Thallasinoides -Sample/1/9
10	0.1-0.2		-TST -Argillaceous -No sample
11	1.45	Packstone	-Reservoir B -Few corals -Massive well cemented packstone with dolomite burrows -Sample 1/11
12	0.5-0.6	Boundstone	-Dolomitized burrows -In-situ Rudists -Hardgrounds with Rudists -1/12 (2 Samples)
13	0.15-0.2		-Recessive -Argillaceous -Sample 1/13

Table 5.1 A: Wadi Rahaba layers log. Transect 1 Reservoirs C & B. Beds (1-13)

Thamama Formation layers in Wadi Rahaba			
Transect 1: Reservoirs C & B			
Bed #	Thickness (m)	Rock Type	Comments
14	1.7	Packstone	-Recessive bed in the middle getting grainy on top -Hardgrounnd
15	0.5		-Very recessive, rubbly -Ostracod
16	0.85	Packstone	-Sample 1/16
17	0.1		-Recessive -Sample 1/17
18	1.2	Packstone	-Lots of bivalves and Gastropods -Sample 1/18
19	0.25		-Recessive -Sample 1/19
20	0.85	Packstone	-Massive, well cemented dolomitized burrows on top, hardground -Mud rich -Sample 1/20
21	0.1		-Recessive -Lots of bedding, parallel cemented veins
22	2.2		-Dolomite filling burrows -Muddy
23	5.3	Packstone	-Recessive -Multiple decimetre layers -Mud rich packstone -Deepening upwards 2 samples 1/23
24	0.4		-Dolomite marker bed 1 -Grainy, burrows
25	6	Floatstone	-Full of floating Rudists and bivalve fragments -Massive layer -Full of coated bivalves -Sample 1/25
26	1.22		-Dolomite marker bed 2 -Grainy -Well cemented -Dolomitized burrows

Table 5.1 B: Wadi Rahaba layers log. Transect 1 Reservoirs C & B. Beds (14-26)

Thamama Formation layers in Wadi Rahaba			
Transect 2: Reservoir B			
Bed #	Thickness (m)	Rock Type	Comments
2/1	0.75	Mudstone	-Starting at the top of the 2nd dolomite layer -Smells like sulphur, organic rich? -Black, organic rich -Sample 2/1
2/2	1.9	Grainstone	-Very grainy, shallower than the bed above -Washed away mud, shoal? -Sample 2/2
2/3	15	Grainstone	-Very grainy -Shallowest sample in the whole succession -Low angle cross-bedding -Sample taken 1m above bed -Sample 2/3
2/4	0.9		-Third dolomite layer -Bioturbation, preferentially dolomitized burrows -Sample 1/4 (2 samples)
2/5	8	Mudstone	-Very fine grained limestone -Muddy and black -Sample taken 1m below bed top -Sample 2/5

Table 5.2: Wadi Rahaba layers log. Transect 2 Reservoir B. Beds (2/1-2/5)

Thamama Formation layers in Wadi Rahaba			
Transect 3: Hawar & Shuaiba			
Bed #	Thickness (m)	Rock Type	Comments
3/1	10	Wack-Packstone	-Dark -Very layery, 5 cycles -Sample 3/1A taken from the bottom of the 1st cycle -Sample 3/1B taken from the mid of the 4th cycle
3/2	3.25	Wack-Packstone	-Grainy comparing to the above bed -Top of Hawar -13.25m below Shuaiba base -Sample 3/2
3/3	3.1	Packstone	-Full of Rudists and corals -Sample 3/3 was taken at 14.5m from the base of transect 3
3/4	9.6	Packstone	-1.6m below the top there's a 0.6m thick dolomite bed -Top of the dolomitized burrowed bed is the beginning of new cycle -Sample 3/4A is taken from base -Sample 3/4B is taken from top
3/5	8	Wack-Packstone	-Sample 3/5 taken from top

Table 5.3: Wadi Rahaba layers log. Transect 2 Reservoir B. Beds (2/1-2/5)

5.4 Results

Thamama C has smallest exposed bedding plane surface of ~6.55 m^2 (Fig. 5.3C). A. Thamama B has the largest bedding plane surface exposure extending to ~138.3 m^2 (Fig. 5.3B). Thamama A dense with Hawar together extend to a bedding plane surface ~33.9 m^2 (Fig. 5.3A).

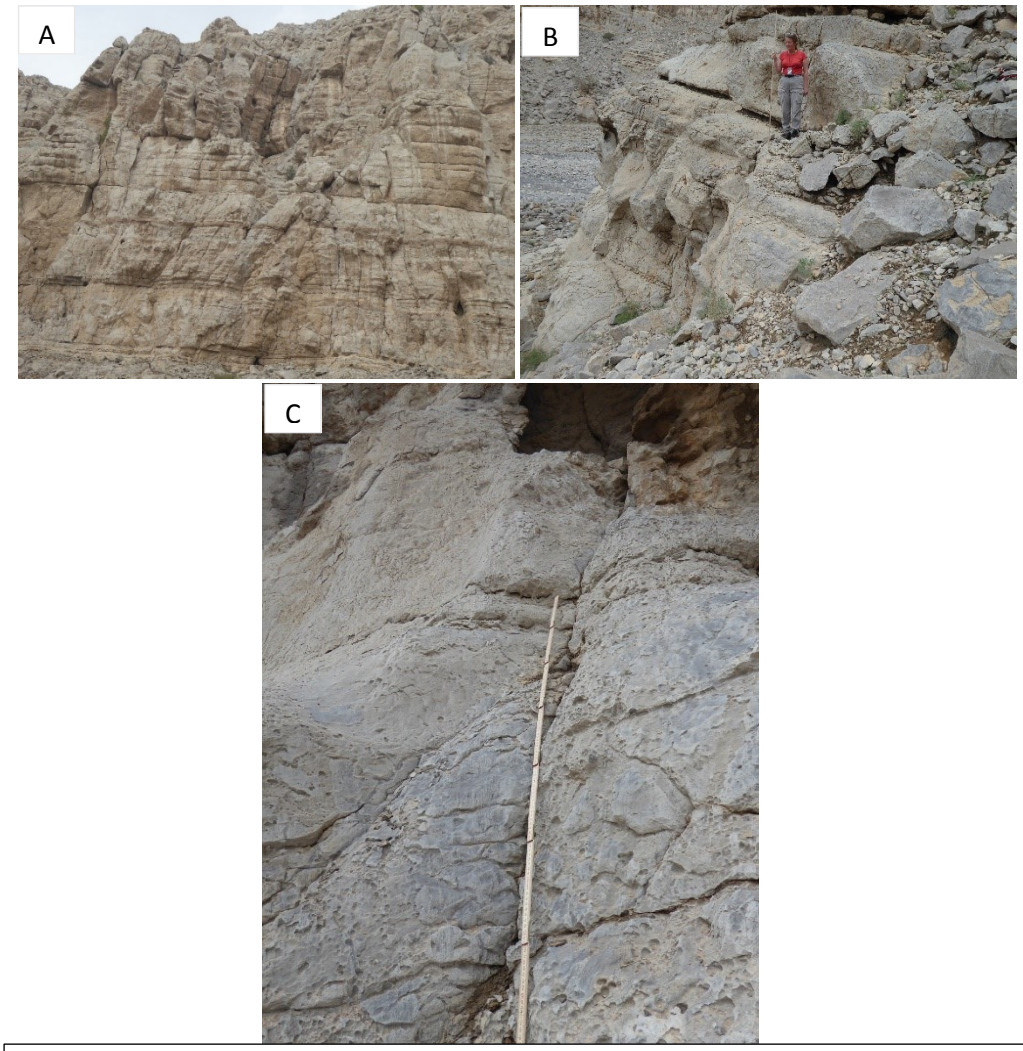

Figure 5.3. Thamama exposures in Wadi Rahaba. A: Thamama C. B: Thamama B. C: Thamama Top Hawar and Dense A.

The number of fractures measured number and types are shown in Table 5.4 following Thamama Reservoir stratigraphy. Abundant fractures were observed in all Thamama reservoirs. Most fractures measured are from Thamama C (192), followed by Thamama A dense (87), and 56 from Thamama B.

Reservoir	Bed	Fracture type					
		Cemented	Open	Partially cemented	Conjugate	En echelon	Cross cutting
C	9	20	19	4			3
	11	5	2	0			
	12	21	4	6			
	18	16	3	1			
	20	24	1	0			
	22	40	3	0			
	23	23	0	0			
B	24 dolomite	4	2	1			
	25	18	1	4	5		
	26	0	5	0			
	2/3	1	3	2			
	2/4	3	1	0			
	2/5	6	0	0		3	
A	4	35	0	0			
		49	3	0		4	

Table 5.4: Fractures numbers and types in Wadi Rahaba

5.4.1 Fracture orientations and dips

Fractures orientations were plotted for each reservoir. Cemented and partially cemented from open fractures for also separated for each individual reservoir.

Reservoir C

The range of orientation is narrow, where the mean direction for cemented and partially cemented fractures is 136.9°, and for the open fractures is 116.7° (Fig. 5.4).

The dip orientation of the fractures was 30°-54°.

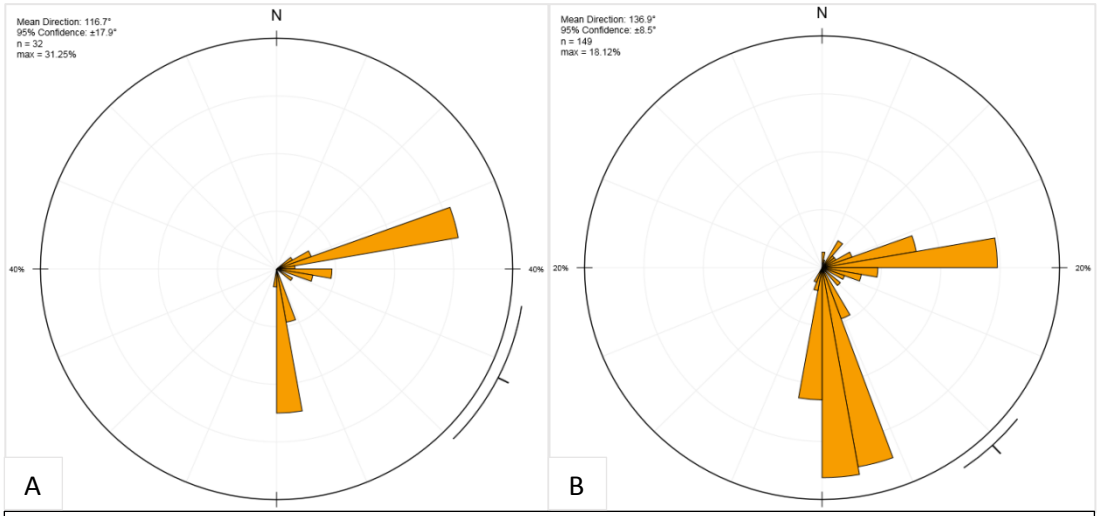

Figure 5.4. Fractures orientations on Reservoir C in Wadi Rahaba. A: Cemented and partially cemented. B: Open

Reservoir B

The range is broad from 30° to 208°, where the mean direction for cemented and partially cemented fractures is 117.3°, and for the open fractures is 95.2 (Fig. 5.5).

The dip orientation of the fractures was 45° and 90°.

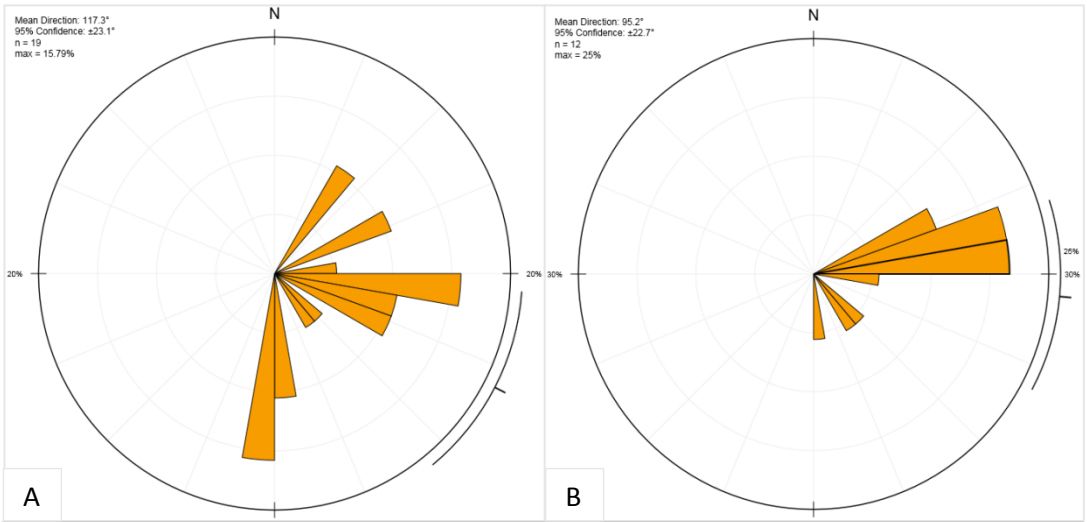

Figure 5.5. Fractures orientations on Reservoir B in Wadi Rahaba. A: Cemented and partially cemented. B: Open

Reservoir A

The range is broad from 32°- 208°, where the mean direction for cemented and partially cemented fractures is 127.1°, and for the open fractures is 156.5° (Fig. 5.6).

The dip orientation of the fractures was 45° and 90°.

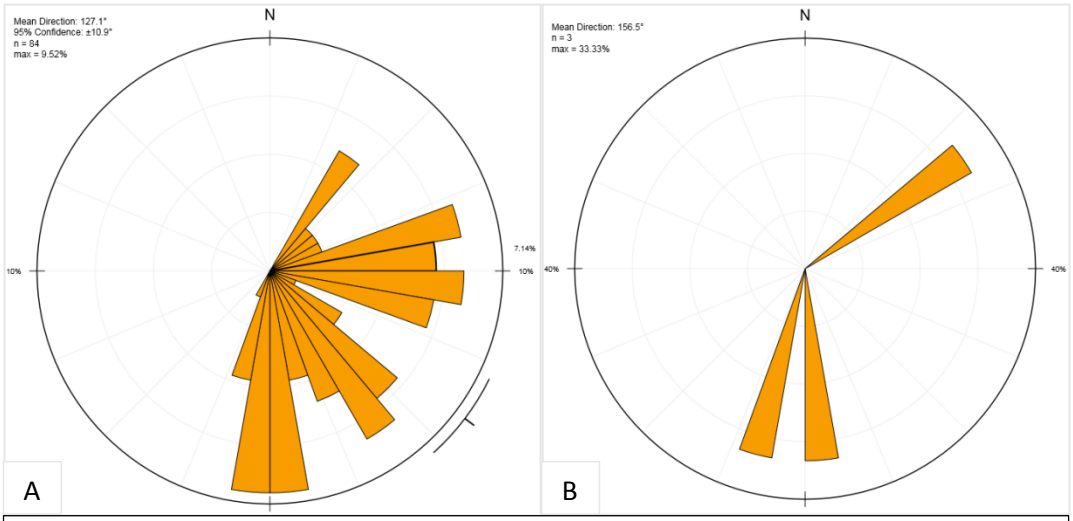

Figure 5.6. Fractures orientations on Reservoir A in Wadi Rahaba. A: Cemented and partially cemented. B: Open

5.4.2 Fractures strike and dip

Strike and dip data measured for Reservoir C are shown in Figure (5.7).

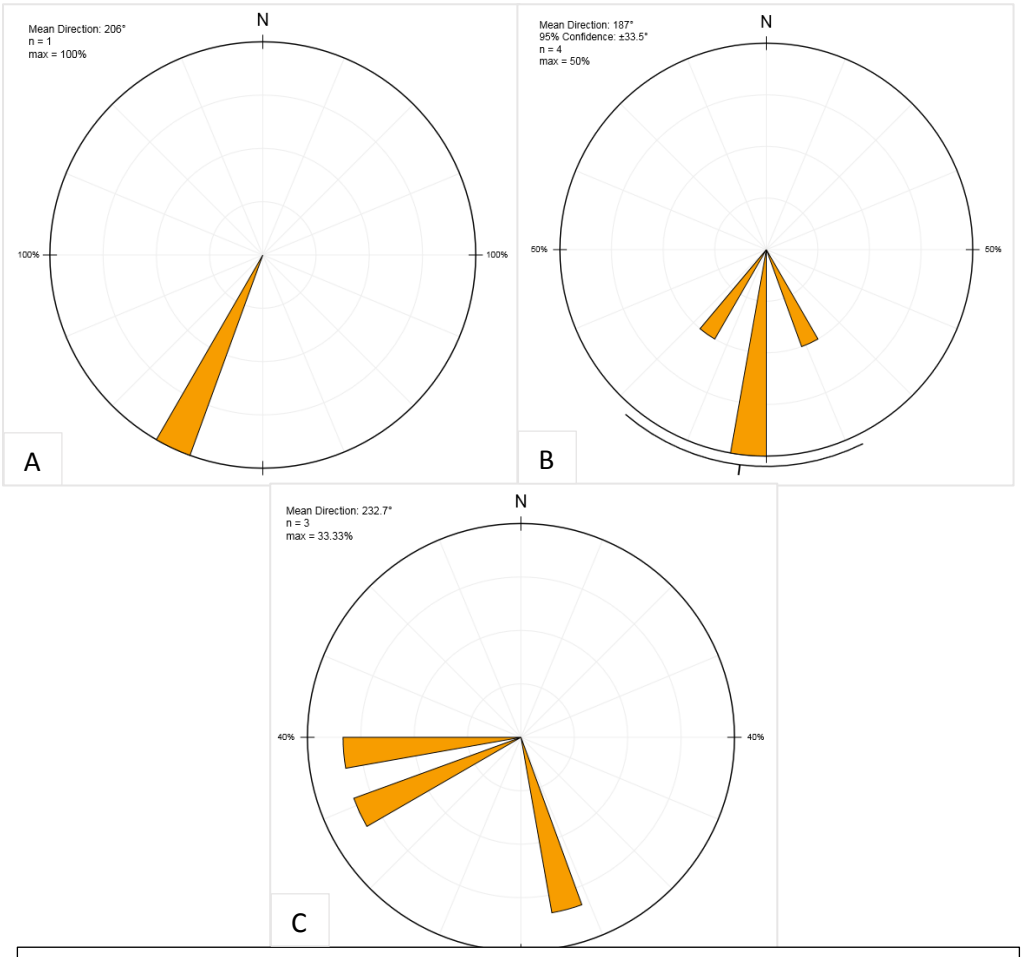

Figure 5.7. Fractures strike and dip data in Reservoir C in Wadi Rahaba. A: F1. B: F2. C: third minor fracture set

5.4.3 Fractures sets and orientation

There were two main fracture sets measured in Wadi Rahaba, and they will be referred to as F1 and F2. Orientation and dips are summarised in Table. 5.5. Both fracture sets F1 and F2 are cemented.

Fracture Sets in Wadi Rahaba						
	Reservoir C		Reservoir B		Reservoir A	
Fracture set	F1	F2	F1	F2	F1	F2
Dip	30°-35°	Vertical	45°	Vertical	Horizontal	Vertical
Orientation	49° NE	90°-105°E	100° NE	20° NS	94°NE	162°-172°
Cemented	Yes	Yes	Yes	Yes	Yes	Yes

Table 5.5. Fractures sets in the Thamama Group, Wadi Rahaba

The main dominant direction for F1 is NS and EW for F2 (Fig. 5.8).

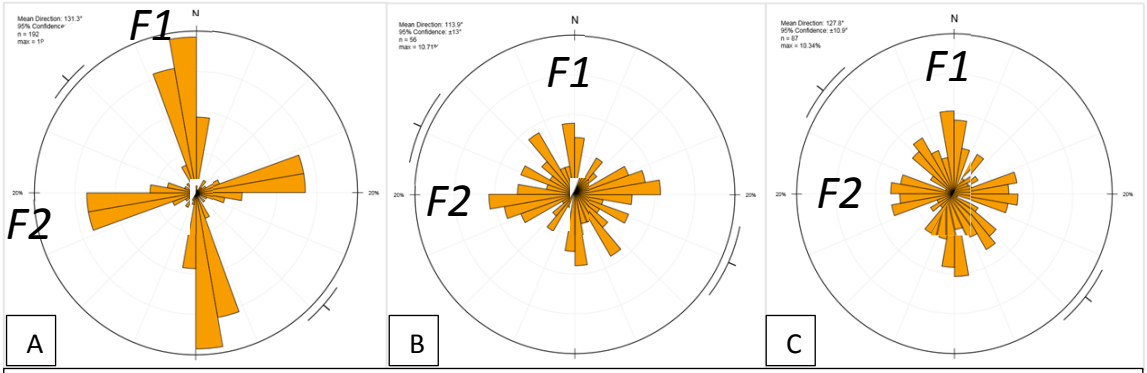

Figure 5.8. Two main fracture sets in Wadi Rahaba F1 & F2. A: Thamama C. B: Thamama B. C: Thamama A.

The oldest fracture set observed in the outcrop is F1, striking N25E in Thamama B (Fig. 5.9A). En-echelon fractures represented F1 in Thamama A and there was noticeable extension throughout the layers (Fig. 5.9B). En-echelon fractures also appeared in Thamama B (Fig. 5.9C). Crosscutting fracture sets appeared in all of the Thamama and they were clear in Thamama A (Fig. 5.9D) and Thamama B (Fig. 5.9E).

Figure 5.9. Fractures in the Thamama outcrop. A: oldest fracture set in Thamama B. B: En-echelon in Thamama B. C: En-echelon in Thamama A. D: Cross-cutting in Thamama A. E: Cross-cutting in Thamama B.

5.4.3 Petrographic analysis

The most dominant rock types in Wadi Rahaba are packstones, wack-packstones, mudstones, and in lesser amounts boundstone, floatstone and grainstone. There was an abundance of miliolid forams, *Thalassinoides* burrows, rudists and other molluscs, algae and corals.

The fracture cement was blocky calcite in all the studied samples. Rhombic dolomite appeared in the matrix of many samples, but no dolomite found in the fracture cement samples

Calcite cemented fractures were found cutting matrix rhombic dolomite in some samples (Fig. 5.10A), and cutting fossils in few other samples (Fig. 5.10B). Open fractures were also found cutting through rhombic dolomite matrix (Fig. 5.10C) as well as cross-cutting other cemented fractures (Fig. 5.10D). There were cross-cutting fractures in all of the reservoirs (Fig. 5.10E) and fractures truncated by stylolites (Fig. 5.10F).

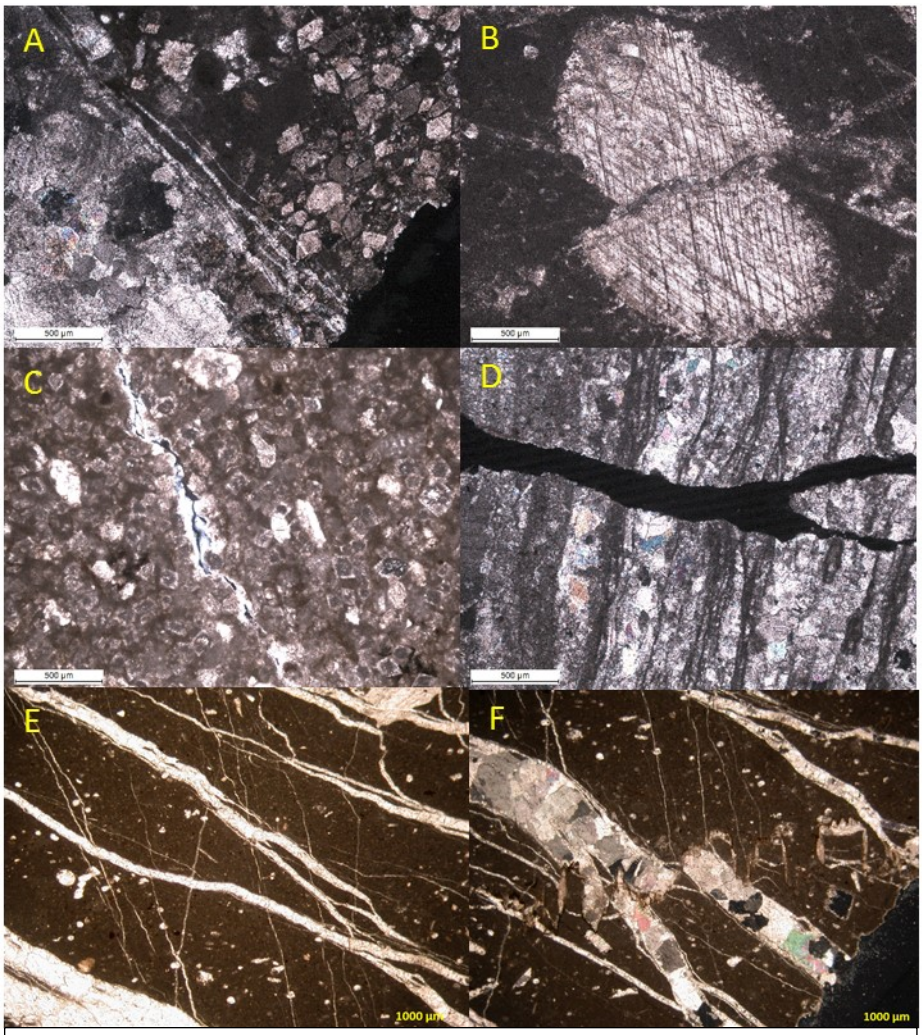

Figure 5.10. Fractures in the Thamama outcrop. A: Cemented fractures cutting dolomite in Thamama C. B: Fractures cutting a fossil in Thamama A. C: Partially-cemented fracture cutting dolomite in Thamama C. D: Open fracture in Thamama B. E: Cross-cutting fractures in Thamama A. F: Fractures cut by stylolites in Thamama A.

The paragenetic sequence for Thamama in Wadi Rahaba is illustrated in Figure 5.11, showing the most important diagenetic and fracturing events.

The two main fracture sets (F1 and F2) formed early in the diagenetic history, while the third set of fractures (following the trend of F1), which is absent in most of the Thamama happened far later, possibly due to uplift. The first set of fractures (F1, en-echelon) started to form early after the dissolution event. F2 was cemented, and followed by the burial stylolization.

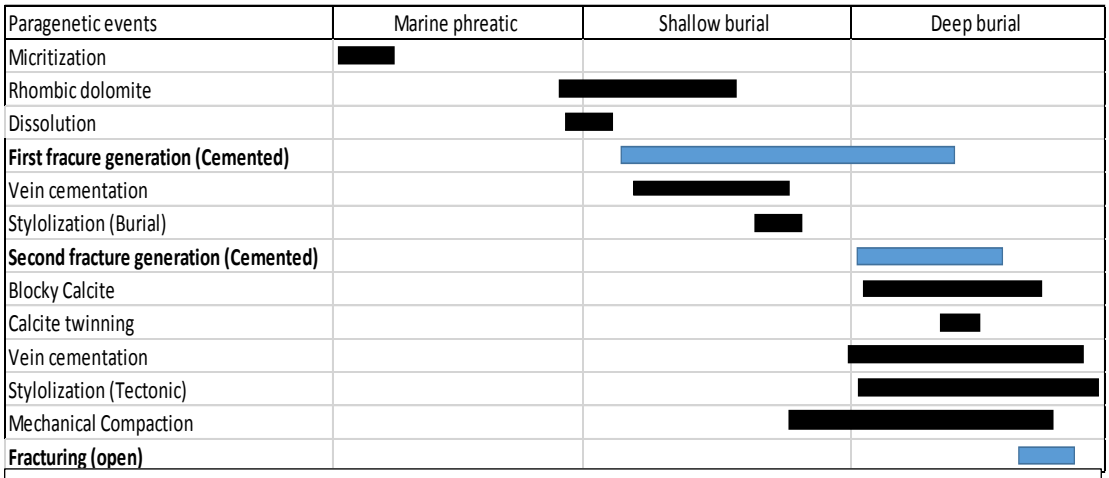

Figure 5.11. Paragenetic sequence of the Thamama in Wadi Rahaba

5.4.4. Cathodoluminescence analysis

CL analysis revealed significant number of cement zones in the fracture calcite cements of field samples.

In all Thamama reservoirs, the fracture cement zones start with dark or medium-dark cement zone. Thamama C has 15 cement zones (Figs. 5.12 and 5.13), and Thamama B (Fig. 5.14) and A (Fig. 5.15) have 7 cement zones (Table 5.6).

Cement zones	Thamama C	Thamama B	Thamama A
1	Dark red	Medium dark red	Medium dark red
2	Bright red	Medium bright red	Medium bright red
3	Medium red	Medium dark red	Medium dark red
4	Bright red	Medium red	Medium red
5	Medium red	Medium dark red	Medium dark red
6	Bright red	Medium red	Medium bright red
7	Medium red	Medium bright red	Medium dark red
8	Bright red		
9	Medium red		
10	**Thin layers of bright and dark red**		
11	Medium red		
12	Bright red		
13	Medium red		
14	Bright red		
15	Medium red		

Table 5.6. Calcite cement zones in F1 and F2 fractures of Thamama of Wadi Rahaba.

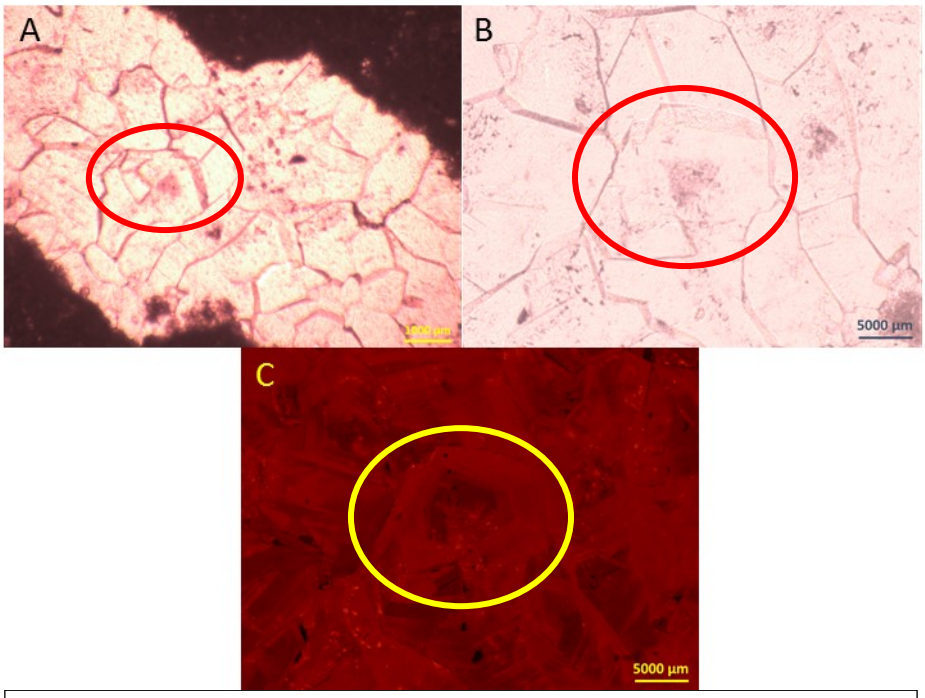

Figure 5.12. CL in Thamama C. A: PPL in highly polished thin section. B: PPL in CL microscope. C: CL showing cement zones. Circles showing the same crystal

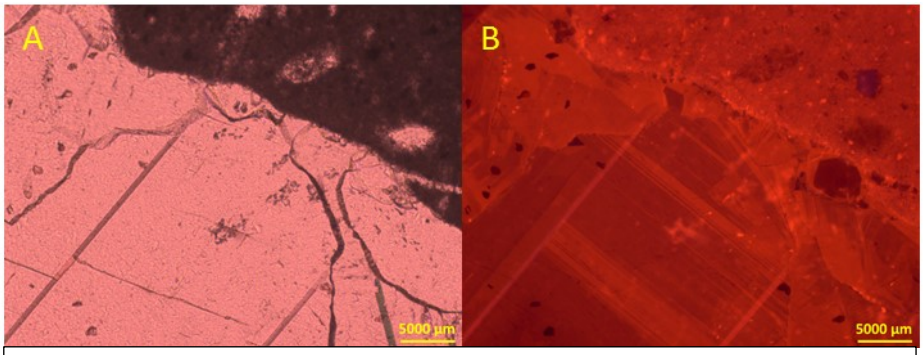

Figure 5.13. CL in Thamama C. A: PPL in CL microscope. B: CL showing cement zones including cement zone 10 (thin layers).

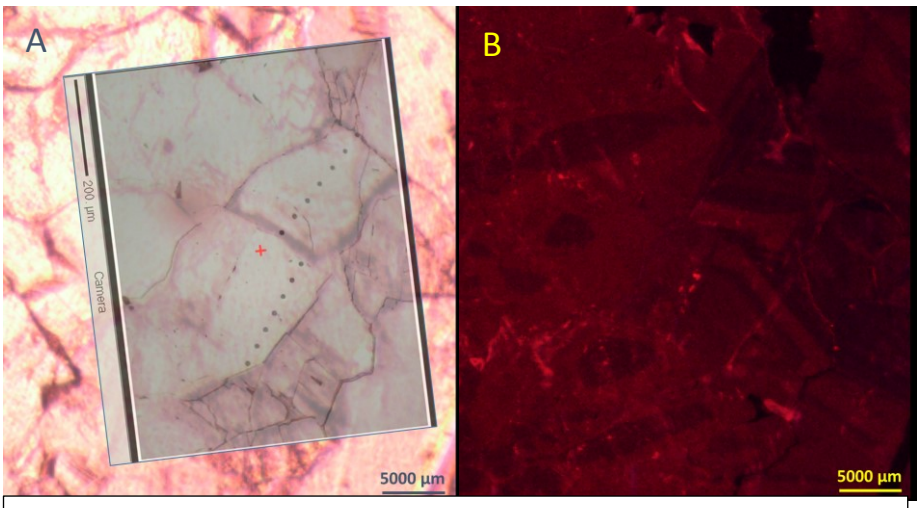

Figure 5.14. CL in Thamama B. A: PPL in CL microscope with superimposed EMPA image. B: CL showing cement zones.

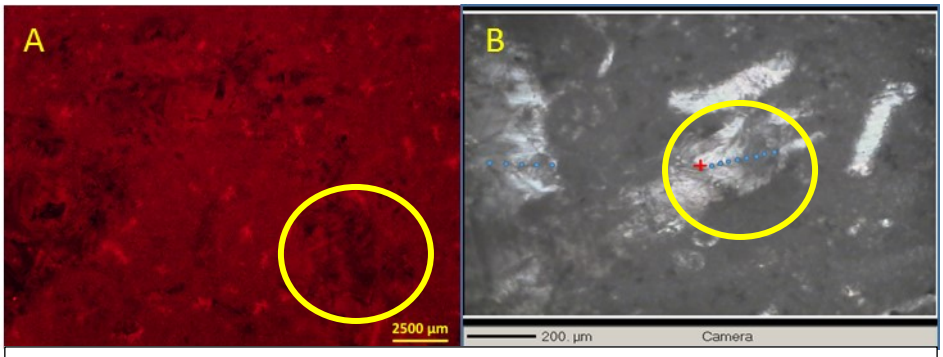

Figure 5.15. CL in Thamama A. A: CL showing cement zones in fracture. B: EMPA image for the same fracture. Circles showing the same crystal

5.4.5 EPMA analysis

^{m}Mg/^{m}Ca, Sr/C, Mn, Fe

Thamama C:

Fig. 5.16A shows the distribution of ^{m}Mg/^{m}Ca values of Thamama C blocky calcite fracture cement in Wadi Rahaba. The mean ratio ranges from 0.4 to 0.9 for all the 15

CL cement zones. The highest mean value is at cement zone 6 (0.9) and lowest is at cement zone 13 (0.4).

The Sr/Ca ratio ranges from means of 0.0064 to 0.027 for all the 15 cement zones (Fig. 5.16B). The highest value is at cement zone 7 (0.0064) and lowest is at cement zone 14 (0.0064).

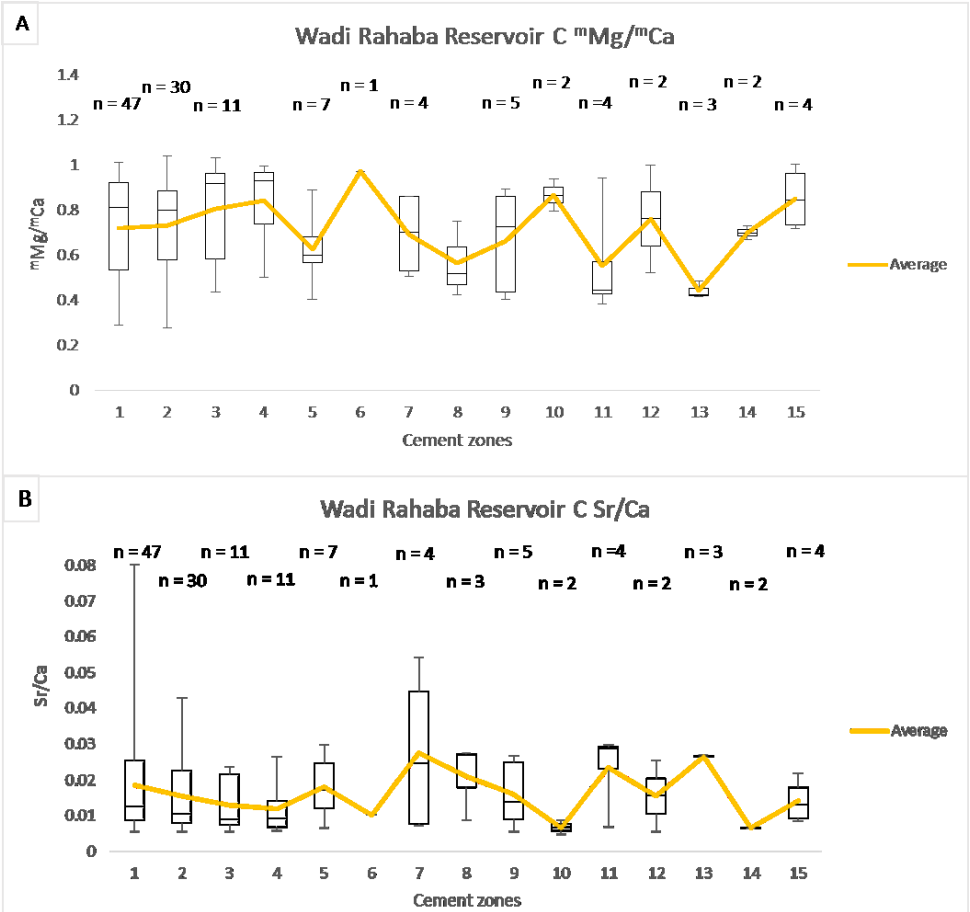

Figure 5.16. Box and whisker plots for ᵐMg/ᵐCa, and Sr/Ca data for each CL cement zone from Fractures in Thamama C in Wadi Rahaba. A: ᵐMg/ᵐCa. B: Sr/Ca. n = number of data points. The yellow lines trace the mean.

Fig. 5.17A shows the Mn ppm values, where they range from 89 ppm in cement zone 6 to 246.7 in cement zone 15. Fe ppm values range between 16 ppm in cement zone 11 to 3638 ppm in cement zone 6 (Fig. 5.17B). The single data point for cement zone 6 is an outlier and appear to be ferroan calcite.

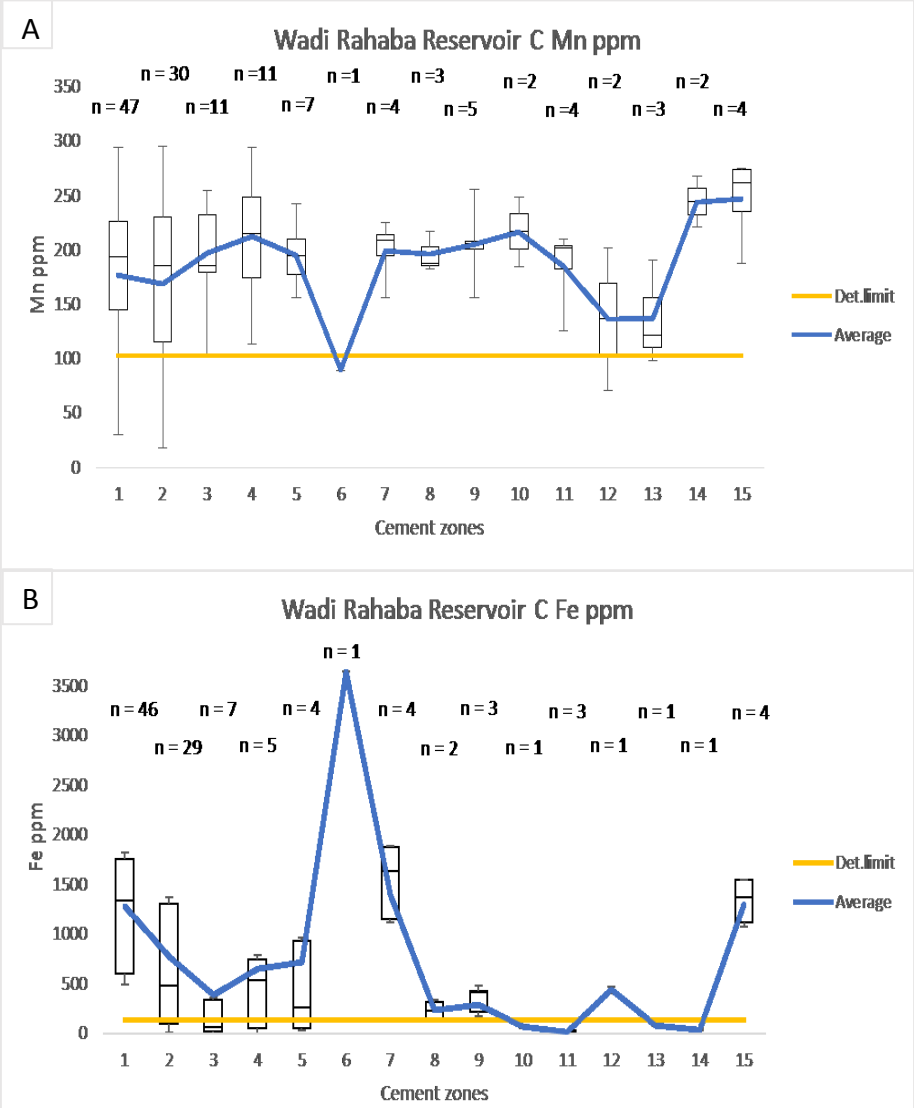

Figure 5.17. Box and whisker plots for Mn ppm and Fe ppm data for each CL cement zone from Fractures in Thamama C in Wadi Rahaba. A: Mn ppm. B: Fe ppm. n = number of data points. The blue lines trace the mean. The straight yellow line is the detection limit.

Thamama B:

Fig. 5.18A illustrates the $^{m}Mg/^{m}Ca$ of Blocky calcite cement of Thamama B fractures In Wadi Rahaba. The mean $^{m}Mg/^{m}Ca$ ratio ranges from 0.1 to 0.3 for all the 7 cement zones. The highest value is at cement zone 1 (0.3) and lowest is at cement zone 7 (0.1).

The Sr/Ca ratio is given in Fig. 5.18B. The mean ratio ranges from 0.0034 to 0.010 for all the 7 cement zones. The highest value is at cement zone 1 (0.0034) and lowest is at cement zone 5 (0.010). All Mn ppm and Fe ppm values were below detection limit (Fig. 5.18C, D).

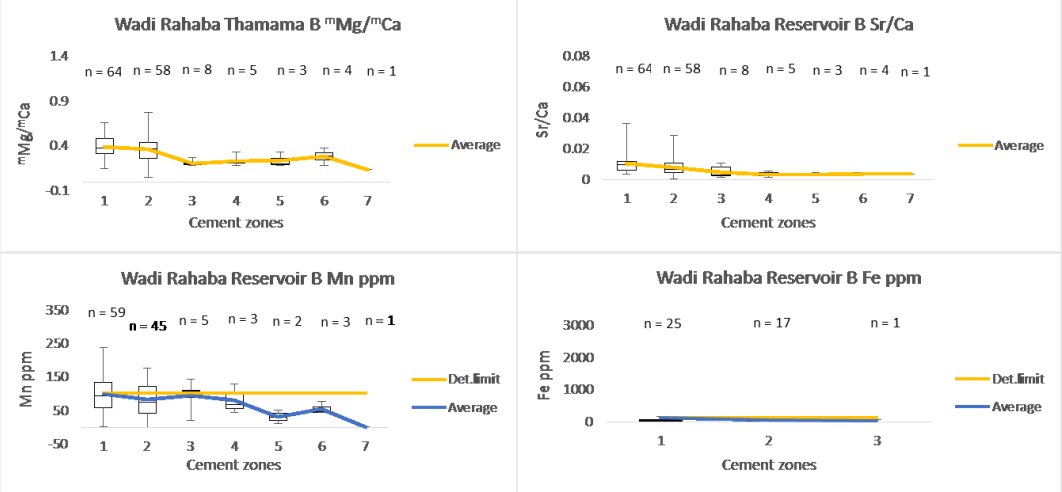

Figure 5.18. Box and whisker plots for $^{m}Mg/^{m}Ca$, Sr/Ca, Mn ppm and Fe ppm data for each CL cement zone from Fractures in Thamama B in Wadi Rahaba. A: $^{m}Mg/^{m}Ca$. B: Sr/Ca. C: Mn ppm. D: Fe ppm. n = number of data points. The yellow and blue lines trace the mean. The straight yellow line is the detection limit.

Thamama A:

Fig. 5.19A shows the trend of $^{m}Mg/^{m}Ca$ values of Thamama A for blocky calcite cement in fractures of Wadi Rahaba. The mean ratio ranges from 0.3 to 0.6 for all the 7 cement zones. The highest mean value is at cement zone 6 (0.6) and lowest is at cement zone 7 (0.3).

The Sr/Ca ratio ranges from about 0.002 to 0.007 for the 7 cement zones (Fig. 5.19B). The highest value is at cement zone 2 (0.007) and lowest is at cement zone 6 (0.002).

The lowest Mn value appears in cement zone 4 (95.2 ppm) and the highest Mn value is in cement zone 1 (138.9 ppm) (Fig. 5.19C). All Fe ppm values are below detection limit (Fig. 5.19D).

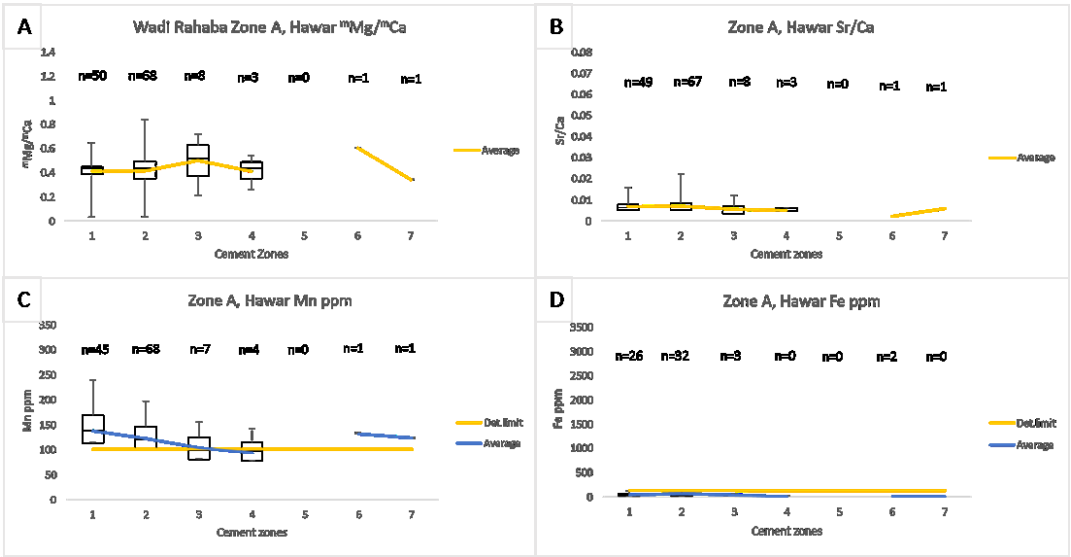

Figure 5.19. Box and whisker plots for $^{m}Mg/^{m}Ca$, Sr/Ca, Mn ppm and Fe ppm data for each CL cement zone from Fractures in Thamama A in Wadi Rahaba. A: $^{m}Mg/^{m}Ca$. B: Sr/Ca. C: Mn ppm. D: Fe ppm. n = number of data points. The yellow and blue lines trace the mean. The straight yellow line is the detection limit.

5.5 Discussion

5.5.1 Outcrop fracture evolution

The outcrop in Wadi Rahaba has two main sets of fractures:

1- F1, cemented with blocky calcite and trending NS, dipping 45°
2- F2, cemented with blocky calcite and trending EW, dipping 90°

There was a third set of fractures (open), but this has not been added to the main sets of fractures because it did not appear in all reservoirs.

Both fracture sets F1 and F2 are most probably following the fracture systems within the Cretaceous in onshore and offshore Abu Dhabi. F1, is related to the NS orientation fracture system consistent with the Arabian Trend sets. That NS orientation fracture system is caused by Cenozoic compression (Breesch et al., 2011). F2 is related to the EW orientation fracture system matching Tethyan extensional trend sets (Morad et al, 2010). The third fracture set follows the orientation of F1, which is NS, and it might be reactivation caused by uplift.

5.5.2 Elemental analysis

^{m}Mg/^{m}Ca

The general ^{m}Mg/^{m}Ca values vary in each reservoir. Thamama C shows a range of ~0.4-0.9, Thamama B ~0.1-0.3, and Thamama A ~0.3-0.6. This might infer that Thamama B precipitated at overall higher temperatures than Thamama A and C. The ^{m}Mg/^{m}Ca values show minor fluctuations in Thamama C, which are inferred to be caused by temperature variations. Temperature is inferred to decrease gradually from cement zone 1 to cement zone 4, elevate at cement zone 5 then drops again at cement zone 6 to record the lowest temperature in the whole section, but it might be an artifact. The value rises again in zones 7 and 8 to drop back at zones 9 and 10. A rapid rise and decline again follows for the rest of cement zones, where the peaks occur in cement zones 11 and 13 and the lowest values in cement zones 12 and 15.

In Thamama B, the ^{m}Mg/^{m}Ca values were less variable than in Thamama C. There was a gradual increase in the temperature from cement zone 1 to cement zone 3, followed by a gradual decrease through zones 4, 5 and 6, to increase again towards cement zone 7.

The ^{m}Mg/^{m}Ca values started to increase in the first 3 cement zones of Thamama A as in Thamama C, suggesting a gradual decrease in the temperature. The temperature increased in cement zone 4 and increased again from cement zone 6 to cement zone 7.

The presence of matrix dolomite might aid in decreasing ^{m}Mg/^{m}Ca due to Mg-Ca exchange (Coggon et al., 2010), and this might be the case in Thamama B which is dolomitised and has the lowest overall ^{m}Mg/^{m}Ca values.

Sr/Ca

The overall values of Sr/Ca in Thamama C were low indicating a burial environment (Hoseinabadi et al., 2016).

The mean Sr/ Ca for Thamama B and A was lower than that in Thamama C, which also suggests a burial environment and no exotic fluid addition to the diagenetic system (Neilson & Oxtoby, 2008).

Mn-Fe

The general Fe and Mn values vary in each reservoir. Thamama C shows a range of ~89-246.7 for Mn and ~16 –3638 for Fe, Thamama B ~1-100 for Mn and ~30 –131 for Fe, and Thamama A ~95-139 for Mn and ~37 –67 for Fe. This might infer that there were dramatic changes in redox during precipitation of the calcite cements.

Mn and Fe ppm values in Thamama C were the highest of the three reservoirs. Considering this fact in addition to the depletion of strontium, strongly supports precipitation in an anoxic burial environment (Huaguo et al., 2014).

In Thamama C, as oxidation is coupled with the reduction of Fe or Mn (Lovely, 1991), the fluid precipitation environment started to become more reducing from cement zone 1 to cement zone 3. A more oxidizing environment is inferred from cement zone 4 and changed to reducing in cement zone 6. The environment started to reduce again in cement zones 7 and 8, to become more oxic again in cement zone 9. The rest of cement zones (10, 11, 13, 14) precipitated in a reducing environment and cement zones 12 and 15 precipitated in a more oxidizing environment.

The very low amounts of Fe and Mn in Thamama B and A suggests an oxidizing environments in general.

5.5.3 Paragenetic sequence and the effect of tectonism on diagenesis

The two main fracture sets (F1 and F2) formed early in the diagenetic history, while the third set of fractures, which is absent in most of the Thamama outcrop happened later and were not cemented, probably as a result of uplift. The first set of fractures (F1 en-echelon) started to form early after the dissolution event, during the Cenozoic compression (Breesch et al., 2011). F2 formed during deep burial, probably due to tectonic movement in the area (Unspecified).

The first stylolization event formed during the shallow burial, and another set of stylolites formed later due to tectonic events, probably the Cenozoic compression (Breesch et al., 2011).

It is observed from the CL analysis that the blocky calcite in the outcrop has more cement zones than the subsurface blocky calcite. The reason might be related to the early dissolution event that predated the fractures filling, allowing the cement to grow uninterrupted by later dissolution events that were present in the subsurface only.

It worth mentioning that the oil charge in the area has no effective role in the diagenesis of the Thamama outcrop in Wadi Rahaba. Oil charge took place during the Late Cretaceous (Alsharhan, 1989; Nielson et al., 1998), and the uplift event that created the Thamama outcrop at Wadi Rahaba occurred during Late Cretaceous as well (Searle, 1988). The substantial amount of cement that was found in the Thamama outcrop fractures and matrix, as well as the absence of a bitumen phase does not support oil migration prior to uplift.

5.5.4 Comparison between outcrop and subsurface data

Table 5.7 shows a comparison between subsurface petrographic data from Abu Dhabi and the outcrop data from Wadi Rahaba in RAK.

	Subsurface	Outcrop
Fracture cement type	Equant, blocky calcite, saddle dolomite	Blocky calcite
Number of cement zones	4 in A 3 in B 1 in C	7 in A 7 in B 15 in C
Number of main fracture sets	3	2
Fractures trend	Not specified	F1: NS F2: EW
Fracture types	Cemented, partially cemented, open	Cemented, partially cemented, open

Table 5.7. Comparison between subsurface and outcrop Thamama fractures

The general $^{m}Mg/^{m}Ca$ values vary in each reservoir. Thamama C shows a range of ~0.4-0.9, Thamama B ~0.1-0.3, and Thamama A ~0.3-0.6. This might infer that Thamama C precipitated at overall lower temperatures than Thamama A and B. This agrees with subsurface $^{m}Mg/^{m}Ca$ values, where Thamama C shows a range of ~0.42-0.48, Thamama B ~0.14-0.072 and Thamama A ~0.37-0.45. This might infer that Thamama C precipitated at overall lower temperatures than Thamama A and B (Fig. 5.20).

A similar pattern of $^{m}Mg/^{m}Ca$ and Sr/Ca where the low Mg/Ca corresponds to high Sr/Ca is also present in the subsurface results (Fig. 5.21).

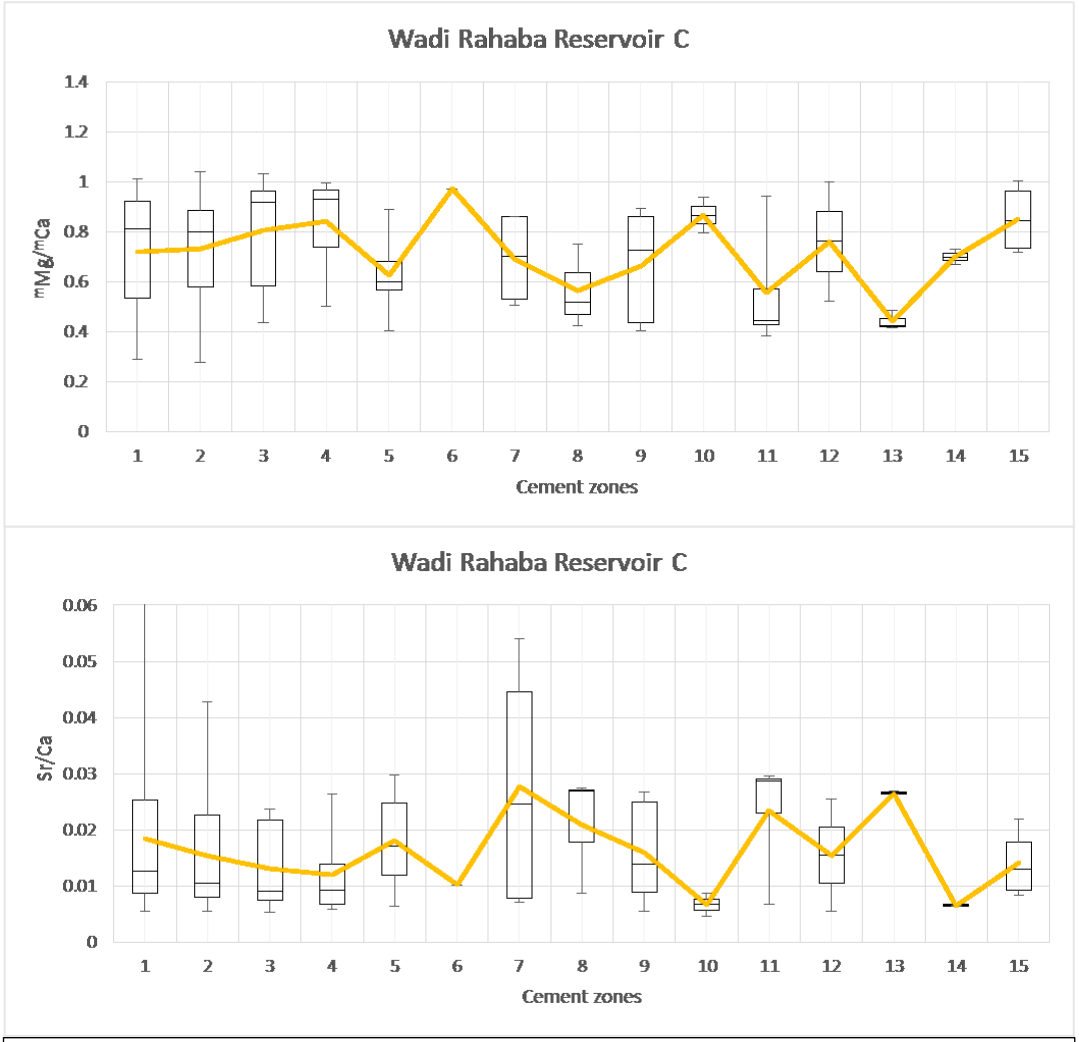

Figure 5.20. Pattern of a mirror trend in $^{m}Mg/^{m}Ca$ and Sr/Ca in Wadi Rahaba

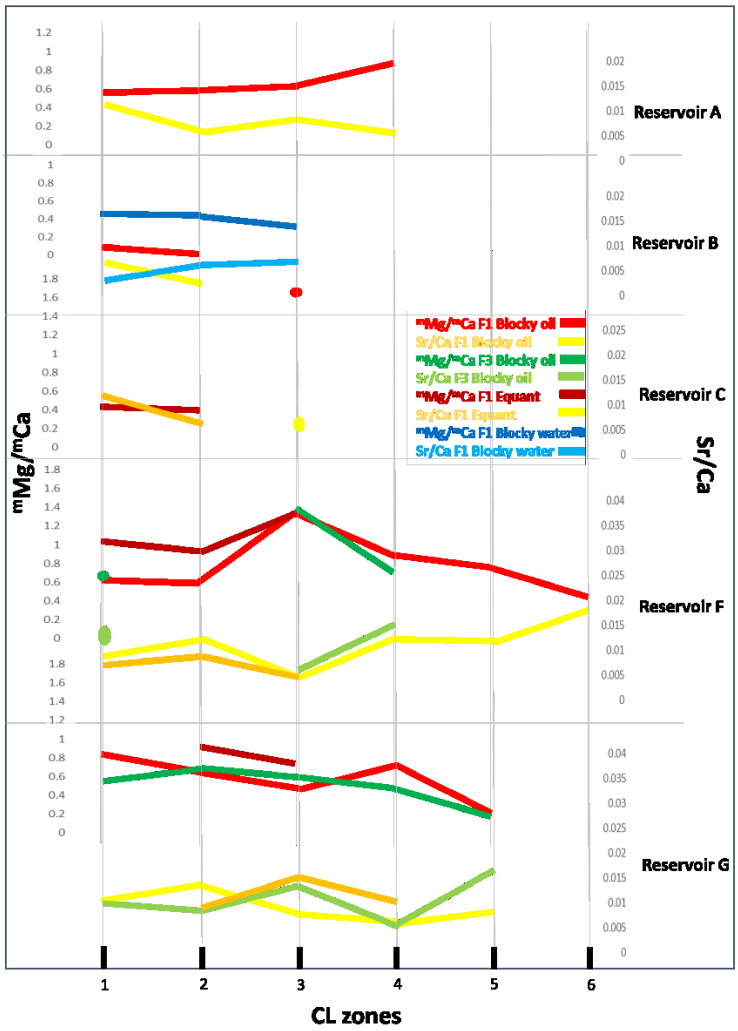

Figure 5.21. Pattern of reversing trend in $^{m}Mg/^{m}Ca$ and Sr/Ca in Subsurface data

5.6 Conclusions

- The outcrop in Wadi Rahaba has two main sets of fractures:

1- F1, cemented with blocky calcite and trending NS, dipping 45°

2- F2, cemented with blocky calcite and trending EW, dipping 90°

- Both fracture sets F1 and F2 are most probably following the fracture systems within the Cretaceous in onshore and offshore Abu Dhabi. F1, is related to the NS orientation fracture system consistent to the Arabian Trend sets

caused by Cenozoic compression. F2 is related to the EW orientation fracture system matching Tethyan extensional trend sets.

- A third open fracture set follows the orientation of F1 (NS), and may be created by reactivation caused by uplift.

- Fractures in the Thamama outcrop differ from the fractures of the Thamama subsurface in the cement type (blocky and equant calcite and saddle dolomite in the subsurface; blocky calcite in the outcrop), the number of cement zones (more in the outcrop than the subsurface) and the number of fracture sets (more in the subsurface than outcrop).

- The general $^{m}Mg/^{m}Ca$ values vary in each reservoir. Thamama C shows a range of ~0.4-0.9, Thamama B ~0.1-0.3, and Thamama A ~0.3-0.6. This might infer that Thamama B precipitated at overall higher temperatures than Thamama A and C.

- This agrees with subsurface $^{m}Mg/^{m}Ca$ values, where Thamama C shows a range of ~0.42-0.48, Thamama B ~0.14-0.072 and Thamama A ~0.37-0.45. This might infer that Thamama C precipitated at overall lower temperatures than Thamama A and B.

- Mn and Fe values were very low for the Upper Thamama in both subsurface and surface, except for the outcrop samples Thamama C Reservoir.

- Sr values were very low in all the outcrop and subsurface reservoirs, meaning no involvement of exotic fluid.

- Based on the above elemental analysis comparison, it can be concluded that the blocky calcite cement in both outcrop and subsurface has the same characteristics (except for the Mn, Fe in outcrop Reservoir C) and was precipitated in a deep burial environment.

- The oil charge had no effect on the outcrop reservoirs, as they were uplifted before oil migration.

CHAPTER 6

In-situ stable oxygen isotope analysis of fracture calcite cements for constraining precipitation temperatures

6.1 Introduction

Growth zonation in calcite crystals registers valuable information about temperature and porewater type conditions changes, during calcite precipitation (Dickson et al., 1990; Swennen, 2010). The in-situ (SIMS) $\delta^{18}O_{VPDB}$ composition of calcite cement can be used to constrain the evolution of the fluid chemistry. Here these data are used to understand the evolution of the fluid chemistry in the reservoir fractures through time, with an emphasis on constraining the temperature of cement precipitation. In the burial environment, the interaction of mesogenetic fluids with limestone results in progressively more negative $\delta^{18}O_{VPDB}$ values (Warren, 2014). The often low $\delta^{18}O_{VPDB}$ values of burial calcite is a result of increasing temperature with increasing depth. The $\delta^{18}O$ evolution of formation waters is variable but usually increases due to reactions of calcite dissolution/re-precipitation. Although these effects may cancel one another out, many analyzed late calcites show decreasing $\delta^{18}O_{VPDB}$ values related to increasing temperature during burial (e.g. Cox et al., 2010).

In a study that analysed Thamama Group matrix macro-cements, the increase of burial temperature with the enrichment of formation waters' ^{18}O, suggests that the formation waters evolved within a closed system of no isotopically different composition external waters involvement (Cox et al., 2010).

The temperatures previously obtained for Thamama calcite matrix cements using $\delta^{18}O_{VPDB}$ composition range from 30°C to 125°C (Neilson et al., 1998; Morad et al., 2010; Al Bloushi, 2013; Vahrenkamp et al., 2014; Barata et al., 2015). The temperature for blocky calcite ranges from 95°C to 108°C (Morad et al., 2016). The temperatures that correspond to shallow burial have been estimated to be 50° - 100° C,

and from 100°C to 125°C for deeper burial using both powders (Neilson et al., 1998) and SIMS analysis (Cox et al., 2010).

There is limited information known for the temperature of precipitation of Thamama calcite cement in fractures. Based on fluid inclusion analysis, the range was found to be very variable. In a study of another field near Field A, a narrow temperature range (92°C-94°C) was found (Al Bloushi, 2013), but a wide range (75°C-135°C) was noted in a Total study (2004). Based on $\delta^{18}O_{VPDB}$ analysis, the fracture calcite precipitation temperature range was found to be 81°C-108°C using the Kim & O'Neil equation (1997) in Breesch et al. (2009).

In this study, cathodoluminescence (CL) was used to identify the calcite cement zones in the fractures of the studied reservoirs and then $\delta^{18}O_{VPDB}$ analysis was performed on each of these. The $\delta^{18}O_{VPDB}$ values were converted to $\delta^{18}O_{SMOW}$ and then the temperatures were calculated using the Kim & O'Neil equation (1997). The resultant temperatures were compared to the $^{m}Mg/^{m}Ca$ data (Chapter 3) in order to understand the changes in precipitation temperatures through the Thamama Group.

6.2 Materials and Methods

Eight samples were chosen as representative of all oil reservoirs (Table 6.1). These were a subset of the samples used for the elemental analysis (Chapter 3) to enable comparison. The water leg contained only dolomite cements and very limited calcite cement.

Fracture Set 1 was analysed in all of the Thamama oil reservoirs, while Fracture Set 3 was analysed only in the Lower Thamama oil Reservoirs (F & G). Fracture Set 2 is open and un-cemented. Only blocky calcite was sampled.

Samples were coated with gold and placed within the Cameca 1270 ion microprobe. A Cs (Cesium) ion beam of 10-15 μm diameter spot was used. Sample points were chosen as transects to enable sampling of all the cathodoluminescence (CL) zones. Samples were reassessed for CL zonation after ion probe work since at this point pits

were visible on the sample site. This revealed that not all the cement zones were sampled, however, due to the slight damage caused by repeated use of the thin sections. This damage also made it difficult to gain a clear CL image after ion-probe analysis.

A calcite standard was included in each sample by drilling a 3 mm hole in the middle of the sample, leaving 2 mm in which to place the standard. The surface of the sample was then covered by a single layer of adhesive tape, with the standard crystal placed inside the drilled hole. The hole was then filled with epoxy and left to dry, at which point the tape was removed using acetone and the standard polished to the same plane as the thin section surface.

Sample no	Reservoir
248-8996.1	A oil
248-8998.8	A oil
193-9188.9	B oil
193-9195.8	B oil
133-9374.5	C oil
64-10322.8	F oil
64-10340.5	G oil
64-10355.4	G oil

Table 6.1: Samples used for $\delta^{18}O_{VPDB}$ analysis.

The internal precision ranges between 0.009 % and 0.015 % (Standard Error) and the external precision was estimated to be 0.3 ‰ as determined by consecutive analysis of a UWC (University of Wisconsin Calcite) standard.

The Friedman and O'Neil (1977) equation was used for converting $\delta^{18}O_{(VPDB)}$ to $\delta^{18}O_{(SMOW)}$ as follows:

$$\delta^{18}O_{SMOW}=1.03086\ (\delta^{18}O_{VPDB})+30.86$$

The Kim and O'Neil (1997) equation was then used for calculating temperature, as follows:

$1000 \ln \alpha_{(calcite\_water)} = 18.03 (10^3 T^{-1}) - 32.42$

All data are given in Appendix 4

6.3 Objectives

To measure the concentration of $\delta^{18}O_{VPDB}$ in fracture cements, in order to obtain the temperature in the fracture cement after Kim and O'Neil (1997).

We aim to:

1- Calculate the temperature of blocky calcite cement in each cement zone, in Fracture Sets 1 and 3
2- Determine the age of the fracture cements in Fracture Sets 1 and 3
3- Compare between Fracture Set 1 and Fracture Set 3, regarding age and cementation history

6.4 Results

Results are first presented as transects of single $\delta^{18}O_{VPDB}$ data points for both Fracture Set 1 and 3 calcite cements in each reservoir, then summarised as graphs for each CL cement zone.

6.4.1 $\delta^{18}O_{VPDB}$ values in fracture cement transects

Reservoir G oil:

Fracture Set 1:

The $\delta^{18}O_{VPDB}$ values ranged between -8.79 ‰ and -7.58 ‰ (Fig. 6.1A). Here sample points were taken by starting from both edges of the fracture and ending in the middle (youngest zones). The change in $\delta^{18}O_{VPDB}$ values was relatively minor (1.21 ‰), with no clear trends.

Fracture Set 3:

The $\delta^{18}O_{VPDB}$ values ranged between -8.41 ‰ and -6.74 ‰ (Fig. 6.1B). Sample points were taken from the left edge (oldest) of the fracture to the right (youngest). The change in $\delta^{18}O_{VPDB}$ values was relatively minor (1.67 ‰), with no clear trends.

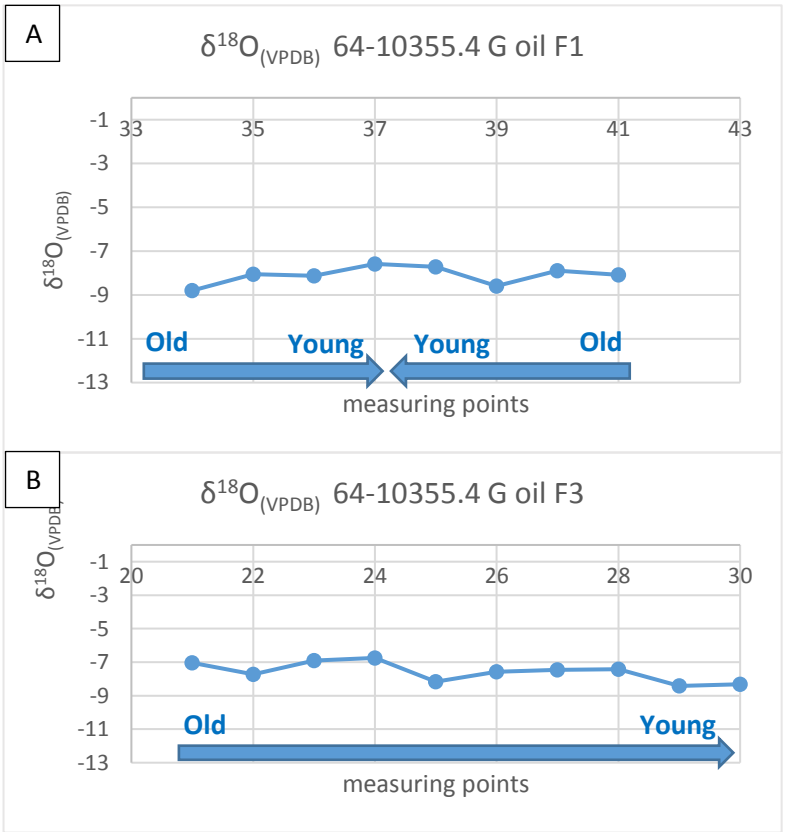

Fig. 6.1: single point measurements of $\delta^{18}O_{(VPDB)}$ values (‰) along fractures in Reservoir G oil. A: Transect through Fracture Set 1. B: Transect through Fracture Set 3. Blue arrows indicate the direction in which of sample points were taken.

Reservoir F oil:

Fracture Set 1:

The $\delta^{18}O_{VPDB}$ values ranged between -9.59 ‰ and -5.98 ‰ (Fig. 6.2A). As the arrow shows, the samples were taken from the left edge (older) of the fracture to the right (younger). The $\delta^{18}O_{VPDB}$ values in the cement zones decreased through time by 3.61 ‰.

Fracture Set 3:

The $\delta^{18}O_{VPDB}$ values ranged between -8.33 ‰ and -6.89 ‰ (Fig. 6.2B). The change in $\delta^{18}O_{VPDB}$ values was relatively minor (1.44 ‰) with no clear trends.

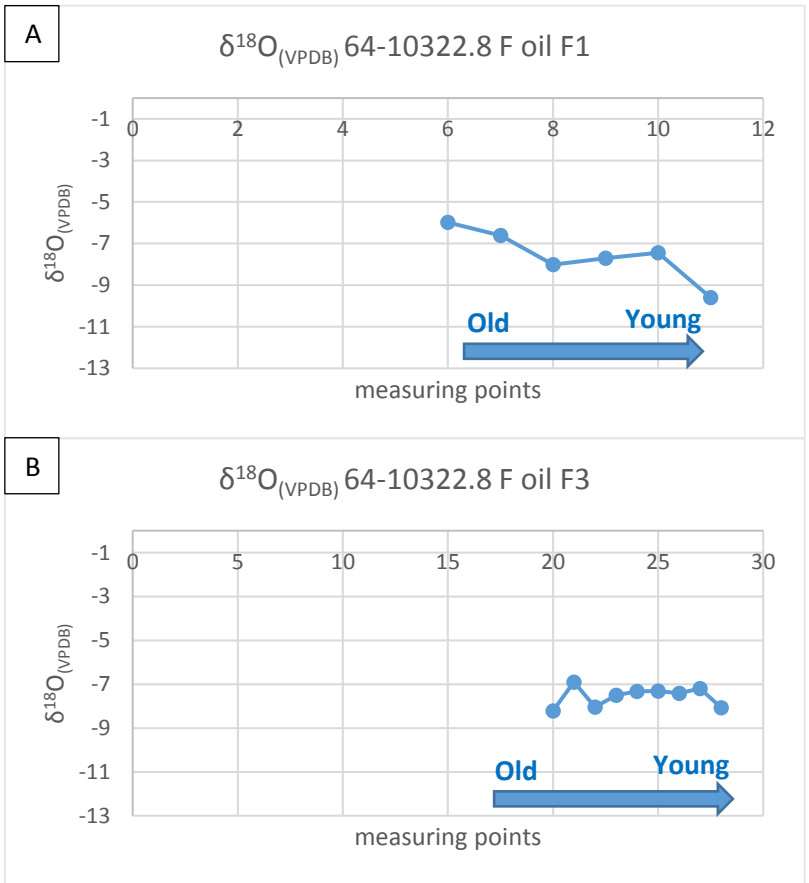

Fig. 6.2: $\delta^{18}O_{(VPDB)}$ values (‰) along fractures in Reservoir F oil. A: Transect through Fracture Set 1. B: Transect through Fracture Set 3. Blue arrows indicate the direction of sampling points taken. Errors are smaller than the plotted symbols.

Reservoir C oil:

Fracture Set 1:

The $\delta^{18}O_{VPDB}$ values ranged between -8.96 ‰ and -2.82 ‰ (Figure 6.3). The change in $\delta^{18}O_{VPDB}$ values is dramatic (6.14 ‰), with a clear trend of decreasing values through time.

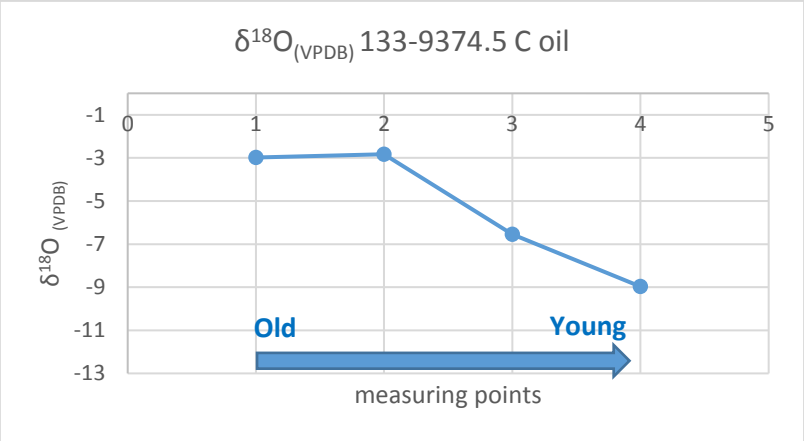

Fig. 6.3: $\delta^{18}O_{(VPDB)}$ values (‰) along the fracture in Fracture Set 1 in Reservoir C oil. The blue arrow indicates the direction of sampling. Errors are smaller than the plotted symbols.

Reservoir B oil:

Fracture Set 1:

The $\delta^{18}O_{VPDB}$ values ranged between -12.80 ‰ and -5.10 ‰ (Fig. 6.4 A, B). Two different fractures were measured. In the first (A) the crystal growth was from the left edge of the fracture (oldest) to the right edge (youngest). Values were very stable except for one low value (-10.56 ‰). There is some uncertainty about the validity of this measurement, however, since the fracture was very narrow and the crystal size very small and thus the growth orientation was unclear.

The second transect (B) was taken where the calcite crystals were growing from the two edges of the fractures (oldest) to the middle of the fracture (youngest). The values show an asymmetry but in both cases gradually become more negative through time to the youngest cements. Both, however, show a rise from the initial values then a subsequent decrease. There is again some uncertainty about the validity of this measurement due to the small crystal size and unclear crystal orientation.

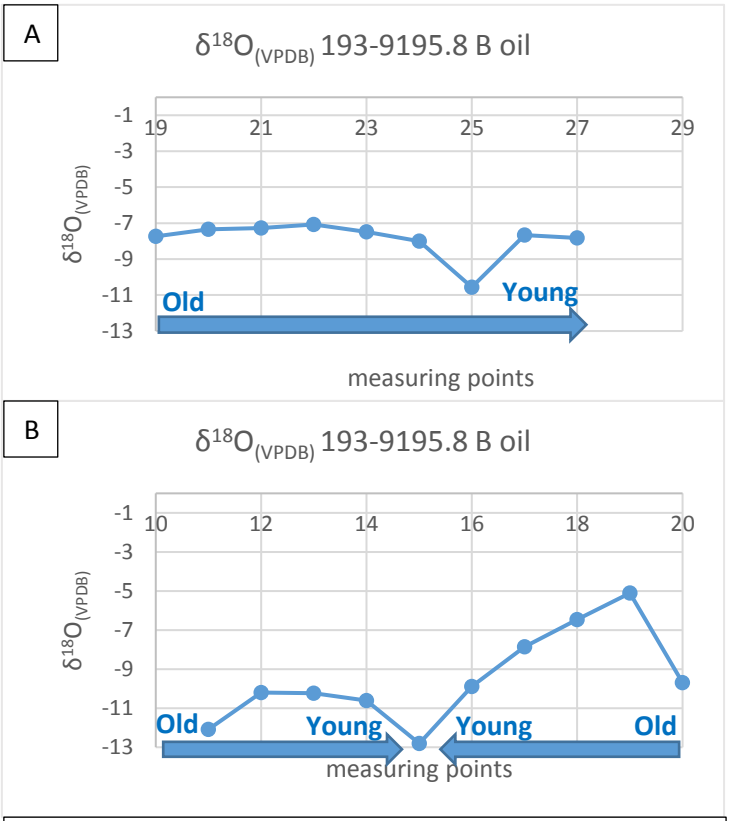

Fig. 6.4: $\delta^{18}O_{(VPDB)}$ values (‰) along fractures in Fracture Set 1 in Reservoir B oil. Blue arrows indicate the direction of sample points taken. Errors are smaller than the plotted symbols.

Reservoir A oil:

Fracture Set 1:

The $\delta_{18}O_{VPDB}$ values ranged between -10.11 ‰ and -8.40 ‰ (Fig. 6.5). The change in $\delta^{18}O_{VPDB}$ values is relatively minor (1.71 ‰) with no clear trends.

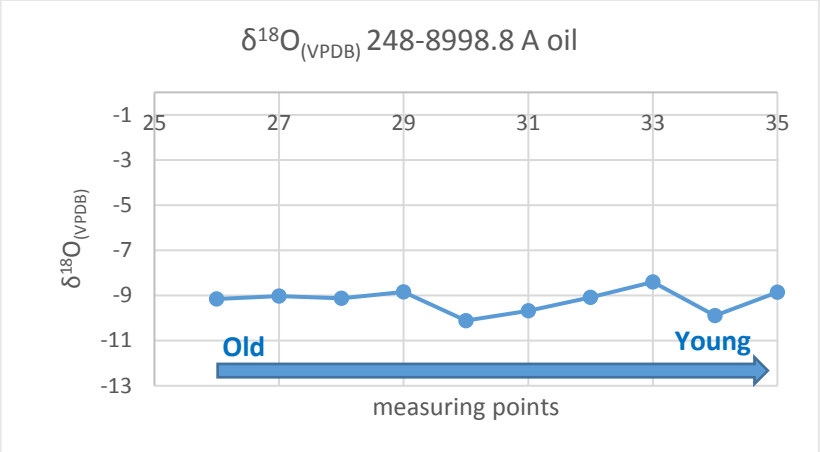

Fig. 6.5: $\delta^{18}O_{(VPDB)}$ values (‰) along fractures in Fracture Set 1 in Reservoir A oil. Blue arrows indicates the direction of sample points taken. Errors are smaller than the plotted symbols.

6.4.2 $\delta^{18}O_{VPDB}$ values in cement CL zones

Reservoir G oil:

Fracture Set 1:

The $\delta^{18}O_{VPDB}$ values measured in Fracture Set 1 were all in cement zone 1 and the mean value is -8.10 ‰ (Fig. 6.6). Sampling in CL zones 2 and 3 could not be clearly detected.

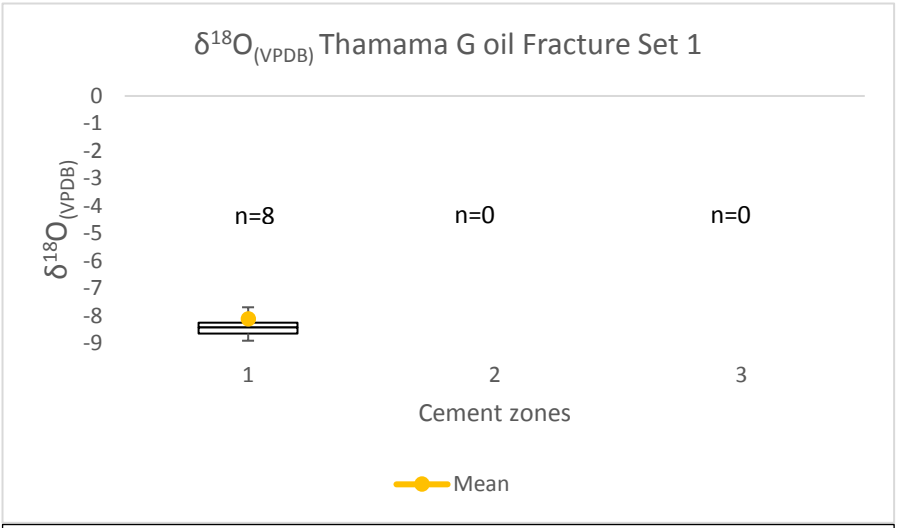

Fig. 6.6: Box and whisker plots for $\delta^{18}O_{(VPDB)}$ data (‰) for each CL blocky calcite cement zone in Fracture Set 1 in Reservoir G oil. n = number of data points. The yellow dot marks the mean value.

Fracture Set 3:

In Fracture Set 3, the $\delta^{18}O_{VPDB}$ values measured were also all in cement zone 1 where the mean value is -7.45 ‰ (Fig. 6.7). Sampling in CL zones 2 and 3 could not be clearly detected.

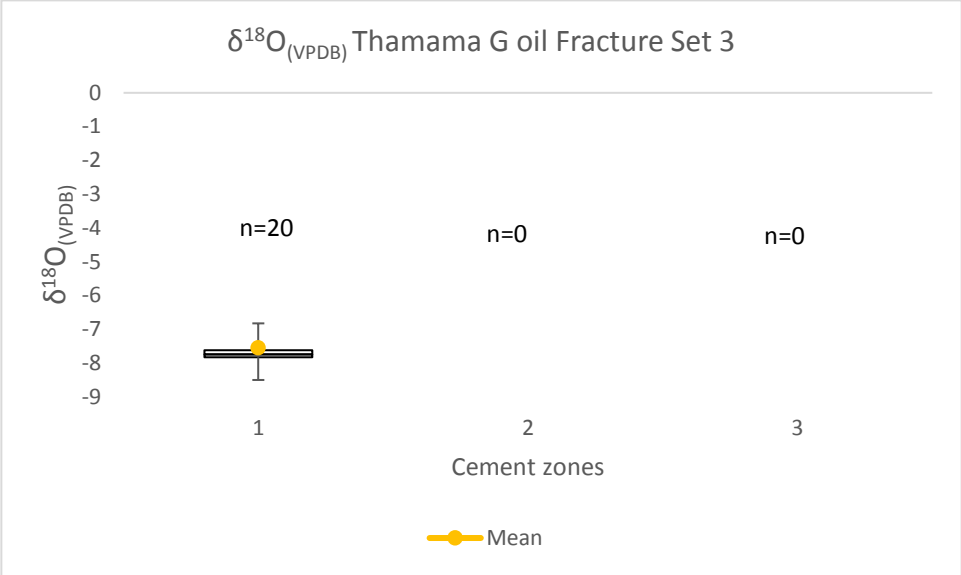

Fig. 6.7: Box and whisker plots for $\delta^{18}O_{(VPDB)}$ data (‰) for each CL blocky calcite cement zone in Fracture Set 3 in Reservoir G oil. n = number of data points. The yellow dot marks the mean value.

Reservoir F oil:

Fracture Set 1:

The $\delta^{18}O_{VPDB}$ values ranged between -7.85 ‰ in cement zone 1 and -5.98 ‰ in cement zone 5 (Fig. 6.8). Four cement zones were sampled (1, 2, 5, 6), while cement zones 3 and 4 do not appear to have been sampled.

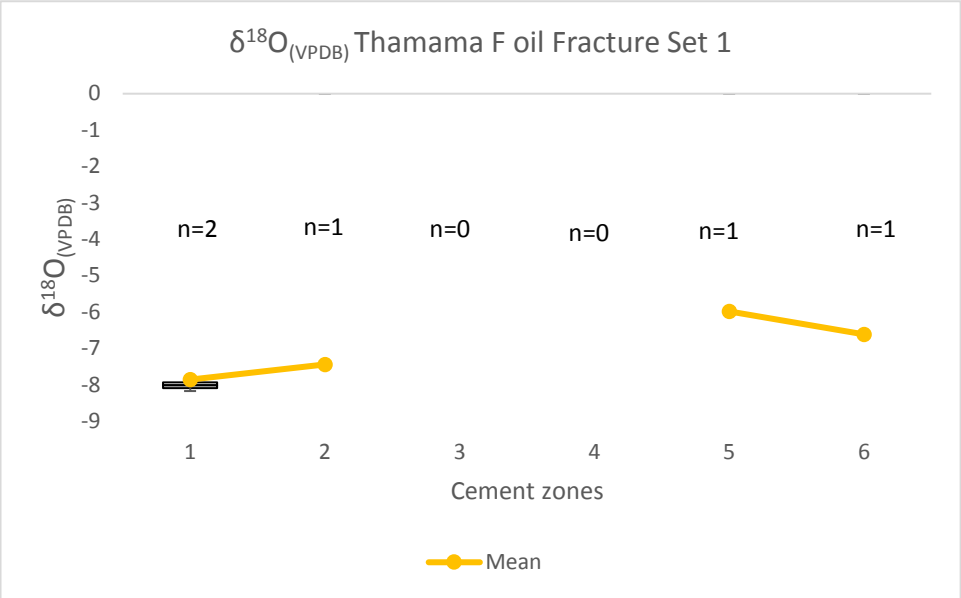

Fig. 6.8: Box and whisker plots for $\delta^{18}O_{(VPDB)}$ data (‰) for each CL blocky calcite cement zone in Fracture Set 1 in Reservoir F oil. n = number of data points. The yellow dots mark the mean values.

Fracture Set 3:

The $\delta^{18}O_{VPDB}$ values ranged between -8.27 ‰ (CL zone 3) and -7.92 ‰ (CL zone 4) (Fig. 6.9).

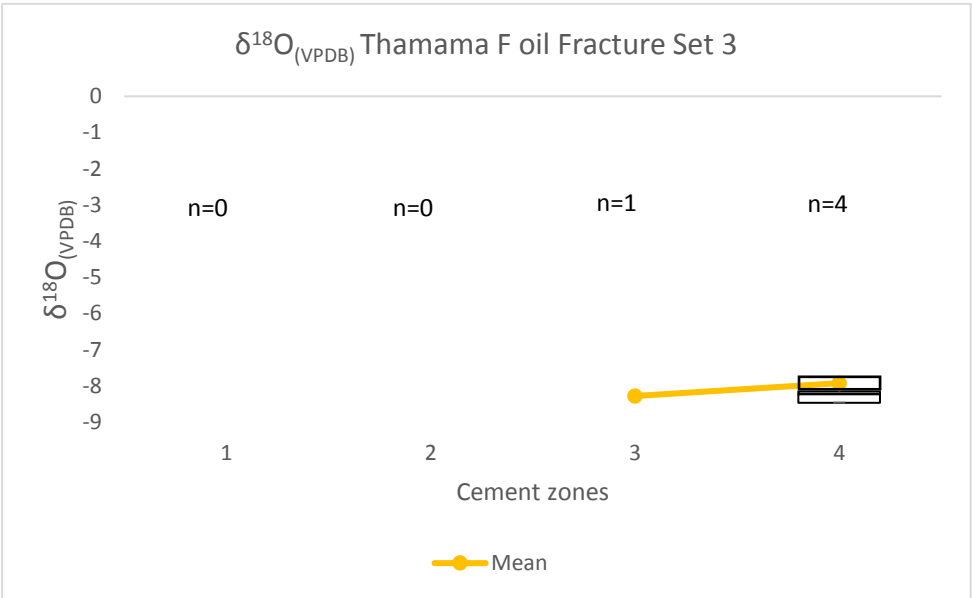

Fig. 6.9: Box and whisker plots for $\delta^{18}O_{(VPDB)}$ data (‰) for each CL blocky calcite cement zone in Fracture Set 3 in Reservoir F oil. n = number of data points. The yellow dots mark the mean values.

Reservoir C oil:

Fracture Set 1:

Reservoir C has only one cement zone sampled which is zone 3. The $\delta^{18}O_{VPDB}$ mean value is -6.15 ‰ (Fig. 6.10).

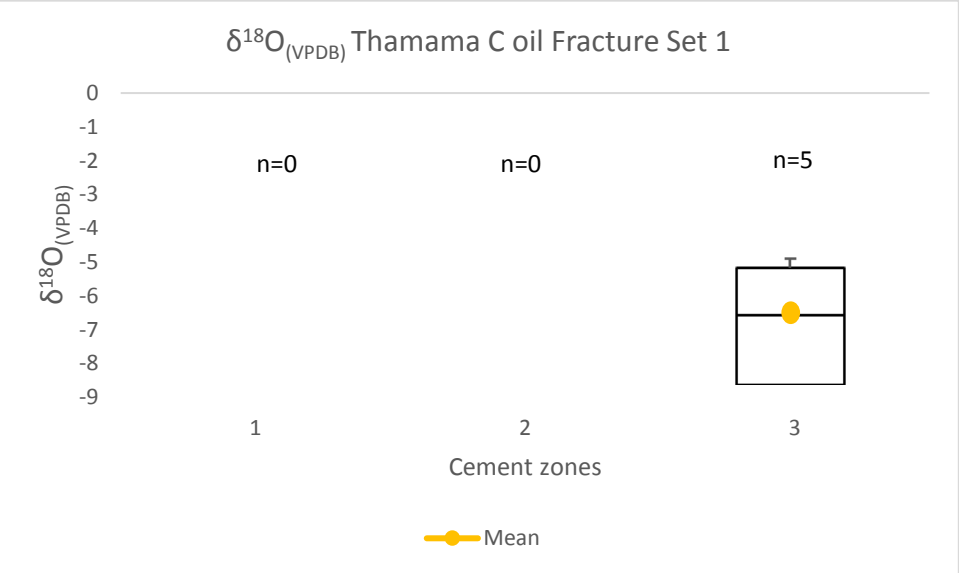

Fig. 6.10: Box and whisker plots for $\delta^{18}O_{(VPDB)}$ data (‰) for each CL blocky calcite cement zone in Fracture Set 1 in Reservoir C oil. n = number of data points. The yellow dot marks the mean value.

Reservoir B oil:

Fracture Set 1:

The $\delta^{18}O_{VPDB}$ values ranged between -9.53 ‰ in cement zone 1 and -9.36 ‰ in cement zone 2 (Fig. 6.11).

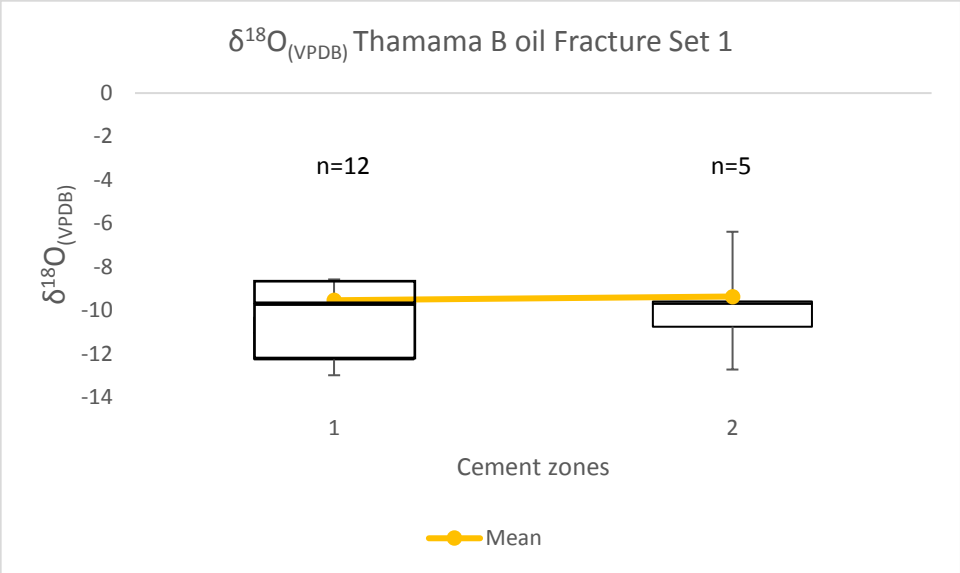

Fig. 6.11: Box and whisker plots for $\delta^{18}O_{(VPDB)}$ data (‰) for each CL blocky calcite cement zone in Fracture Set 1 in Reservoir B oil. n = number of data points. The yellow dots and line trace the mean.

Reservoir A oil:

Fracture Set 1:

The $\delta^{18}O_{VPDB}$ values ranged between -9.06 ‰ in cement zone 3 and -8.71 ‰ in cement zone 2 (Fig. 6.12).

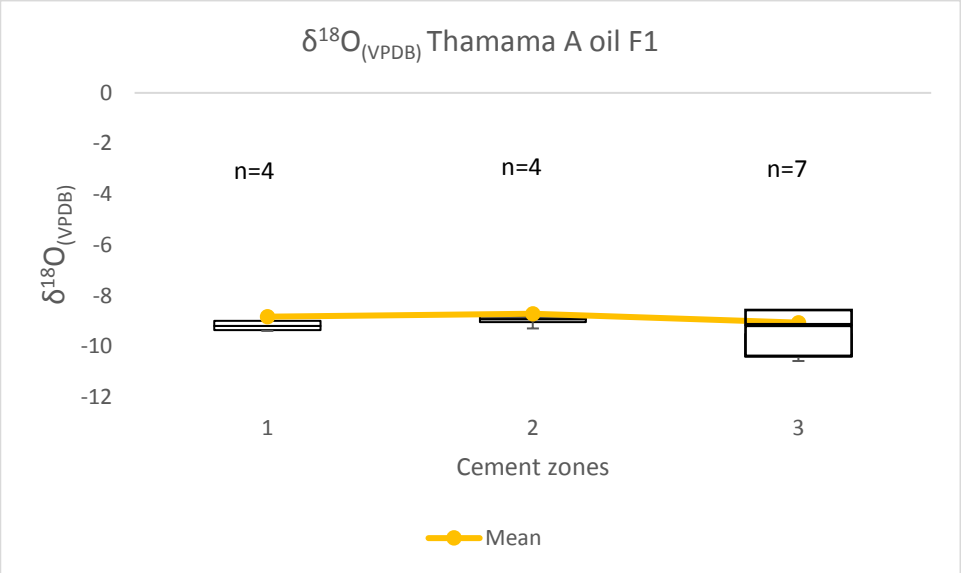

Fig. 6.12: Box and whisker plots for $\delta^{18}O_{(VPDB)}$ data (‰) for each CL blocky calcite cement zone in Fracture Set 1 in Reservoir A oil. n = number of data points. The yellow dots mark the mean values.

6.4.1. Summary

Fig. 6.13 shows the $\delta^{18}O_{VPDB}$ values for Fracture Sets 1 and 3 in the Thamama reservoir fractures as box and whisker plots.

In Fracture Set 1, the $\delta^{18}O_{VPDB}$ values ranged between -5.98 ‰ to -9.53 ‰, suggesting a range of burial depths of precipitation. Reservoirs A and G in particular show very small change (-9.06 ‰ to -8.10 ‰). By contrast, Reservoir B and C oil have the biggest difference in $\delta^{18}O_{VPDB}$ values of all reservoirs (-9.53 ‰ to -6.15 ‰).

The narrower range of $\delta^{18}O_{VPDB}$ values in Fracture Set 3 in both Reservoirs F and G (-7.45 ‰ to -8.27 ‰) suggests relatively rapid precipitation over a shorter time period.

In general, the $\delta^{18}O_{VPDB}$ values for the Lower Thamama were lower than those of the Upper Thamama.

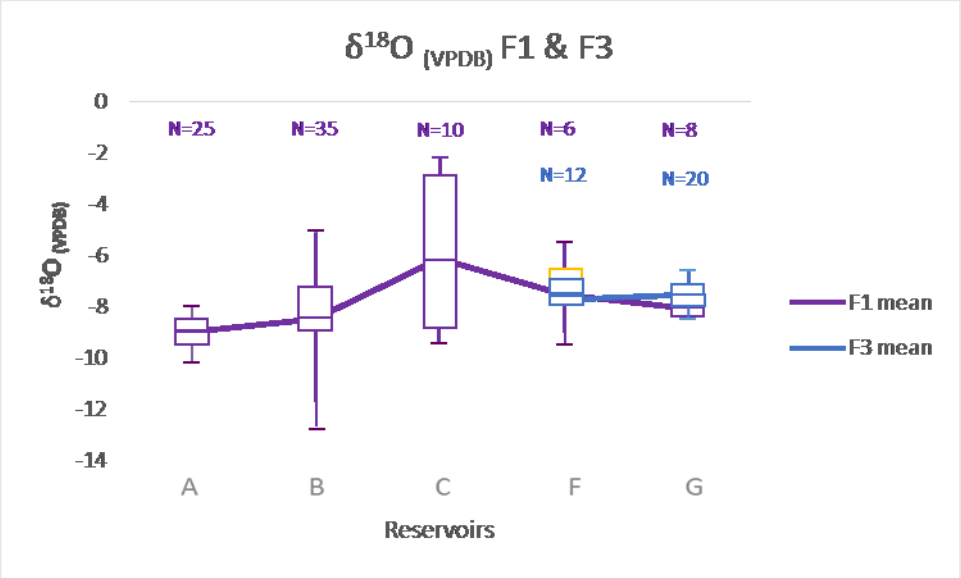

Fig. 6.13: $\delta^{18}O_{VPDB}$ values in the Thamama reservoirs for F1 and F3 calcite fracture cements

Fig. 6.14 shows the temperature values for Fracture Sets 1 and 3 in the Thamama reservoirs, after Kim and O'Neil (1997).

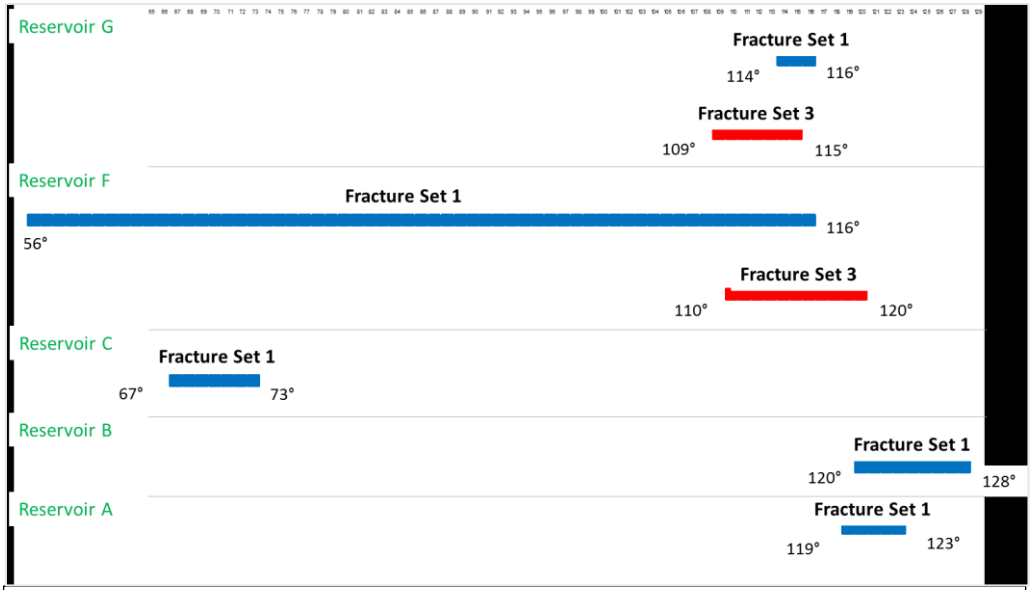

Figure 6.14. Comparison between temperature in Fracture Set 1 and Fracture Set 3 of the subsurface Thamama

6.4.2 Conversion $\delta^{18}O_{VPDB}$ to $\delta^{18}O_{SMOW}$

$\delta^{18}O_{SMOW}$ values were obtained from mean $\delta^{18}O_{VPDB}$ values for each CL zone using the Friedman and O'Neil (1977) equation (Table. 6.3).

Reservoir	Fracture Set	Cement Zone	$\delta^{18}O_{(VPDB)}$	$\delta^{18}O_{(SMOW)}$
G oil	1	1	-8.1	22.510034
	3	1	-7.45	23.180093
F oil	1	1	-7.85	22.767749
	1	2	-7.44	23.1904016
	1	5	-5.98	24.6954572
	1	6	-6.6	24.056324
	3	3	-8.27	22.3347878
	3	4	-7.92	22.6955888
C oil	1	3	-6.15	24.520211
B oil	1	1	-9.53	21.0359042
	1	2	-9.36	21.2111504
A oil	1	1	-8.82	21.7678148
	1	2	-8.71	21.8812094
	1	3	-9.06	21.5204084

Table 6.3: Mean $\delta^{18}O_{(VPDB)}$ values (‰) for CL zones converted to $\delta^{18}O_{(SMOW)}$.

Obtained $\delta^{18}O_{SMOW}$ values agree with the Friedman and O'Neil (1977) relationship between PDB, SMOW graph (Fig. 6.15).

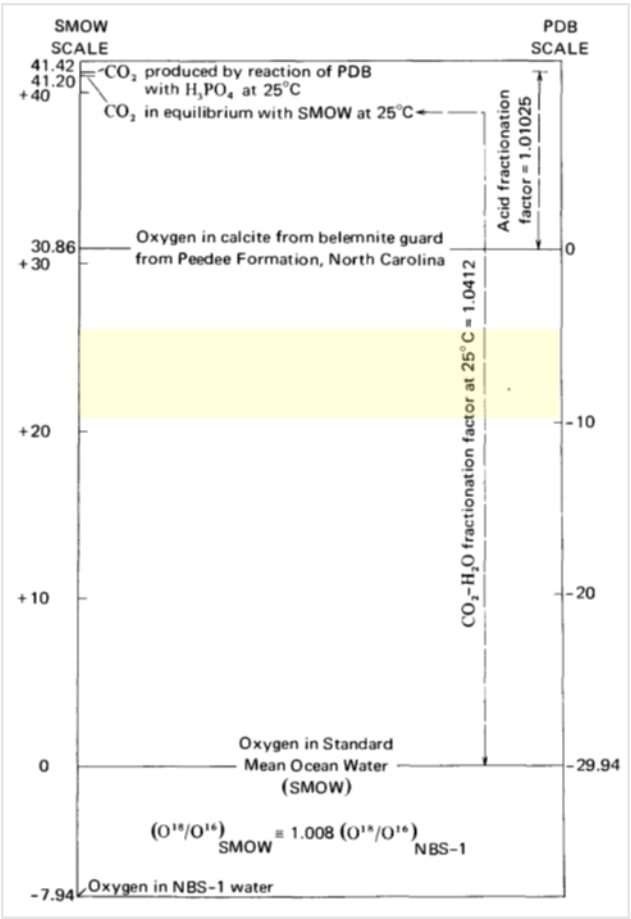

Fig. 6.15: Relationship between PDB, SMOW and other Oxygen standards. Area in yellow represents the studied samples (After Friedman & O'Neil (1977).

6.4.5 Calculating precipitation temperatures of fracture cements

For $\delta^{18}O_{(VPDB)}$ values from −12‰ to −9‰, the upper temperature limit used as maximum burial temperature was of 125 °C (Neilson et al., 1998; Morad et al., 2010). And for $\delta^{18}O_{(VPDB)}$ values from −8‰ to −5‰, the upper temperature limit was 100 °C as for burial temperature (Cox et al., 2010; Vahrenkamp et al., 2014; Barata et al., 2015).

Table 6.4 shows the range and mean temperature for each CL zone.

Reservoir	Fracture Set	Cement Zone	Temperature °C Range	Mean Temperature °C
G oil	1	1	114-116	115
	3	1	109-115	112
F oil	1	1	110-116	113
	1	2	106-113	109
	1	5	56-60	58
	1	6	67-73	70
	3	3	112-120	116
	3	4	110-117	114
C oil	1	3	67-73	68
B oil	1	1	120-128	125
	1	2	121-125	123
A oil	1	1	120-123	121
	1	2	119-121	120
	1	3	121-123	122

Table 6.4.: Ranges and means of calculated temperature for calcite cement CL zones

Using the Kim and O'Neil (1997) equation, the temperature for both Fracture Sets 1 & 3 in all of the Thamama Reservoirs was calculated and plotted against $\delta^{18}O_{SMOW}$ (Fig. 6.16).

Temperature values range from a lowest of 56°C in Reservoir F, to a highest of 128°C in Reservoir B.

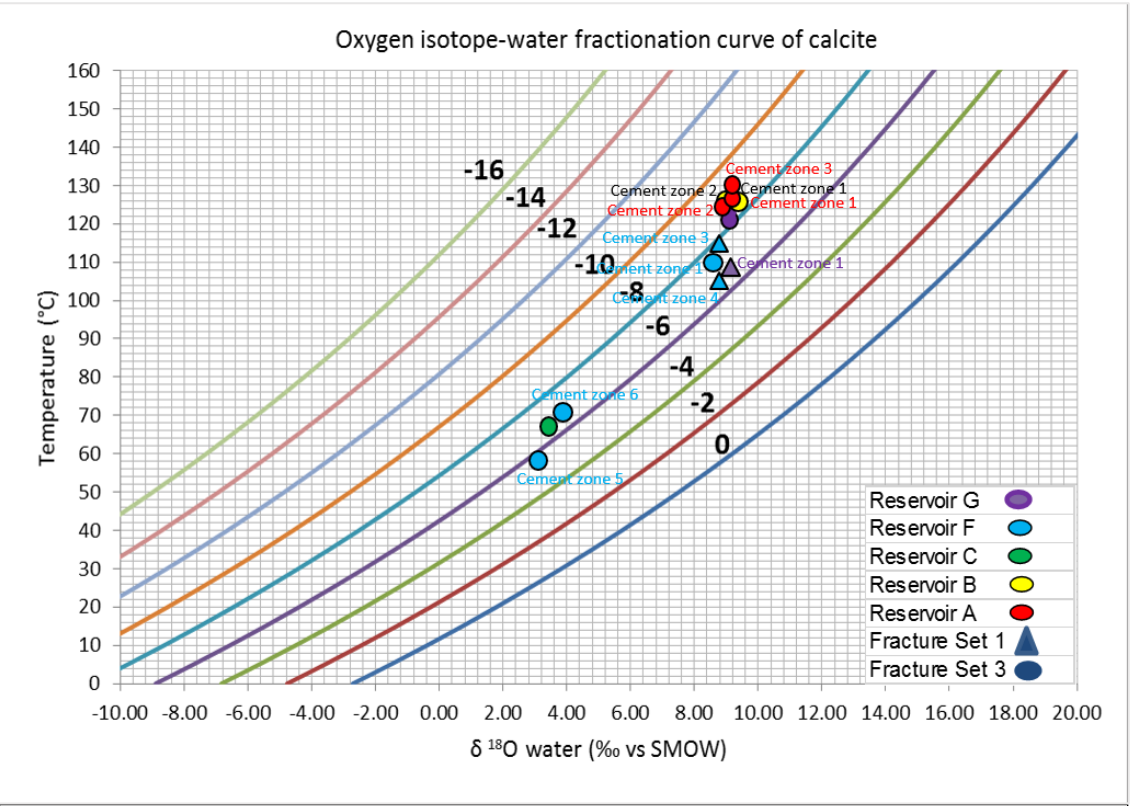

Fig. 6.16: Oxygen isotope-water fractionation curve of calcite for the range of cement zones in Fracture sets 1 and 3 in the sampled Thamama reservoirs (Kim & O'Neil, 1977).

6.5 Discussion

6.5.1 $\delta^{18}O_{VPDB}$ values in diagenetic environments

The luminescence of cement zones and $\delta^{18}O_{VPDB}$ values are given in Table 6.2. On the basis of paragenetic sequence analysis (Chapter 2), most blocky calcite in the fractures is younger than most matrix cements. These cements precipitated after lithification of sediments and opening of the fractures. The low $\delta^{18}O_{VPDB}$ values included both non-luminescent and bright luminescent zones. This fact does not make dark non-luminescent cement zones an indication of light $\delta^{18}O_{VPDB}$ (Rush and Chafetz, 1990) and therefore seawater derived cements, since all of the fracture cements were precipitated in burial environments.

Reservoir	Fracture Set	Cement Zone	CL	Mean $\delta^{18}O_{(VPDB)}$
G oil	1	1	non-luminescent	-8.1
	3	1	dull-dark	-7.45
F oil	1	1	dull-red	-7.85
	1	2	med-bright red	-7.44
	1	5	dull-med red	-5.98
	1	6	bright red	-6.6
	3	3	dark-dull red	-8.27
	3	4	bright red	-7.92
C oil	1	3	bright red	-6.15
B oil	1	1	dull-med red	-9.53
	1	2	bright red	-9.36
A oil	1	1	dull-dark red	-8.82
	1	2	med red	-8.71
	1	3	bright red	-9.06

Table 6.2: In-situ $\delta^{18}O_{(VPDB)}$ average data (‰) for each CL blocky calcite cement zone in Fracture Sets 1 & 3 in all Thamama Reservoirs

6.5.2 Temperature (°C) evolution

Fig. 6.17A presents the mean calculated temperature for fracture calcite cements in all reservoirs. Reservoir B oil has the highest average temperature (124 °C), while Reservoir C has the lowest average temperature (68°C).

Fracture Set 1 in Reservoirs B and C has wider range of temperatures (68°C to 125°C) and so an inferred longer burial history. Fracture Set 3 has a very limited temperate range (112°C to 116°C).

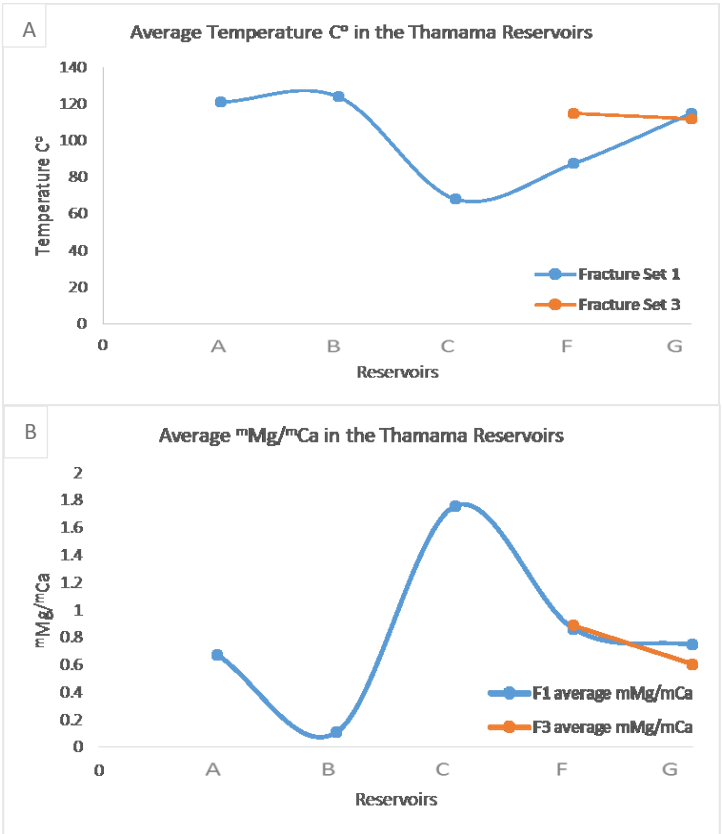

Fig. 6.17: Comparison between mean temperature °C derived from $\delta^{18}O$and $^{m}Mg/^{m}Ca$ in Fracture Sets 1 & 3 in the Thamama Reservoirs. (A): Temperature °C from $\delta^{18}O$. (B): $^{m}Mg/^{m}Ca$.

When plotting the average values of temperature (°C) derived from $\delta^{18}O$ and comparing this to the average $^{m}Mg/^{m}Ca$ values (Chapter 3), Fracture Set 1 shows a good agreement ($R^2 = 0.8047$) while Fracture Set 3 shows a considerable disagreement ($R^2 = 0.1366$), specifically in Reservoir G (Figs. 6.17B, 6.18). But with only two data points available this is statistically under sampled.

In Fracture Set 1 this implies that $\delta^{18}O$ and $^{m}Mg/^{m}Ca$ values are correlated with temperature.

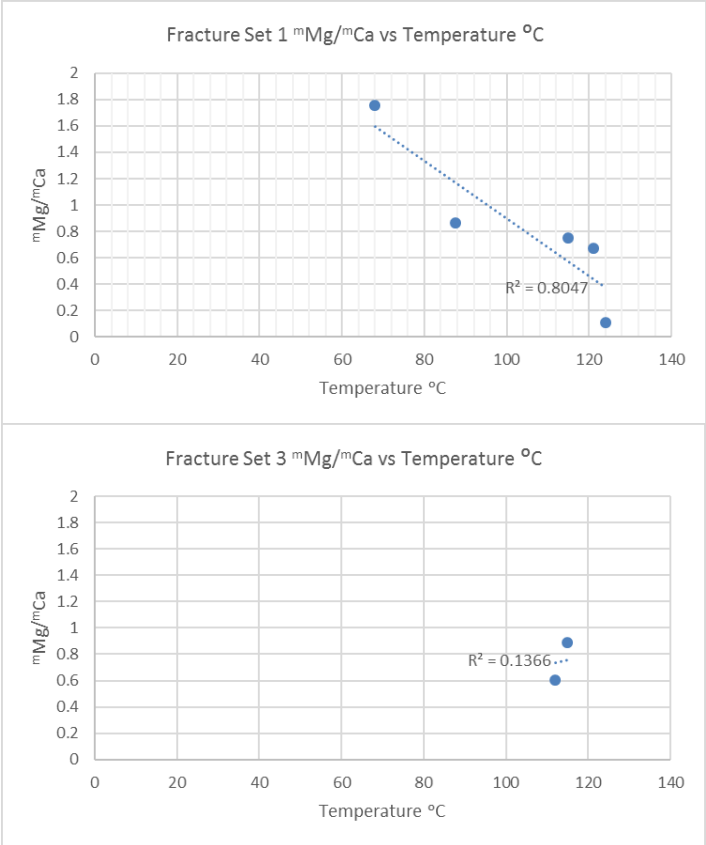

Fig. 6.18: Comparison between Temperature C° and $^{m}Mg/^{m}Ca$ in Fracture Sets 1&3 in the Thamama Reservoirs. (A): Temperature C°. (B): $^{m}Mg/^{m}Ca$.

Fracture Set 1 overall had a higher temperature and longer burial history than Fracture Set 3 (Figure 6.19).

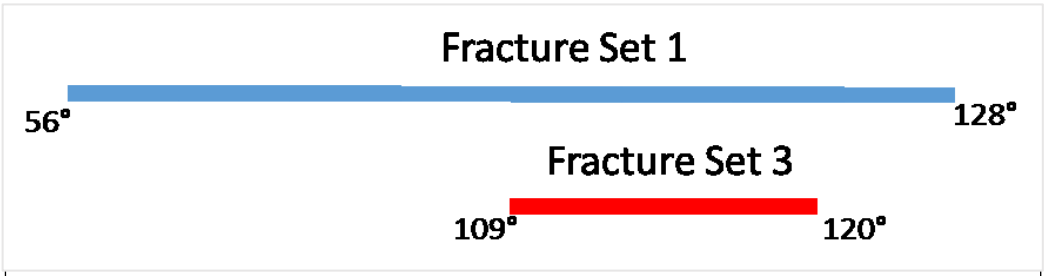

Figure 6.19. Comparison between temperature in Fracture Set 1 and Fracture Set 3 of the subsurface Thamama

Field A is known as being highly faulted with compartmentalization between its reservoirs. The lowest average temperature (58°C) recorded for cement zone 5 in Fracture Set 1 of Reservoir F oil, might be a result fluids entering from other reservoirs via faults, since the samples for Reservoir F oil were taken from a well lying inside the main graben of Field A (Figure 6.20). The main graben of Field A has two faults with the greatest fault throws in the entire field, and the only well drilled inside it is highly fractured.

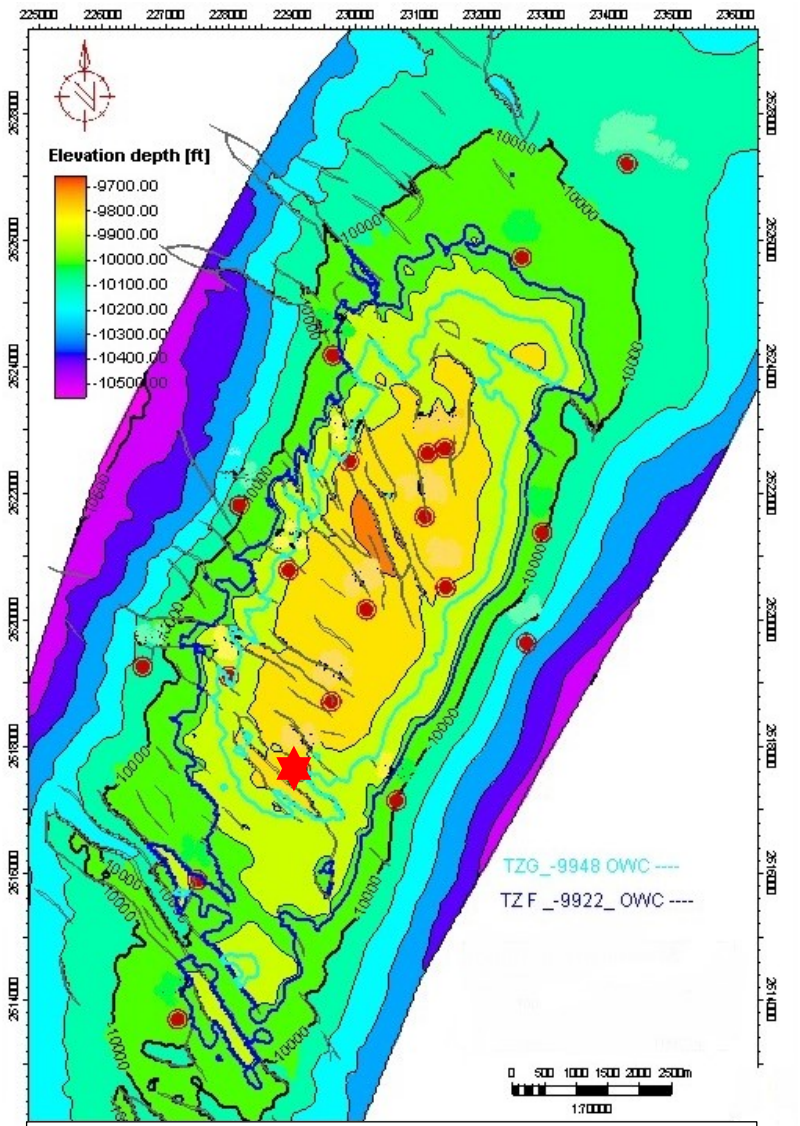

Figure 6.19. Location of Reservoir F oil well (star) in the graben of Field A. OWC: oil water contact. Red dots: other wells.

6.5 Conclusion

- The cement in the form of blocky calcite in the fractures is relatively late and young, and of generally deep burial origin showing temperature ranges of 109°C - 125°C. Reservoirs C and F, however, show temperatures lower ranges of 58°C- 70°C in the older cement zones, and 116°C in Reservoir F younger zones. There is no evidence for precipitation in the meteoric environment.

- Based on the large range of calcite cement growth temperatures (58°C - 125°C) and CL patterns, a prolonged period of cement precipitation is present in Fracture Set 1.

- The $\delta^{18}O$ results show good agreement with $^{m}Mg/^{m}Ca$ results in Fracture Set 1, implying that both methods provide a consistent record of temperature of cement formation.

- Each Reservoir shows a different range of temperatures of precipitation: Reservoir A 119°C –123°C, Reservoir B 120°C –128°C, Reservoir C 67°C – 73°C, Reservoir F 56°C –120°C, and Reservoir G 109°C –116°C.

- Fracture Set 1 had a higher temperature and longer burial history than Fracture Set 3.

CHAPTER 7: Conclusion

7.1 Introduction

This thesis is concerned about the relationship between fractures and diagenesis and their effect on reservoir quality. It elaborates on the role of tectonism on the formation of fractures, and the type of cementation fluids. In this chapter, the main findings of each area of research is covered emphasizing on the new findings that were not covered in the literature earlier to this study. The study covers two main locations, the subsurface (Field A) in Abu Dhabi and the outcrop in Ras Al Khaimah, both located in the United Arab Emirates. The studied carbonate reservoirs are part of the Thamama Formation (Early Cretaceous), which is divided into two sections; The Upper Thamama including Reservoirs A, B and C and the Lower Thamama including Reservoirs F and G. The whole Thamama section was covered in the subsurface but only the upper Thamama was covered in the outcrop. This work intended to cover and compare the fracture diagenesis in both the oil legs and water legs of Field A, yet it was found during the analysis that the water leg had less representative samples for fracture cements. The reason can be referred to dissolution of fracture cements. The result was to compare water leg and oil leg for blocky calcite and saddle dolomite in Reservoir B. Saddle dolomite was found in the Reservoir F water leg but not in the oil leg. All the rest of the data for equant and blocky calcite and saddle dolomite were in the oil leg. Suggestions for results improvement and future work will be covered by the end of the chapter.

7.2 Fractures in relation to the tectonic events

The Arabian platform where the subsurface field exists is believed to been affected by three main tectonic events. They are; the opening of the Neotethys Ocean

(Permian to Late Jurrasic), uplift and erosion of the shelf margin (Late Jurassic to Early Cretaceous) and the obduction of the Oman-UAE Semail ophiolite (Late Cretaceous). The Musandam peninsula though, where the outcrop lays was locally subjected to another three tectonic events. Those are; the foreland autochthon (Precambrian to Lower Cretaceous), the frontal triangle zone (Neogene) and Dibba zone (Triassic to Cretaceous) and lastly the Sumeini units (Lower to Middle Cretaceous). The activity of these tectonic events aided in the formation of the faults and fractures in both subsurface and outcrop.

The obduction of Oman ophiolites is believed not only to aid in fracture forming, but also in providing hot basinal brines which were the main source of saddle dolomite and blocky calcite fracture cements (Morad et al, 2018) as well as stylolization.

7.3 Cement types in fractures and diagenetic environments

There are differences between the Lower and Upper Thamama reservoirs. Lower Thamama reservoirs (F & G) are more fractured than the Upper Thamama (A, B and C). Lower Thamama reservoirs show Fractures Sets 1, 2 and 3, but the Upper Thamama only shows Fractures Sets 1 and 2. The fractures in the Thamama that formed during the tectonic activity of the Late Cretaceous are those which are of relatively large aperture (reaching few centimetres in the Lower Thamama). The other hairline fractures may have formed as a result of the pressure from in-situ hydrocarbon generation. Fracture Set 1 was opened by Late Cretaceous Ophiolite obduction and was cemented with equant calcite in the Lower Thamama. Fracture Set 2 was opened after Fracture Set 1, possibly by the Red Sea horizontal stress. It either was never cemented due to the ongoing horizontal movement, or the cement was dissolved. Fracture Set 3 was opened in the Lower Thamama Reservoirs F and G due to tectonic movements, or due to pressure-temperature gradient. Another possibility that it formed due to overburden pressure. Each Fracture Set shows a short history of cementation, due to the late type of blocky calcite cement (Bourque and Raymond, 1994). Nonetheless, Fracture Set 1 has longer cementation history

than Fracture Set 3, due to the additional presence of equant calcite cement and the greater number of cement zones. The cements in the Thamama subsurface were post-kinematic. The extensive cementation that appears in the Lower Thamama shows that fractures were conduits that allowed the flow of alien formation fluids through the system. The cements in the fractures are mainly filled by blocky calcite and saddle dolomite. Equant calcite was found in Fracture Set 1 in Reservoirs G, F and C only. Saddle dolomite appeared in Fracture Set 1 in Reservoirs G, F and B and in Fracture set 3 of Reservoir G. The timing of fracture formation is very variable, ranging between very early to very late in the paragenetic sequence. But in general it is observed that the fractures sets appeared during the middle and the late phase of the paragenetic sequence (shallow to deep marine), except for Reservoir F where Fracture Set 1 formed very early, inferred to be during marine phreatic conditions. Fracture Set 3 only exists only in these two reservoirs, and formed late, during deep burial and is associated with stylolites. The characteristics found in many cements (either calcite or dolomite and sometimes anhydrite) of the samples indicates in sum a burial environment: the crystals cross-cut stylolites, crystals appear in fractures, crystals fill compacted pores, crystals have relatively large size, blocky and equant crystals, crystals showing well defined cathodoluminescence zonation ranging from bright to quenched repeatedly. The dissolution event appeared to happen after the oil charge to the Thamama reservoirs, because the bitumen appeared earlier than the dissolution.

7.4 Elemental analysis of calcite cement

In general the Upper Thamama Reservoirs (A, B, and C) show lower $^{m}Mg/^{m}Ca$ than the Lower Thamama reservoirs (F,G). The Upper Thamama fracture calcite cements were therefore precipitated at higher overall temperatures than the Lower Thamama examples. The change in temperature in equant calcite cement zones is different from the blocky calcite zones. Equant calcite shows higher temperature in all of the reservoirs except Reservoir F oil, where the overall temperature is low (except in cement zone 2) and increases gradually through the cement zones. However, blocky

calcite cement shows an overall high temperature in all the Reservoirs, and the temperature increases gradually through the cement zones in the Lower Thamama Reservoirs F and G oil. The change in temperature also differs from Fracture Set 1 and Fracture Set 3. Fracture Set 3 in Reservoir G oil shows higher overall temperatures than Fracture Set 1 in Resrvoir G and Reservoir F oil. Both fracture sets show gradual increase in temperature through the cement zones. Lower Thamama reservoirs (F and G) have variations in temperature between the different cement zones. The temperature drops in cement zone 5 in Reservoir G oil and in cement zone 3 in Reservoir F oil. While the Upper Thamama reservoirs (A, B and C) have a consistent overall temperature through the reservoir. That might be due to fewer cement zones in the Upper Thamama reservoirs, which is in turn may be due to the smaller fractures and cement infilling them. Most of the Thamama fracture cement in both oil and water reservoirs was precipitated in the burial environments. The low amount of Sr confirms that no exotic fluid has entered the diagenetic system. Upper Thamama Reservoirs (A, B, and C) have far lower Fe and Mn concentrations and Lower Thamama reservoirs (F,G). Fracture Set 3 cements show similar values to Fracture Set 1 cements. This suggests an overall environment of oxic conditions Upper Thamama Reservoirs (A, B, and C) and reducing conditions in the Lower Thamama reservoirs (F,G).

7.5 Elemental analysis of dolomite cement

Saddle dolomite indicative of precipitation from hot fluids was found associated with fractures, with a greater volume present in the lower Thamama (Reservoirs F and G) than the Upper Thamama (Reservoir B). Saddle dolomite is localised to fractures and large pores close to the faults only, confirming precipitation from fluids that flowed through the fractures. The occurrence of hydrocarbon inclusions in both burial dolomite cements can indicate that cementation was at least partly coincident with hydrocarbon migration. Fractures probably aided in the flow of hot, dolomitising fluids and hydrocarbons. Saddle dolomite was sometimes associated with stylolites in reservoirs G oil and B water, which indicates that both dolomitization and

stylolitization took place during the same time in some areas of these two reservoirs. Sr is low in all dolomite in fractures indicating no influence of exotic fluids. Dolomite in fractures in the Thamama is ferroan dolomite, indicating of formation in a reducing and deep burial setting. Fracture Set 1 has more is more Fe rich than Fracture Set 3. Dolomite cement zone 1 in the reservoirs shows different Mg:Ca values, with Reservoir G showing ~2.45 , Reservoir G ~2.2, and Reservoir B ~1.8. These values therefore decrease (becoming more calcic) through geological time. It is possible that this is due to changes in seawater, which is known to show marked changes in Mg:Ca during the Lower Cretaceous.

7.5 Fractures and cement fill geochemistry: Wadi Al Rahaba outcrop

The outcrop in Wadi Rahaba has two main sets of fractures:

1- F1, cemented with blocky calcite and trending NS, dipping 45°
2- F2, cemented with blocky calcite and trending EW, dipping 90°

Both fracture sets F1 and F2 are most probably following the fracture systems within the Cretaceous in onshore and offshore Abu Dhabi. F1, is related to the NS orientation fracture system consistent to the Arabian Trend sets caused by Cenozoic compression. F2 is related to the EW orientation fracture system matching Tethyan extensional trend sets. A third open fracture set follows the orientation of F1 (NS), and may be created by reactivation caused by uplift. Fractures in the Thamama outcrop differ from the fractures of the Thamama subsurface in the cement type (blocky and equant calcite and saddle dolomite in the subsurface; blocky calcite in the outcrop), the number of cement zones (more in the outcrop than the subsurface) and the number of fracture sets (more in the subsurface than outcrop).

The general $^{m}Mg/^{m}Ca$ values vary in each reservoir. Thamama C shows a range of ~0.4-0.9, Thamama B ~0.1-0.3, and Thamama A ~0.3-0.6. This might infer

that Thamama B precipitated at overall higher temperatures than Thamama A and C. This agrees with subsurface $^{m}Mg/^{m}Ca$ values, where Thamama C shows a range of ~0.42-0.48, Thamama B ~0.14-0.072 and Thamama A ~0.37-0.45. This might infer that Thamama C precipitated at overall lower temperatures than Thamama A and B. Mn and Fe values were very low for the Upper Thamama in both subsurface and surface, except for the outcrop samples Thamama C Reservoir. Sr values were very low in all the outcrop and subsurface reservoirs, meaning no involvement of exotic fluid. Based on the above elemental analysis comparison, it can be concluded that the blocky calcite cement in both outcrop and subsurface has the same characteristics (except for the Mn, Fe in outcrop Reservoir C) and was precipitated in deep burial environment. The oil charge had no effect on the outcrop Reservoirs, as they were uplifted before oil migration.

7.5 In-situ stable oxygen isotope analysis of fracture calcite cements for constraining precipitation temperatures

The cement in blocky calcite in the fractures is relatively late and young, and of generally deep burial origin showing temperature ranges of 109°C - 125°C. Reservoirs C and F, however, show temperatures lower ranges of 58°C - 70°C in the older cement zones, and 116°C in Reservoir F younger zones. There is no evidence for precipitation in the meteoric environment. Based on the large range of calcite cement growth temperatures (58°C -125°C) and CL patterns, a prolonged period of cement precipitation is present in Fracture Set 1. The $\delta^{18}O$ results showed good agreement with $^{m}Mg/^{m}Ca$ results in Fracture Set 1. Each Reservoir shows a different range of temperatures of precipitation: Reservoir A 119°C –123°C, Reservoir B 120°C –128°C, Reservoir C 67°C –73°C, Reservoir F 56°C –120°C, and Reservoir G 109°C –116°C. Fracture Set 1 had a higher temperature and longer burial history than Fracture Set 3 (Fig. 7.1).

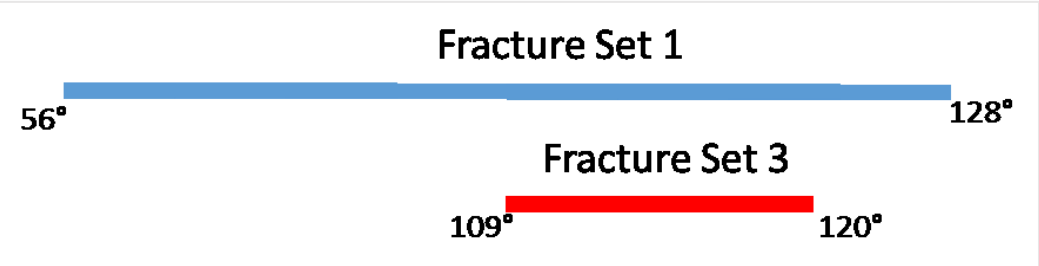

Figure 7.1. Comparison between temperature in Fracture Set 1 and Fracture Set 3 of the subsurface Thamama

7.6 Discussion

The complicated nature of Field A due to faulting and fracturing can make reservoir development planning challenging. The current field simulation models for the five Thamama Reservoirs lack the fractures effect on the reservoirs fluid flow, as they are considered insignificant (Khoori, pers comm). Fractures are sub-seismic features and do not appear in the latest high resolution 3D seismic survey (2006-2007) and the 3D VSP (Vertical seismic profile) conducted in the field. The current understanding of the fractures in Field A that this study provides, can be implemented in the field development plan. Drilling through a highly faulted field can cause a water cut, where the chances are high to encounter major faults.

However, the presence of open fractures can enhance oil productivity as they can markedly increase permeability, and provide a connection with matrix porosity where most oil is found (Sirat et al., 2013). Fracture Set 2 in Field A, found in all reservoirs can play an important role in field productivity, particularly as it is observed from petrographic analysis (Chapter 2) that most of these open fractures are connected.

The confirmed availability of open fractures in Field A is of great importance for field development plans, where fractures existence must be taken into consideration especially for Lower Thamama wells where the fracture apertures were substantial (30 mm). Cooperation of reservoir engineers and geologists is essential when deciding for future drilling campaigns. The future wells are preferred to be drilled in

high fracture intensity areas of the field within the oil pool, as drilling close to OWC (Oil-water contact) can result in early water cut to the wells.

7.7 Conclusion

In this thesis, a comprehensive study on the Thamama Formation to figure out the origin of fractures cements both in subsurface and outcrop was achieved, as well as creating a scheme for the number for fracture sets in each Thamama reservoir. Fracture sets were related to paragenetic sequences in each of the Thamama reservoirs. They showed to form very early in Reservoir F, as middle and late stages of the paragenetic sequence. For the rest of the reservoirs they formed in middle and late stages of the whole paragenetic sequence.

A suggested history for the relation of tectonic events with the fractures formations was explained based on the resulting paragenetic sequences, where the timing of fractures was correlated to major stress changes in the area.

In situ isotopes values were measured for the first time in Field A fracture cements. The temperature results assured previous studies results in the area in general, but came up with higher temperatures results for the fracture late fracture cements. The chemistry of the evolving fluids was studied by analysing trace elements found in the fractures' cements acquired from well cores and outcrop samples.

7.8 Future work

This PhD work has suggested several avenues for future studies:

1- Fluid inclusion analysis for oil and water would help in constraining the absolute temperature in the reservoirs.
2- An outcrop field study for the Lower Thamama exposures in Oman could be undertaken, to enable a more complete comparison between subsurface and outcrop.

3- 3D images for the outcrop in Wadi Rahaba is recommended, by using GEOREKA software newly issued in the industry. The new software uses videos and images taken from the field to create 3D images that can help in mapping fractures in details without needing to return to the location. Imaging fractures in 3D can help in measuring fractures directions and layers dipping and in building a geological model for the outcrop.
4- Fracture modelling using the results of this study in building DFN (Discrete Fracture Network) for Field A, and incorporating this into the reservoir model. This model is generated stochastically, conditioned with available data from boreholes image data, cores, (microseismic) and seismic (Moos, 2012). This will help in future well planning and operation.
5- Compare fracture data gained from this study with image logs available for Field A for the same wells to better understanding of reservoir characterization.
6- More studies on fracture cement elemental and ion probe analysis is suggested to be done on the water wells
7- Tracing Fracture Set 2 through the entire field, using the large numbers of available cores in the field core store, as well as coring new drilled wells in the Upper and Lower Thamama will give an enhanced picture for the distribution of open fractures throughout Field A.
8- Reservoir history matching is recommended from wells both close and further away from faults that are orientated with the open Fracture Set 2. This will help in understanding the real effect of Fracture Set 2 in the fluid flow in Field A.

References

Abidi, R., N. Slim-Shimi, A. Somarin, and Henchiri, M., 2010, Mineralogy and fluid inclusions study of carbonate-hosted Mississippi valley-type Ain Allega Pb-Zn-Sr-Ba ore deposit, Northern Tunisia: Journal of African Earth Sciences, v. 57, no. 3, p. 262–272, doi:10.1016/j.jafrearsci.2009.08.006.

Accumulation, S., and S. Spreading, 1974, Geological Society of America Bulletin: Geological Society Of America Bulletin, v. 104, no. 5, p. 528–542, doi:10.1130/0016-7606(1954)65.

Agosta, F., M. Alessandroni, M. Antonellini, E. Tondi, and Giorgioni, M., 2010, From fractures to flow : A field-based quantitative analysis of an outcropping carbonate reservoir: Tectonophysics, v. 490, p. 197–213, doi:10.1016/j.tecto.2010.05.005.

Ahlbrandt, T. S., R. M. Pollastro, T. R. Klett, C. J. Schenk, S. J. Lindquist, and J. E. Fox, 2000, Region 2 Assessment summary — Middle East And North Africa in U.S.: Geological Survey Digital Data Series 60.

Alaabed, S., and A. M. Soltan, 2014, United Arab Emirates limestones : impact of petrography on thermal behaviour: Mineralogy and Petrology, p. 837–852, doi:10.1007/s00710-014-0329-3.

Al-Aasm, I. S., F. Ghazban, and M. Ranjbaran, 2009, Dolomitization And Related Fluid Evolution In The Oligocene - Miocene Asmari Formation, Gachsaran Area, Sw Iran: Petrographic And Isotopic Evidence: Journal of Petroleum Geology, v. 32, no. 3, p. 287–304, doi:10.1111/j.1747-5457.2009.00449.x.

Al-Aasm, I. S., and J. J. Packard, 2000, Stabilization of early-formed dolomite : a tale of divergence from two Mississippian dolomites: Sedimentary Geology, v. 131, p. 97–108.

Al Bloushi M., 2013, Diagenesis Study of The Thamama Zone-A, Asab Field, UAE, Master's thesis, The Petroleum Institute, Abu Dhabi, UAE, 131 p.

Ali, M. Y., and A. Farid, 2016, Cretaceous – Neogene Structural Evolution Of SE Abu Dhabi, United Arab Emirates: Journal of Petroleum Geology, v. 39, no. July, p. 221–245.

Allen, M., J. Jackson, and R. Walker, 2004, Late Cenozoic reorganization of the Arabia-Eurasia collision and the comparison of short-term and long-term deformation rates: Tectonics, v. 23, doi:10.1029/2003TC001530.

Alsharhan, A., 1985, Petrography, sedimentology, diagenesis and reservoir characteristics of the Shuaiba and Kharaib formations Barremian-mid Aptian carbonate sediments of Abu Dhabi, United Arab Emirates, Degree of Doctor of Philosophy, University of South Carolina, USA, 159 p.

Alsharhan, A. S., and D. F. Williams, 1987, Petrography and stable isotope composition of baroque dolomite from the Shuaiba formation (lower cretaceous), Abu Dhabi, United Arab Emirates: Journal of African Earth Sciences (1983), v. 6, no. 6, p. 881–890, doi:10.1016/0899-5362(87)90047-9.

Alsharhan, A. S., 1989, Petroleum Geology of The United Arab Emirates: Journal of Petroleum Geology v. 12, no. 3, p. 253–288.

Alsharhan, A. S., and C. G. S. C. Kendall, 1991, Cretaceous chronostratigraphy, unconformities and eustatic sealevel changes in the sediments of Abu Dhabi, United Arab Emirates: Cretaceous Research, v. 12, no. 4, p. 379–401, doi:10.1016/0195-6671(91)90016-6.

Alsharhan, A., and A. Nairn, 2003, Hydrocarbon Habitat Of The Greater Arabian Basin: Sedimentary Basins and Petroleum Geology of the Middle East, p. 525–649, doi:10.1016/b978-044482465-3/50012-7.

Alsharhan, A. S., Rollinson, H.R., Searle, M.P., Abbasi, A.I., Al-Lazki, A.I. and Al Kindi, M.H., Eds., 2014, Petroleum systems in the Middle East: Tectonic Evolution of the Oman Mountains: Geological Society. v. 392, London, 361-408.

Armenteros, I., 2010, Diagenesis of Carbonates in Continental Settings: Elsevier, 61-151 p., doi:10.1016/S0070-4571(09)06202-5.

Austermann, J., and G. Iaffaldano, 2013, The role of the Zagros orogeny in slowing down Arabia-Eurasia convergence since ~ 5 Ma: Tectonics, v. 32, no. February, p. 351–363, doi:10.1002/tect.20027.

Awad, A., I. Mohamed, H. Belhaj, J. S. Gomes, and A. Bera, 2017, Petrographic and diagenetic studies of thick transition zone of a middle-east carbonate reservoir: v. 8, no. 1, p. 1–10, doi:10.5897/JPGE2016.0244.

Aydin, A., 2000, Fractures , faults , and hydrocarbon entrapment , migration and flow: Marine and petroleum geology, v. 17, 797-814.

Baker, P. A., J. M. Gieskes, and H. Elderfield, 1982, Diagenesis Of Carbonates In Deep-Sea Sediments--Evidence From Sr/Ca Ratios And Interstitial Dissolved Sr^{2+} Data: Journal of Sedimentary Petrology, v. 52, no. 1, p. 71–82.

Balter, V., C. Lécuyer, and J. Barrat, 2011, Reconstructing seawater Sr / Ca during the last 70 My using fossil fish tooth enamel: Palaeogeography, Palaeoclimatology, Palaeoecology, v. 310, no. 1–2, p. 133–138, doi:10.1016/j.palaeo.2011.02.024.

Barber, D. J., R. J. Reeder, and D. J. Smith, 1985, A tem microstructural study of dolomite with curved faces (saddle dolomite): p. 82–92.

Barnaby, R. J., and J. D. Rimstidt, 1989, Redox conditions of calcite cementation interpreted from Mn and Fe contents of authigenic calcites: Geological Society of America Bulletin, v. 101, no. 6, p. 795–804, doi:10.1130/0016-7606(1989)101<0795:RCOCCI>2.3.CO;2.

Barrientos, N., C. H. Lear, M. Jakobsson, C. Stranne, M. O. Regan, T. M. Cronin, A. Y. Gukov, and H. K. Coxall, 2018, ScienceDirect Arctic Ocean benthic foraminifera Mg/Ca ratios and global Mg/Ca-temperature calibrations: New constraints at low temperatures: Geochimica et Cosmochimica Acta, doi:10.1016/j.gca.2018.02.036.

Bertotti, G., K. Bisdom, M. Van Eijk, F. Hameka, A. Vis, H. Bezerra, and J. Reijmer, 2014, Fractures and Fracture Networks in Carbonate Reservoirs : A Geological Perspective: In AAPG International Conference & Exhibition, v. 41470.

Bjørlykke, K., 2015, Sedimentary Geochemistry How Sediments are Produced: v. 105, doi:10.1007/978-3-642-34132-8.

Boggs, S., & Krinsley, D., 2006, Application of cathodoluminescence imaging to the study of sedimentary rock, New York, NY: Cambridge University Press.

Bourque, P.-A., and L. Raymond, 1994, Diagenetic alteration of early marine cements of Upper Silurian stromatactis: Sedimentology, v. 41, no. 2, p. 255–269, doi:10.1111/j.1365-3091.1994.tb01404.x.

Breesch, L., R. Swennen, B. Vincent, R. Ellison, and B. Dewever, 2010, Dolomite cementation and recrystallization of sedimentary breccias along the Musandam Platform margin (United Arab Emirates): Journal of Geochemical Exploration, v. 106, no. 1–3, p. 34–43, doi:10.1016/j.gexplo.2010.02.005.

Breesch, L., R. Swennen, B. Dewever, F. Roure, and B. Vincent, 2009, Diagenesis and fluid system evolution in the Northern Oman Mountains , United Arab Emirates Diagenesis and fluid system evolution in the northern Oman Mountains , United Arab Emirates : Implications for petroleum exploration: no. April, doi:10.1016/j.gexplo.2008.12.046.

Breesch, L., R. Swennen, and B. Vincent, 2009, Fluid flow reconstruction in hanging and footwall carbonates : Compartmentalization by Cenozoic reverse faulting in the Northern Oman Mountains (UAE): v. 26, p. 113–128, doi:10.1016/j.marpetgeo.2007.10.004.

Buchem, F. S. P. Van, B. Pittet, H. Hillgärtner, and I. Français, 2015, High-resolution sequence stratigraphic architecture of Barremian/Aptian carbonate systems in Northern Oman and the United Arab Emirates (Kharaib and Shu ' aiba formations) High-resolution Sequence Stratigraphic Architecture of Barremian/Aptian Carbonate Systems in Northern Oman and the United Arab Emirates (Kharaib and Shuaiba Formations): no. January 2002.

Buchem, F., Razin, P., Homewood, P., Philip, J., Eberli, G., Platel, J., Roger, J., Eschard, R., Desaubliaux, G., Boisseau, T., Leduc, J., Labourdette, R., and Cantaloube, S., 1996, High Resolution Sequence Stratigraphy of the Natih Formation (Cenomanian/Turonian) in Northern Oman: Distribution of Source Rocks and Reservoir Facies: GeoArabia, v. 1, p. 56-91.

Budd, D. A., 1989, Micro-rhombic calcite and microporosity in limestones: a geochemical study of the lower cretaceous thamama group, U.A.E.: Sedimentary Geology, v. 63, no. 3–4, p. 293–311, doi:10.1016/0037-0738(89)90137-1.

Budd, D. A., E. L. Frost, K. W. Huntington, and P. F. Allwardt, 2013, Syndepositional Deformation Features in High-Relief Carbonate Platforms: Long-Lived Conduits For Diagenetic Fluids: p. 12–36, doi:10.2110/jsr.2013.3.

Burns, S. J., P. A. Baker, N. Carolina, and C. Martinez, 1987, A Geochemical Study of Dolomite in the Monterey Formation, California: Journal of Sedimentary Research, v. 57, no. 1, p. 128–139.

Callen, J. M., 2016, In Situ Geochemistry of Middle Ordovician Dolomites of the Upper Mississippi Valley : Evaluation of the Dorag Model and New Implications for Dolomitizing Fluids.

Callot, J., and L. Breesch, 2010, Paleo-fluids characterisation and fluid flow modelling along a regional transect in Northern United Arab Emirates (UAE): p. 413–437, doi:10.1007/s12517-010-0233-z.

Callot, J., and L. Breesch, 2013, Paleo-fluids characterisation and fluid flow modelling along a regional transect in Northern United Arab Emirates (UAE): no. January 2015, doi:10.1007/s12517-010-0233-z.

Chilingarian, G., Wolf, K., 2018, Diagenesis Gulf 2: Developments in Sedimentology, no. 43.

Chowdhury, A. H., and J. P. A. Noble, 1996, Origin, distribution and significance of carbonate cements in the Albert formation reservoir sandstones, New Brunswick, Canada: Marine and Petroleum Geology, v. 13, no. 7, p. 837–846, doi:10.1016/0264-8172(96)00002-5.

Clark, W. J., and Herron, M., 2009, Dolomite : Perspectives on a Dolomite is a metastable carbonate: Oilfield Review Autumn, p. 32–45.

Coggon, R. M., Teagle, D. A. H. and Smith-duque, C. E., 2010, Reconstructing Past Seawater Mg/Ca: Science, v. 327, p. 1114-1117.

Collins, J. F., and S. W. Buol, 1970, Effects of fluctuations in the Eh-pH environment on iron and/or manganese equilibria: Soil Science, p. 111–118, doi:10.1097/00010694-197008000-00006.

Controls, D., and P. Organic, n.d., Diagenesis Diagenesis Diagenesis Diagenesis vs . Metamorphism Controls on Diagenesis Shallow Carbonate Diagenesis.

Cooper, D. J. W., M. Y. Ali, M. P. Searle, C. Park, T. Wells, P. O. Box, A. Dhabi, and U. A. Emirates, 2015, Structure of the northern Oman Mountains from the Semail Ophiolite to the Foreland Basin: p. 129–153.

Cox, P., R. Wood, J. Dickson, H. A. Rougha, H. Shebl, and P. Corbett, 2010, Dynamics of cementation in response to oil charge: Evidence from a Cretaceous carbonate field, U.A.E.: Sedimentary Geology, v. 228, no. 3-4, p. 246–254, doi:10.1016/j.sedgeo.2010.04.016.

Craig J. R., and D.J. Vaughan, Ore Microscopy and Ore Petrography, 2nd Edition, Chichester and New York (John Wiley and Sons, Ltd). 1995 xiv 434 pp. Price s ISBN 0-471-115991., 1997: Mineralogical Magazine, v. 61, no. 404, p. 150–151, doi:10.1180/minmag.1997.061.404.17

Croizé, D., K. Bjørlykke, J. Jahren, and F. Renard, 2010, Experimental mechanical and chemical compaction of carbonate sand: Journal of Geophysical Research, v. 115, no. B11, doi:10.1029/2010jb007697.

Czerniakowski, L. A., K. C. Lohmann, and J. Wilson, 1984, Closed-system marine burial diagenesis: isotopic data from the Austin Chalk and its components: Sedimentology, v. 31, no. 6, p. 863–877, doi:10.1111/j.1365-3091.1984.tb00892.x.

Davies, G. R., and L. B. Smith, 2007, Structurally controlled hydrothermal dolomite reservoir facies: An overview: Reply: AAPG Bulletin, v. 91, no. 9, p. 1342–1344, doi:10.1306/04290707031.

Demény, A., S. Kele, and Z. Siklósy, 2010, Empirical equations for the temperature dependence of calcite-water oxygen isotope fractionation from 10 to 70°C: Rapid Communications in Mass Spectrometry, v. 24, no. 24, p. 3521–3526, doi:10.1002/rcm.4799.

Deschamps, R., E. Kohler, M. Gasparrini, O. Durand, T. Euzen, and F. Nader, 2012, Impact of Mineralogy and Diagenesis on Reservoir Quality of the Lower Cretaceous Upper: Oil & Gas Science and Technology, v. 67, no. 1, doi:10.2516/ogst/2011153.

Dickson, J., P. C. Smalley, A. Råheim, and D. E. Stijfhoorn, 1990, Intracrystalline carbon and oxygen isotope variations in calcite revealed by laser microsampling: Geology, v. 18, no. 9, p. 809, doi:10.1130/0091-7613(1990)018<0809:icaoiv>2.3.co;2.

Dix, G. R., S. Sharma, I. S. Al-Aasm, M. Coniglio, R. Linnen, J. F. V. Riva, and A. Achab, 2010, Hydrothermal dolomite in the Timiskaming outlier, central

Canadian Shield: Proxy for Late Ordovician tectonic activity: American Journal of Science, v. 310, no. 5, p. 405–423, doi:10.2475/05.2010.03.

Elmahdy, S. I., and M. M. Mohamed, 2013, Influence of geological structures on groundwater accumulation and groundwater salinity in Musandam Peninsula, UAE and Oman: Geocarto International, v. 28, no. 5, p. 453–472, doi:10.1080/10106049.2012.724455.

Ehrenberg, S. N., S. W. Lokier, L. I. U. Yaxin, and R. Chen, 2018, Depositional Cycles in A Lower Cretaceous Limestone Reservoir, Onshore Abu Dhabi: Journal of Sedimentary Research, v. 88, p. 753–776.

Ehrenberg, S. N., S. Morad, L. Yaxin, and R. Chen, 2016, Stylolites and Porosity In A Lower Cretaceous Limestone Reservoir, Onshore Abu Dhabi, U.A.E.: Journal of Sedimentary Research, v. 86, no. 10, p. 1228–1247, doi:10.2110/jsr.2016.68.

Eyles, N., 1993, Earth's glacial record and its tectonic setting: Earth-Science Reviews, v. 35, p. 1–2.

Ferket, H., N. Guilhaumou, F. Roure, and R. Swennen, 2011, Insights from fluid inclusions , thermal and PVT modeling for paleo-burial and ´ rdoba petroleum system (NE Mexico) thermal reconstruction of the Co: Marine and Petroleum Geology, v. 28, no. 4, p. 936–958, doi:10.1016/j.marpetgeo.2010.01.020.

Fleischer, M., and R. L. Parker, 1967, Data of geochemistry, sixth edition: Washington, D.C., U.S. G.P.O.

Flynn, G. J. et al., 2006, Elemental Compositions of Comet 81P/Wild 2 Samples Collected by Stardust, Science, v. 314, p. 1731-1735.

Fontana, S., F. H. Nader, S. Morad, A. Ceriani, and I. S. Al-Aasm, 2010, Diagenesis of the Khuff Formation (Permian–Triassic), northern United Arab Emirates: Arabian Journal of Geosciences, v. 3, no. 4, p. 351–368, doi:10.1007/s12517-010-0198-y

Fontana, S., F. H. Nader, S. Morad, and J. Mengus, 2014, Fluid – rock interactions associated with regional tectonics and basin evolution: Arabian Journal of Geosciences, p. 660–690, doi:10.1111/sed.12073.

Fouke, B. W., and R. J. Reeder, 1992, Surface structural controls on dolomite composition: Evidence from sectoral zoning: Geochimica et Cosmochimica Acta, v. 56, no. 11, p. 4015–4024, doi:10.1016/0016-7037(92)90013-9.

Gale, J. F. W., S. E. Laubach, R. A. Marrett, J. E. Olson, J. Holder, and R. M. Reed, 2004, Predicting and characterizing fractures in dolostone reservoirs: using the link between diagenesis and fracturing: Geological Society, London, Special Publications, v. 235, no. 1, p. 177–192, doi:10.1144/gsl.sp.2004.235.01.08.

Geske, A., J. Zorlu, D. K. Richter, D. Buhl, A. Niedermayr, and A. Immenhauser, 2012, Impact of diagenesis and low grade metamorphosis on isotope ($\delta^{26}Mg$, $\delta^{13}C$, $\delta^{18}O$ and $Sr/^{86}Sr$) and elemental (Ca, Mg, Mn, Fe and Sr) signatures of Triassic sabkha dolomites: Chemical Geology, v. 332–333, p. 45–64, doi:10.1016/j.chemgeo.2012.09.014.

Glennie, K. W., 2001, Evolution of the Emirates' land surface: an introduction. United Arab Emirates, a new perspective. London: Trident Press Ltd. p, 9-27.

Gonzalez, L. A., 2016, Diagenetic Model of Carbonate Rocks of Guri Member of Mishan Formation (Lower to Middle Miocene) SE Zagros Basin-Iran Diagenetic Model of Carbonate Rocks of Guri Member of Mishan Formation (Lower to Middle Miocene) SE Zagros Basin , Iran: Geological Society of India, doi:10.1007/s12594-014-0112-4.

Goodenough, K. M., R. J. Thomas, M. T. Styles, D. I. Schofield, and C. J. Macleod, 2014, Records of Ocean Growth and Destruction in the Oman-UAE Ophiolite: Elements, v. 10, no. 2, p. 109–114, doi:10.2113/gselements.10.2.109.

Cosgrove, J., and Ameen, M., 2015, A comparison of the geometry , spatial organization and fracture patterns associated with forced folds and buckle folds: The Geological Society of London, 169, 7 21. 1-86239-060-6/00/15.00.

Gregg, J. M., and S. E. Kaczmarek, 2015, Mineralogy, nucleation and growth of dolomite in the laboratory and sedimentary environment : A review: Sedimentology, doi:10.1111/sed.12202.

Grötsch, J., Suwaina, O., Ajlani, G., Taher, A., El-Khassawneh, R., Lokier, S., Coy, G., Weerd, E., Masalmeh, S., and Dorp, J., 2003, The Arab Formation in central Abu Dhabi : 3-D reservoir architecture and static and dynamic modeling The Arab Formation in central Abu Dhabi : GeoArabia, Vol. 8, No. 1, 2003.

Gumati, Y., 1993, Kinetic modelling, thermal maturation and hydrocarbon generation in the United Arab Emirates: Marine and Petroleum Geology, v. 10, no. 2, p. 153–161, doi:10.1016/0264-8172(93)90020-s.

Haeri-Ardakani, O., I. Al-Aasm, and M. Coniglio, 2013, Petrologic and geochemical attributes of fracture-related dolomitization in Ordovician carbonates and their spatial distribution in southwestern Ontario, Canada: Marine and Petroleum Geology, v. 43, p. 409–422, doi:10.1016/j.marpetgeo.2012.12.006.

Hamdan, A. R. A., and A. S. Alsharhan, 1991, Palaeoenvironments and palaeoecology of the rudists in the Shuaiba formation (aptian) United Arab Emirates: Journal of African Earth Sciences (and the Middle East), v. 12, no. 4, p. 569–581, doi: 10.1016/0899-5362(91)90018-T.

Hardie, L. A., 1996, Secular variation in seawater chemistry : An explanation for the coupled secular variation in the mineralogies of marine limestones and potash evaporites over the past 600 m. y.: Geology, 3, p. 279–283.

Heasley, E. C., R. H. Worden, and J. P. Hendry, 2000, Cement distribution in a carbonate reservoir: recognition of a palaeo oil–water contact and its relationship to reservoir quality in the Humbly Grove field, onshore, UK: Marine and Petroleum Geology, v. 17, no. 5, p. 639–654, doi:10.1016/s0264-8172(99)00057-4.

Hollis, C., 2011, Diagenetic controls on reservoir properties of carbonate successions within the Albian – Turonian of the Arabian Plate: Petroleum Geoscience, no. 2001, doi: 10.1144/1354-079310-032.

Hood, A. V. S., and M. W. Wallace, 2015, Extreme ocean anoxia during the Late Cryogenian recorded in reefal carbonates of Southern Australia: Precambrian Research, v. 261, p. 96–111, doi:10.1016/j.precamres.2015.02.008.

Hoseinabadi, M., Mahboubi, A., Shabestari, G., and Motamed, M., 2016, Depositional environment, diagenesis, and geochemistry of Devonian Bahram formation carbonates, Eastern Iran: Arabian Journal of Geosciences, 9(1), 1-25.

Hossain, H. M. Z., J. S. Armstrong-altrin, and A. N. Sial, 2013, Stable Carbon And Oxygen Isotopic Composition Of Mio- Pliocene Bivalve Shells And Calcareous Sediments In Nhila Anticline, Southeast Bengal Basin, Bangladesh: Journal of Life and Earth Science v. 8.

Huc, A. Y., P. Nederlof, R. Debarre, and B. Carpentier, 2000, Pyrobitumen occurrence and formation in a Cambro – Ordovician sandstone reservoir , Fahud Salt Basin , North Oman: Chemical Geology, p. 99–112.

Huck, S., S. Wohlwend, R. Coimbra, N. Christ, and H. Weissert, 2017, Disentangling shallow-water bulk carbonate carbon isotope archives with evidence for multi-stage diagenesis : An in-depth component-specific petrographic and geochemical study from Oman (mid-Cretaceous): The Depositional Record, p. 233–257, doi:10.1002/dep2.35.

Hughes, G. W., 1998, Middle East Aptian rudist-foraminiferal-algal associations and their possible modern Arabian Gulf analogue: Geobios, v. 31, p. 147–158, doi: 10.1016/S0016-6995(98)80073-9.

Huntington, K. W., D. A. Budd, B. P. Wernicke, and J. M. Eiler, 2011, Use of Clumped-Isotope Thermometry To Constrain the Crystallization Temperature of Diagenetic Calcite: Journal of Sedimentary Research, v. 81, no. 9, p. 656–669, doi:10.2110/jsr.2011.51.

Husson, J. M., J. A. Higgins, A. C. Maloof, and B. Schoene, 2015, ScienceDirect Ca and Mg isotope constraints on the origin of Earth's deepest d 13 C excursion: Geochimica Et Cosmochimica Acta, v. 160, p. 243–266, doi:10.1016/j.gca.2015.03.012.

Jacquemyn, C., H. El, D. Hunt, G. Casini, and R. Swennen, 2014, Dolomitization of the Latemar platform : Fluid flow and dolomite evolution: Marine and Petroleum Geology, v. 55, p. 43–67, doi:10.1016/j.marpetgeo.2014.01.017.

Jeong, J., A. A. Al-Ali, H. Jung, A. Abdelrahman, A. Dhafra, H. T. Shebl, J. Kang, A. Bonin, M. D. D. Perriere, and A. Foote, 2017, Controls on Reservoir Quality and Reservoir Architecture of Early Cretaceous carbonates in an Abu Dhabi Onshore Field Lekhwair, Kharaib and Lower Shuaiba Formations: Abu Dhabi International Petroleum Exhibition & Conference, doi:10.2118/188420-ms.

Kaczmarek, S. E., J. A. Y. M. Gregg, B. Pickens, D. L. Bish, H. G. Machel, B. W. Fouke, and B. W. Fouke, 2017, Dolomite, Very High-Magnesium Calcite , And Microbes — Implications For The Microbial Model Of Dolomitization: no. 109, p. 1–14.

Kaczmarek, S. E., and D. F. Sibley, 2011, On the evolution of dolomite stoichiometry and cation order during high-temperature synthesis experiments : An alternative model for the geochemical evolution of natural dolomites: Sedimentary Geology, p. 1–11, doi:10.1016/j.sedgeo.2011.07.003.

Kahle, B. J. C. F., 1986, Dendritic Calcite Crystals Formed by Calcification of Algal Filaments in a Vadose Environment: SEPM Journal of Sedimentary Research, v. Vol. 56, doi:10.1306/212f88c3-2b24-11d7-8648000102c1865d.

Kaldi, J., 1989, Diagenetic microporosity (chalky porosity), Middle Devonian Kee Scarp reef complex, Norman Wells, Northwest Territories, Canada: Sedimentary Geology, v. 63, no. 3–4, p. 241–252, doi:10.1016/0037-0738(89)90134-6.

Kendall, C. G., B. Bowen, A. Alsharhan, D.-K. Cheong, and D. Stoudt, 1991, Eustatic controls on carbonate facies in reservoirs, and seals associated with Mesozoic hydrocaron fields of the Arabian Gulf and the Gulf of Mexico: Marine Geology, v. 102, no. 1-4, p. 215–238, doi:10.1016/0025-3227(91)90009-s.

Kennedy, L. A., 2001, Low-temperature recrystallization in calcite : Mechanisms and consequences: no. 11, p. 1027–1030.

Kim, S., and O'Neil, J., 1997, Equilibrium and nonequilibrium oxygen isotope effects in synthetic carbonates: Geochimica et Cosmochimica Acta, v. 61, no. 16, p. 3461–3475.

Kolchugin, A. N., A. Immenhauser, B. F. Walter, and V. P. Morozov, 2016, Diagenesis of the palaeo-oil-water transition zone in a Lower Pennsylvanian carbonate reservoir: Constraints from cathodoluminescence microscopy, microthermometry, and isotope geochemistry: Marine and Petroleum Geology, v. 72, p. 45–61, doi:10.1016/j.marpetgeo.2016.01.014.

Kusky, T., C. Robinson, and F. El-Baz, 2005, Tertiary-Quaternary faulting and uplift in the northern Oman Hajar Mountains: Journal of the Geological Society, v. 162, no. 5, p. 871–888, doi:10.1144/0016-764904-122.

Lambert, L., C. Durlet, J.-P. Loreau, and G. Marnier, 2006, Burial dissolution of micrite in Middle East carbonate reservoirs (Jurassic–Cretaceous): keys for recognition and timing: Marine and Petroleum Geology, v. 23, no. 1, p. 79–92, doi:10.1016/j.marpetgeo.2005.04.003.

Laubach, S. E., J. E. Olson, P. Eichhubl, S. Fomel, and R. A. Marrett, 2010, Natural Fractures from the Perspective of Diagenesis: CSEG Recorder, p. 26–30.

Lavenu, A. P. C., J. Lamarche, A. Gallois, and B. D. M. Gauthier, 2013, Tectonic versus diagenetic origin of fractures in a naturally fractured carbonate reservoir analog (Nerthe anticline , southeastern France): AAPG Bulletin, v. 12, no. 12, p. 2207–2232, doi:10.1306/04041312225.

Lavenu, A. P. C., J. Lamarche, R. Salardon, A. Gallois, L. Marié, and B. D. M. Gauthier, 2014, Relating background fractures to diagenesis and rock physical properties in a platform e slope transect . Example of the Maiella Mountain (central Italy): Marine and Petroleum Geology, v. 51, p. 2–19, doi:10.1016/j.marpetgeo.2013.11.012.

Lea, D. W., and S. Barbara, 2014, Author's personal copy Elemental and Isotopic Proxies of Past Ocean Temperatures: Elsevier Ltd., 373-397 p., doi:10.1016/B978-0-08-095975-7.00614-8.

Li, M., M. Y. Ali, G. Tao, W. Alakberi, and H. Alnuaimi, 2017, monitoring of induced microseismicity in an onshore oilfield from Abu Dhabi, United Arab Emirates_ Implications for carbonate reservoir monitoring: Journal of Petroleum Science and Engineering, v. 152, no. September 2016, p. 33–48, doi:10.1016/j.petrol.2017.02.012.

Lu, P., and Cantrell, D., 2016, Reactive transport modelling of reflux dolomitization in the Arab-D reservoir, Ghawar field, Saudi Arabia: Sedimentology, p. 865–892, doi:10.1111/sed.12241.

Lueftinger, T., R. Kuschnig, N. E. Piskunov, and W. W. Weiss, 2003, Astrophysics Doppler Imaging of the Ap star Ursae Majoris : Ca, Cr, Fe, Mg, Mn, Ti, Sr: Astronomy & Astrophysics, v. 1042, p. 1033–1042.

Machel, H., 2004, Concepts and models of dolomitization : a critical reappraisal: The Geological Society of London, v. 3, p. 7–63.

Machel, H. G., B. Jonathan, Patricia, N., Kambesis, J. R., Mylroie, J. E,. Mylroie, M. J., 2014, Episodic Fluid Flow and Dolomitization By Methane-Bearing Pore Water of Marine Parentage In An Accretionary Prism Setting, Barbados, West Indies: Journal of Sedimentary Research, 84 (2): 58-71.

Marchitto, T. M., W. B. Curry, J. Lynch-stieglitz, S. P. Bryan, K. M. Cobb, and D. C. Lund, 2014, ScienceDirect Improved oxygen isotope temperature calibrations

for cosmopolitan benthic foraminifera: Geochimica et Cosmochimica Acta, v. 130, p. 1–11, doi:10.1016/j.gca.2013.12.034.

Maurer, F., K. Al-mehsin, B. J. Pierson, G. P. Eberli, G. Warrlich, D. Drysdale, and H. J. Droste, 2010, Facies characteristics and architecture of Upper Aptian Shu'aiba clinoforms in Abu Dhabi: GeoArabia Special Publication, v. 2 p. 445–468.

Maurer, F., R. Rettori, and R. Martini, 2007, Triassic stratigraphy, facies and evolution of the Arabian shelf in the northern United Arab Emirates: International Journal of Earth Sciences, v. 97, no. 4, p. 765–784, doi:10.1007/s00531-007-0194-y.

Mclaren, S. J., and S. J. Mclaren, 2018, Effects of Sea Spray on Vadose Diagenesis of Late Quaternary Aeolianites , Bermuda: Journal of Coastal Research, v. 17, no. 1, p. 228–240.

Meyers, W. J., and K. C. Lohmann, 1978, Microdolomite-Rich Syntaxial Cements: Proposed Meteoric-Marine Mixing Zone Phreatic Cements from Mississippian Limestones, New Mexico: SEPM Journal of Sedimentary Research, v. 48, no. 2.

Meyers, W., 1980, Compaction in Mississippian Skeletal Limestones, Southwestern New Mexico: Jouanal of Sedimentary Petrology, v. 50, no. 2, p. 457–474.

Minoletti, F., M. Hermoso, Y. Candelier, and I. Probert, 2014, Calibration of stable isotope composition ofThoracosphaera heimii(dinoflagellate) calcite for reconstructing paleotemperatures in the intermediate photic zone: Paleoceanography, v. 29, no. 12, p. 1111–1126, doi:10.1002/2014pa002694.

Mohammed, H. Q., 2017, Geomechanical Analysis of the Wellbore Instability Problems In Nahr Umr Formation Southern Iraq, Master thesis, Missouri University Of Science And Technology, USA, 85 p.

Moos, D., 2012, The Importance of Stress and Fractures in Hydrofracturing and Stimulation Performance : A Geomechanics Overview: v. 80255, doi: 10.2118/14589-PA.

Morad, S., Al-Aasm, I., Nader, F., Ceriani, A., Gasparrini, M., and Mansurbeg, H., 2012, Impact of diagenesis on the spatial and temporal distribution of reservoir quality in the Jurassic Arab D and C Members offshore Abu Dhabi oilfield, United Arab Emirates: GeoArabia, v. 17, no. 3, p. 17-56

Morad, D., F. H. Nader, M. Gasparrini, S. Morad, C. Rossi, E. Marchionda, F. Al, M. Martines, and H. Hellevang, 2018, Comparison of the diagenetic and reservoir quality evolution between the anticline crest and fl ank of an Upper Jurassic carbonate gas reservoir , Abu Dhabi , United Arab Emirates: Sedimentary Geology, v. 367, p. 96–113, doi:10.1016/j.sedgeo.2018.02.008.

Morad, D., M. Paganoni, A. A. Harthi, S. Morad, A. Ceriani, H. Mansurbeg, A. A. Suwaidi, I. S. Al-Aasm, and S. N. Ehrenberg, 2016, Origin and evolution of microporosity in packstones and grainstones in a Lower Cretaceous carbonate reservoir, United Arab Emirates: Geological Society, London, Special Publications, v. 435, no. 1, p. 47–66, doi:10.1144/sp435.20.

Morad, S., I. S. Al-Aasm, M. Sirat, and M. M. Sattar, 2010, Vein calcite in cretaceous carbonate reservoirs of Abu Dhabi: Record of origin of fluids and diagenetic conditions: Journal of Geochemical Exploration, v. 106, no. 1–3, p. 156–170, doi:10.1016/j.gexplo.2010.03.002.

Morse, J. W., R. K. Given, and B. H. Wilkinson, 1985, Kinetic control of morphology, composition, and mineralogy of abiotic sedimentary carbonates; discussion and reply: Journal of Sedimentary Research, v. 55, no. 6, p. 919–926, doi:10.1306/212f8846-2b24-11d7-8648000102c1865d.

Moshier, S. O., 1989, Development of microporosity in a micritic limestone reservoir, Lower Cretaceous, Middle East: Sedimentary Geology, v. 63, no. 3–4, p. 217–240, doi:10.1016/0037-0738(89)90133-4.

Murris, J., 2009, Hydrocarbon Habitat of The Middle East: Canadian Society of Petroleum Geologists, v. 6, no. 1980.

Muttoni, G., M. Gaetani, D. V Kent, D. Sciunnach, F. Berra, E. Garzanti, M. Mattei, and A. Zanchi, 2009, Opening of the Neo-Tethys Ocean and the Pangea B to Pangea A transformation during the Permian: GeoArabia, v. 14, no. 4.

Neilson, J. E., and N. H. Oxtoby, 2008, The relationship between petroleum, exotic cements and reservoir quality in carbonates – A review: v. 25, p. 778–790, doi:10.1016/j.marpetgeo.2008.02.004.

Neilson, J. E., N. H. Oxtoby, M. D. Simmons, I. R. Simpson, and N. K. Fortunatova, 1998, The relationship between petroleum emplacement and carbonate reservoir quality : examples from Abu Dhabi and the Amu Darya Basin: Marine and Petroleum Geology, v. 15, p. 57–72.

Nissen, E., M. Tatar, J. A. Jackson, and M. B. Allen, 2018, New views on earthquake faulting in the Zagros fold-and-thrust belt of Iran: Geophysical Journal International, p. 928–944, doi:10.1111/j.1365-246X.2011.5119.x.

No, R. C., and E. S., 2013, Diagenesis study of the Thamama Zone-A , Asab Field , UAE (ADNOC Onshore report).

Northern, O. F., and M. Y. Alkuwairan, n.d., Polygenetic Dolomite In Subtidal Sediments Of Northern Kuwait Bay, PhD thesis, Colorado School of Mines, USA.

Noufal, A., and M. Y. Ali, 2016, SPE-183108-MS Tectonic Map of Abu Dhabi, UAE: Society of Petroleum Engineers, doi:10.2118/183108-MS.

Online, C. B., 2018, Luminescence characteristics and diagenesis of carbonate sedimentary rocks: p. 109–133.

Paganoni, M., A. Al Harthi, D. Morad, S. Morad, A. Ceriani, H. Mansurbeg, A. Al Suwaidi, I. S. Al-Aasm, S. N. Ehrenberg, and M. Sirat, 2016, Impact of

stylolitization on diagenesis of a Lower Cretaceous carbonate reservoir from a giant oilfield, Abu Dhabi, United Arab Emirates: Sedimentary Geology, v. 335, p. 70–92, doi:10.1016/j.sedgeo.2016.02.004.

Pagel, M. et al., 2018, Improving paleohydrological and diagenetic reconstructions in calcite veins and breccia of a sedimentary basin by combining Δ47 temperature, δ18Owater and U-Pb age: Chemical Geology, v. 481, p. 1–17, doi:10.1016/j.chemgeo.2017.12.026.

Parrish, R. R., C. M. Parrish, and S. Lasalle, 2018, Vein calcite dating reveals Pyrenean orogen as cause of Paleogene deformation in southern England: Journal of the Geological Society, v. 175, no. 3, p. 425–442, doi:10.1144/jgs2017-107.

Pei-yuan, C., T. A. N. Xiu-cheng, L. I. U. Hong, and M. A. Teng, 2014, Formation mechanism of reservoir oolitic dolomite in Lower Triassic Feixianguan formation , northeastern Sichuan Basin , southwest China: Journal of Central South University, p. 3263–3274, doi:10.1007/s11771-014-2299-3.

Perkins, R. D., 1989, Origin of micro-rhombic calcite matrix within Cretaceous reservoir rock, West Stuart City Trend, Texas: Sedimentary Geology, v. 63, no. 3–4, p. 313–321, doi:10.1016/0037-0738(89)90138-3.

Perrin, C., L. Prestimonaco, G. Servelle, R. Tilhac, M. Maury, and P. Cabrol, 2014, Aragonite – calcite speleothems : identifying original and diagenetic features: Journal of Sedimentary Research, v. 84, p. 245–269.

Phillips, E., B. G. Survey, C. N. Waters, and B. G. Survey, 2013, Basin evolution: Frontiers in Earth Sciences, doi:10.1007/978-3-642-30609-9.

Powers, R., L. Ramirez, C. Redmond, and E. Elberg, 1966, Geology of the Arabian Peninsula; sedimentary geology of Saudi Arabia: Professional Paper, doi:10.3133/pp560d

Prentice, K., T. Dunkley, J. Lees, J. Young, P. Bown, G. Langer, and S. Fearn, 2014, ScienceDirect Trace metal (Mg / Ca and Sr / Ca) analyses of single coccoliths by Secondary Ion Mass Spectrometry: Geochimica et Cosmochimica Acta, v. 146, p. 90–106, doi:10.1016/j.gca.2014.09.041.

Pucéat, E., C. Lécuyer, S. M. F. Sheppard, G. Dromart, S. Reboulet, and P. Grandjean, 2003, Thermal evolution of Cretaceous Tethyan marine waters inferred from oxygen isotope composition of fish tooth enamels: Paleoceanography, v. 18, no. 2, doi:10.1029/2002pa000823.

Qing, H., 1998, Petrography and geochemistry of early-stage, fine- and medium-crystalline dolomites in the Middle Devonian Presquile Barrier at Pine Point, Canada: Sedimentology, v. 45, no. 2, p. 433–446, doi:10.1046/j.1365-3091.1998.0154f.x.

Radke, B. M., and R. L. Mathis, 1980, On the Formation and Occurrence of Saddle Dolomite: Journal of Sedimentary Petrology, v. 50, no. 4, p. 1149–1168.

Ramberg, H., 2003, Effect of spatial distribution of Hormuz salt on deformation style in the Zagros fold and thrust belt : an analogue modelling approach: Journal ofthe Geological Society, v. 160, p. 719–733.

Ranier, B. G., A. S. Al Suwaidi, R. B. Usnardo, S. K. A. Ziz, and R. S. Chroeder, 2003, New insight on the stratigraphy of the " Upper Thamama " in offshore Abu Dhabi (U. A. E): Notebooks on Geology, v. 05, p. 1–17.

Reeder, R. J., 2000, Constraints on Cation Order in Calcium-rich Sedimentary Dolomite: Aquatic Geochemistry, no. 1958, p. 213–226.

Reinhardt, E. G., W. Cavazza, R. T. Patterson, and J. Blenkinsop, 2000, Differential diagenesis of sedimentary components and the implication for strontium isotope analysis of carbonate rocks: Chemical Geology, v. 164, no. 3–4, p. 331–343, doi:10.1016/S0009-2541(99)00147-3.

Renard, F., 2010, Experimental and chemical compaction of carbonate sand: Journal of Geophysical Research Atmospheres, doi:10.1029/2010JB007697.

Renshaw, C. E., J. S. Dadakis, and S. R. Brown, 2000, Measuring fracture apertures : A comparison of methods: Geophysical Research Letters, v. 27, no. 2, p. 289–292.

Ries, J. B., 2010, Review : geological and experimental evidence for secular variation in seawater Mg/Ca (calcite-aragonite seas) and its effects on marine biological calcification: European Geosciences Union, p. 2795–2849, doi:10.5194/bg-7-2795-2010.

Rifai, R. I., Kolkas, M. M., Holail, H. M., & Khaled, K. A., 2006, Diagenesis and geochemistry of the Aptian dolomite (Cretaceous) in the Razzak oil field, western desert, Egypt: Carbonates and evaporates, 21.2: 176.

Road, P., N. Environment, and B. G. Survey, 2015, Subduction zone polarity in the Oman Mountains : implications for ophiolite emplacement: The Geological Society of London, p. 467–480.

Rodriguez-Blanco, J. D., S. Shaw, and L. G. Benning, 2015, A route for the direct crystallization of dolomite: American Mineralogist, v. 100, no. 5-6, p. 1172–1181, doi:10.2138/am-2015-4963.

Russell, S., 2001, Reservoir Characterization of the Shuaiba Formation (Lower Cretaceous) Abu Dhabi, United Arab Emirates and Jebel Akhdar, Sultanate of Oman, PhD thesis, University of Aberdeen, The United Kingdom, 1004 p.

Sadekov, A., S. M. Eggins, P. D. Deckker, and D. Kroon, 2008, Uncertainties in seawater thermometry deriving from intratest and intertest Mg/Ca variability in Globigerinoides ruber: Paleoceanography, v. 23, no. 1, doi:10.1029/2007pa001452.

Saunders, P., M. Rogerson, J. D. Wadhawan, G. Greenway, and H. M. Pedley, 2014, ScienceDirect Mg / Ca ratios in freshwater microbial carbonates :

Thermodynamic , kinetic and vital effects: Geochimica et Cosmochimica Acta, v. 147, p. 107–118, doi:10.1016/j.gca.2014.10.014.

Schneider, F., J. L. Potdevin, S. Wolf, and I. Faille, 1996, Mechanical and chemical compaction model for sedimentary basin simulators: Tectonophysics, v. 263, p. 307–317.

Scholle, P. A., and D. S. Ulmer-scholle, 2003, A Color Guide to the Petrography of Carbonate Rocks: The American Association of Petroleum Geologists, ISBN: 0-89181-358-6.

Searl, A., 1988, The limitations of "cement stratigraphy " as revealed in some Lower Carboniferous oolites from South Wales: Sedimentary Geology, v. 57, p. 171–183.

Searle, M. P., and L. Le, 1988, Structure of the Musandam culmination (Sultanate of Oman and United Arab Emirates) and the Straits of Hormuz syntaxis: Journal of the Geological Society, London, v. 145, p. 831–845.

Searl, A., 1989, Saddle dolomite : a new view of its nature and origin: Mineralogical Magazine, v. 53, p. 547–555.

Searle, M. P., A. G. Cherry, M. Y. Ali, and D. J. W. Cooper, 2016, Tectonics of the Musandam Peninsula and northern Oman Mountains : From ophiolite obduction to continental collision: GeoArabia, p. 135–174.

Shafiei, A., and M. B. Dusseault, 2018, Natural Fractures Characterization and Reservoir — An Integrated Approach: Energies, doi:10.3390/en11020312.

Shakeri, A. R., 2013, Microfacies , Depositional Environment and Diagenetic Processes of the Mauddud Member , in a Field in the Persian Gulf: Geology & Geosciences, v. 2, no. 2, doi:10.4172/2329-6755.1000122.

Shackleton, N., 1987, Oxygen isotopes, ice volume and sea level: Quaternary Science Reviews, v. 6, no. 3-4, p. 183–190, doi:10.1016/0277-3791(87)90003-5.

Sibley, D. F., and J. A. Y. M. Gregg, 1987, Classification of Dolomite Rock Textures: Journal Of Sedimentary Petrolog, v. 57, no. 6, p. 967–975.

Sims, D. W., A. P. Morris, D. Y. Wyrick, D. A. Ferrill, D. J. Waiting, N. M. Franklin, S. L. Colton, Y. T. Umezawa, M. Takanashi, and E. J. Beverly, 2013, Analog modeling of normal faulting above Middle East domes during regional extension: Geohorizon, v. 6, no. 6, p. 877–898, doi:10.1306/02101209136.

Sirat, M., Al-Dayyani, T., Singh, M., Rehman, A., Samad, A., Al-Zaabi, N., and Moge, M., 2012, Characterisation and Modeling of Fractures in Large Onshore Abu Dhabi Carbonate Field: In Abu Dhabi International Petroleum Conference and Exhibition. Society of Petroleum Engineers, doi:10.2118/162342-MS.

Stanley, S. M., and L. A. Hardie, 1998, Secular oscillations in the carbonate mineralogy of reef-building and sediment-producing organisms driven by tectonically forced shifts in seawater chemistry: Palaeogeography, Palaeoclimatology, Palaeoecology, v. 144, no. 1-2, p. 3–19, doi:10.1016/s0031-0182(98)00109-6.

Stoll, H. M., and D. P. Schrag, 2001, Sr/Ca variations in Cretaceous carbonates : relation to productivity and sea level changes: Palaeogeography, Palaeoclimatology, Palaeoecology, v. 168.

Strohmenger, C. J., Steuber, T., A. Ghani, D. G. Barwick, S. H. A. Al-Mazrooei, and N. O. Al-Zaabi, 2016, Sedimentology and chemostratigraphy of Shu'aiba depositional sequences Sedimentology and chemostratigraphy of the Hawar and Shu'aiba depositional sequences , Abu Dhabi , United Arab Emirates: GeoArabia Special Publication, no. 4, 341-365.

Sultan, M., R. E. Arvidson, I. J. Duncan, S. Louis, and R. J. Stern, 1988, Extension of The Najd Shear System From Saudi Arabia to The Central Eastern Desert of

Egypt Based on Integrated Field and Landsat Observations: Tectonics, v. 7, no. 6, p. 1291–1306.

Swart, P. K., D. L. Cantrell, H. Westphal, C. R. Handford, and C. G. Kendall, 2005, Origin Of Dolomite In The Arab-D Reservoir From The Ghawar Field , Saudi Arabia : Evidence From Petrographic And Geochemical Constraints: Journal Of Sedimentary Research, v. 75, doi:10.2110/jsr.2005.037.

Syme, C. E., K. Welsh, E. M. Roberts, and S. W. Salisbury, 2016, Depositional environment of the Lower Cretaceous (upper Albian) Winton Formation at Isisford, central-west Queensland, inferred from sandstone concretions: Journal of Sedimentary Research, v. 86, no. September, p. 1067–1082, doi:dx.doi.org/10.2110/jsr.2016.67.

Taylor, T. R., and F. Sibley, 1986, Petrographic and geochemical characteristics of dolomite types and the origin of ferroan dolomite in the Trenton Formation, Ordovician, Michigan Basin, U.S.A.: Sedimentology, p. 61–86.

The, I. et al., 1948, Chapter 10 Hydrocarbon Habitat Of The Middle East : An Overview.

Timothy, D., and T. B. Sc, 2014, Controls on reservoir quality in Early Cretaceous carbonate oil fields and implications for basin modelling, PhD thesis, University of Edinburgh. UK. 386 p.

Tucker, M. E., P. Wright, and E. Maurice, 1990, Carbonate Sedimentology.

Turpin, M., F. H. Nader, and E. Kohler, 2012, Empirical Calibration for Dolomite Stoichiometry Calculation : Application on Triassic Muschelkalk- Lettenkohle Carbonates (French Jura): Oil & Gas Science and Technology, v. 67, no. 1, doi:10.2516/ogst/2011173.

Vahrenkamp, V. C., 2016, Chemostratigraphy of the Lower Cretaceous Shu'aiba Formation: A $\delta^{13}C$ reference profile for the Aptian Stage from the southern Neo-Tethys Ocean: GeoArabia, v. 1, p. 107-137.

Vahrenkamp, V. C., P. H. Swart, and S. T. Murray, 2015, A Regional Analysis of Clumped Isotope Geochemistry to Define the Timing of Creation of Micro-Porosity in a Lower Cretaceous Giant Reservoir SPE-177922-MS A Regional Analysis of Clumped Isotope Geochemistry to Define the Timing of Creation of Micro-Porosity in a Lower Cretaceous Giant Reservoir: Society of Petroleum Engineers, no. November, doi: 10.2118/177922-MS.

Veevers, J. J., 2004, Gondwanaland from 650 – 500 Ma assembly through 320 Ma merger in Pangea to 185 – 100 Ma breakup : supercontinental tectonics via stratigraphy and radiometric dating: Earth-Science Review, v. 68, p. 1–132, doi:10.1016/j.earscirev.2004.05.002.

Vincent, S. J., A. C. Morton, A. Carter, S. Gibbs, and G. Teimuraz, 2007, Oligocene uplift of the Western Greater Caucasus : an effect of initial Arabia – Eurasia collision: Terra Nova, v. 19, p. 160-166, doi:10.1111/j.1365-3121.2007.00731.x.

Voorn, M., U. Exner, A. Barnhoorn, P. Baud, and T. Reuschlé, 2015, Porosity, permeability and 3D fracture network characterisation of dolomite reservoir rock samples: Journal of Petroleum Science and Engineering, v. 127, p. 270–285, doi:10.1016/j.petrol.2014.12.019.

Wagner, P. D., 1990, Geochemical stratigraphy and porosity controls in Cretaceous carbonates near the Oman Mountains: Geological Society Special Publication: no. 49, p. 127–137.

Warren, J. K., 2014, Dolomite : Occurrence, Evolution and Economically Important Associations Dolomite : occurrence, evolution and economically important: Earth-Science Reviews, doi: 10.1016/S0012-8252(00)00022-2.

Wen, H., L. Wen, H. Chen, R. Zheng, L. Dang, and Y. Li, 2014, Geochemical characteristics and diagenetic fluids of dolomite reservoirs in the Huanglong Formation, Eastern Sichuan Basin, China: Petroleum Science, v. 11, no. 1, p. 52–66, doi:10.1007/s12182-014-0317-6.

Wendte, J., Sargent, D., Chi, G., and Al-Aasm, I., 2009, Fault/fracture controlled hydrothermal dolomitization and associated diagenesis of the Upper Devonian Jean Marie Member (Redknife Formation) in the July Lake area of northeastern British Columbia: Bulletin of Canadian Petroleum Geology, 57(3), 275-322.

Wennberg, O. P., G. Casini, S. Jonoud, and D. C. P. Peacock, 2016, The characteristics of open fractures in carbonate reservoirs and their impact on fluid flow: a discussion: The Geological Society of London, doi:10.1144/petgeo2015-003.

Wilkinson, M., R. S. Haszeldine, R. M. Ellam, and A. Fallick, 2004, Hydrocarbon filling history from diagenetic evidence: Brent Group, UK North Sea: Marine and Petroleum Geology, v. 21, no. 4, p. 443–455, doi:10.1016/s0264-8172(03)00092-8.

Williams, G. E., 2015, Hydrothermal alteration of Britain's oldest palaeosols : saddle dolomite and smectite at the Lewisian – Torridon Group (early Neoproterozoic) unconformity, NW Scotland: Scottish Journal of Geology, doi:10.1144/sjg2014-014.

Wilson, M. E. J., E. Chang, E. Wah, S. Dorobek, and P. Lunt, 2013, Onshore to offshore trends in carbonate sequence development , diagenesis and reservoir quality across a land-attached shelf in SE Asia: JMPG, v. 45, p. 349–376, doi:10.1016/j.marpetgeo.2013.03.011.

Woodcock, N. H., and M. Fischer, 1986, Strike-slip duplexes: Journal of Structural Geology, v. 8, no. 7, p. 725–735, doi:10.1016/0191-8141(86)90021-0.

Wright, D. T., and D. Wacey, 2004, Sedimentary dolomite: a reality check: Geological Society, London, Special Publications, v. 235, no. 1, p. 65–74, doi:10.1144/gsl.sp.2004.235.01.03.

Yamin Ali, M., 1995, Carbonate cement stratigraphy and timing of diagenesis in a Miocene mixed carbonate-clastic sequence, offshore Sabah, Malaysia: constraints from cathodoluminescence, geochemistry, and isotope studies:

Sedimentary Geology, v. 99, no. 3–4, p. 191–214, doi:10.1016/0037-0738(95)00044-9.

Zheng, Y., 2015, On the theoretical calculations of oxygen isotope fractionation factors for carbonate-water systems On the theoretical calculations of oxygen isotope fractionation factors for carbonate-water systems: no. February, doi:10.2343/geochemj.1.0125.

Ziegler, M. A., 2001, Late Permian to Holocene Paleofacies Evolution of the Arabian Plate and its Hydrocarbon Occurrences: GeoArabia, v. 6, no. 3, p. 445–504.

Zurich, L., S. Naeher, A. Gilli, R. P. North, Y. Hamann, and C. J. Schubert, 2013, Tracing bottom water oxygenation with sedimentary Mn / Fe ratios in: Chemical Geology, v. 352, p. 125–133, doi:10.1016/j.chemgeo.2013.06.006.

Appendices

Appendix 1

Elemental Analysis Data (EPMA) for subsurface calcite

	Oxide						Weight%						
DataSet/P	CaO	MgO	MnO	FeO	SrO	Total	Ca	Mg	Mn	Fe	Sr	O	Total
1 / 1 .	55.8389	0.7485	0.021	0.0078	0.0459	56.6622	39.9077	0.4514	0.0163	0.0061	0.0388	16.2419	56.6622
1 / 2 .	56.2328	0.8313	0.0358	0.0009	0.0443	57.1451	40.1893	0.5013	0.0277	0.0007	0.0374	16.3887	57.1451
1 / 3 .	44.2029	0.2547	0.0022	0.0249	0.0775	44.5622	31.5916	0.1536	0.0017	0.0193	0.0655	12.7305	44.5622
1 / 4 .	55.6735	0.5785	0.0372	-0.0069	0.0885	56.3709	39.7895	0.3489	0.0288	-0.0053	0.0748	16.1342	56.3709
1 / 5 .	56.0459	0.8081	0.0191	0.0015	0.0447	56.9194	40.0557	0.4873	0.0148	0.0012	0.0378	16.3226	56.9194
1 / 6 .	55.9888	0.6552	0.0305	0.0042	0.0557	56.7344	40.0149	0.3951	0.0236	0.0032	0.0471	16.2505	56.7344
1 / 7 .	56.3729	0.5834	0.0263	-0.003	0.076	57.0556	40.2894	0.3518	0.0204	-0.0023	0.0643	16.3321	57.0556
1 / 8 .	56.3029	0.3315	0.034	-0.0061	0.1207	56.7832	40.2394	0.1999	0.0263	-0.0047	0.1021	16.2201	56.7832
1 / 9 .	56.2307	0.4536	0.0317	-0.0012	0.0739	56.7888	40.1877	0.2736	0.0246	-0.0009	0.0625	16.2413	56.7888
1 / 10 .	55.8233	0.5951	0.026	0.006	0.0621	56.5126	39.8966	0.3589	0.0201	0.0047	0.0525	16.1798	56.5126
1 / 11 .	55.7441	0.5822	0.0313	0.0051	0.0665	56.4291	39.84	0.3511	0.0242	0.0039	0.0562	16.1537	56.4291
1 / 12 .	55.8085	0.8053	0.0254	0.0181	0.0455	56.7027	39.886	0.4856	0.0197	0.014	0.0385	16.259	56.7027
1 / 13 .	55.6141	0.531	0.0193	0.0295	0.0593	56.2533	39.7471	0.3202	0.015	0.023	0.0502	16.0979	56.2533
1 / 14 .	55.6347	0.8416	0.0295	0.0319	0.0413	56.579	39.7618	0.5075	0.0228	0.0248	0.0349	16.2271	56.579
1 / 15 .	55.9825	0.8401	0.0314	0.0575	0.0357	56.9473	40.0104	0.5066	0.0243	0.0447	0.0302	16.3311	56.9473
1 / 16 .	49.4371	6.8834	0.0086	0.1308	0.0264	56.4863	35.3324	4.1509	0.0067	0.1017	0.0223	16.8724	56.4863
1 / 17 .	56.2754	0.8419	0.0365	0.0343	0.0411	57.2292	40.2197	0.5077	0.0283	0.0267	0.0348	16.4121	57.2292
1 / 18 .	55.6099	0.676	0.0241	0.0343	0.0459	56.3901	39.7441	0.4076	0.0187	0.0267	0.0388	16.1543	56.3901
1 / 19 .	56.5546	0.856	0.0363	0.0516	0.0409	57.5395	40.4193	0.5162	0.0281	0.0401	0.0346	16.5012	57.5395
1 / 20 .	56.0969	0.7855	0.0224	0.0022	0.0483	56.9553	40.0921	0.4737	0.0173	0.0017	0.0408	16.3296	56.9553
2 / 1 .	56.22	0.6874	0.0238	0.0057	0.043	56.98	40.1801	0.4145	0.0184	0.0044	0.0364	16.3261	56.9799
2 / 2 .	55.4935	0.7135	0.0261	-0.0055	0.0358	56.2634	39.6608	0.4303	0.0202	-0.0043	0.0303	16.1261	56.2634
2 / 3 .	55.6938	0.7232	0.0365	0.0003	0.0408	56.4945	39.804	0.4361	0.0282	0.0002	0.0345	16.1914	56.4945
2 / 4 .	56.4641	0.7342	0.0323	-0.0019	0.0593	57.288	40.3546	0.4427	0.025	-0.0015	0.0502	16.417	57.288
2 / 5 .	55.6836	0.7163	0.0258	-0.0074	0.0421	56.4604	39.7967	0.4319	0.02	-0.0058	0.0356	16.1819	56.4604
2 / 6 .	55.878	0.7463	0.04	0.0075	0.0351	56.7069	39.9357	0.45	0.031	0.0058	0.0296	16.2547	56.7069
2 / 7 .	56.0448	0.571	0.0358	0.0021	0.0587	56.7125	40.0549	0.3444	0.0277	0.0017	0.0497	16.2342	56.7125
2 / 8 .	56.1922	0.327	0.0266	-0.0022	0.0948	56.6384	40.1602	0.1972	0.0206	-0.0017	0.0801	16.1819	56.6384
3 / 1 .	31.0388	24.2516	0.0098	0.0753	0.0008	55.3762	22.1832	14.6244	0.0076	0.0585	0.0006	18.5018	55.3761
3 / 2 .	29.0781	19.0519	0.0255	6.7712	0.0052	54.9318	20.7819	11.4888	0.0197	5.2633	0.0044	17.3737	54.9318
3 / 3 .	30.0244	20.1526	0.0185	6.1681	0.0008	56.3643	21.4582	12.1526	0.0143	4.7945	0.0007	17.944	56.3643
3 / 4 .	29.7324	19.0398	0.0288	6.6592	0.0132	55.4735	21.2496	11.4816	0.0223	5.1763	0.0112	17.5326	55.4735
3 / 5 .	29.7057	19.7646	0.0329	6.939	0.005	56.4472	21.2305	11.9186	0.0255	5.3937	0.0042	17.8747	56.4472
3 / 6 .	30.0119	18.7543	0.0278	6.5768	0.0141	55.3849	21.4494	11.3094	0.0215	5.1122	0.0119	17.4806	55.3849
4 / 1 .	55.966	0.7214	0.0309	0.3903	0.028	57.1366	39.9986	0.435	0.0239	0.3034	0.0237	16.352	57.1366
4 / 2 .	55.4774	0.6895	0.0366	0.3839	0.028	56.6154	39.6494	0.4158	0.0284	0.2984	0.0237	16.1998	56.6154
4 / 3 .	55.7233	0.7329	0.034	0.3852	0.0267	56.9021	39.8251	0.4419	0.0263	0.2994	0.0226	16.2867	56.9021
4 / 4 .	56.2025	0.4446	0.0289	0.3292	0.0272	57.0325	40.1676	0.2681	0.0224	0.2559	0.023	16.2954	57.0325
4 / 5 .	55.454	0.771	0.0285	0.4407	0.0351	56.7292	39.6326	0.4649	0.022	0.3425	0.0297	16.2374	56.7292
4 / 6 .	55.1635	0.7507	0.0408	0.4005	0.0321	56.3877	39.425	0.4527	0.0316	0.3113	0.0272	16.1399	56.3877
4 / 7 .	54.8583	0.6708	0.0284	0.3977	0.0468	56.002	39.2069	0.4045	0.022	0.3091	0.0396	16.0199	56.002
4 / 8 .	55.2071	0.6723	0.03	0.4051	0.0429	56.3574	39.4562	0.4054	0.0232	0.3149	0.0363	16.1214	56.3574
4 / 9 .	55.7187	0.6995	0.0297	0.3824	0.0428	56.8731	39.8218	0.4218	0.023	0.2972	0.0362	16.273	56.8731
4 / 10 .	48.8834	0.646	0.013	0.5799	0.0354	50.1577	34.9367	0.3895	0.0101	0.4508	0.0299	14.3407	50.1577
4 / 11 .	54.6225	0.7396	0.0367	0.391	0.0199	55.8097	39.0384	0.446	0.0284	0.3039	0.0168	15.9762	55.8097
4 / 12 .	54.8278	0.7462	0.0151	0.6779	0.0281	56.2951	39.1851	0.45	0.0117	0.527	0.0237	16.0976	56.2951
4 / 13 .	55.3531	0.6523	0.0253	0.4368	0.0381	56.5056	39.5605	0.3934	0.0196	0.3395	0.0322	16.1604	56.5056
4 / 14 .	55.386	0.6587	0.0314	0.3762	0.0534	56.5058	39.5841	0.3972	0.0244	0.2924	0.0452	16.1626	56.5058
4 / 15 .	55.2418	0.6733	0.0326	0.3818	0.0433	56.3728	39.481	0.406	0.0252	0.2968	0.0366	16.1272	56.3728
4 / 16 .	55.5584	0.5158	0.0255	0.3433	0.0614	56.5043	39.7072	0.311	0.0198	0.2668	0.0519	16.1476	56.5043
4 / 17 .	55.1075	0.4775	0.0228	0.3304	0.0592	55.9974	39.385	0.2879	0.0177	0.2569	0.05	15.9999	55.9974
4 / 18 .	55.555	0.4248	0.0052	0.4476	0.0598	56.4923	39.7048	0.2561	0.004	0.3479	0.0505	16.1289	56.4923

4 / 19 .	55.0047	0.7402	0.0357	0.3791	0.0265	56.1862	39.3115	0.4464	0.0277	0.2947	0.0224	16.0836	56.1862
4 / 20 .	55.2978	0.7481	0.0246	0.4164	0.0361	56.523	39.521	0.4511	0.0191	0.3237	0.0305	16.1776	56.523
5 / 1 .	55.7672	0.5474	0.0229	0.0032	0.0484	56.3891	39.8565	0.3301	0.0177	0.0025	0.0409	16.1414	56.3891
5 / 2 .	56.322	0.6707	0.0237	0	0.0491	57.0656	40.253	0.4045	0.0184	0	0.0415	16.3482	57.0656
5 / 3 .	56.1678	0.2854	0.013	-0.0052	0.0347	56.4957	40.1428	0.1721	0.0101	-0.0041	0.0293	16.1454	56.4957
6 / 1 .	32.5697	22.1308	0.0139	-0.0024	0.0184	54.7303	23.2774	13.3455	0.0107	-0.0019	0.0156	18.083	54.7303
6 / 2 .	32.1143	22.5194	0.0196	-0.0008	0.0153	54.6678	22.9519	13.5798	0.0152	-0.0006	0.013	18.1086	54.6678
6 / 3 .	32.0888	21.8707	0.0142	-0.0108	0.0131	53.9759	22.9337	13.1886	0.011	-0.0084	0.011	17.84	53.9759
6 / 4 .	31.6483	22.5939	0.0236	-0.0016	0.0099	54.274	22.6188	13.6248	0.0183	-0.0013	0.0083	18.0051	54.274
6 / 5 .	31.7508	22.4663	0.0122	-0.0017	0.0023	54.23	22.6921	13.5478	0.0095	-0.0013	0.002	17.9799	54.23
6 / 6 .	32.1615	22.4707	0.0101	0.0002	0.0094	54.6519	22.9856	13.5505	0.0078	0.0002	0.008	18.0999	54.6519
6 / 7 .	32.0318	22.1456	0.0154	-0.0029	0.0015	54.1914	22.8929	13.3544	0.0119	-0.0023	0.0013	17.9331	54.1914
1 / 1 .	55.9638	0.5853	0.0245	0.3569	0.0762	57.0067	39.997	0.353	0.019	0.2774	0.0644	16.2959	57.0067
1 / 2 .	55.8289	0.4824	0.0367	0.2244	0.1032	56.6756	39.9006	0.2909	0.0284	0.1745	0.0873	16.194	56.6756
1 / 3 .	55.4261	0.9034	0.0246	0.3017	0.0634	56.7192	39.6127	0.5448	0.0191	0.2345	0.0536	16.2546	56.7192
1 / 4 .	55.9934	0.5035	0.0292	0.2682	0.0829	56.8773	40.0182	0.3037	0.0226	0.2085	0.0701	16.2543	56.8773
1 / 5 .	55.2665	0.6275	0.0237	0.3227	0.0814	56.3218	39.4987	0.3784	0.0183	0.2509	0.0688	16.1067	56.3218
1 / 6 .	55.8454	0.4959	0.021	0.3586	0.088	56.8088	39.9124	0.299	0.0163	0.2787	0.0744	16.2281	56.8088
1 / 7 .	56.5964	0.0967	0.0288	0.167	0.0248	56.9137	40.4491	0.0583	0.0223	0.1298	0.021	16.2332	56.9137
1 / 8 .	55.7815	0.5748	0.0354	0.2805	0.0363	56.7086	39.8667	0.3466	0.0274	0.218	0.0307	16.2191	56.7086
1 / 9 .	56.9472	0.2313	0.0361	0.2353	0.031	57.4809	40.6999	0.1395	0.028	0.1829	0.0262	16.4045	57.4809

1 / 10 .	55.4167	0.9782	0.0367	0.3925	0.0295	56.8536	39.606	0.5899	0.0284	0.3051	0.025	16.2993	56.8536
1 / 11 .	55.7082	0.5375	0.0282	0.1914	0.078	56.5433	39.8143	0.3242	0.0219	0.1487	0.066	16.1683	56.5433
1 / 12 .	56.115	0.5348	0.0294	-0.0017	0.0298	56.7073	40.1051	0.3225	0.0228	-0.0013	0.0252	16.2331	56.7073
1 / 13 .	55.8329	0.5491	0.0324	0.3115	0.0616	56.7875	39.9035	0.3311	0.0251	0.2421	0.0521	16.2336	56.7875
1 / 14 .	55.2624	0.8727	0.0325	0.3914	0.0217	56.5807	39.4957	0.5262	0.0252	0.3042	0.0184	16.211	56.5807
1 / 15 .	56.966	0.2203	0.0374	0.1829	0.03	57.4366	40.7133	0.1329	0.0289	0.1422	0.0254	16.394	57.4366
1 / 16 .	56.1439	0.4465	0.0343	0.2237	0.0726	56.921	40.1257	0.2692	0.0266	0.1739	0.0614	16.2642	56.921
1 / 17 .	56.3386	0.5415	0.0333	0.1909	0.0754	57.1798	40.2649	0.3265	0.0258	0.1484	0.0638	16.3504	57.1798
1 / 18 .	55.8305	1.0064	0.0502	0.2543	0.0361	57.1776	39.9017	0.6069	0.0389	0.1977	0.0305	16.4018	57.1776
1 / 19 .	56.1098	0.5268	0.0286	0.1126	0.0685	56.8462	40.1013	0.3177	0.0221	0.0875	0.058	16.2597	56.8462
1 / 20 .	54.6208	1.2778	0.0447	0.3361	0.0418	56.3212	39.0372	0.7706	0.0346	0.2613	0.0353	16.1823	56.3212
2 / 1 .	54.6658	1.0981	0.022	1.3717	0.0326	57.1901	39.0693	0.6622	0.017	1.0663	0.0275	16.3478	57.1901
2 / 2 .	54.5631	1.0751	0.0235	1.1818	0.0332	56.8767	38.9959	0.6483	0.0182	0.9186	0.0281	16.2676	56.8767
2 / 3 .	54.3713	0.9748	0.0203	1.1393	0.0116	56.5173	38.8588	0.5879	0.0157	0.8856	0.0098	16.1595	56.5173
1 / 2 .	56.6594	0.4506	0.0267	0.0984	0.0646	57.2998	40.4942	0.2717	0.0207	0.0765	0.0546	16.3821	57.2998
1 / 3 .	54.9672	1.1555	0.0264	0.3528	0.0289	56.5308	39.2847	0.6968	0.0204	0.2743	0.0245	16.2302	56.5308
2 / 1 .	55.8037	1.1178	0.0397	0.2368	0.0313	57.2293	39.8826	0.674	0.0308	0.1841	0.0264	16.4314	57.2293
3 / 1 .	56.1176	0.6465	0.0353	0.387	0.0173	57.2038	40.107	0.3899	0.0274	0.3008	0.0147	16.3642	57.2038
4 / 1 .	55.4281	1.0346	0.0268	0.321	0.0432	56.8537	39.6141	0.6239	0.0208	0.2495	0.0365	16.3089	56.8537
5 / 1 .	56.1923	1.0058	0.0469	0.0221	0.0174	57.2845	40.1603	0.6065	0.0363	0.0172	0.0147	16.4495	57.2845
6 / 1 .	54.5699	1.32	0.0388	0.3968	0.0298	56.3552	39.0008	0.796	0.03	0.3084	0.0252	16.1948	56.3552
7 / 1 .	54.9765	1.1323	0.0421	0.1352	0.028	56.3141	39.2914	0.6828	0.0326	0.1051	0.0237	16.1785	56.3141
7 / 2 .	55.4339	1.1324	0.0399	0.1549	0.0212	56.7824	39.6183	0.6829	0.0309	0.1204	0.0179	16.3119	56.7824
7 / 3 .	55.9725	1.1651	0.0297	0.1448	0.0304	57.3425	40.0032	0.7026	0.023	0.1125	0.0257	16.4754	57.3425
10 / 1 .	56.4438	0.8253	0.0377	0.1725	0.0451	57.5245	40.34	0.4977	0.0292	0.1341	0.0381	16.4853	57.5245

11 / 1 .	56.5055	0.9501	0.1317	0.0216	0.0348	57.6437	40.3842	0.5729	0.102	0.0168	0.0294	16.5384	57.6437
12 / 1 .	54.8964	0.8983	0.0392	0.335	0.0438	56.2127	39.2341	0.5417	0.0304	0.2604	0.037	16.1091	56.2127
12 / 2 .	54.5061	1.0671	0.0262	0.7565	0.0317	56.3876	38.9552	0.6435	0.0203	0.588	0.0268	16.1538	56.3876
12 / 3 .	54.9787	1.1142	0.0295	0.7464	0.0261	56.8949	39.2929	0.6719	0.0229	0.5801	0.0221	16.305	56.8949
12 / 5 .	55.0501	1.1948	0.0246	0.812	0.0267	57.1082	39.344	0.7205	0.0191	0.6312	0.0225	16.3709	57.1082
13 / 2 .	55.3364	1.1491	0.0282	0.7466	0.0433	57.3036	39.5486	0.6929	0.0218	0.5804	0.0366	16.4233	57.3036
13 / 3 .	54.5464	1.3382	0.0205	0.8255	0.0415	56.7721	38.984	0.807	0.0159	0.6417	0.0351	16.2885	56.7721
13 / 4 .	54.9614	1.0924	0.0214	0.8765	0.0221	56.9738	39.2806	0.6587	0.0166	0.6813	0.0187	16.3179	56.9738
13 / 5 .	55.518	0.9118	0.0328	0.0946	0.0375	56.5947	39.6784	0.5498	0.0254	0.0736	0.0317	16.2358	56.5947
1 / 1 .	55.3494	0.9401	0.0302	0.4517	0.0418	56.8133	39.5579	0.5669	0.0234	0.3511	0.0354	16.2786	56.8133
1 / 2 .	55.6667	0.7813	0.0146	0.4464	0.0254	56.9343	39.7847	0.4711	0.0113	0.347	0.0215	16.2988	56.9343
1 / 3 .	55.5685	0.8347	0.0201	0.4704	0.02	56.9138	39.7144	0.5034	0.0156	0.3656	0.017	16.2978	56.9138
1 / 4 .	55.1709	0.8467	0.0191	0.2749	0.0449	56.3564	39.4303	0.5106	0.0148	0.2136	0.0379	16.1491	56.3564
1 / 5 .	55.3859	0.8268	0.0228	0.2514	0.0265	56.5135	39.584	0.4986	0.0177	0.1954	0.0224	16.1954	56.5135

Appendix 2

Elemental Analysis Data (EPMA) for subsurface dolomite

	Oxide						Weight%						
DataSet/P	CaO	MgO	MnO	FeO	SrO	Total	Ca	Mg	Mn	Fe	Sr	O	Total
1 / 1 .	32.3098	19.2742	0.0208	1.5113	0.0244	53.1404	23.0916	11.6229	0.0161	1.1747	0.0206	17.2145	53.1404
1 / 2 .	33.9089	20.218	0.0101	0.035	0.0481	54.22	24.2345	12.192	0.0078	0.0272	0.0407	17.7179	54.22
1 / 3 .	33.2678	21.064	0.0142	0.0195	0.0481	54.4136	23.7763	12.7022	0.011	0.0152	0.0407	17.8683	54.4136
1 / 4 .	33.685	20.608	0.0133	0.0112	0.0499	54.3675	24.0745	12.4272	0.0103	0.0087	0.0422	17.8045	54.3675
1 / 5 .	33.6022	20.1229	0.0127	0.0148	0.0459	53.7984	24.0153	12.1347	0.0098	0.0115	0.0388	17.5884	53.7984
2 / 1 .	33.8317	20.7238	0.0094	0.0568	0.0539	54.6758	24.1793	12.4971	0.0073	0.0442	0.0456	17.9023	54.6758
2 / 2 .	33.9565	20.8472	0.0149	0.0227	0.0411	54.8824	24.2685	12.5715	0.0116	0.0177	0.0347	17.9785	54.8824
2 / 3 .	34.1732	19.9918	0.0128	0.0225	0.0482	54.2484	24.4234	12.0556	0.0099	0.0175	0.0407	17.7013	54.2484
2 / 4 .	33.1906	20.2221	0.0129	0.0664	0.0405	53.5326	23.7211	12.1945	0.01	0.0516	0.0343	17.5211	53.5326
3 / 1 .	31.4551	20.2021	0.0242	2.3512	0.0163	54.0488	22.4808	12.1824	0.0187	1.8276	0.0138	17.5256	54.0488
4 / 1 .	33.6223	21.0799	0.0145	0.0384	0.0271	54.7822	24.0297	12.7118	0.0112	0.0298	0.0229	17.9768	54.7822
5 / 1 .	33.6265	19.8298	0.0105	0.0257	0.0547	53.5472	24.0327	11.9579	0.0081	0.02	0.0462	17.4823	53.5472
6 / 1 .	33.8253	21.4775	0.0185	0.057	0.0276	55.4059	24.1748	12.9515	0.0144	0.0443	0.0233	18.1977	55.4059
7 / 1 .	33.6849	20.4098	0.0124	0.0135	0.0455	54.1661	24.0744	12.3077	0.0096	0.0105	0.0385	17.7255	54.1661
8 / 1 .	33.9909	20.5215	0.015	0.0268	0.0367	54.5908	24.2931	12.3751	0.0116	0.0208	0.031	17.8593	54.5908
9 / 1 .	32.0379	18.1297	0.022	1.6618	0.0242	51.8756	22.8973	10.9327	0.017	1.2917	0.0205	16.7164	51.8756
10 / 1 .	33.5795	20.0092	0.0095	0.054	0.0477	53.7	23.9991	12.0661	0.0074	0.042	0.0403	17.5451	53.7
11 / 1 .	34.1669	20.0622	0.0114	0.0365	0.0483	54.3252	24.4188	12.098	0.0088	0.0284	0.0408	17.7303	54.3252
12 / 1 .	33.4566	20.9654	0.0123	0.2933	0.0374	54.7649	23.9112	12.6427	0.0095	0.228	0.0316	17.9419	54.7649
13 / 1 .	32.8715	20.8003	0.0096	0.6401	0.0273	54.3487	23.4931	12.5431	0.0074	0.4976	0.0231	17.7845	54.3487
13 / 2 .	33.4517	20.2881	0.0135	0.0367	0.0397	53.8297	23.9077	12.2343	0.0105	0.0285	0.0336	17.6151	53.8297
13 / 3 .	33.3966	20.8357	0.0147	0.0102	0.0409	54.2982	23.8683	12.5645	0.0114	0.0079	0.0346	17.8114	54.2982
13 / 4 .	33.9374	19.735	0.0135	0.0128	0.0442	53.743	24.2549	11.9008	0.0105	0.01	0.0374	17.5295	53.743
13 / 5 .	33.1301	19.4986	0.0076	0.0661	0.0527	52.7551	23.6779	11.7582	0.0059	0.0514	0.0446	17.2172	52.7551
13 / 6 .	33.8539	20.6687	0.0137	0.0175	0.0425	54.5962	24.1952	12.4638	0.0106	0.0136	0.0359	17.8772	54.5962
13 / 7 .	33.1876	20.0439	0.0132	0.1166	0.0312	53.3925	23.719	12.087	0.0102	0.0907	0.0264	17.4592	53.3925
14 / 1 .	33.5455	20.4254	0.0163	0.4343	0.0261	54.4477	23.9748	12.3171	0.0126	0.3376	0.0221	17.7835	54.4477
14 / 2 .	33.934	20.2542	0.011	0.0356	0.0494	54.2842	24.2524	12.2138	0.0085	0.0277	0.0418	17.74	54.2842
14 / 3 .	32.6793	18.1452	0.0184	0.0549	0.0504	50.9482	23.3557	10.9421	0.0142	0.0427	0.0426	16.5509	50.9482
14 / 4 .	33.3638	20.6445	0.0163	0.0041	0.0513	54.0799	23.8449	12.4492	0.0126	0.0032	0.0434	17.7267	54.0799
14 / 5 .	32.8796	20.7142	0.0169	0.0287	0.0461	53.6855	23.4989	12.4912	0.0131	0.0223	0.039	17.621	53.6855
14 / 6 .	32.8102	20.6351	0.0147	0.1937	0.0358	53.6896	23.4493	12.4435	0.0114	0.1506	0.0303	17.6045	53.6896
15 / 1 .	31.9208	18.8467	0.0205	3.506	0.0189	54.3128	22.8136	11.3651	0.0158	2.7252	0.016	17.3771	54.3128
16 / 1 .	33.0056	20.4801	0.0063	0.0133	0.0537	53.5591	23.5889	12.3501	0.0049	0.0103	0.0454	17.5594	53.5591
17 / 1 .	33.6914	19.9341	0.0187	0.0099	0.0418	53.6959	24.0791	12.0208	0.0145	0.0077	0.0354	17.5385	53.6959
18 / 1 .	33.8331	20.6894	0.0103	0.0111	0.0357	54.5796	24.1803	12.4763	0.008	0.0086	0.0302	17.8762	54.5796
19 / 1 .	30.7965	19.3061	0.0308	3.1526	0.0186	53.3045	22.0101	11.6421	0.0238	2.4505	0.0157	17.1623	53.3045
20 / 1 .	32.0701	19.3973	0.0227	1.5264	0.0239	53.0404	22.9203	11.6971	0.0176	1.1865	0.0202	17.1987	53.0404
21 / 1 .	32.4765	20.6458	0.0166	0.0557	0.0398	53.2344	23.2107	12.45	0.0129	0.0433	0.0336	17.4839	53.2344
22 / 1 .	33.9393	19.5089	0.0162	0.0408	0.0563	53.5615	24.2562	11.7644	0.0126	0.0317	0.0476	17.449	53.5615
23 / 1 .	33.5327	19.7563	0.0122	0.2175	0.0262	53.545	23.9656	11.9136	0.0095	0.1691	0.0221	17.465	53.545
24 / 1 .	33.0686	20.3539	0.015	0.0969	0.041	53.5754	23.634	12.2739	0.0116	0.0753	0.0346	17.5459	53.5753
25 / 1 .	32.5655	19.3548	0.0164	1.4629	0.0311	53.4308	23.2744	11.6715	0.0127	1.1371	0.0263	17.3088	53.4308
26 / 1 .	32.2979	19.3961	0.0237	1.26	0.0311	53.0088	23.0831	11.6964	0.0184	0.9794	0.0263	17.2053	53.0088
1 / 1 .	31.8595	20.5615	0.0176	0.1994	0.011	52.6489	22.7698	12.3992	0.0136	0.155	0.0093	17.3021	52.6489
1 / 2 .	31.715	20.969	0.0241	0.0503	0.007	52.7654	22.6665	12.6449	0.0187	0.0391	0.0059	17.3903	52.7654
1 / 3 .	31.5406	21.2151	0.0307	0.0563	0.0088	52.8515	22.5419	12.7933	0.0238	0.0438	0.0074	17.4413	52.8515
1 / 4 .	31.6406	20.9991	0.0249	0.0393	0.0152	52.7191	22.6133	12.663	0.0193	0.0306	0.0129	17.38	52.7191
1 / 5 .	31.526	21.3876	0.0307	0.0287	0.0095	52.9825	22.5314	12.8973	0.0238	0.0223	0.008	17.4996	52.9825
1 / 6 .	31.539	21.057	0.0275	0.0234	0.0123	52.6591	22.5407	12.6979	0.0213	0.0182	0.0104	17.3706	52.6591
1 / 7 .	32.037	21.2677	0.0299	0.0129	0.01	53.3574	22.8967	12.825	0.0231	0.01	0.0084	17.5942	53.3574
1 / 8 .	31.4149	21.1803	0.0262	0.0153	0.0105	52.6472	22.4521	12.7723	0.0203	0.0119	0.0089	17.3818	52.6472
1 / 9 .	31.7991	21.4915	0.0342	-0.0207	0.0069	53.3108	22.7266	12.96	0.0265	-0.0161	0.0058	17.6081	53.3108
1 / 10 .	31.6121	21.3472	0.0389	-0.0057	0.0108	53.0033	22.593	12.873	0.0301	-0.0044	0.0091	17.5025	53.0033
2 / 1 .	32.5289	15.3143	0.0414	7.3779	0.0084	55.271	23.2482	9.235	0.0321	5.7349	0.0071	17.0137	55.271

3 / 1 .	28.937	18.1778	0.0362	7.4307	0.002	54.5837	20.6811	10.9617	0.028	5.7759	0.0017	17.1352	54.5837
4 / 1 .	31.2712	21.6556	0.024	0.1945	0.017	53.1622	22.3494	13.0589	0.0186	0.1512	0.0144	17.5699	53.1622
5 / 1 .	30.9808	21.4508	0.0212	0.0848	0.0116	52.5491	22.1418	12.9354	0.0164	0.0659	0.0098	17.3798	52.5491
6 / 1 .	31.375	22.0499	0.028	1.2359	0.0008	54.6895	22.4235	13.2967	0.0217	0.9607	0.0007	17.9863	54.6895
7 / 1 .	31.6857	20.7367	0.0317	0.1216	0.0083	52.5839	22.6456	12.5048	0.0245	0.0945	0.007	17.3075	52.5839
8 / 1 .	32.1152	21.2562	0.0369	0.0192	0.0158	53.4433	22.9525	12.8181	0.0286	0.0149	0.0133	17.6158	53.4433
9 / 1 .	31.9145	20.8289	0.0363	0.0522	0.0069	52.8388	22.8091	12.5604	0.0281	0.0406	0.0058	17.3948	52.8388
10 / 1 .	31.5946	21.4158	0.0357	0.0349	0.0052	53.0861	22.5805	12.9143	0.0276	0.0271	0.0044	17.5322	53.0861
11 / 1 .	31.7015	21.0036	0.034	0.165	0.0127	52.9168	22.6569	12.6658	0.0264	0.1282	0.0107	17.4289	52.9168
12 / 1 .	31.3803	20.8002	0.0333	0.1124	0.0111	52.3374	22.4273	12.5431	0.0258	0.0874	0.0094	17.2444	52.3374
13 / 1 .	31.9881	21.1457	0.0374	0.1194	0.0141	53.3047	22.8617	12.7514	0.029	0.0928	0.012	17.5579	53.3047
14 / 1 .	31.5541	20.8067	0.0272	0.1249	0.0097	52.5226	22.5515	12.547	0.0211	0.0971	0.0082	17.2977	52.5226
15 / 1 .	31.6464	20.8727	0.0311	0.0841	0.01	52.6443	22.6175	12.5868	0.0241	0.0654	0.0085	17.3421	52.6443
16 / 1 .	31.6573	21.0985	0.0525	0.0774	0.0089	52.8945	22.6253	12.723	0.0406	0.0602	0.0075	17.438	52.8945
17 / 1 .	30.0435	17.4495	0.043	6.4065	0.009	53.9515	21.4719	10.5226	0.0333	4.9798	0.0076	16.9363	53.9515
18 / 1 .	30.3187	17.0915	0.0493	6.3361	0.0152	53.8107	21.6686	10.3066	0.0382	4.9251	0.0128	16.8594	53.8107
1 / 1 .	32.5234	18.2002	0.0241	0.0103	0.0015	50.7595	23.2443	10.9752	0.0187	0.008	0.0013	16.5121	50.7595
1 / 2 .	31.0076	18.6959	0.0232	1.0831	0.0125	50.8223	22.1609	11.2741	0.018	0.8419	0.0106	16.5168	50.8223

1 / 3 .	31.3676	18.9873	0.0318	0.1593	0.0153	50.5614	22.4182	11.4499	0.0247	0.1238	0.013	16.5318	50.5614
1 / 4 .	30.6113	17.2464	0.0266	2.738	0.0094	50.6317	21.8777	10.4001	0.0206	2.1283	0.008	16.1971	50.6317
1 / 5 .	31.3551	16.862	0.0268	3.2318	0.0138	51.4894	22.4093	10.1682	0.0208	2.5121	0.0117	16.3674	51.4894
1 / 6 .	31.172	17.1804	0.0217	3.4251	0.0121	51.8114	22.2785	10.3603	0.0168	2.6624	0.0102	16.4832	51.8114
1 / 7 .	30.1537	18.1141	0.0142	3.2628	0.0121	51.557	21.5507	10.9233	0.011	2.5362	0.0103	16.5255	51.557
1 / 8 .	30.9985	16.031	0.0216	4.3907	0.021	51.4628	22.1545	9.6671	0.0167	3.4129	0.0177	16.1938	51.4628
1 / 9 .	30.6488	15.814	0.027	5.5186	0.0099	52.0183	21.9045	9.5363	0.0209	4.2896	0.0084	16.2586	52.0183
1 / 10 .	31.3423	15.2223	0.0294	5.5744	0.0132	52.1816	22.4002	9.1795	0.0227	4.333	0.0112	16.235	52.1816
1 / 11 .	34.8355	13.1048	0.0215	5.4125	0.0161	53.3904	24.8967	7.9026	0.0167	4.2071	0.0136	16.3537	53.3904
1 / 12 .	31.6792	15.5191	0.0238	5.636	0.016	52.8741	22.6409	9.3585	0.0185	4.3809	0.0135	16.4619	52.8741
1 / 13 .	29.5052	16.7729	0.0215	5.3989	0.0079	51.7063	21.0872	10.1145	0.0167	4.1966	0.0066	16.2847	51.7063
1 / 14 .	39.895	5.6161	0.024	4.2013	0.0166	49.7529	28.5127	3.3867	0.0186	3.2657	0.014	14.5553	49.7529
1 / 15 .	32.509	14.2509	0.0309	5.2982	0.0127	52.1017	23.234	8.5937	0.0239	4.1183	0.0107	16.121	52.1017
1 / 16 .	32.4071	14.5488	0.0361	5.8859	0.0188	52.8966	23.1611	8.7733	0.028	4.5751	0.0159	16.3432	52.8966
1 / 17 .	32.1156	14.9098	0.0226	5.6878	0.0107	52.7464	22.9528	8.991	0.0175	4.4211	0.009	16.3549	52.7464

1 / 1 .	30.8515	15.4723	0.0234	6.2008	0.012	52.5599	22.0494	9.3302	0.0181	4.8199	0.0101	16.3322	52.5599
1 / 2 .	30.0842	15.807	0.0242	6.0019	0.0143	51.9315	21.501	9.5321	0.0187	4.6653	0.0121	16.2024	51.9315
1 / 3 .	30.3005	16.8452	0.0169	5.4087	0.0108	52.5821	21.6556	10.1581	0.0131	4.2042	0.0091	16.542	52.5821
1 / 4 .	33.6854	13.3394	0.0276	5.7803	0.0233	52.856	24.0747	8.044	0.0214	4.493	0.0197	16.2031	52.856
1 / 5 .	30.2548	15.9584	0.02	5.7193	0.0148	51.9673	21.6229	9.6234	0.0155	4.4457	0.0125	16.2474	51.9673
1 / 6 .	30.2046	15.9371	0.0206	5.628	0.0092	51.7994	21.587	9.6105	0.0159	4.3747	0.0078	16.2035	51.7994
1 / 7 .	34.9466	12.5735	0.0255	5.4944	0.0047	53.0447	24.9761	7.5821	0.0197	4.2709	0.004	16.1918	53.0447
1 / 8 .	30.2317	16.4314	0.0243	5.607	0.0074	52.3018	21.6064	9.9086	0.0189	4.3583	0.0062	16.4034	52.3018
1 / 9 .	31.2127	15.9587	0.0245	5.5307	0.0084	52.7349	22.3075	9.6235	0.019	4.299	0.0071	16.4788	52.7349
1 / 10 .	32.2607	15.3472	0.0314	5.2396	0.0191	52.8982	23.0566	9.2548	0.0243	4.0728	0.0162	16.4735	52.8982
1 / 11 .	29.7213	16.09	0.0307	4.8701	0.0088	50.721	21.2416	9.7027	0.0238	3.7856	0.0075	15.9598	50.7211
1 / 12 .	30.82	16.4914	0.0259	4.0287	0.0156	51.3816	22.0269	9.9448	0.02	3.1315	0.0132	16.2452	51.3816
1 / 13 .	30.705	17.4751	0.031	3.4604	0.0165	51.688	21.9447	10.538	0.024	2.6898	0.014	16.4776	51.688
1 / 14 .	31.438	16.3223	0.0261	3.2268	0.0044	51.0175	22.4686	9.8428	0.0202	2.5082	0.0037	16.1741	51.0175
1 / 15 .	31.2882	18.6623	0.0198	0.1796	0.0125	50.1624	22.3615	11.2539	0.0153	0.1396	0.0105	16.3815	50.1624
1 / 16 .	30.4946	18.7606	0.02	0.6436	0.0131	49.9318	21.7943	11.3131	0.0155	0.5002	0.0111	16.2976	49.9318

Appendix 3

Elemental Analysis Data (EPMA) for outcrop calcite

	Oxide						Weight%						
DataSet/P	CaO	MgO	MnO	FeO	SrO	Total	Ca	Mg	Mn	Fe	Sr	O	Total
1 / 1 .	56.1987	0.1722	0.0129	0.0017	0.0375	56.4232	40.1649	0.1039	0.01	0.0013	0.0317	16.1113	56.4232
2 / 1 .	55.2257	0.3125	0.0005	-0.008	0.0586	55.5893	39.4695	0.1885	0.0004	-0.0062	0.0495	15.8877	55.5893
3 / 1 .	55.273	0.3392	0.016	0.0036	0.0624	55.6942	39.5033	0.2045	0.0124	0.0028	0.0528	15.9184	55.6942
4 / 1 .	0.8837	0.2934	0.0144	0.0058	0.0714	1.2687	0.6316	0.1769	0.0111	0.0045	0.0604	0.3842	1.2687
5 / 1 .	74.3234	0.2811	0.0177	-0.0135	0.0571	74.6658	53.1185	0.1695	0.0137	-0.0105	0.0483	21.3263	74.6658
6 / 1 .	55.826	0.2535	-0.0034	0.0038	0.0422	56.122	39.8985	0.1528	-0.0026	0.0029	0.0357	16.0347	56.122
7 / 1 .	56.7917	0.2481	0.0127	0.0015	0.0345	57.0885	40.5887	0.1496	0.0098	0.0011	0.0292	16.31	57.0885
8 / 1 .	55.9426	0.2307	0.0172	0.0033	0.0359	56.2296	39.9818	0.1391	0.0133	0.0026	0.0303	16.0625	56.2296
9 / 1 .	56.4309	0.1923	0.0157	0.0018	0.039	56.6797	40.3308	0.116	0.0122	0.0014	0.033	16.1864	56.6797
10 / 1 .	55.9665	0.2641	0.0192	-0.0027	0.0692	56.3164	39.999	0.1593	0.0149	-0.0021	0.0585	16.0869	56.3164
11 / 1 .	55.4292	0.1976	0.0168	-0.0073	0.0565	55.6928	39.6149	0.1191	0.013	-0.0057	0.0478	15.9036	55.6928
12 / 1 .	55.5599	0.2964	0.0215	0.0007	0.0404	55.919	39.7084	0.1788	0.0167	0.0005	0.0342	15.9805	55.919
13 / 1 .	55.5182	0.3354	0.0106	0.0077	0.0384	55.9103	39.6785	0.2023	0.0082	0.006	0.0324	15.9829	55.9104
14 / 1 .	56.0455	0.3134	0.0119	-0.0198	0.0419	56.3929	40.0554	0.189	0.0092	-0.0154	0.0355	16.1193	56.3929
15 / 1 .	55.4293	0.229	0.0227	0.0022	0.032	55.7152	39.615	0.1381	0.0176	0.0017	0.027	15.9158	55.7152
16 / 1 .	56.4626	0.3145	0.0027	-0.002	0.0242	56.802	40.3535	0.1897	0.0021	-0.0016	0.0205	16.2379	56.802
17 / 1 .	55.9775	0.2718	0.0141	0.002	0.0283	56.2938	40.0068	0.1639	0.0109	0.0016	0.024	16.0866	56.2938
18 / 1 .	56.168	0.3024	0.0212	-0.0043	0.0215	56.5088	40.1429	0.1824	0.0164	-0.0033	0.0182	16.1523	56.5088
19 / 1 .	56.0888	0.2996	0.0182	-0.013	0.0151	56.4088	40.0863	0.1807	0.0141	-0.0101	0.0128	16.125	56.4088
20 / 1 .	53.7674	0.3354	0.0075	0.0036	0.0501	54.1639	38.4273	0.2022	0.0058	0.0028	0.0423	15.4835	54.1639
21 / 1 .	56.2209	0.413	0.011	-0.0014	0.0365	56.6801	40.1807	0.2491	0.0085	-0.0011	0.0309	16.2119	56.6801
22 / 1 .	56.1524	0.3205	0.0124	0.0022	0.0552	56.5427	40.1318	0.1933	0.0096	0.0017	0.0466	16.1597	56.5427
23 / 1 .	56.1317	0.307	0.0214	0.003	0.0396	56.5027	40.117	0.1852	0.0166	0.0023	0.0335	16.1482	56.5027
24 / 1 .	54.7744	0.3328	0.0102	0.0025	0.0741	55.194	39.1469	0.2007	0.0079	0.0019	0.0627	15.7739	55.194
25 / 1 .	53.9346	0.3494	0.0108	0.0086	0.0424	54.3458	38.5467	0.2107	0.0084	0.0067	0.0359	15.5375	54.3458
26 / 1 .	56.2935	0.2923	0.011	-0.0045	0.0679	56.6601	40.2326	0.1763	0.0085	-0.0035	0.0574	16.1888	56.6601
27 / 1 .	55.7721	0.3405	0.0168	-0.0119	0.0651	56.1826	39.86	0.2053	0.013	-0.0092	0.055	16.0585	56.1826
28 / 1 .	56.1272	0.2178	0.018	-0.0064	0.0232	56.3798	40.1138	0.1313	0.0139	-0.005	0.0196	16.1061	56.3798
29 / 1 .	56.27	0.2823	0.0031	0.0126	0.0233	56.5913	40.2158	0.1702	0.0024	0.0098	0.0197	16.1733	56.5913
30 / 1 .	56.3292	0.2501	0.0156	-0.0047	0.0258	56.6161	40.2582	0.1508	0.0121	-0.0036	0.0218	16.1768	56.6161
31 / 1 .	56.1218	0.2494	0.0148	-0.0022	0.0213	56.405	40.1099	0.1504	0.0114	-0.0017	0.018	16.117	56.405
32 / 1 .	56.6016	0.239	0.0017	-0.0087	0.025	56.8585	40.4528	0.1441	0.0013	-0.0068	0.0212	16.2459	56.8586
33 / 1 .	56.2218	0.2743	-0.0141	0.0049	0.0234	56.5103	40.1814	0.1654	-0.0109	0.0038	0.0198	16.1508	56.5103
34 / 1 .	57.1818	0.0946	0.0024	0.0007	0.0076	57.2872	40.8675	0.0571	0.0019	0.0006	0.0065	16.3538	57.2872
35 / 1 .	56.4357	0.1441	0.0177	-0.0052	0.0302	56.6224	40.3342	0.0869	0.0137	-0.004	0.0255	16.1661	56.6224
36 / 1 .	56.1476	0.2637	0.0108	-0.0015	0.029	56.4496	40.1284	0.159	0.0084	-0.0012	0.0245	16.1305	56.4496
37 / 1 .	56.0761	0.2753	0.0143	-0.0046	0.0187	56.3798	40.0773	0.166	0.011	-0.0036	0.0158	16.1132	56.3798
38 / 1 .	56.6847	0.2863	0.0124	-0.0015	0.0208	57.0027	40.5122	0.1727	0.0096	-0.0011	0.0176	16.2918	57.0027
39 / 1 .	56.1261	0.198	0.0189	0.0011	0.0212	56.3653	40.113	0.1194	0.0146	0.0008	0.0179	16.0995	56.3653
40 / 1 .	56.5098	0.2373	0.0168	-0.0117	0.0332	56.7854	40.3872	0.1431	0.013	-0.0091	0.028	16.2231	56.7854
41 / 1 .	55.584	0.2067	0.014	-0.0033	0.0269	55.8284	39.7256	0.1247	0.0108	-0.0025	0.0228	15.9471	55.8284
42 / 1 .	56.045	0.1756	0.0147	-0.0064	0.0204	56.2493	40.055	0.1059	0.0114	-0.005	0.0172	16.0647	56.2493
43 / 1 .	56.3425	0.1841	0.0127	-0.0066	0.0165	56.5492	40.2676	0.111	0.0098	-0.0051	0.014	16.1519	56.5492

44 / 1 .	56.0629	0.0979	0.0142	-0.0007	0.0101	56.1844	40.0678	0.059	0.011	-0.0005	0.0086	16.0385	56.1844
45 / 1 .	55.8687	0.2126	0.016	0.0013	0.022	56.1206	39.929	0.1282	0.0124	0.001	0.0186	16.0314	56.1206
46 / 1 .	56.4303	0.1883	0.0141	-0.0106	0.0347	56.6569	40.3304	0.1136	0.0109	-0.0082	0.0294	16.1809	56.6569
1 / 1 .	55.7095	0.3876	0.0253	0.1428	0.1205	56.3858	39.8153	0.2337	0.0196	0.111	0.1019	16.1042	56.3858
1 / 2 .	55.2373	0.7291	0.0055	0.2174	0.0438	56.233	39.4778	0.4397	0.0043	0.169	0.037	16.1054	56.2331
1 / 3 .	56.2732	0.5052	0.012	0.2176	0.1034	57.1114	40.2181	0.3047	0.0093	0.1692	0.0874	16.3228	57.1114
1 / 4 .	55.4392	0.661	0.0303	0.1205	0.038	56.2891	39.6221	0.3986	0.0235	0.0937	0.0322	16.1191	56.2891
2 / 1 .	55.7851	0.4677	0.0329	-0.0116	0.0918	56.3658	39.8693	0.282	0.0255	-0.009	0.0776	16.1205	56.3658
2 / 2 .	55.3932	0.3737	0.0271	0.0001	0.1137	55.9078	39.5892	0.2253	0.021	0.0001	0.0961	15.9761	55.9078
2 / 3 .	56.0289	0.6173	0.0346	0.0048	0.0262	56.7118	40.0435	0.3723	0.0268	0.0037	0.0221	16.2434	56.7118
2 / 4 .	55.6582	0.6224	0.0356	0.09	0.0665	56.4728	39.7786	0.3754	0.0275	0.07	0.0562	16.1651	56.4728
2 / 5 .	55.152	0.5962	0.0324	0.1623	0.0869	56.0298	39.4168	0.3595	0.0251	0.1262	0.0735	16.0287	56.0298
2 / 6 .	55.1233	0.8358	0.0353	0.1899	0.0379	56.2221	39.3963	0.504	0.0273	0.1476	0.0321	16.1149	56.2221
2 / 7 .	55.2286	0.7905	0.0243	0.224	0.0333	56.3007	39.4715	0.4767	0.0188	0.1741	0.0282	16.1314	56.3007
3 / 1 .	55.1911	0.8122	0.0237	0.3178	0.0352	56.3801	39.4448	0.4898	0.0184	0.2471	0.0298	16.1503	56.3801
3 / 2 .	55.1236	0.4612	0.0321	0.1863	0.07	55.8732	39.3965	0.2781	0.0248	0.1448	0.0592	15.9697	55.8732
3 / 3 .	55.524	0.7263	0.0317	0.3003	0.0313	56.6136	39.6827	0.438	0.0246	0.2334	0.0265	16.2085	56.6136
3 / 4 .	55.496	0.6956	0.0262	0.241	0.0352	56.4939	39.6627	0.4195	0.0203	0.1873	0.0297	16.1745	56.4939
3 / 5 .	56.0799	0.2345	0.0274	0.1546	0.1341	56.6305	40.08	0.1414	0.0212	0.1202	0.1134	16.1543	56.6305
4 / 1 .	54.8017	0.5081	0.0023	0.3742	0.0686	55.7549	39.1664	0.3064	0.0018	0.2909	0.058	15.9314	55.7549
4 / 2 .	55.0787	0.4023	0.0185	0.2086	0.0976	55.8056	39.3644	0.2426	0.0143	0.1621	0.0825	15.9397	55.8056
4 / 3 .	54.6327	0.4922	0.0039	0.3547	0.0538	55.5373	39.0457	0.2968	0.003	0.2757	0.0455	15.8706	55.5373
4 / 4 .	56.2001	0.5277	0.0205	0.2496	0.0714	57.0693	40.1659	0.3182	0.0159	0.194	0.0604	16.3149	57.0693
4 / 5 .	55.147	0.3857	0.0223	0.172	0.0946	55.8215	39.4132	0.2326	0.0173	0.1337	0.08	15.9448	55.8215
5 / 1 .	56.029	0.4323	0.016	0.1789	0.0756	56.7317	40.0436	0.2607	0.0124	0.1391	0.0639	16.2121	56.7317
5 / 2 .	56.2712	0.6887	0.0256	0.2269	0.0259	57.2383	40.2167	0.4153	0.0198	0.1764	0.0219	16.3882	57.2383
5 / 3 .	55.2922	0.7801	0.0266	0.2228	0.0313	56.353	39.517	0.4704	0.0206	0.1732	0.0265	16.1453	56.353
5 / 4 .	55.6157	0.727	0.0344	0.2375	0.046	56.6606	39.7482	0.4384	0.0267	0.1846	0.0389	16.2238	56.6606
5 / 5 .	55.0011	0.3742	0.0131	0.2604	0.3185	55.9673	39.309	0.2256	0.0101	0.2024	0.2693	15.9508	55.9673
5 / 6 .	55.0737	0.8422	0.0291	0.298	0.0325	56.2755	39.3608	0.5079	0.0225	0.2316	0.0275	16.1251	56.2755
6 / 1 .	55.9481	0.5926	0.0262	-0.0005	0.0781	56.6444	39.9858	0.3574	0.0203	-0.0004	0.066	16.2154	56.6444
6 / 2 .	55.1886	0.3372	0.0262	0.0089	0.1182	55.6791	39.443	0.2033	0.0203	0.0069	0.1	15.9056	55.6791
6 / 3 .	55.1755	0.3518	0.0236	-0.0009	0.1092	55.6592	39.4336	0.2121	0.0183	-0.0007	0.0923	15.9035	55.6592
6 / 4 .	55.6863	0.6675	0.0322	-0.0008	0.0352	56.4205	39.7987	0.4025	0.0249	-0.0006	0.0298	16.1652	56.4205
6 / 5 .	55.5602	0.3221	0.0163	-0.0011	0.1159	56.0135	39.7086	0.1942	0.0126	-0.0009	0.098	16.0009	56.0135
6 / 6 .	56.1577	0.3561	0.0247	-0.0009	0.1065	56.6441	40.1356	0.2147	0.0191	-0.0007	0.0901	16.1853	56.6441
6 / 7 .	55.9974	0.3515	0.0158	-0.0016	0.1085	56.4716	40.021	0.212	0.0122	-0.0013	0.0918	16.1359	56.4716
6 / 8 .	56.1054	0.4116	0.0126	0.0107	0.1068	56.647	40.0982	0.2482	0.0098	0.0083	0.0903	16.1923	56.647
6 / 9 .	55.6243	0.5613	0.0285	-0.0015	0.0262	56.2388	39.7544	0.3385	0.0221	-0.0012	0.0221	16.1029	56.2388
6 / 10 .	39.4044	0.5003	0.0039	0.086	0.0304	40.0249	28.1621	0.3017	0.003	0.0669	0.0257	11.4656	40.0249
7 / 1 .	54.7834	0.8	0.0066	0.1547	0.0394	55.7842	39.1534	0.4825	0.0051	0.1203	0.0333	15.9897	55.7842
7 / 2 .	55.1763	0.3039	0.0254	0.1648	0.2977	55.9682	39.4342	0.1833	0.0197	0.1281	0.2518	15.9512	55.9682
7 / 3 .	55.701	0.3205	0.0165	0.1909	0.1314	56.3602	39.8092	0.1933	0.0128	0.1484	0.1111	16.0856	56.3602
7 / 4 .	55.2049	0.2453	0.025	0.1955	0.1354	55.8062	39.4546	0.148	0.0194	0.152	0.1145	15.9178	55.8062
7 / 5 .	54.7316	0.2871	0.0223	0.1932	0.1368	55.371	39.1164	0.1731	0.0173	0.1502	0.1157	15.7984	55.371
8 / 1 .	55.0316	0.5983	0.0368	0.064	0.0508	55.7815	39.3307	0.3608	0.0285	0.0498	0.043	15.9687	55.7815
8 / 2 .	55.8637	0.6906	0.0195	-0.0009	0.0269	56.5999	39.9255	0.4165	0.0151	-0.0007	0.0228	16.2208	56.5999
8 / 3 .	55.7497	0.258	0.0163	0.0477	0.1259	56.1976	39.844	0.1556	0.0126	0.0371	0.1064	16.0419	56.1976
8 / 4 .	55.2183	0.2698	0.0248	0.0293	0.1245	55.6667	39.4642	0.1627	0.0192	0.0228	0.1052	15.8926	55.6667
9 / 1 .	54.6759	1.0204	0.0066	0.1058	0.0374	55.8462	39.0766	0.6153	0.0051	0.0822	0.0317	16.0353	55.8462
9 / 2 .	55.6671	0.5121	0.0157	0.0006	0.0323	56.2277	39.7849	0.3088	0.0121	0.0005	0.0273	16.0941	56.2277
9 / 3 .	56.1106	0.3334	0.0184	-0.0009	0.057	56.5186	40.1019	0.201	0.0142	-0.0007	0.0482	16.1538	56.5186
10 / 1 .	54.722	0.7106	0.0231	0.0603	0.0323	55.5483	39.1095	0.4285	0.0179	0.0469	0.0273	15.9182	55.5483
10 / 2 .	54.9681	0.6133	0.0316	0.0401	0.0227	55.6759	39.2854	0.3699	0.0245	0.0312	0.0192	15.9458	55.6759
10 / 3 .	55.1263	0.668	0.0211	0.0232	0.0255	55.8641	39.3984	0.4028	0.0163	0.018	0.0216	16.0069	55.8641
10 / 4 .	55.3911	0.6453	0.0166	0.006	0.0229	56.0819	39.5877	0.3891	0.0129	0.0047	0.0194	16.0682	56.0819
10 / 5 .	55.2289	0.5854	0.018	-0.0006	0.0348	55.8666	39.4718	0.353	0.0139	-0.0004	0.0295	15.9988	55.8666
10 / 6 .	54.8508	0.5141	0.0196	-0.0044	0.0467	55.4268	39.2015	0.31	0.0152	-0.0035	0.0395	15.864	55.4268
10 / 7 .	55.1495	0.4489	0.0267	0.1954	0.215	56.0355	39.415	0.2707	0.0207	0.1519	0.1818	15.9954	56.0355
11 / 1 .	50.2015	0.7463	0.0051	0.2001	0.0282	51.1812	35.8787	0.45	0.0039	0.1555	0.0239	14.6691	51.1812
11 / 2 .	55.488	0.7522	0.0356	0.0717	0.0393	56.3869	39.657	0.4536	0.0276	0.0558	0.0332	16.1597	56.3869
11 / 3 .	55.5884	0.7389	0.0249	0.0543	0.0396	56.4461	39.7287	0.4456	0.0193	0.0422	0.0335	16.1769	56.4461
11 / 4 .	55.8035	0.4942	0.0226	0.0469	0.0951	56.4622	39.8824	0.298	0.0175	0.0364	0.0804	16.1475	56.4622
11 / 5 .	55.6958	0.3657	0.0236	0.0385	0.0891	56.2127	39.8055	0.2205	0.0183	0.0299	0.0754	16.0632	56.2127
11 / 6 .	56.1729	0.4893	0.0215	-0.0012	0.0617	56.7441	40.1464	0.2951	0.0167	-0.001	0.0521	16.2348	56.7441
11 / 7 .	56.1162	0.3408	0.0201	-0.0069	0.1007	56.5709	40.1059	0.2055	0.0156	-0.0054	0.0852	16.1641	56.5709
11 / 8 .	56.1677	0.3762	0.0259	0.0027	0.1198	56.6923	40.1427	0.2269	0.0201	0.0021	0.1013	16.1993	56.6923
11 / 9 .	56.1928	0.4432	0.0092	-0.0082	0.1031	56.7401	40.1607	0.2672	0.0071	-0.0063	0.0872	16.2243	56.7401
11 / 10 .	53.0152	0.6383	0.011	0.0005	0.0726	53.7376	37.8896	0.3849	0.0085	0.0004	0.0614	15.3927	53.7376

Appendix 4

Isotope data for subsurface

16/18	% Std Err	18/16	% Std Err	16 cps	% Std Err	18 cps	% Std Err	d18O
494.0403	0.00746	0.002024	0.00746	3970512000	0.265368	8037364	0.2675091	22.49242
493.7352	0.007019	0.002025	0.00702	3938371000	0.200593	7977221	0.2022477	22.49242
493.6334	0.008382	0.002026	0.008382	4020054000	0.264418	8144163	0.2675724	22.70345
493.5559	0.00687	0.002026	0.006869	3960564000	0.097833	8024886	0.09692434	22.86398
493.5122	0.006381	0.002026	0.006381	3967216000	0.311376	8039012	0.3131675	22.95486
493.5335	0.008155	0.002026	0.008152	3868985000	0.241305	7838982	0.2480115	22.91043
493.5912	0.008118	0.002026	0.008118	3884034000	0.235994	7868679	0.2398747	22.79078
493.4852	0.009659	0.002026	0.009659	3918487000	0.243456	7940447	0.2469846	23.01039
493.4312	0.013106	0.002027	0.01311	3914276000	0.230064	7932771	0.2299552	23.12297
493.5285	0.005827	0.002026	0.005827	3920314000	0.155323	7943663	0.1536138	22.92053
493.0558	0.00958	0.002028	0.00958	3913268000	0.227293	7936764	0.2268336	23.90143
493.3059	0.007424	0.002027	0.007424	3892155000	0.168818	7889640	0.1690848	23.38246
493.2675	0.010497	0.002027	0.010495	3762309000	0.216026	7627327	0.2184244	23.46222
493.3016	0.007219	0.002027	0.007219	3878831000	0.208844	7862712	0.2105619	23.39154
493.1442	0.007398	0.002028	0.007397	3792150000	0.130961	7689740	0.1322868	23.71818
493.1437	0.006438	0.002028	0.006438	3847851000	0.196695	7802606	0.1993676	23.71918
493.0565	0.00785	0.002028	0.00785	3903856000	0.129322	7918201	0.1266731	23.89992
492.993	0.005423	0.002028	0.005422	3901254000	0.183001	7912916	0.186147	24.03168
493.2343	0.007682	0.002027	0.007682	3851051000	0.178798	7814514	0.1677886	23.53088
493.2431	0.005622	0.002027	0.005621	3842333000	0.152206	7789946	0.1535449	23.5127

4.93E+02	1.80E-02	2.03E-03	1.80E-02	2.76E+09	5.19E-01	5.59E+06	5.06E-01	***23.78***
4.93E+02	2.49E-02	2.03E-03	2.49E-02	2.58E+09	4.78E-01	5.22E+06	4.57E-01	***23.31***
4.93E+02	1.90E-02	2.03E-03	1.90E-02	2.72E+09	5.55E-01	5.51E+06	5.38E-01	***23.29***
4.93E+02	1.68E-02	2.03E-03	1.68E-02	2.71E+09	4.42E-01	5.48E+06	4.28E-01	***23.57***
4.94E+02	1.30E-02	2.02E-03	1.30E-02	2.60E+09	4.69E-01	5.27E+06	4.59E-01	***22.37***
4.94E+02	2.38E-02	2.03E-03	2.38E-02	2.58E+09	4.46E-01	6.39E+06	5.53E-01	***22.90***
4.93E+02	1.63E-02	2.03E-03	1.63E-02	2.59E+09	5.25E-01	6.34E+06	7.66E-01	***23.26***
4.94E+02	2.04E-02	2.03E-03	2.05E-02	2.50E+09	5.70E-01	6.42E+06	8.98E-01	***22.98***
4.93E+02	1.66E-02	2.03E-03	1.66E-02	2.56E+09	4.35E-01	6.18E+06	7.27E-01	***23.35***
4.94E+02	1.21E-02	2.02E-03	1.21E-02	2.58E+09	5.51E-01	6.35E+06	6.57E-01	***22.55***
4.93E+02	1.72E-02	2.03E-03	1.72E-02	2.53E+09	4.68E-01	5.12E+06	4.55E-01	***23.64***
4.93E+02	1.76E-02	2.03E-03	1.76E-02	2.52E+09	5.24E-01	5.11E+06	5.08E-01	***23.70***
4.93E+02	1.47E-02	2.03E-03	1.47E-02	2.47E+09	6.38E-01	5.00E+06	6.24E-01	***23.47***
4.93E+02	1.90E-02	2.03E-03	1.90E-02	2.46E+09	1.94E-01	4.99E+06	1.82E-01	***23.52***
4.93E+02	1.40E-02	2.03E-03	1.40E-02	2.56E+09	7.02E-01	5.18E+06	6.90E-01	***23.51***
4.93E+02	1.80E-02	2.03E-03	1.80E-02	2.35E+09	6.60E-01	4.77E+06	6.46E-01	***23.58***
4.93E+02	1.82E-02	2.03E-03	1.82E-02	2.48E+09	5.04E-01	5.03E+06	4.90E-01	***24.04***
4.93E+02	1.99E-02	2.03E-03	1.99E-02	2.48E+09	6.83E-01	5.03E+06	6.66E-01	***23.41***